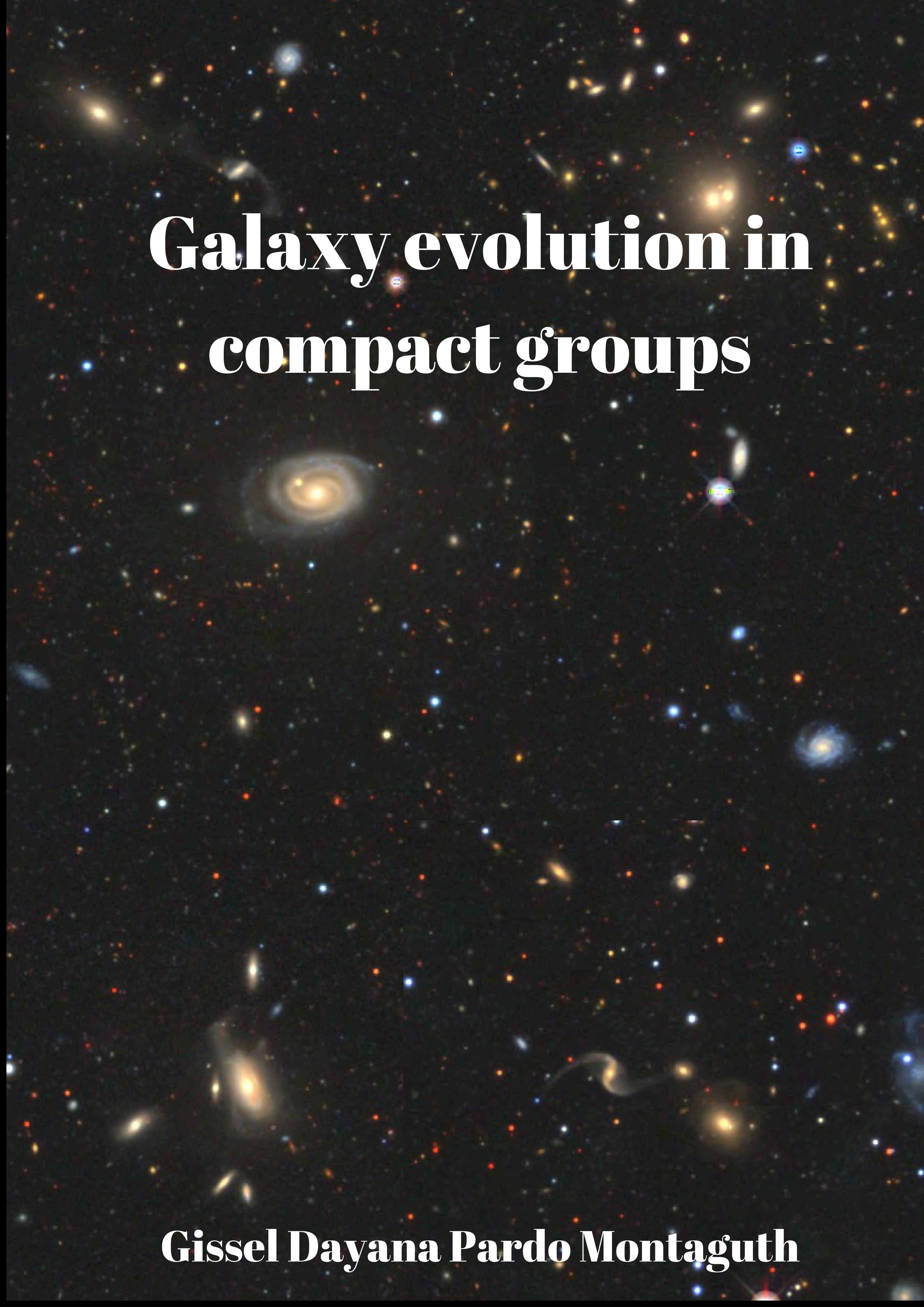

Galaxy evolution in compact groups

Gissel Dayana Pardo Montaguth

Galaxy evolution in Compact Groups

Gissel D. Pardo Montaguth

UNIVERSIDAD
DE LA SERENA
CHILE

Doctoral Thesis

To fulfill the requirements for the degree of Doctorate in Astronomy
at Universidad de La Serena by

Gissel Dayana Pardo Montaguth

under the supervision of
Dr. Antonela Monachesi and Dr. Sergio Torres Flores

October 7, 2024

Dissertation Committee:
Dr. Yara Jaffe (Universidad de Valparaiso)
Dr. Analía V. Smith Castelli (Instituto de Astrofísica de La Plata)
Dr. Rodrigo Carrasco (Gemini Observatory/NSF's NOIRLab)
Dr. Ricardo Amorín (Centro de Estudios de Física del Cosmos de Aragón)

Doctoral Advisory Committee:
Dr. Claudia Mendes de Oliveira (Universidade de São Paulo)
Dr. Ricardo Amorín (Centro de Estudios de Física del Cosmos de Aragón)

Cover Image: A collage of compact group images created using Sky Viewer from the Legacy Survey. The images were generated using data from the z, r, and g filters to create the RGB composite.

Credit: The images were taken from the Legacy Surveys / D. Lang (Perimeter Institute).

Cuando era niña, me decían que tenía una estrella que me cuidaba desde el cielo... Este trabajo es un homenaje a la memoria de papá, Dagoberto Pardo, y a todos aquellos que han sufrido en medio de la violencia del conflicto armado colombiano.

Contents

Abstract

The study of galaxy evolution often focuses on the transition from late-type, star-forming galaxies to early-type, quiescent ones, involving both internal mechanisms, such as star formation and Active Galactic Nucleus feedback, and external environmental interactions. Compact Groups (CGs) of galaxies are ideal for examining how galaxy-galaxy interactions shape properties due to their high galaxy densities and low velocity dispersions. This thesis investigates the physical properties and dynamics of 340 CGs in the Stripe 82 region using multi-band data from the Southern Photometric Local Universe Survey (S-PLUS) project, structural parameters from the MegaMorph code, star formation rates from the GALEX-SDSS-WISE LEGACY catalogue, and emission line data from Sloan Digital Sky Survey (SDSS) spectra. This analysis aims to understand how dense environments, particularly CGs, impact the evolution and properties of galaxies.

We classify the galaxies based on their morphology using the Sérsic index (n) in the r band and colour ($u-r$). Our analysis shows that CGs contain a higher fraction of early-type galaxies (ETGs), characterised by $(u-r) > 2.3$ and $n > 2.5$, and a lower fraction of late-type galaxies (LTGs), with $(u-r) \leq 2.3$ and $n \leq 2.5$, as well as smaller effective radii, compared to a control sample of field galaxies. We suggest that the smaller effective radii observed in galaxies within CGs may indicate that tidal interactions contribute to material loss.

Our study also reveals a higher proportion of quenched galaxies in CGs, with a notable anticorrelation between the Sérsic index and specific star formation rate (sSFR) for *transition galaxies* in CGs, defined as those with $(u-r) > 2.3$ and $n \leq 2.5$, suggesting an ongoing transformation process. We find a bimodal distribution in the $R_e - n$ plane for *transition galaxies* in CGs, which is not observed in the control sample. This suggests a *peculiar population* of smaller, more compact galaxies in CGs, possibly undergoing morphological transformation.

Furthermore, we identify that not all CGs are isolated; some are subsets of larger groups or clusters, which we refer to as non-isolated CGs. We find that non-isolated CGs exhibit higher velocity dispersions and a greater prevalence of quenched galaxies compared to isolated CGs. Additionally, they contribute to the fraction of *peculiar galaxies* among *transition galaxies*.

We propose an evolutionary scenario for CGs, suggesting that larger structures accelerate the quenching process and morphological transformation of their member galaxies, highlighting the importance of the environment in which CGs are embedded for the evolution of their galaxies. Therefore, in this thesis, we analyse the morphological properties of galaxy groups located in dense environments such as Abell 1644.

Given the richness of the physical processes taking place in galaxies within CGs, we performed a spatially resolved analysis of the properties of galaxies in CGs. We used integral field spectrographs (IFS) data to study the ionised gas and stellar components from a 3D perspective. Our sample is extended to include CGs from the northern hemisphere to ensure a comprehensive analysis of galaxies, considering that the MaNGA data largely focuses on the northern sky. We identify a sample of 549 galaxies in CGs and 1098 field galaxies. The results show that galaxies in denser environments, like CGs, tend to have older populations compared to the control sample. Additionally, for star-forming galaxies, we study the median Σ_{SFR} profiles and find no significant differences between galaxies in CGs and the control sample. The profiles are comparable when considering the uncertainties. For galaxies with nuclear activity, CGs have higher Σ_{SFR} values and flatter slopes than the control sample. We do not observe significant differences in the median metallicity gradients between CGs and the control sample.

Overall, this thesis underscores the importance of considering the broader environment in the study of CGs and offers a comprehensive analysis of how dense and interacting environments accelerate mor-

phological transformations and quenching processes, thereby enriching our understanding of galaxy evolution.

Chapter 1

Introduction

“The last night of navigation, while keeping watch next to the general’s hammock, José Palacios heard Carreño say from the bow of the champán: ‘Seven thousand eight hundred and eighty-two.’ ‘What are we talking about?’ José Palacios asked. ‘About the stars,’ Carreño said. The general opened his eyes, convinced that Carreño was talking in his sleep, and sat up in the hammock to see the night through the window. It was immense and radiant, and the sharp stars left no space in the sky. ’There must be like ten times more,’ said the general. ‘They are the ones I mentioned,’ said Carreño, ‘plus two wandering ones that passed by while I was counting them.’ Then, the general left the hammock, and he saw him lying on his back on the bow, more awake than ever, with his bare torso crossed with tangled scars, and counting the stars with the stump of his arm.” Fragment from the book “The General in his labyrinth” by Gabriel García Márquez.

In this little piece from one of Gabo’s books, he talks about the romantic side of looking at the stars, which is something that has fascinated people for generations. Those dots and patches in the sky have led to countless questions, from deep thoughts to scientific ones. About 100 years ago, there was a big question among astronomers: was the Andromeda Nebula part of our own Milky Way or not? This debate, called “The Great Debate,” happened between Curtis and Shapley. Curtis thought Andromeda was a galaxy on its own, while Shapley thought it was part of ours (Shapley & Curtis 1921). But this debate ended when Hubble (1925), using Cepheid stars, calculated the distance of Andromeda and found it was 285 kpc away, bigger than Shapley’s 70 kpc estimate for the Milky Way. Therefore, it was outside our Galaxy. At that moment, the Andromeda Nebula became the Andromeda Galaxy. This changed how astronomers saw things and led to new areas of study, such as extragalactic astronomy.

Currently, one of the questions that has been widely investigated and remains open in extragalactic astronomy is how galaxies transform from star-forming galaxies into passive galaxies with little to no star formation. Additionally, it has been studied how the environment in which galaxies reside can either facilitate or impede this transformation. This chapter aims to provide a general context of what is currently known about how galaxies evolve in the local universe and how the environment influences galaxy evolution, especially how dense structures with low-velocity dispersion affect galaxy properties. Therefore, we will embark on a journey from morphological classification and the main properties of each galaxy type (section 1.1), to the importance of the environment in which galaxies reside, as well as their internal mechanisms, for understanding their evolution (see section 1.2). Additionally, we will explore the properties of Compact Groups (CGs) of galaxies and their relevance deduces how dense environments drive and shape the properties of their galaxy members (see section 1.3). Finally, given the context provided in the previous sections, we will explain the objectives of this thesis, which aims to study galaxies in CGs to understand how galaxies evolve in dense environments (see section 1.4).

1.1 Galaxy morphology: building block for understanding their evolution

Galaxies have been classified over the past 100 years based on how their morphology (e.g. Hubble 1926, De Vaucouleurs 1959, Kormendy & Bender 1996, Vika et al. 2015a), their ionise gas (Baldwin et al. 1981, Veilleux & Osterbrock 1987, Cid Fernandes et al. 2010), and their environment (isolated, pair or in groups) (e.g. Yang et al., 2007). The study of galaxy morphology aims to understand galaxy shapes to uncover the physical nature behind the observed differences. Different methods have been used to classify the morphologies of the galaxies, from visual inspection by expert astronomers or by volunteers through citizen science projects like Galaxy Zoo (Lintott et al. 2008). Volunteers help classify images to determine if they show stars or galaxies and their shapes. Other methods involving galaxy colors and light concentration (Vika et al. 2013) are among the techniques that have been implemented. These parameters are easy to measure and allow the classification of many galaxies with minimal effort. Nowadays, artificial intelligence and machine learning are being used to classify morphologically large datasets of galaxies (e.g. Variawa et al. 2022).

Hubble (1926), performed the first visual classification of galaxies, known as the Hubble sequence or Hubble Tuning Fork diagram (Variawa et al. 2022), which is shown in Figure 1.1.1. Today, this classification is still used with some variations. Galaxies are categorized into four types: elliptical (E), lenticular (S0), spiral (S), and irregular (Irr). Hubble called ellipticals and lenticulars "early-type" galaxies and spirals and irregulars "late-type." He believed galaxies evolved from ellipticals to spirals, but now we know late-type ones have more cold gas and young stars. Therefore, Hubble's idea was incorrect, but the terms "late-type" and "early-type" are still used, though with caution.

1.1.1 Elliptical galaxies

Elliptical galaxies have an ellipsoidal mass distribution, which is where their name comes from. They contain little cold gas and dust and generally have reddish photometric colours, indicating dominance by old stars. The small amount of gas they contain is usually hot and highly ionised (Blanton & Moustakas 2009). In the Hubble sequence, elliptical galaxies are classified as 'E', followed by a number, which is defined as 10(1-b/a), with b/a being the apparent flattening, that indicates how elongated they are; in other words, a higher number signifies that the galaxy appears more stretched out relative to its width.

On the other hand, when measuring the internal rotation velocities of elliptical galaxies, it is found that they have mean rotation velocities much lower than their velocity dispersions, indicating that the shapes of these galaxies are not due to the rotation but rather to the dispersion of the velocities of the stars (Ballesteros & Gonzalez 1994). The kinematic and photometric properties of elliptical galaxies are correlated, through the relationship known as the Faber-Jackson relation (Faber & Jackson 1976), which is an empirical relationship where the luminosity of the galaxy is proportional to its central velocity dispersion raised to a power that is approximately 4.

1.1.2 Spiral galaxies

Spiral galaxies consist of a disk with spiral arm structures, where young stars, gas, and dust are observed. They typically have a reddish central bulge mainly composed of old stars. In Hubble's

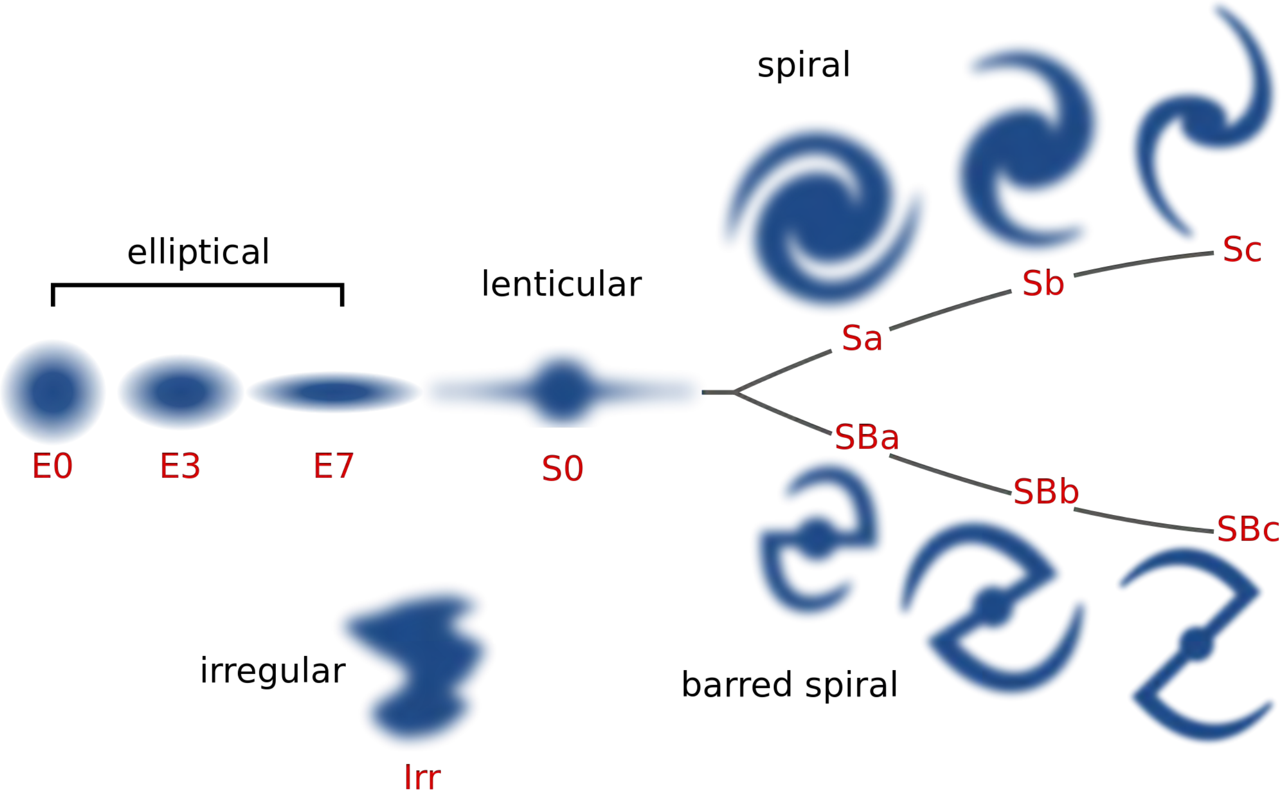

Figure 1.1.1: Hubble sequence or Hubble Tuning Fork diagram by Variawa et al. (2022).

classification, they are symbolized with the letter S. Additionally, they are subclassified into three classes: Sa, Sb, and Sc. This subdivision depends on three factors: the first is the fraction of the bulge's luminosity with respect to the disk, the second is how tightly the spiral arms wind, indicated by the pitch angle, which is the angle between the arm and the tangent to the circle of radius (Hubble 1936, de Vaucouleurs 1959), and the last factor relates to the ratio of M_{H_2}/M_{H_I} in the galaxies. It has been observed that these characteristics are related; for example, galaxies with bright bulges have more tightly wound arms with higher ratios of M_{H_2}/M_{H_I}, and these galaxies are known as Sa, while those opposite to them have small bulges, broad arms, and lower ratios of M_{H_2}/M_{H_I} regions, and are called Sc galaxies. Furthermore, spiral galaxies are classified into two types: barred (SB) and normal (S) galaxies, where barred galaxies have a central bar of stars, while normal spiral galaxies do not have this central bar. In this classification, the Milky Way is an SBbc, meaning it is a barred galaxy with a less predominant bulge (Carroll & Ostlie 2017)

Unlike elliptical galaxies, spirals with the same luminosity as ellipticals tend to be bluer, mainly because there is a greater amount of gas available for the star formation process (Blanton & Moustakas 2009). In general, spiral galaxies exhibit color gradients (Choi et al. 2007), with the inner parts being redder than the outer parts.

The kinematics of stars and gas in the disk of spiral galaxies are characterized by circular orbits. By measuring the velocity at different galactic radii, the rotation curve $V_{rot}(R)$ is obtained. With the rotation curve, the gravitational mass of the galaxy can be estimated, assuming spherical symmetry for simplicity. The total mass enclosed within the radius r is given by:

$$M(r) = \frac{rV_{rot}^2(r)}{G} \tag{1.1.1}$$

where G is the gravitational constant. The velocity observed in the rotation curves of spiral galaxies becomes almost constant at large radii, a behaviour explained by the existence of a dark matter halo (Rubin & Ford 1970). Moreover, the kinematics of the bulge are slightly more complex to study because the light coming from the bulge is contaminated by the brightness and extinction of the disk, but data suggest that it rotates faster than the disk (Kormendy & Illingworth 1982). Another feature is that there is a relationship between the maximum rotation velocity of the disk and the galaxy's luminosity, known as the Tully-Fisher relation (Tully & Fisher 1977), where $L \propto V_{max}^{\alpha}$, and the observed value of α is between 2.5 and 4. This relation is used to find the distances to galaxies.

1.1.3 Lenticular galaxies

Lenticular galaxies are an intermediate case between ellipticals and spirals; they are represented by in Hubble's classification. Like spiral galaxies, they have a disk, but spiral arms are not observed in lenticular galaxies. They have a large central bulge, where the bulge-to-disk luminosity ratio is much larger than in spiral galaxies. They are characterized by having consumed or lost most of their neutral gas, therefore having very little or no star formation. However they contain large amounts of dust in their disks (Caldwell et al. 1993). Despite the morphological differences, lenticular and elliptical galaxies share common spectral characteristics.

In terms of kinematical properties, the lenticulars share similarities with spiral and elliptical galaxies. The bulge is similar to elliptical galaxies, where velocity dispersion dominates the gravitational support. Also, the kinematic of lenticular galaxies are dominated by the disk, which is stable due to the rotation of the stars. Lenticular galaxies have much higher ratios of rotation and dispersion velocities than elliptical galaxies because the rotation velocity of the disk is not negligible. Lenticular galaxies also follow the Tully-Fisher relation, but with a displacement in the luminosity axis because they are dominated by old and red stars (den Heijer et al. 2015).

1.1.4 Irregular galaxies

Irregular galaxies, classified as Irr in Hubble's scheme, are amorphous and among the smallest galaxies. They contain significant amounts of gas and dust and are distinguished by their high star formation rates, which makes them particularly bright in blue wavelengths (Hunter et al. 1982). Despite their lack of defined structure, they share some characteristics with spiral galaxies, such as hosting both old and young stars, along with atomic, molecular, and ionized gas. Their irregular internal kinematics further highlight their unordered nature (Carroll & Ostlie 2017).

This type of galaxy is divided into Irr I and Irr II, with the former showing some structure, while the latter is completely amorphous. In fact, Irr II includes various types of chaotic galaxies, for which there are apparently many different explanations, most commonly resulting from galaxy-galaxy interactions. Typically, irregular galaxies have masses between $10^8 M_\odot$ and $10^{10} M_\odot$, with diameters ranging from 1 to 10 kpc (Hunter & Elmegreen 2004).

1.2 The role of environment in galaxy evolution

In general, early-type galaxies have redder colours than late-type galaxies. This shows that galaxy morphology is correlated with the physical properties of galaxies. Interestingly, when observing the colours of galaxies in the Local Universe, they can be separated into two groups, based on their star formation activity, in a color-magnitude diagram (CMD). Figure 1.2.1 shows a schematic view of this bimodal distribution, where the y-axis represents colour and the x-axis represents magnitude: blue galaxies with star formation (blue cloud) and red galaxies with little or no recent star formation (red sequence) (e.g. Strateva et al. 2001, Bell et al. 2004, Baldry et al. 2006). Between these populations, there is a narrow region sparsely populated by galaxies, known as the green valley (Martin et al. 2007), which exhibits intermediate characteristics (Pan et al. 2013). Galaxies migrate in the CMD from high star-forming galaxies to cease star-forming galaxies in a process known as quenching (e.g. Peng et al. 2010b), where the green valley is considered a transitional stage. It has also been found that galaxies can migrate from the red sequence to the green valley through a rejuvenation process and then return to the red sequence (e.g. Graham et al. 2017). The details of the processes that drive galaxies from the blue cloud to the red sequence are an ongoing topic of current research.

Additionally, observational studies show a clear relationship between galaxy morphology and galaxy number density. Dressler (1980) was the first to demonstrate this by studying 55 rich clusters. Dressler (1980) shows that the fraction of elliptical galaxies increases as a function of local density. Whilst, the fraction of late-type galaxies decreases (see Figure 1.2.2). For lenticular galaxies, their number fraction also grows in dense environments, but less noticeably than the fraction of ellipticals. This is known as the morphology-density relation.

Another important relationship found in galaxy cluster studies is the link between galaxy morphology and distance from the cluster centre. Whitmore & Gilmore (1991) reviewed the same clusters as Dressler (1980) and found that the fraction of elliptical galaxies increases in the central regions of clusters. Later, Goto et al. (2003), using a larger data sample from SDSS, confirmed both relationships. These studies show a connection between the environment and galaxy evolution.

Haines et al. (2015) conducted a similar analysis, considering 30 massive clusters. They studied much farther from the cluster centre, reaching $5 \times R_{500}$, where R_{500} is the radius where the density is

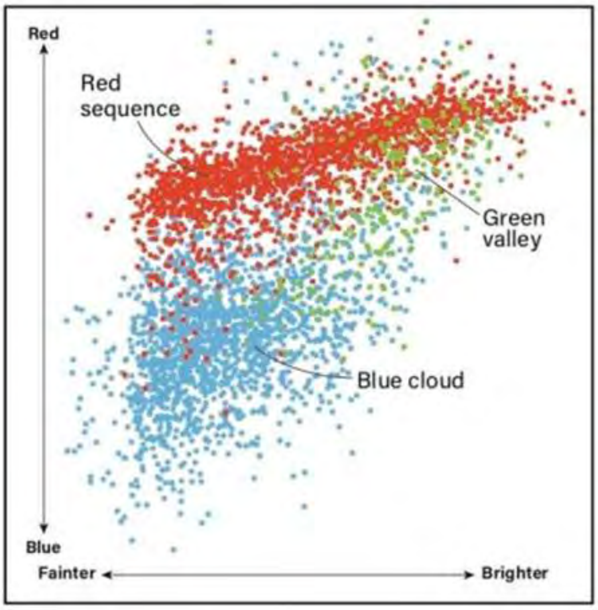

Figure 1.2.1: Color-magnitude diagram scheme of a population of galaxies showing the three main regions: the blue cloud, the green valley, and the red sequence. Credit: Astronomy: Roen Kelly, after Gavazzi et al. (2010).

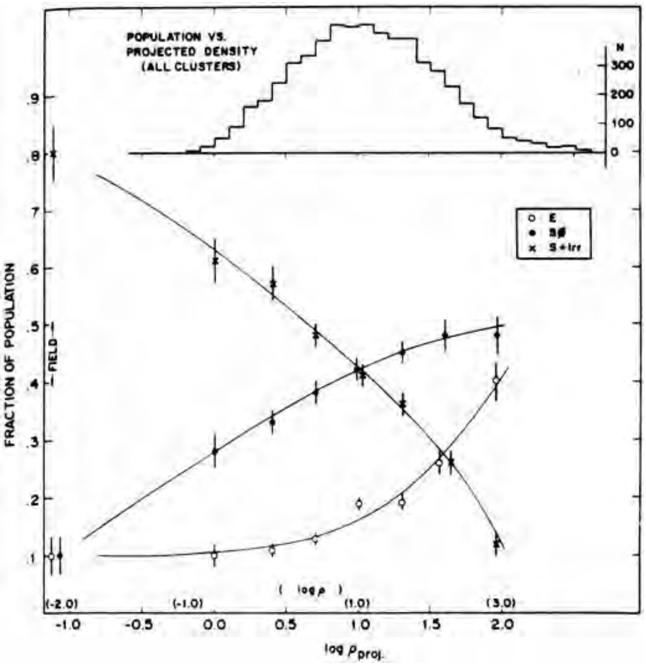

Figure 1.2.2: Fraction of each morphological type as a function of local density. The unfilled circles represent elliptical galaxies, the filled circles represent lenticular galaxies, and the crosses represent irregular and spiral galaxies combined. Figure extracted from Dressler (1980).

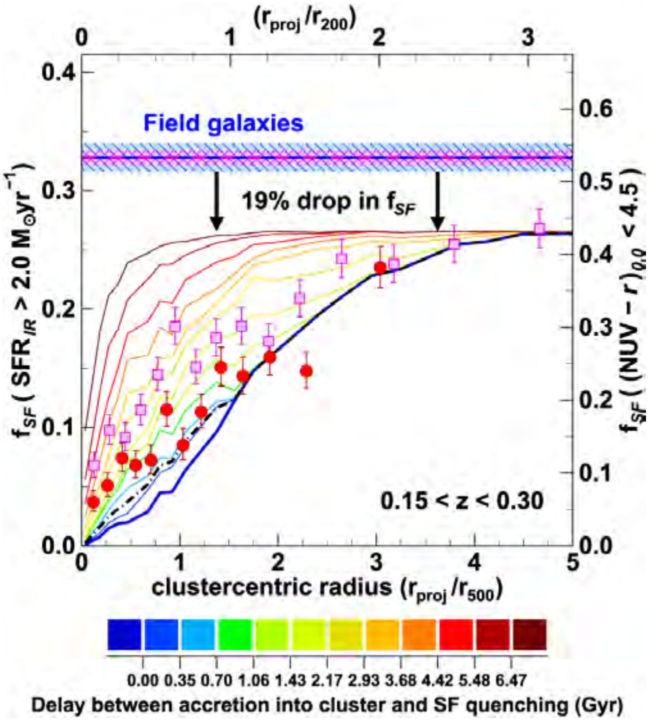

Figure 1.2.3: Fraction of star-forming galaxies as a function of distance from the cluster centre. The red and magenta points show the observed star formation fraction as a function of cluster-centric radius, based on infrared and ultraviolet data, respectively. The blue horizontal line represents the fraction of star-forming galaxies observed in the field, with the shaded region indicating 1 confidence levels. The coloured curves depict the predicted SF-radius relations from simulations, assuming various delays in the quenching of star formation after galaxies are accreted into the cluster. The simulations in this figure assume that the fraction of star-forming galaxies in infalling groups is reduced by 19% compared to the field. The black dot-dashed curve represents the scenario where star formation is instantaneously quenched when galaxies reach the pericentre. Figure extracted from Haines et al. (2015).

500 times that of the universe. They looked at the fraction of star-forming galaxies as a function of distance from the cluster centre, as shown in Figure 1.2.3. In this figure, the magenta points represent the fraction of star-forming galaxies measured using ultraviolet data, and the red points use infrared data. The fraction of star-forming galaxies increases with distance from the cluster centre, indicating that the fraction is small in the cluster centres. This confirms that the environment affects galaxy properties, favouring quenching.

Additionally, the figure compares these fractions to those observed in field galaxies, represented by the blue horizontal line. However, even at large distances from the cluster centre, the fraction of star-forming galaxies does not reach the level observed in the field. To reconcile their observations with simulations (depicted by the solid lines), Haines et al. (2015) had to assume that the fraction of star-forming galaxies falling into clusters was 19% lower than in the field. This reduction suggests that galaxies experience environmental effects before entering the cluster, a phenomenon known as pre-processing. In galaxy groups, star formation is often suppressed, leading to a fraction of star-forming and early-type galaxies that is intermediate between those in the field and those in the cluster (e.g., Zabludoff & Mulchaey 1998, Wilman et al. 2005).

A recent study by Lopes et al. (2024) analysed 238 clusters with a redshift of $z \leq 0.1$ to determine

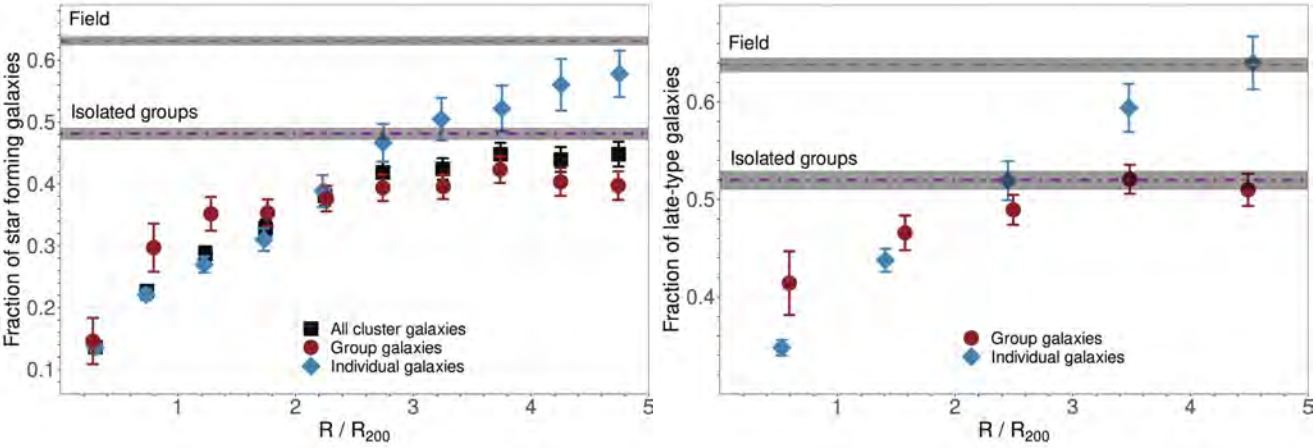

Figure 1.2.4: Left panel: Fraction of star-forming galaxies as a function of distance from the centre. In black, the fraction of all galaxies in the clusters; in red, those in groups; and in blue, the fraction of galaxies infalling into the clusters as isolated galaxies. The red dashed line represents the fraction of star-forming galaxies in isolated groups, and the grey dashed horizontal line indicates the fraction of these galaxies in the field. Right panel: This panel is similar to the left panel but shows the fraction of LTGs. These figures were published by Lopes et al. (2024).

if galaxies entering clusters, either alone or in groups, experience quenching up to 5 times their R_{200} radius. They discovered that star-forming galaxies in infalling groups behave differently compared to those infalling as isolated galaxies. As shown by the red points in Figure 1.2.4, group galaxies (red points in left panel in Figure 1.2.4) show a lower fraction of star-forming objects even at $5 \times R_{200}$. Interestingly, at this radius, individual galaxies have star formation rates similar to those in the field (blue points in left panel in Figure 1.2.4). This indicates that the group environment quenches star formation before the galaxies arrive in the cluster. They also found that the pre-processing effect is more pronounced in more massive groups, evidenced by fewer star-forming galaxies in larger groups. This highlights the importance of studying galaxy groups to understand pre-processing across different group masses. Lopes et al. (2024) also investigate how the fraction of LTGs varies with distance from the cluster centre (see the right panel of Figure 1.2.4). To classify galaxies as LTGs, they employed the T-type classification system, identifying galaxies with T-type values greater than 0, in addition to using a bulge-to-disk probability of less than 0.6 and a disk probability greater than 0.8, as estimated by Domínguez Sánchez et al. (2018).They found that there is also morphological pre-processing in galaxies that fall in groups compared to those that fall individually.

Oxland et al. (2024) studied galaxies in groups with masses between $13 \leq log(M_{\rm halo}/M_{\odot}) < 14$ and clusters with $\log(M_{\rm halo}/M_{\odot}) \geq 14$, comparing them to field galaxies. They used the projected phase space to estimate the time since infall and examined the specific star formation rate and morphology of each galaxy. They observed clear trends, increasing quenched and elliptical fractions with infall time for galaxies in both groups and clusters, especially for low-mass galaxies in clusters.

Furthermore, they estimated the time scales for quenching and morphological transformation. Consistent with Lopes et al. (2024), they found that star formation quenching happens faster than morphological changes in both environments. By comparing field galaxies to recently infalling galaxies, they concluded that pre-processing affects both star formation and morphology, with a stronger impact on star formation rates. Their findings support mechanisms that quickly suppress star formation, while other processes, acting over longer timescales, drive morphological changes.

1.2.1 Internal and environmental processes that affect galaxy evolution

To understand how the environment affects galaxy evolution, we need to comprehend the mechanisms that inhibit star formation and promote the transition from the blue cloud to the red sequence in the colour-magnitude diagram. (see Figure 1.2.1). There's a dichotomy in the mechanisms causing quenching because both internal and environmental processes can affect the gas reservoir in galaxies, hindering their ability to form new stars.

Internal processes, often referred to as "mass quenching" or "internal quenching," are related to the galaxy's stellar mass and typically involve gravitational instabilities or energetic feedback effects. Among these mechanisms are "star formation feedback," which includes stellar and supernova feedback. Stellar feedback involves hot stars, including pre-main-sequence stars and early stars, producing stellar winds and ionising radiation, heating surrounding molecular clouds (e.g., Cantalupo 2010, Hayward & Hopkins 2017). Supernova feedback occurs when supernova explosions generate shockwaves that heat the surrounding gas, preventing it from cooling and collapsing to form new stars, even stripping material from galaxies (e.g., Efstathiou 2000).

Another internal feedback mechanism is the one linked to "Active Galactic Nuclei (AGN)". It occurs when radiation, winds, and jets from massive AGN interact with the interstellar medium, potentially ejecting or heating gas from galaxies (e.g., Fabian 2012, Zhu et al. 2023b). In addition to the previous mechanisms, "bar quenching" is a process related to disk galaxies with a stellar bar, where the bar helps transfer gas from the outskirts to the central regions, increasing star formation in the nucleus and along the bar. However, this process can also suppress star formation in the area between the nucleus and the bar's ends, reducing the overall star formation rate of the galaxy (e.g., Khoperskov et al. 2018, George et al. 2019).

On the other hand, "morphological quenching" affects spiral galaxies differently. In these galaxies, where most of the stellar mass is in a rotating disk, gas in the disk can efficiently form stars. However, in an early-type galaxy, the high concentration of stellar mass in the centre and the transition from the stellar disk into a spheroid create a steeper potential well and reduce the self-gravity of the gas disk. This prevents the gas from forming star clusters because disruptive tidal forces cannot be balanced by the gas's self-gravity (e.g., Martig et al. 2009).

In contrast, environmental processes, known as "environmental quenching," refer to mechanisms that affect galaxies due to their surroundings and the characteristics of their neighbourhood. Galaxy mergers are an important environmental mechanism, especially in galaxy groups, where the relative velocities among the galaxies are low enough for collisions to occur. Depending on the mass of the galaxies, these mergers are called major or minor mergers. When galaxies have similar masses, it is known as a major merger, which can turn two gas-rich spiral galaxies into a gas-poor elliptical galaxy (eg. Toomre & Toomre 1972). In contrast, if the mass ratio is about 1:10, it is considered a minor merger, which does not drastically change the morphology of the massive galaxy but allows it to grow in mass and size (e.g Lambas et al. 2012).

Another important mechanism is "galaxy harassment." This occurs due to tidal interactions when a galaxy passes rapidly close to another without merging, particularly in the inner regions of clusters (Moore et al. 1996a). These interactions can induce star formation and create tidal tails, deformations, bars, and asymmetries in the galaxy. Additionally, this process can destroy the disks of satellite galaxies.

"Ram pressure stripping" (e.g., Gunn & Gott 1972, Abadi et al. 1999) is another mechanism that involves the interaction between a galaxy and the intracluster or intragroup medium. This process occurs when a galaxy enters a cluster, and the pressure exerted by the intracluster gas on the galactic gas moving through it overcomes the restoring pressure from the galaxy's surface mass density. Con-

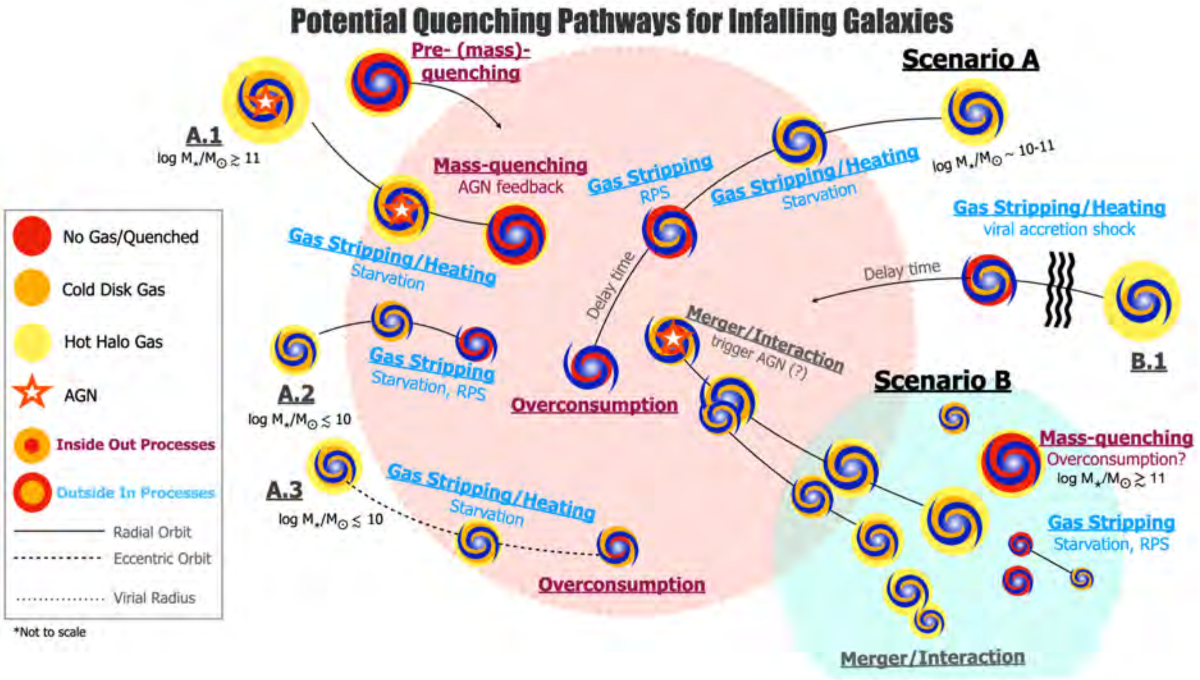

Figure 1.2.5: Diagram of the different pathways galaxies can take upon entering a cluster, emphasising simplified mechanisms galaxies may undergo. This schematic was created by Alberts & Noble (2022).

sequently, the galaxy loses its gas, reducing its gas reservoir and leading to a decrease or cessation in star formation.

Finally, "galaxy strangulation" occurs when a galaxy enters a cluster and its gas supply is cut off. Despite this, a galaxy can continue forming stars for several gigayears, increasing its stellar mass and metallicity. However, eventually, star formation stops due to the lack of gas supply (e.g. Peng et al. 2015).

The balance between internal and external processes experienced by a galaxy is crucial for understanding its evolution. Gas accretion and cooling are necessary elements, but feedback processes counteract cooling by expelling gas from galaxies. It is expected that star formation in galaxies is regulated to some extent by these processes. In galaxies of different masses, the balance between feedback and star formation can occur at very different scales. This is why it is important to consider galaxy masses when comparing galaxy properties. Indeed, Peng et al. (2010a) shows that in the local universe, mass quenching dominates in massive galaxies ($M_* > 10^{10.2} M_\odot$), while environmental quenching dominates in smaller galaxies. However, quenching processes are complex, making it difficult to separate the different mechanisms. It is expected that at least some of these processes act simultaneously and are effective in overlapping ways. Figure 1.2.5 summarises the different mechanisms that galaxies can experience in different environments (figure taken from Alberts & Noble 2022). For simplicity, morphological transformations are not shown in this cartoon. Depending on their mass, galaxies can reach clusters in isolation, pre-quenched by mass quenching, or fall in through groups where they have already undergone environmental effects. Then, when galaxies and groups fall into clusters, the galaxies experience environmental effects, known as post-processing (e.g. Kelkar et al. 2023).

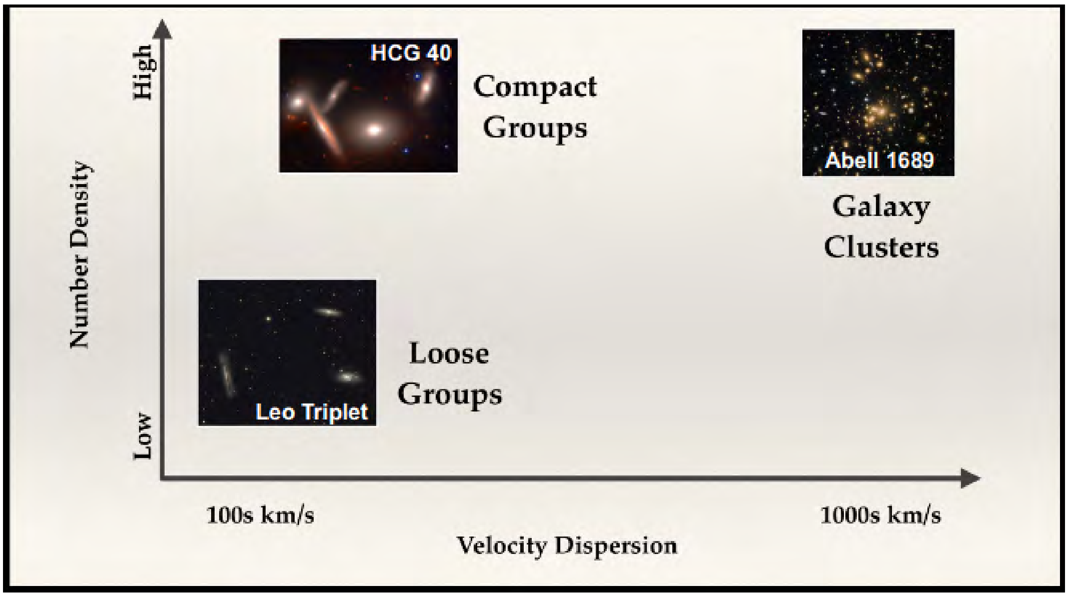

Figure 1.2.6: Diagram representing the galaxy density in compact groups, loose groups, and clusters as a function of the velocity dispersion of these systems. This schematic was created by S. Gallagher.

1.2.2 The importance of galaxy groups in the study of galaxy evolution

As we have seen throughout this chapter, studying galaxies in different environments is crucial to understanding their evolution. In the local Universe, galaxies are most commonly found in groups (Eke et al. 2006), making galaxy groups a good target for understanding how the environment affects the evolution of galaxies. Additionally, they allow us to understand the preprocessing.

Although there is no clear classification between clusters and groups, it is usually said that any structure with fewer than 50 galaxies is a group, and any with more is a cluster. Typically, groups are divided into three main categories: loose, fossil, and compact groups (CGs). Loose groups (LG) are collections of galaxies where the relative separations between galaxies are much larger than the sizes of the galaxies themselves. They have very low velocity dispersions, around 150 km/s Lovisari et al. 2021).

Fossil groups are dominated by a single bright elliptical galaxy (Jones et al. 2003). It was suggested that fossil groups formed earlier, but studies have shown that fossil groups probably formed and evolved similarly to non-fossil groups. For example, the central galaxies in fossil groups have been found to show similar stellar ages and metallicities to the brightest cluster galaxies in non-fossil groups. The large magnitude gap observed within the galaxies of each fossil group might represent a transient phase in the evolution of groups and clusters, related to recent mergers rather than ancient formation (see citations in Aguerri & Zarattini 2021).

Compact groups (CGs) contain between 3 and 10 galaxies, where the relative separations between the galaxies are comparable to the sizes of the galaxies. Therefore, they occupy a radius of about hundreds of kiloparsecs (Sohn et al. 2016), with average velocity dispersions around 200 km/s (Hickson 1982).

In Figure 1.2.6, a schematic comparison between loose groups, compact CGs, and clusters is presented, showing the relationship between galaxy density and velocity dispersion. In groups, galaxy interactions are expected to take longer due to their low velocity dispersion, while in clusters, these encounters are quicker. However, because of the higher galaxy density in CGs and clusters compared to loose groups, more interactions are expected in these environments. In particular, CGs are unique in that they allow for numerous, yet slow, interactions among galaxies. This makes CGs ideal envi-

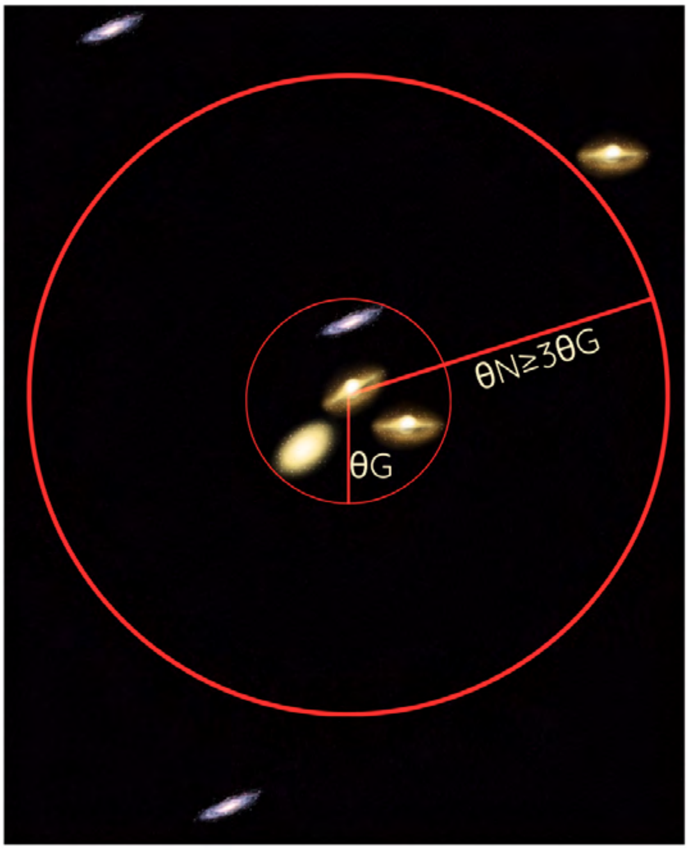

Figure 1.3.1: Cartoon illustrating the isolation criterion proposed by Hickson (1982) for identifying Compact Groups (CGs). This criterion states that the radius containing the nearest bright galaxy to the group (θ_N) must be equal to or greater than three times the radius of the circle containing all galaxies in the group (θ_G).

ronments for studying the effects of galaxy interactions on their evolution, which is why this thesis focuses on these systems.

1.3 The objects of study in this thesis: compact groups of galaxies

The first discovered CG was Stephan's Quintet (Stephan 1877), a group of five galaxies located in the constellation Pegasus, although one of them was later identified as a foreground galaxy (Burbidge & Burbidge 1959). The first catalog of CGs was developed by Rose (1977), where he attempted to systematize the search for these groups. A little later, Hickson (1982) optimized the search. According to Hickson, compact galaxy groups must meet three criteria:

- Population: The number of galaxies must be four or more.
- Isolation: The angular diameter of the largest concentric circle (θ_N) that includes the first external galaxy with a similar or brighter magnitude than those in the group must be at least three times the angular diameter (θ_G) formed by the galaxies in the group (see Figure 1.2.6).
- Compactness: The surface brightness of the galaxies within the angular diameter of the group must be brighter than 26 mag arcsec^{-2}.

Using this method, Hickson found 100 compact groups (HGC) containing 451 galaxies, which are currently the most studied sample of CGs. The method proposed by Hickson is still in use but with modifications (e.g., McConnachie et al. 2009, Díaz-Giménez et al. 2012, Zheng & Shen 2020). The population criterion has changed somewhat, and triplets are now also considered. An additional criterion, radial velocity, has been added, which consists of: $\Delta v = |v_i - \langle v \rangle| \leq 1000$ km/s, where v_i is the radial velocity of each member galaxy, and $\langle v \rangle$ is the median velocity of the member galaxies, in order to avoid spurious members.

However, this is not the only method for selecting CGs. Another criterion is based on the Friends-of-Friends identification algorithm. This criterion combines the projected separation (ΔD) and their line-of-sight velocity difference (Δv), along with possible compactness considerations. The specific values of these parameters, such as $\Delta D \leq 50$ kpc/h and a proximity of $\Delta v \leq 1000$ km/s, are chosen to identify groups that have properties similar to those of the CGs identified by Hickson (Sohn et al. 2016). The inclusion or exclusion of the compactness criterion, represented by a limit on surface brightness (e.g., Barton et al. 1996, Sohn et al. 2016), is also considered.

1.3.1 Morphology properties and physical properties of galaxies belonging to CGs

The CG environment contains a high fraction of galaxies that have morphological (Mendes de Oliveira & Hickson 1994, Coziol & Plauchu-Frayn 2007) or kinematic (Rubin et al. 1991, Mendes de Oliveira et al. 2003, Torres-Flores et al. 2013a) peculiarities, which are typically associated to tidal interactions and mergers. Besides, when comparing CGs with less dense environments, such as the field or loose groups (LGs), it can be seen that CGs members have redder colours, which indicate a higher fraction of early-type galaxies (Lee et al. 2004, Deng et al. 2008, Coenda et al. 2012, Poliakov et al. 2021). Galaxies located in CGs have preferentially larger concentration index, i.e. they are more compact, compared to galaxies located in less dense environments (Deng et al. 2008). For example, Coenda et al. (2012) found different distributions of galaxy parameters in LGs and the field compared to CGs, as can be seen in Figure 1.3.2. In all the plots, the distributions shown with thick black lines represent CGs. In the first row, field galaxies are shown in purple. In the second row, low-mass LGs ($log(M_*[M_\odot]) < 13.2$) are shown in blue. In the third row, high-mass LGs ($log(M_*[M_\odot]) > 13.6$) are shown in red. In the last row, a subset of LGs with a similar total luminosity distribution to CGs is shown in gray.

These plots show that CG galaxies are slightly more luminous compared to field galaxies. In contrast, when compared with LGs, slight differences are observed only in the case of LGs with similar luminosities to CGs, where CGs are systematically brighter. For size, the half-light radius (r_{50}), CGs have an excess of galaxies with $r_{50} \leq 2kpc$ and a deficit between $2-3kpc$ compared to the other two environments, therefore, CGs are systematically more concentrated than their counterparts in a less dense environment. In the color distribution, galaxies in CGs show a larger fraction of red galaxies and tend to have higher stellar masses than those in the field and LGs. This demonstrates that CG galaxies differ from galaxies in other environments.

CGs have been studied to characterise the presence of intra-group light (e.g. Da Rocha & Mendes de Oliveira 2005). For instance, Poliakov et al. (2021) found that the surface brightnesses of the intra-group light component correlate with the mean CG morphology, such that brighter systems are dominated by early-type galaxies. Thus, a correlation exists between the dominant galaxy morphology and inter-group light in CGs.

A gap or so-called “canyon” has been observed in the mid-infrared (MIR) colour space for CG galaxies; galaxies with those colours are called infrared green valley galaxies, which are located between

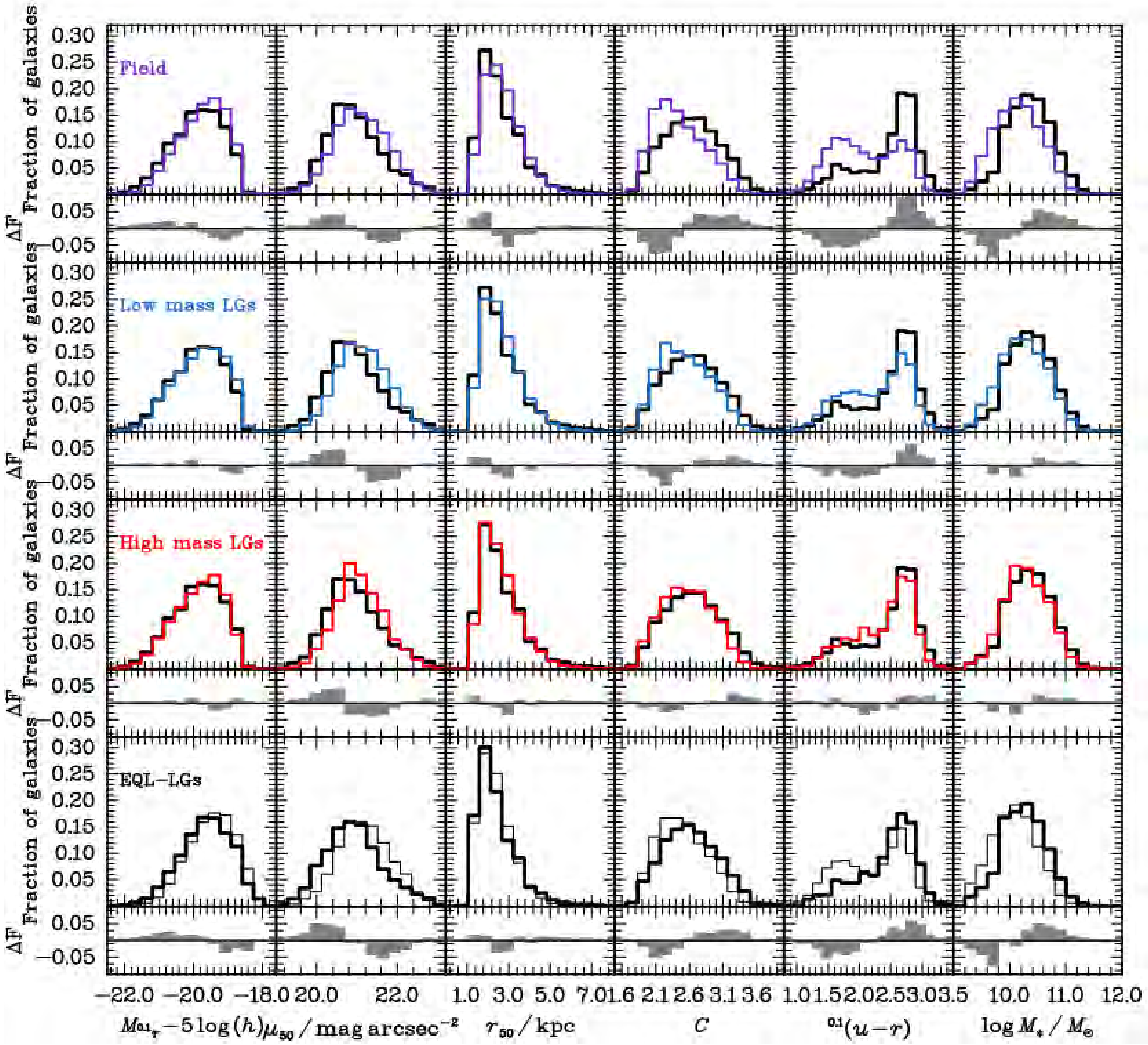

Figure 1.3.2: Distributions of galaxy properties in different environmental samples: CGs sample (thick black line), field (violet), low-mass LGs (blue), high-mass LGs (red), and LGs with a similar luminosity distribution to CGs (gray). Below each panel, shaded histograms represent the residuals between the distributions. This figure was published by Coenda et al. (2012).

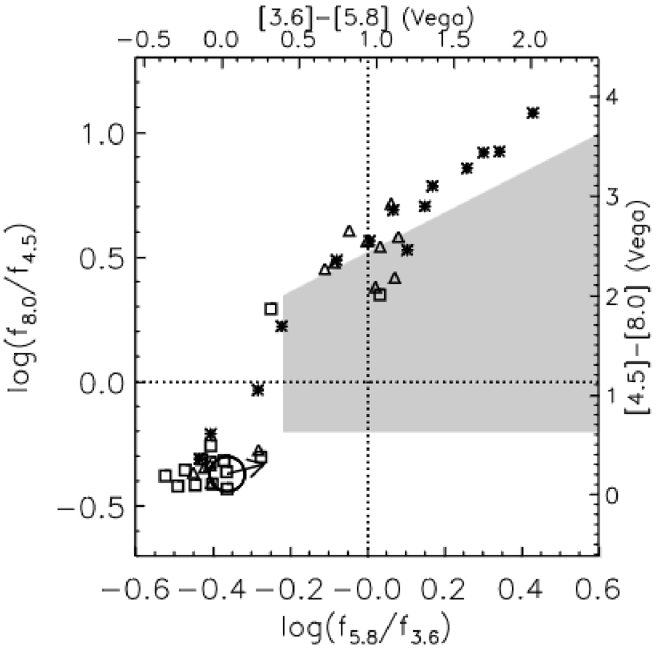

Figure 1.3.3: IRAC colour-colour diagram, the galaxies separated into three categories: $log(M_{H_I})/log(M_{dyn}) < 0.8$ as squares, $log(M_{H_I})/log(M_{dyn}) < 0.9$ as triangles, and $log(M_{H_I})/log(Mdyn) > 0.9$ as stars. The shaded area indicates the colour selection criteria for AGNs according to Lacy et al. (2004). This figure was published by Johnson et al. (2007).

star-forming galaxies and quiescent galaxies in MIR, The first to notice this were Johnson et al. (2007). In Figure 1.3.3, I show the IRAC colour-colour diagram they presented. The galaxies are separated into three categories: $log(M_{H_I})/log(M_{dyn}) < 0.8$ as squares, $log(M_{H_I})/log(M_{dyn}) < 0.9$ as triangles, and $log(M_{H_I})/log(M_{dyn}) > 0.9$ as stars. In this figure it can be seen a relative gap in the galaxy population found at moderate colors ($-0.2 < log(f_{8.0}/f_{4.5}) < 0.2$, and $-0.3 < log(f_{5.8}/f_{3.6}) < -0.1$). This feature is not detected in field galaxies (Johnson et al. 2007, Gallagher et al. 2008, Walker et al. 2012, Zucker et al. 2016), and it is only seen in a weaker form in galaxies falling in the Coma cluster (Walker et al. 2010). Walker et al. (2013) found that galaxies in this MIR gap have already transitioned to the optical red sequence; in fact, the mid-IR gap in the optical fall in $0.73 < g-r < 0.77$. Moreover, it has been found that it is correlated with the specific star formation rate (sSFR) of their galaxies. The few galaxies found in this gap have moderate sSFRs, between the high and low values observed in the bimodal sSFR distribution of galaxies (Tzanavaris et al. 2010, Walker et al. 2010, Walker et al. 2012, Lenkić et al. 2016). This makes CGs an extreme environment for galaxy evolution, where the processes that transform galaxies from star-forming to quiescence act in an efficient way, and where photometric studies have been extremely useful.

The interaction history of galaxies in CGs can also be traced by studying their HI distribution. This allowed the proposal of an evolutionary scenario for CGs of galaxies based on the amount and distribution of neutral hydrogen. Verdes-Montenegro et al. (2001) found that HCG members are deficient in HI, which may be caused by tidal stripping and/or heating. This lack of neutral gas affects the physical properties of galaxies in CGs.

Furthermore, studies based on molecular gas (Alatalo et al., 2015) and neutral gas (Jones et al., 2023) showed that only by knowing the amount of HI or H_2 gas that galaxies in HCGs have, is not enough to infer their star formation activity. Indeed, HI-deficient galaxies still are active in infrared (i.e. star-forming galaxies can be detected in the infrared), suggesting that these galaxies, even though they lose their H I, still are able to maintain their star formation thanks to H_2 (Jones et al. 2023). On the other hand, Alatalo et al. (2015) found that galaxies in HCGs do not need to eject their gas reservoirs in order to quench and undergo a transformation from blue spirals to red early-type galaxies. They also found that many of the galaxies in the "canyon" or infrared green valley galaxies contain molecular gas but cannot form stars efficiently. This could be attributed to the existence of turbulence and shocks in the gas (Alatalo et al. 2015), or because many of these warm H_2 galaxies have experienced a significant reduction in their molecular gas content and star formation rates (Lisenfeld et al. 2014) for HCG. Nevertheless, Bitsakis et al. (2016), who used a larger sample of CGs, also found that shocks and turbulence have a relevant role in the cessation of star formation, and that the morphological transformation of late-types to earlier types occurs in the infrared green valley. All these studies further indicate that physical and morphological processes in CG environments are quite complex.

1.3.2 Nuclear activity in CG galaxies

Galaxy interactions are believed to play a crucial role in feeding the central black holes of Active Galactic Nuclei (AGN). Interactions may lead to gravitational instabilities, allowing gas to move inward, providing the needed fuel for black hole growth through accretion (Sanders et al. 1988, Kauffmann & Haehnelt 2000, Alonso et al. 2007, Ellison et al. 2011, Ellison et al. 2019 Byrne-Mamahit et al. 2023). However, not all studies find a clear link between interactions and the presence of AGN (Schmitt 2001, Ellison et al. 2008), leading to ongoing debate about the connection between the local environment and AGN prevalence.

Sabater et al. (2013) suggest two competing scenarios: the influence of the large-scale environment and one to one interactions among galaxies. In denser environments like groups and clusters, there's typically less cold gas available to fuel AGN compared to isolated galaxies. However, within these environments, one to one interactions between galaxies can help channel gas toward central regions. Furthermore, Sabater et al. (2015) point out that, even after considering factors like stellar mass and star formation, the presence of AGN is indirectly influenced by the environment and interactions among galaxies, impacting the availability of gas for the central regions of galaxies. Moreover, certain studies have identified a higher proportion of low-luminosity AGN (LLAGN) in galaxies displaying features of tidal interactions or distorted morphologies compared to AGN galaxies without signs of interaction (Ellison et al. 2011, Ellison et al. 2019, Sabater et al. 2013, Argudo-Fernández et al. 2016). Therefore, CGs provide a good opportunity to investigate the mechanisms driving nuclear activity.

Multiple studies consistently report a notable presence of AGN in CGs, ranging from 40% to 73% (Coziol et al. 1998, Shimada et al. 2000, Martinez et al. 2007, 2008, 2010). Coziol et al. (1998) studied the activity of galaxies in HCGs, focusing on AGN and star-forming galaxies. In the top panel of Figure 1.3.4, they show the number of galaxies with AGN as a function of absolute magnitude in the *B* band. The black bars represent low-luminosity AGN, and the white bars represent high-luminosity AGN. They found that AGN are located in the most luminous galaxies, and half of the AGN are low-luminosity.

In the bottom panel of Figure 1.3.4, the number of galaxies without emission (black) and starburst (white) are shown for different ranges of absolute magnitude. Star-forming and non-emission galaxies are distributed across all magnitudes. Overall, the brightest galaxies in HCGs show some type of activity, either AGN or star formation. Additionally, they found that AGN hosts are preferably ETGs, and these AGN hosts appear to be systematically concentrated towards the central parts of HCGs. With these results, Coziol et al. (1998) suggest a correlation between activity types, morphologies, and densities of galaxies in CGs. They propose that CG galaxies evolve through interactions with each other, where gravitational interactions and mergers trigger star formation and Seyfert activity.

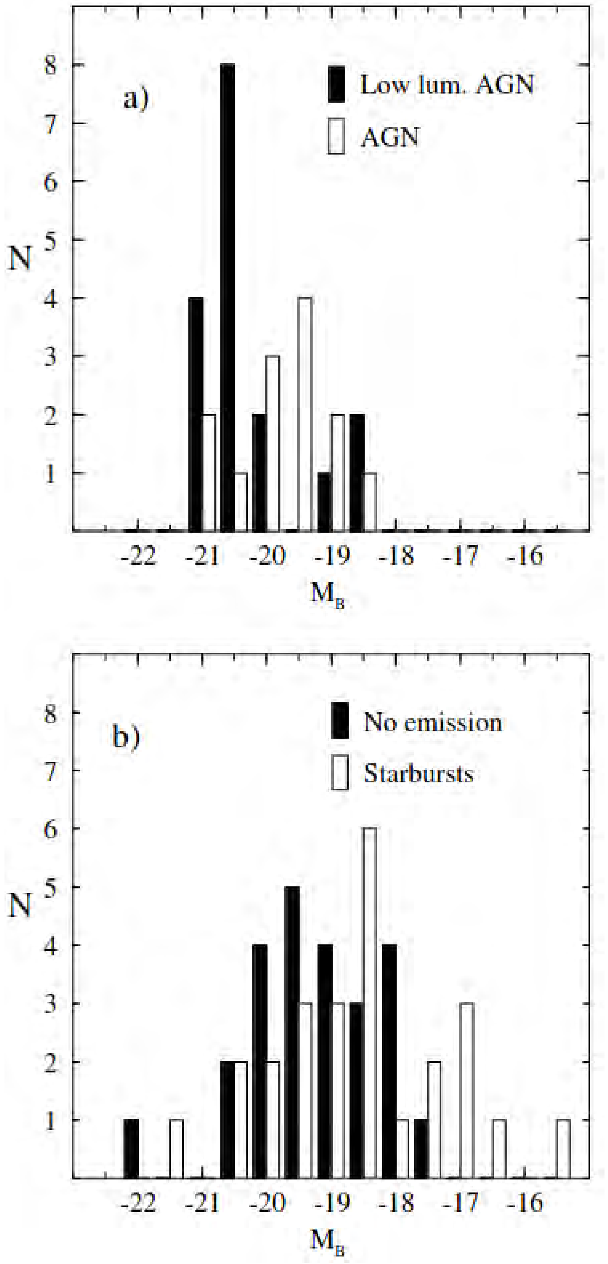

Figure 1.3.4: Upper panel: The number of galaxies in HCGs that are low-luminosity AGN (black) and AGN (white) across various ranges of absolute magnitude. Bottom panel: The figure shows the number of galaxies in HCGs without emission (black) and starburst galaxies (white) across different ranges of absolute magnitude. These figures were published by Coziol et al. (1998).

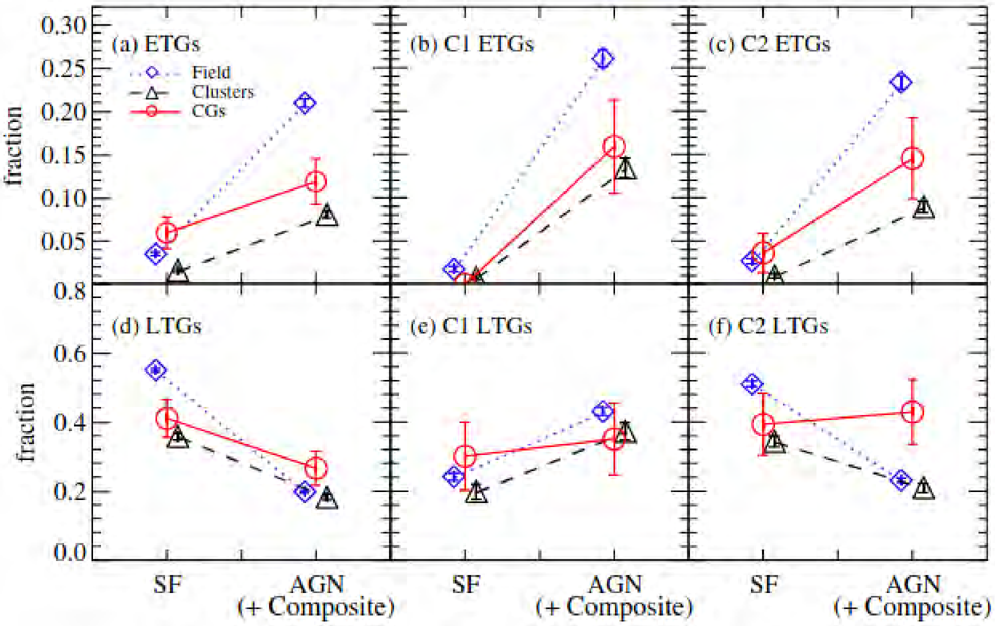

Figure 1.3.5: Fractions of each morphological type for early-type (upper panels) and late-type (lower panels) galaxies across various galaxy environments are depicted: field (diamonds), clusters (triangles), and compact groups (circles). Panels a and d show fractions for the entire sample, panels b and e for the sample of bright galaxies ($-22.5 < M_r < 21.5$), and panels c and f for the faint galaxies sample ($-21.5 < M_r < 20.5$). Figure published by Sohn et al. (2013a).

As the gas reservoir depletes, AGNs remain as low-luminosity AGNs or galaxies without emission, while the morphology of the galaxies evolves towards more early types.

Interestingly, Shimada et al. (2000) observed that low-luminosity AGN are often found in the most luminous galaxies within HCGs, while galaxies lacking emission lines and star-forming galaxies are primarily associated with the less luminous members. Additionally, they compared the fraction of AGN and star-forming galaxies in HCGs with field galaxies. In the case of star forming galaxies, they found that HCGs have a lower fraction compared to the field. This difference is due to a lower fraction of LTGs in HCGs. After accounting for this morphological bias, they did not find significant differences in the frequency of emission-line galaxies between HCGs and the field. For AGN, they also considered the bias of potentially overlooking less luminous AGN in CGs. They found that the distributions of these activity types in HCG galaxies are indistinguishable from those in field galaxies. This implies that the dense galaxy environment in HCGs does not affect the triggering of AGN or nuclear star formation bursts.

Martínez et al. (2010) also conducted an analysis to characterize the nuclear activity of HCGs, but with more data, allowing them to increase the sample size. They found that AGN activity is the most frequent activity type in HCGs. Additionally, they found that AGNs in CGs are characterized by low luminosity and the near absence of broad-line AGNs, suggesting a deficiency of HI in these galaxies.

According to Sohn et al. (2013a), who analysed SDSS data from a larger sample of CGs, the AGN fraction in CG galaxies ranged from 17% to 42%, varying with the method of classification. The study observed an inverse relationship between the AGN fraction and galaxy number density in early-type galaxies. In contrast, late-type galaxies maintained a relatively steady AGN fraction, indicating a possible recent accretion and the ability to retain gas for supermassive black hole fuel. Additionally, mid-infrared data revealed a shortage of AGN-hosting galaxies, suggesting weak nuclear activity in

CGs due to a lack of gas supply. They also conducted an analysis comparing with other environments. In Figure 1.3.5, they present the fractions of each spectral type segregated by absolute magnitude and morphology, where C1 contains the brightest galaxies between $-22.5 < M_r < 21.5$ and C2 is the faint subsample between $-21.5 < M_r < 20.5$. For all ETGs presented in the top left panel, they found that the AGN fraction seems to decrease from field regions to cluster regions. This is also evident for two magnitude subsamples, as shown in the top middle and right panels. In the case of LTGs (see bottom left panel of Figure 1.3.5), the differences in AGN fractions among different environments are insignificant. The two magnitude subsamples show similar trends.

Insights into AGN activity in CGs have also emerged from X-ray observations. Tzanavaris et al. (2014) analyzed nine CGs using Chandra X-ray data and found predominantly weak X-ray emissions from nuclei, consistent with low-luminosity AGN. They proposed that spiral galaxies with high specific star formation rates were likely dominated by star formation, while those in earlier galaxy types, likely hosted less active AGN, particularly with lower specific star formation rates. Similarly, De Rosa et al. (2015) explored a specific CG (SDSSJ0959+1259) and identified two Seyfert 2, one Seyfert 1, two LINERs, and three star-forming galaxies, resulting in an AGN fraction of 60%. Moreover, Oda et al. (2018) studied HCG 16 using hard X-ray data and identified two galaxies as AGN with luminosities ranging between 3×10^{41} erg s^{-1} in the 2-10 keV range. These X-ray investigations highlight the trend of CG nuclei, which often exhibit weak emissions consistent with LLAGN. Despite the discrepancy in the AGN fraction within CGs, all these studies consistently suggest that the lack of powerful AGN in CGs results from gas depletion due to tidal stripping, leading to reduced accretion onto supermassive black holes.

Coziol et al. (2004) and Tovmassian et al. (2006) found an anti-correlation between AGN and star-forming galaxy fractions and CGs' velocity dispersion and the environment where they are located. Tovmassian et al. (2006) propose that nuclear activity and galaxy transformation via merging are prompted by effective gravitational interactions in low-velocity dispersion CGs, which then dynamically evolve into higher-velocity dispersion CGs through virialization processes, resulting in a larger fraction of early-type galaxies. In this case, the 22 studied CGs were within loose groups, leading to the conclusion that these were elongated systems.

1.3.3 Kinematic anomalies and the Tully-Fisher relation

As mentioned throughout this introduction, galaxy encounters are common in CGs due to their low velocity dispersion. Kinematic studies of these environments have shown that galaxies in CGs generally follow the Tully-Fisher (TF) relation for less dense environments in the K and B bands, but with greater scatter (de Oliveira et al. 2003,Torres-Flores et al. 2010,2013b). However, low-mass galaxies in CGs are outliers in the TF relation as they are too bright (high luminosity) for their mass. This could be due to increased brightness from star formation and/or lower maximum rotation velocities due to tidal stripping. Torres-Flores et al. (2013b) showed that considering both stellar and gas mass reduces the scatter, but it still persists. These subtle differences and outliers indicate intrinsic differences between these dense environments and less dense ones. It is important to note that the three previous studies found some rotation curves with strong asymmetries, suggesting recent interactions that have not yet relaxed or a disturbed halo.

Torres-Flores et al. (2014) studied 42 CGs, they described their kinematics and connected them with observed morphological characteristics. Rotation curves were derived for 15 out of 42 observed galaxies, with only two showing no interaction disturbances. Asymmetries were observed between both sides of the rotation curve, unexpected solid body behavior, or truncated rotation curves. In Figure 1.3.6, two galaxies in the CG VV304 can be seen, galaxy VV304a (left panel) is more symmetric

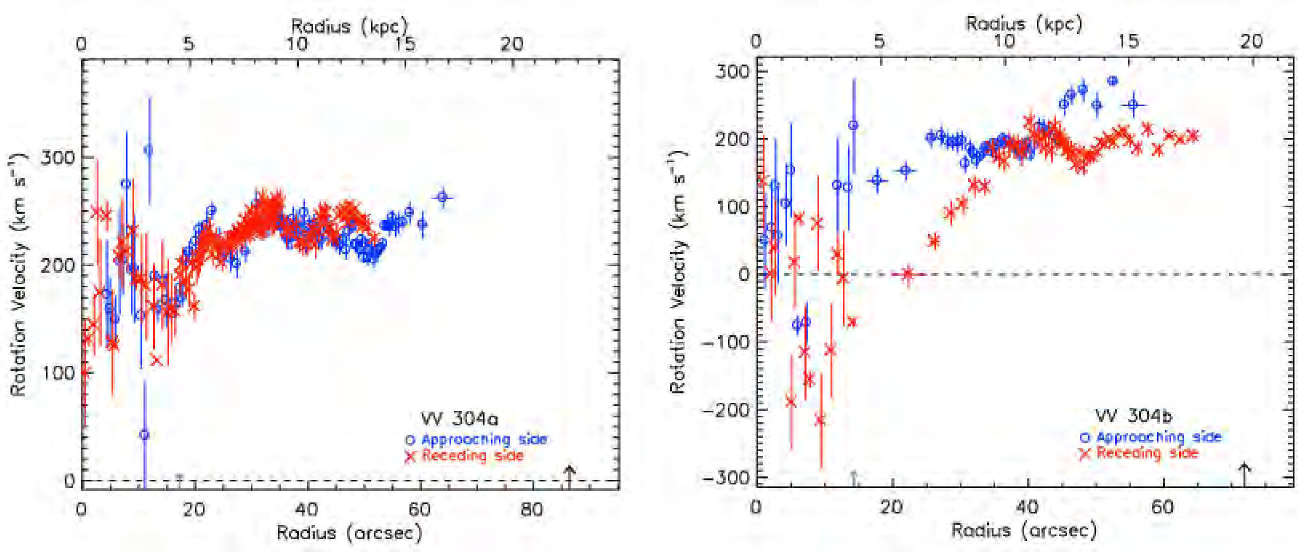

Figure 1.3.6: Rotation curves for two galaxies in the CG VV304. Galaxy VV304a (left panel) is more symmetric compared to galaxy VV304b (right panel), which is completely asymmetrical. Figures published by Torres-Flores et al. (2014).

compared to galaxy VV304b (right panel), which is completely asymmetric. Additionally, due to the lack of $H\alpha$ emission compared to what is expected for the galaxy's morphological type, they suggest that past galaxy interactions stripped away their gas components, ceasing star formation. However, this could also be due to the detection limit of their sample.

1.3.4 Dynamics of compact groups: insights from observations and simulations

In the survey of CGs conducted by Rose (1977), it was found that nearly every CG studied has at least one galaxy closer to it than would be expected for randomly distributed field galaxies. Therefore, it is concluded that CGs are small subsystems of larger groups of galaxies. This raises the question of whether CGs are truly dense virialized systems or just chance configurations projected onto the sky. Ribeiro et al. (1998) studied 17 HCGs and their surroundings, categorizing the groups into three families based on their environment and how the group's density and surface brightness changed with the newly detected galaxies.

In Figure 1.3.7, the average surface density profile for each type of group is shown. The HCGs that appear truly isolated and compact, with no visible extension, are called real CGs or compact systems and are represented by the dotted line, where 3 out of the 17 HCGs were classified as real CGs. In other cases, they observed that the surface density of the HCGs plus the surrounding galaxies behaved as if there were two regions: a bright, compact core and an extended, low surface brightness halo. These groups are classified as core-halo systems, shown by the dashed-dotted line in Figure 1.3.7, classifying 4 HCGs in this category. The third classification includes groups with a smooth decrease in both surface brightness and spatial density, probably corresponding to the central parts of larger, looser structures with no clear division as in the previous case. These groups are called loose groups, represented by the solid line in Figure 1.3.7, where 7 HCGs are part of these loose groups.

These differences in the surface brightness profiles of the groups suggest that they probably correspond to three different dynamical stages of groups, each presenting a distinct surface density profile

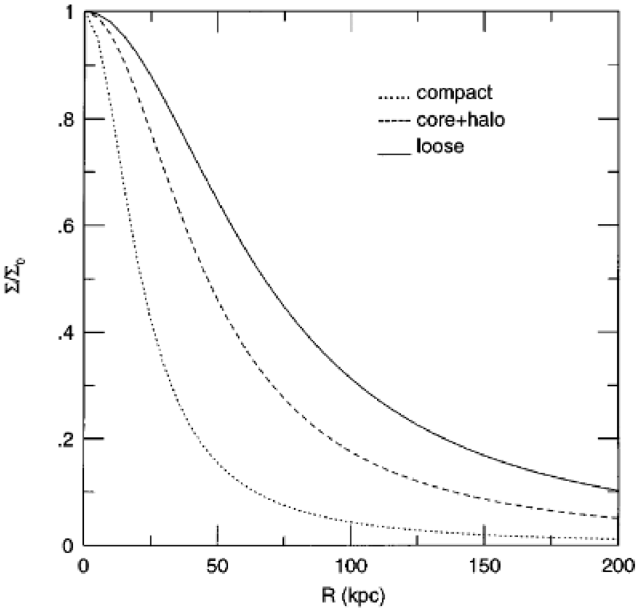

Figure 1.3.7: The average surface density profile for each type of group identified by Ribeiro et al. (1998) when analysing the HCGs and their surroundings.

for the galaxy distribution. In Ribeiro et al. (1998) analysis, three groups were excluded: one for having a very low surface brightness, another for being part of the ACO 1060 cluster, and a third one for having inconsistencies in the radial velocity of two galaxies, classifying it as a possible chance alignment. Ribeiro et al. (1998) concluded that HCGs are not always a representative sample of strictly compact systems and that the three identified families possibly correspond to dynamic snapshots showing different dynamical stages. However, they emphasise that HCGs are very useful for investigating the possible ways a compact system forms and evolves.

There is a series of papers by McConnachie et al. (2008), Brasseur et al. (2009), McConnachie et al. (2009) and Mendel et al. (2011) where they studied the properties of CGs using observational data and looking CGs in the Millennium simulations. In the first paper, McConnachie et al. (2008) used a mock galaxy catalogue and applied Hickson's original criteria for identifying CGs. Notably, they did not apply the velocity dispersion criterion between galaxies. Using Friends of Friend, they determined the linking length (l) of each CG to determine if they were dense 3D structures. They found that 29% of CGs were compact associations, considering only those with $l < 200/hKpc$. They also identified structures with a dense structure of 4 galaxies plus one or more interlopers, representing 6% of the CG sample. Therefore, in total, 35% of the CGs identified with photometry were 3D CGs. The remaining groups consisted of triplets with interlopers (24%), pairs with interlopers (18%), and physically unbound systems (23%). Interestingly, half of the CGs that were truly 3D dense structures with 4 or more galaxies were embedded in larger groups. In a subsequent paper, Brasseur et al. (2009) studied the properties of CGs in these simulations. They found that if a filter is applied for line-of-sight velocity dispersion less than 1000 km/s, contamination for not truly compact association is significantly reduced to 30%.

These authors also explored CGs by creating a catalog from observations using SDSS, as documented by McConnachie et al. (2009). Mendel et al. (2011) studied the connection of CGs with the large-scale structure using their catalogue, and found that approximately 50% of their CGs were embedded in larger groups. To explore whether these CGs were simply caused by projections, they conducted 1000 Monte Carlo simulations where they varied the positions of galaxies within the groups. For each realization, they matched the projected distance distribution of the CGs with respect to the parent group. Then, they measured the surface density [galaxies h^2/Mpc^2] around the embedded CGs and compared it with these "simulations". They found that the results of the simulations only explained the outer part of the observed CG profile, but not the central part where the surface density was higher in the observed CGs. They concluded that the CGs were substructures in rich groups.

Another series of papers by Díaz-Giménez et al. (2020), Diaz-Gimenez et al. (2021), Taverna et al. (2022), Zandivarez et al. (2023) and Taverna et al. (2024), also studied the Millennium simulations but used different SAMs to examine the dependency of CG nature on cosmological parameters. In Díaz-Giménez et al. (2020) found that between 35 to 56% were dense 3D systems and isolated, depending on which SAM was analyzed. The remaining CGs were chance alignments of galaxies within larger loose groups or filaments.

In Taverna et al. (2022), they searched for CGs in the Millennium simulations, considering CGs with 3 or more galaxies. To determine if they were dense 3D systems, they used a linking length less than or equal to $90/h\ Kpc$. They found that 10% were isolated dense systems, 55% were dense systems but not isolated, and 32% were chance alignments within loose groups, the remaining 3% were chance alignments in the field or filaments. Therefore, from the Millennium simulations, they find that between 35 to 65% are dense systems, which may be isolated or embedded in larger groups.

Additionally, Zheng & Shen (2021) studied the dynamics of CGs in their catalogue (Zheng & Shen 2020). They identified the environment of their CGs by cross-matching with the groups catalogued by Yang et al. (2007), where the structures are classified using the halo-based group method, which employs an iterative approach to estimate the group mass. This classification ranges from isolated galaxies to groups with varying numbers of members. With this catalogue Zheng & Shen (2021) found three cases:

- Both catalogs, Zheng & Shen (2020) and Yang et al. (2007), coincide in identifying groups with the same number of members. Zheng & Shen (2021) refer to these as isolated CGs. In the top left panel of Figure 1.3.8, they show an example of this case, where the small white circles represent the galaxies identified by Zheng & Shen (2020) in the CGs and the smaller green circles represent the galaxies identified by Yang et al. (2007). They found that 27% of their CGs are isolated.

- The galaxies of the identified CGs belong to different groups in Yang et al. (2007). For example, in the bottom right panel of Figure 1.3.8, the four galaxies of the CG identified according to Yang et al. (2007)'s catalog correspond to two pairs of galaxies. Zheng & Shen (2021) attribute this to the high radial velocity cut used in their selection criteria, which overestimates the number of CGs. They found that 21% of CGs fall into this category.

- The non-isolated CGs that, according to Yang et al. (2007), actually have more galaxies around them than those found by Zheng & Shen (2020). In Figure 1.3.8, examples corresponding to the top right and bottom left panels show that Yang et al. (2007) identifies many more galaxies, indicating that these CGs are not truly isolated structures.

They differentiate non-isolated groups into embedded systems and predominant CGs based on luminosity. If the luminosity of the CG does not dominate over the luminosity of the group it belongs to, it is considered an embedded CG. This is the case for the CG presented in the bottom left panel of Figure 1.3.8. Conversely, if the luminosity of the CG galaxies dominates, it is considered a predominant CG, as shown in the top right panel of Figure 1.3.8. Zheng & Shen (2021) focus on embedded CGs and explore whether they are truly dense systems by plotting the velocity dispersion of the CGs

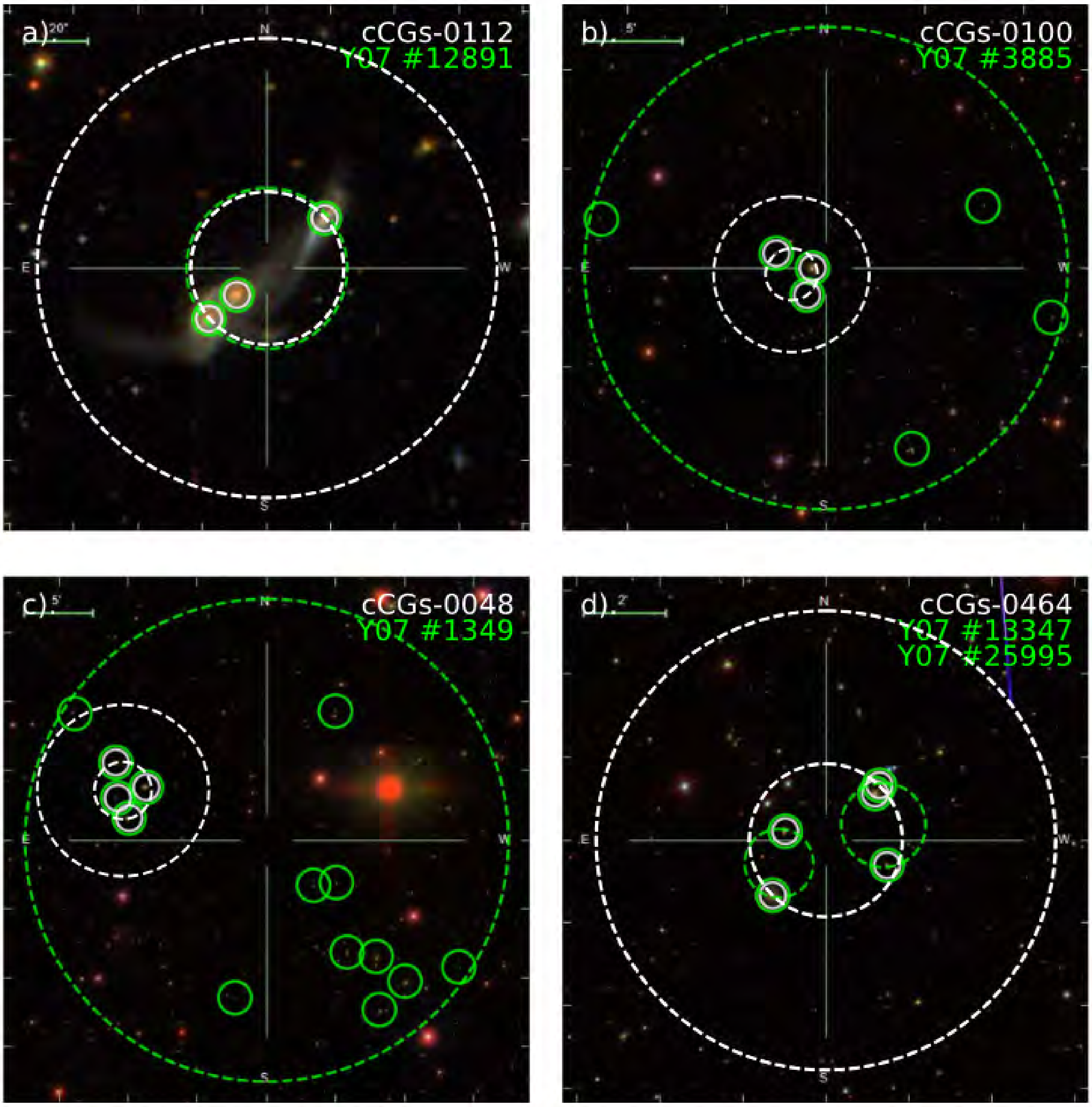

Figure 1.3.8: Zheng & Shen (2021) identified various types of CGs through an analysis of their surrounding environments, using the catalog by Yang et al. (2007). The images for this analysis were sourced from SDSS. The top left panel (a) shows an example of Isolated CGs with no external galaxy host in the same halo. The top right panel (b) presents predominant CGs with other fainter galaxies sharing the same halo. The bottom left panel (c) shows embedded CGs with brighter galaxies occupying the same halo as nondominant subsystems. The bottom right panel (d) displays split CGs whose members belong to at least two different groups according to Yang et al. (2007). The inner white dashed circles represent the smallest enclosed circles θ_G; the outer white dashed circles represent the concentric circles $3 \times \theta_G$. Solid circles mark the member galaxies of CGs (white) or their corresponding Yang et al. (2007) groups (green).

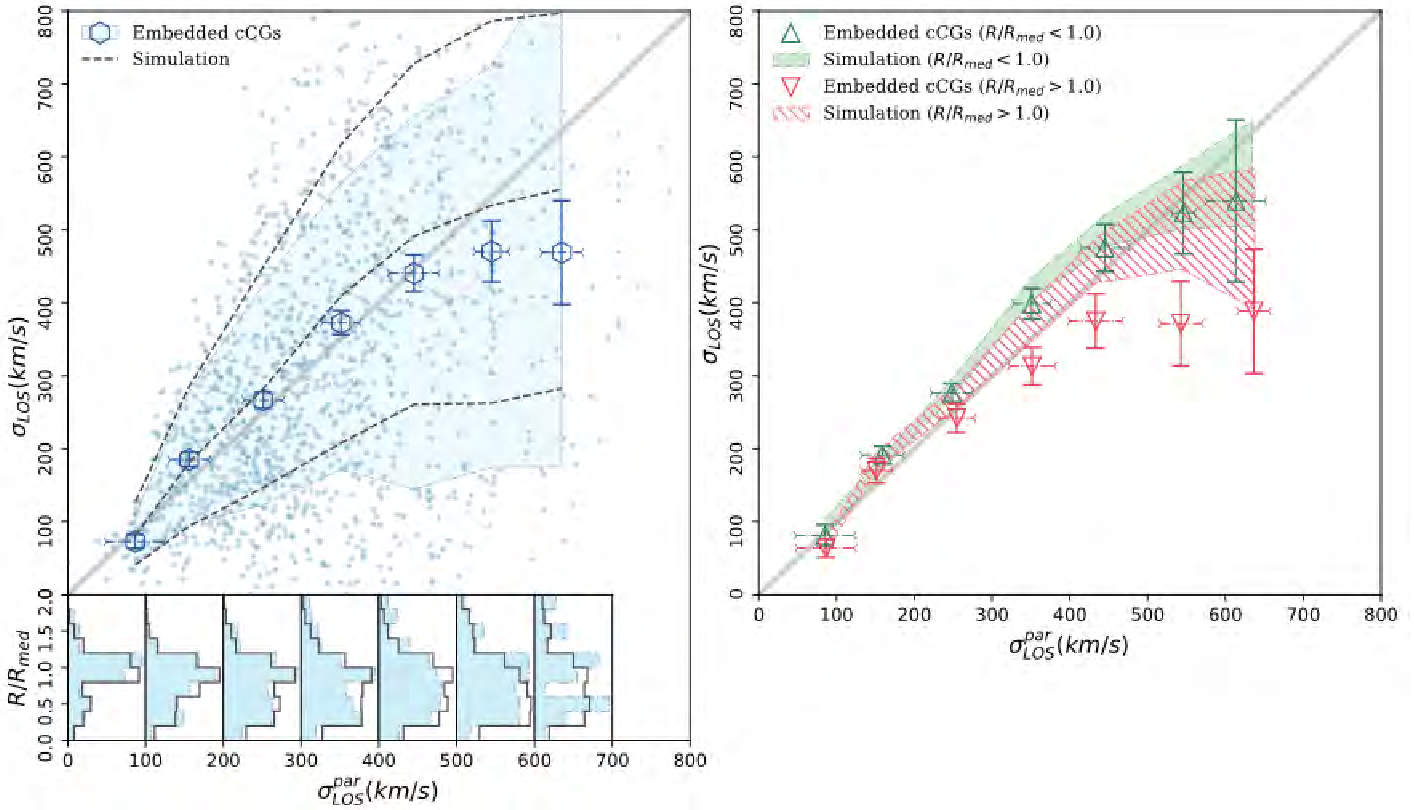

Figure 1.3.9: Left panel: Velocity dispersion of the parent group where the compact groups are embedded (σ_{par}) compared to the velocity dispersion of the CGs (σ_{LOS}). Additionally, Zheng & Shen (2021) compares the embedded CGs with mock CGs from Monte Carlo simulations. The open hexagons represent the median values. The shaded area shows the 16th and 84th percentiles, whereas the three dashed lines show the 16th, 50th, and 84th percentiles for the mock CGs. Right panel: This is similar to the left panel but in this case, the CGs are separated according to their location relative to the median radius of the galaxies in the groups, $R/R_{med} > 1$ (red) and $R/R_{med} < 1$ (green), respectively. The triangles show the observed embedded CGs, while the shaded and hatched areas represent the standard deviation of the median σ_{LOS} of mock CGs. The bold lines in both panels indicate the one-to-one correspondence.

versus the velocity dispersion of the groups (see left panel in Figure 1.3.9). They observe a one-to-one relationship for σ less than 500 km/s, suggesting that dynamically, the CGs are not different from the groups they are embedded in, and that these CGs could be caused by projections.

To test this hypothesis, they conducted Monte Carlo simulations where they randomized the projected azimuthal position of the CGs with respect to the group. They created 100 mocks for each CG. The dashed lines in the left panel of Figure 1.3.9 show the results of these simulations, where they find that for σ less than 300 km/s, the mock reproduces the behavior of the embedded CGs, validating the chance alignment hypothesis. However, they note that while embedded CGs are selected to not dominate the luminosity of their host groups, the richness of these parent groups is not necessarily significantly higher. A few additional bright galaxies in the parent group could double the overall luminosity. In such cases, the parent group's velocity dispersion (σ_{par}) would be dominated by that of the embedded CGs, making it challenging to distinguish a genuinely dynamically bound CG from one that merely appears to be due to chance alignment.

For σ greater than 300 km/s, differences between the simulated and observed data begin to appear, indicating that the chance alignment hypothesis is no longer valid. They propose the hypothesis that these differences may be caused by CGs that are recently falling into larger groups. Therefore, in the right panel in Figure 1.3.9, they divide the CGs according to the distance to the host group, where R is the distance from the CG to the center of the host group, and R_{med} is the median radius of all galaxies in the host group. From this plot, they conclude that CGs located at outside of host groups are more likely to be recently accreted substructures, with lower σ than the host groups, while chance alignments dominate CGs located inside part of the host groups, as they follow a closer one-to-one relationship.

1.3.5 Evolutionary Scenarios of compact groups: from gas deficiency to nuclear activity

Verdes-Montenegro et al. (2001) proposed an evolutionary scenario based on observations of HI, which was subsequently updated by Jones et al. (2023). As mentioned in section 1.3.1, Verdes-Montenegro et al. (2001) found that galaxies in compact groups are deficient in neutral hydrogen. Additionally, they classified the HCGs into three phases based on the ratio of the gas content within the galaxies to the total gas observed in the group (see Figure 1.3.10). In Phase 1, HI emission is mainly found within the discs of the galaxies in the HCG. By Phase 2, notable tidal features appear, and a substantial portion of the observed HI is located outside the galaxies. In Phase 3a, nearly all the gas has either been stripped from the galaxies or becomes undetectable inside the HCGs. There is also a Phase 3b, which they mention as the least common. It involves HCGs where the HI gas forms a large cloud encompassing all the galaxies, with a single velocity gradient. The total HI spectrum has a characteristic single-peaked shape.

This scheme was updated by Jones et al. (2023). In Figure 1.3.11, the x-axis shows how deficient the HCGs are. This parameter is estimated by comparing the predicted HI mass, based on the B-band luminosity and the scaling relation of Jones et al. (2018), with the HI mass estimated from observations. The y-axis shows the HI mass that is extended outside the galaxies in the HCGs, normalized by the total HI mass in the HCGs. The marker shape indicates the IR classification by Zucker et al. (2016) of each CG: stars for HCGs dominated by IR active galaxies, crosses for HCGs not dominated by either active or quiescent galaxies, squares for HCGs dominated by quiescent galaxies, and rings for HCGs with too many members without IR classifications.

The plot shows three phases. In the first phase, the gas is within the galaxies and less than 25% of the detected HI is in extended features. In the second phase, between 25% and 75% of the detected HI

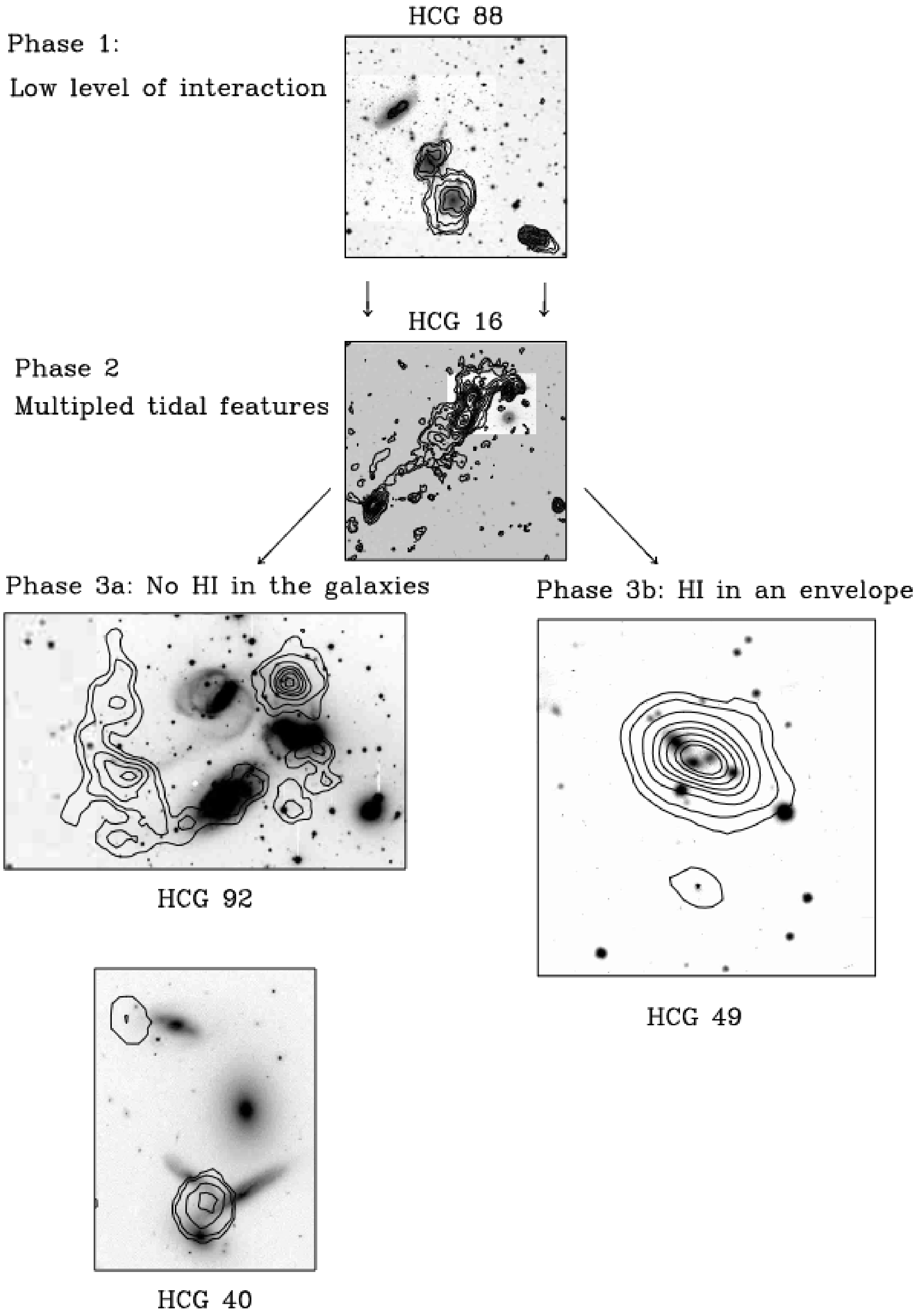

Figure 1.3.10: The evolutionary scheme proposed by Verdes-Montenegro et al. (2001), where the contours are levels N(HI) = 10, 20, 40, 65, 85, 110, 140, 160, 200, 250, 350, 450, 570 $\times 10^{19}$ cm^{-2}.

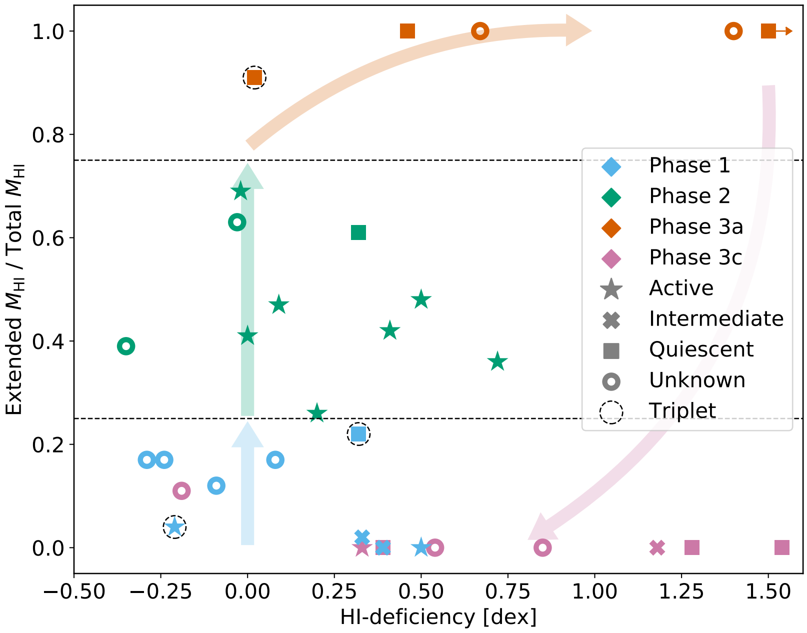

Figure 1.3.11: This plot shows how extended HI mass outside galaxies in HCGs varies with HI deficiency in CG galaxies. Marker shapes indicate the IR classification by Zucker et al. (2016) of each HCG: stars for HCGs dominated by IR active galaxies, crosses for HCGs not dominated by either active or quiescent galaxies, squares for HCGs dominated by quiescent galaxies, and rings for HCGs with too many members without IR classifications. Figure by Jones et al. (2023).

is in extended features. In the third phase, most of the detected HI (more than 75%) is extended and outside the galaxies. In Figure 1.3.11, Phase 3 is divided into 3a and 3c, but 3b proposed by Verdes-Montenegro et al. (2001) does not appear. This is because later studies have shown that no HCG convincingly fits this scenario (Verdes-Montenegro et al. 2002). Phase 3c was proposed by Jones et al. (2023) to indicate HCGs that would be classified as Phase 1, but where only a single galaxy is detected in HI. This galaxy is always an LTG, while the other members of the group are generally ETGs. In many cases, this single galaxy is likely a recent addition to the CG, rejuvenating the HI content. Therefore, these groups are probably in the later stages of their evolution but have recently acquired a new member. Additionally, with new observations using the Five-hundred-meter Aperture Spherical Telescope (FAST), Cheng et al. (2023a) demonstrate that HCGs are not HI deficient. Instead, the gas might be hidden in a low-density diffuse neutral gas rather than in the ionized gas, which has been stripped from galaxies due to tidal interactions. This finding is significant as it challenges the previous understanding and highlights the need for further investigation into the gas content and its distribution in CGs.

Coziol et al. (2004) classified the HCGs into three main types based on their ionization mechanisms and internal dynamics. In Figure 1.3.12, I show the relationship between the median morphology of the galaxies and their average activity that they presented, where $T > 3$ generally represents LTGs and $T < 1$ represents ETGs. The average activity is the mean equivalent width between $6500 - 6600\AA$, noting that generally, SFGs and luminous AGNs have $log(EW_{act}) > 0.8$. They find a relationship between the morphology of the HCGs and the level of nuclear activity, where HCGs with a higher fraction of LTGs have a higher fraction of active galaxies, either star-forming or AGNs. They classify the HCGs into three categories based on the median morphology, which are the three vertical lines in Figure 1.3.12.

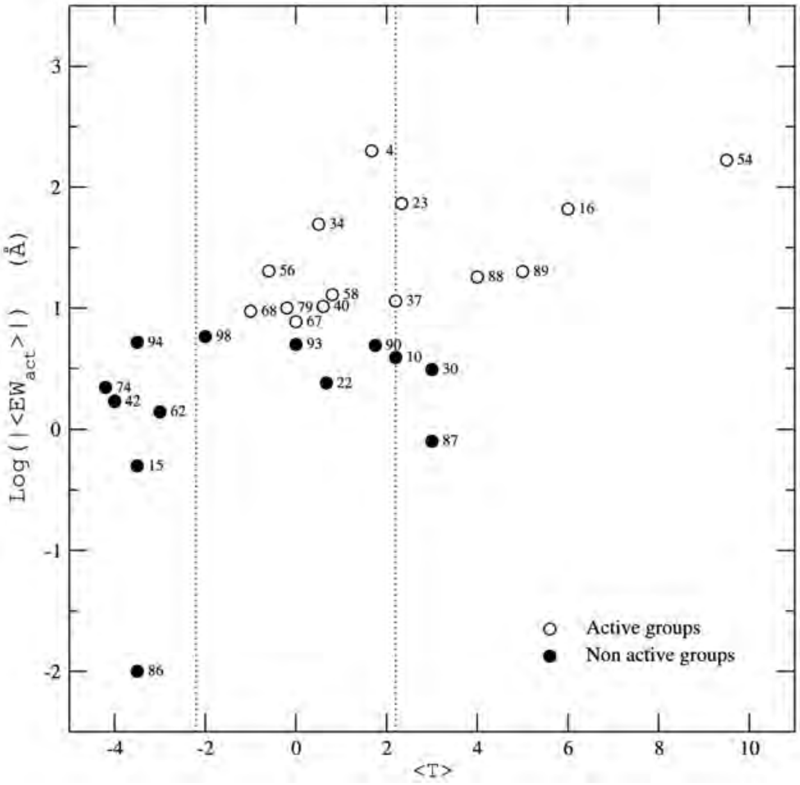

Figure 1.3.12: This figure shows the mean activity index as a function of mean morphology, where $T > 3$ generally represents LTGs and $T < 1$ represents ETGs. The average activity is the mean equivalent width between $6500 - 6600\mathring{A}$, noting that generally, SFGs and luminous AGNs have $log(EW_{act}) > 0.8$. Figure published by Coziol et al. (2004).

They also found a relationship between the activity of the galaxies and the dynamical state of HCGs. CGs with a higher fraction of SFGs and AGNs generally have low velocity dispersions compared to CGs without nuclear activity. The three types of HCGs are characterized as follows:

- Type A CGs: Low-velocity dispersions with a median of 135 km/s, containing a large fraction of LTGs with active star formation or AGN.
- Type B CGs: Intermediate velocity dispersions with a median of 302 km/s, consisting of a significant fraction of interacting or merging galaxies, with nuclear activity.
- Type C CGs: High velocity dispersions with a median of 567 km/s, dominated by elliptical galaxies that are passive.

Groups with a mean $T > 2.2$ are all type A systems. Those with a mean $T < -2.2$ are all of type C. The CGs with intermedia values are classified as type B. These authors suggest that CGs evolve from Type A to Type C, proposing that the evolutionary state of a CG increases with its velocity dispersion. Their sample was based on 27 Hickson CGs, where about 30% were isolated, and 70% were part of groups and clusters. They suggest that this relationship between morphology, nuclear activity, and dynamics of the HCGs seems to be linked with the masses of the environmental structures where the HCGs are located, indicating that the evolutionary state of a HCGs increases with the mass of the structure in which it is embedded. For isolated CGs, their evolution must depend on their masses. This suggests that either galaxies in CGs evolve more rapidly when the CGs are inside massive structures or that the formation of CGs embedded in massive structures preceded the formation of isolated CGs. Although both proposed schemes are derived from different data sets, they point to the same conclusion: the lack of gas reservoirs in galaxies within CGs. In Summary, the evolutionary scenarios proposed by Verdes-Montenegro et al. (2001), Coziol et al. (2004), and Jones et al. (2023) provide a comprehensive framework for understanding the gas content, ionisation mechanisms, and morphological evolution of galaxies in HCG. While Verdes-Montenegro et al. (2001) and Coziol et al. (2004) highlight different aspects of gas depletion and ionization mechanisms, Jones et al. (2023) introduces a revised perspective on gas distribution, emphasizing the potential presence of diffuse neutral gas. This updated view challenges previous assumptions and underscores the necessity for further research into the dynamic processes affecting gas reservoirs in CGs.

The classification schemes and observed trends suggest a complex interplay between gas content, galaxy morphology, and group dynamics. Therefore, a study is needed to investigate how the properties of galaxies within CGs are affected by their presence in such a dense environment and how the dynamics within CGs influence these properties. Moreover, it explores how the broader environment in which the CGs themselves are embedded may further affect the evolution of their member galaxies. Understanding this complex interplay between internal dynamics and external environmental factors is key to comprehending how the properties of galaxies shape and, thus, understanding how CGs evolve.

1.4 This Thesis

In the context of CGs, the impact of these environments on the morphology and physical properties of galaxies compared to those in less dense regions remains an open question. Although much of the research has focused on HCGs, it is essential to investigate a broader sample of CGs to gain a more comprehensive understanding. Specifically, in what ways does the CG environment influence the morphological evolution of galaxies differently than in less dense environments? Does the CG environment promote the cessation of star formation in galaxies, implying a role in the pre-processing of galaxies? How does the dynamical state of a CG influence the evolutionary stage of its member galaxies, and what role does the larger-scale environment play in the evolution of CGs? Does nuclear activity decrease as CGs evolve faster due to becoming part of larger environments? What differences, if any, are observed in the 2D profiles of ionised gas between galaxies in CGs and those in a control sample from the field?

The main objective of this Thesis is to understand how dense environments, particularly CGs, affect the evolution of galaxies, and how morphological and physical properties of their member galaxies are impacted. To achieve this objective, I have outlined the following specific goals:

1. To investigate the morphological differences between galaxies in CGs and those in less dense environments, and to determine how the CG environment influences morphological transformations.

2. To examine whether the CG environment promotes the cessation of star formation.

3. To understand the impact of the dynamical state of a CG on the evolutionary stage of its member galaxies, and to discern the role of the larger-scale environment in the evolution of CGs. This will involve analysing how the dynamical interactions within CGs and their surroundings influence the morphological and star-forming properties of the galaxies.

4. To examine the influence of the surrounding environment on nuclear activity in galaxies within CGs. This involves analysing variations in ionisation mechanisms across different morphological types of CG galaxies and understanding the impact of mass and the larger-scale environment on these phenomena.

5. To conduct a comprehensive study investigating the influence of galaxy interactions within CGs on the physical properties of galaxies by analysing 2D profiles of ionised gas and stellar components. This study will include a comparative analysis with galaxies from a control sample in the field.

I will study the CG galaxies mainly using photometric images from the Southern Photometric Local Universe Survey (S-PLUS) (Mendes de Oliveira et al. 2019). This survey has the advantage of having a unique set of 12 filters in the visible range of the spectrum, allowing us to explore how the properties of galaxies change among them. This will enable me to explore the morphological and physical properties of galaxies, which carry information about their formation and evolution. This thesis will focus on CGs located in the Stripe 82 (Abazajian et al. 2009), which also have information available from other surveys such as the Sloan Digital Sky Survey (SDSS) (Adelman-McCarthy et al. 2006). Thus, we will also explore the emission lines and other physical information available in the literature (e.g., Salim et al. 2018, Thomas et al. 2013). Additionally, we will use IFS data from the Mapping Nearby Galaxies at APO (MaNGA) project to resolve the physical properties of the galaxies (Wake et al. 2017).

This thesis is organized as follows:

In Chapter 2, I will present the morphological analysis of galaxies in CGs using S-PLUS images, which is based on modelling the surface brightness profiles of the galaxies. Additionally, I will explore how star formation in CG galaxies compares with a control sample of field galaxies. This chapter aims to address the first two specific objectives of this thesis. In Chapter 3, I will present the results of a dynamical analysis of the CGs and explore how these dynamical states are connected with the morphology and results obtained in Chapter 2. In addition, I will explore their correlation with the surrounding environment of CGs and investigate how this environment influences the evolution of CG members. This chapter focuses on the third specific objective.

In Chapter 4, I will present an analysis of emission lines, particularly using diagnostic maps to identify the primary ionisation mechanisms. Additionally, we will explore how these mechanisms are related to the host properties studied in Chapter 2 and the environment of the CGs explored in Chapter 3. This chapter addresses the fourth specific objective.

In Chapter 5, I will aim to conduct a detailed investigation into the impact of galaxy interactions within CG on their physical properties, focusing particularly on ionized gas characteristics. This study will involve a comparative analysis of galaxies from a field control sample, using IFS data provided by MaNGA project. This chapter will focuses on the fifth specific objective.

In Chapter 6, I will study how the morphological properties of galaxies change in groups falling into the Abell 1644 galaxy cluster. Using S-PLUS data covering a region out to $5 \times R_{200}$, this study aims to explore how the preprocessing of galaxies is influenced by their location within substructures and their distance from the cluster centre. I will also compare the morphological properties of galaxies identified as part of a substructure with those that are not, as well as with galaxies in CGs and the control sample. This comparison aims to provide a deeper understanding of how different environments, such as substructures and CGs, influence the evolution of galaxies.

Finally, in Chapter 7, I will present a summary of the main results and conclusions of these chapters, aiming to answer how dense environments like CGs affect the evolution of galaxies. In Chapter 8, I propose potential future research avenues to deepen our understanding of how the environment influences galaxy properties.

Chapter 2

Revealing a transitional galaxy population through a multiwavelength approach

In this chapter, I present how we selected galaxies in Compact Groups (CGs) and field galaxies to serve as our control sample. These two samples will be analysed in this chapter and the next two (Chapters 3 and 4). This sample consists of 340 CGs in the Stripe 82 region, totaling 1083 galaxies, and a control sample of 2281 field galaxies. With these data, we performed a multiwavelength morphological fitting process using Southern Photometric Local Universe Survey (S-PLUS) data. We divided our sample into early-type galaxies (ETGs), late-type galaxies (LTGs), and *transition galaxies* using the r-band Sérsic index and the colour $(u - r)$. We found a bimodal distribution in the effective radius–Sérsic index plane, where a secondary 'peculiar' galaxy population of smaller and more compact galaxies is observed in CGs, which is not observed in the control sample. This indicates that galaxies are undergoing a morphological transformation in CGs. Additionally, we found significant statistical differences in the distribution of specific star-formation rate (sSFR) when comparing both environments for LTGs and ETGs. We also found a higher fraction of quenched galaxies and a lower median sSFR in CGs than in the control sample, suggesting the existence of environmental effects favouring the cessation of star formation, regardless of galaxy type. Our results support the notion that CGs promote morphological and physical transformations, highlighting their potential as ideal systems for galaxy pre-processing.

This chapter is organised as follows: in Section 2.1, we describe the data used and how we select the CGs as well as our control field sample. In Section 2.2, we present the methodology for obtaining the structural parameters in a multi-wavelength analysis of each galaxy. In Sections 2.3 and 2.4 we present and discuss our results, and we summarise and conclude our work in section 2.5

Based on Montaguth et al. (2023), published in MNRAS.

2.1 Data

In this Section, we describe the selection of the CGs of galaxies that we analyse, their photometric data as well as the control sample of field galaxies. We analyse a region inside the stripe data from the Stripe 82 region (Abazajian et al. 2009) because it was associated with the first data release (DR1) of the S-PLUS project (Mendes de Oliveira et al. 2019). We note, however, that the analysis shown in this thesis is based on the Data Release 3 (DR3) of S-PLUS, where the photometry has been improved. We complement these data with the GALEX-SDSS-WISE LEGACY catalog (Salim et al. 2018) to obtain Star Formation Rates (SFR) and stellar masses. Throughout this thesis we have adopted a flat cosmology with $H_0 = 70 km\ s^{-1}\ Mpc^{-1}$, $\Omega_M = 0.3$, and $\Omega_\lambda = 0.7$ (Spergel et al. 2003)

2.1.1 Compact groups sample

To identify CGs in the S-PLUS catalogue we use two catalogues which cover a larger region of the sky because they are produced from SDSS data. The first one was published by Sohn et al. (2016), and it is built based on a sample of galaxies extracted from the SDSS-DR12. Groups were selected from photometric and spectroscopic information and using a Friends Of Friends code (FOF). Their CG selection is based on the following criteria: i) the absolute value of the average velocity of the group (V) minus the radial velocity of each member (V_i) should be lower than 1000 km s^{-1}; ii) each group must contain at least 3 members within $\Delta mag_r < 3$ mag of the brightest member of the group; iii) galaxies should have a magnitude in r-band < 17.77; iv) the CG should satisfy the compactness criterion, i.e. the surface brightness of the group, that is defined as the total magnitude of the group galaxies averaged over the smallest circle containing the galaxies (Hickson 1982), should be lower than 26 mag arcsec^{-2} in the r-band. The second catalogue was produced by Zheng & Shen (2020), who used data from SDSS-DR14, LAMOST spectra, and GAMA survey. These authors select the CGs based on the combination of two methods: i) the Hickson (1982) photometric criterion and ii) the spectroscopic technique, i.e. it uses the difference in radial velocities between the group and each individual galaxy. The second catalogue contains a greater number of CGs, although there are some CGs that appear in both catalogues, with 46% of the CGs that are in the Sohn et al. (2016) catalogue also listed in the Zheng & Shen (2020) catalogue. However, the Sohn et al. (2016) complements the Zheng & Shen (2020) catalogue, especially at low redshift, since the latter catalogue contains galaxies brighter than 14.0 mag (petrosian magnitude in the r-band), whereas there is no bright limit applied on the magnitudes of the galaxies in the Sohn et al. (2016) catalogue. It should be noted that these two catalogues do not have any colour selection. The combination of these two catalogues produces an initial galaxy position and redshift catalogue of 424 CGs, which will be cross-match with S-PLUS, as described below.

2.1.1.1 S-PLUS Photometric data

S-PLUS is an ongoing imaging survey that began its observations in 2016 and will cover a region of ~ 9300 deg^2 on the sky, using a robotic 0.8m aperture telescope at the Cerro Tololo Inter-American Observatory (CTIO), Chile. S-PLUS uses the Javalambre 12-band magnitude system (Cenarro et al. 2019), which includes the 5 broad-band filters u, g, r, i, z and 7 narrow-band filters centred on prominent stellar spectral features: the Balmer jump/[OII], Ca H+K, Hδ, G-band, Mg b triplet, Hα, and the Ca triplet ($J0378$, $J0395$, $J0410$, $J0430$, $J0515$, $J0660$ and $J0861$) (Mendes de Oliveira et al. 2019). S-PLUS is divided into five sub-surveys and the Stripe 82 region belongs to the Main Survey (MS). Stripe 82 comprises the coordinates between 0° to 60° and 300° to 360° in right ascension and $-1.4°$

to 1.4° in declination. More details about the survey can be found in Mendes de Oliveira et al. (2019). The exposure times per image of the MS are 227, 220, 118, 59, 57, 33, 61, 40, 290, 46, 80, and 56 seconds for filters u, $J0378$, $J0395$, $J0410$, $J0430$, g, $J0515$, r, $J0660$, i, $J0861$ and, z, respectively. For the MS, three images are taken for each filter

The S-PLUS data were reduced by using the *jype* pipeline designed for J-PLUS and J-PAS (Cristóbal-Hornillos et al. 2015). Almeida-Fernandes et al. (2022) explained in detail the procedure to generate the S-PLUS catalogues. The source detection and photometry are done with the SExtractor software (Bertin & Arnouts 1996) and the zero-point photometric calibrations were estimated by using an optimized technique for wide-field multi-filter photometry[1]. The photometric depths of S-PLUS were defined for different values of S/N, where the lowest value is S/N=3. Then, the limiting magnitude is defined as the peak of the magnitude distribution at that S/N. In the case of a S/N=3, the shallowest filter is $J0861$ with a petrosian magnitude of 19.9. The deepest magnitudes are reached in filters g and r with 21.3 (Almeida-Fernandes et al. 2022). Reaching surface brightness of $\sim$ 24.5 mag arcsec^{-2} in the r-band.

The S-PLUS DR3 catalogue contains astrometric, structural, and photometric information for each source, such as the celestial coordinates (RA, DEC) in the J2000 system, the physical position on the CCD (X, Y), the size of the different photometric apertures, their magnitudes and errors, the signal to noise ratio, the FWHM, the parameters on the isophotes (A, B, and THETA), the light fraction radii (FLUXRADIUS). The different apertures included were ”AUTO”, ”PETRO”, ”ISO”, ”APER3”, ”APER6”, ”PSTOTAL”, where ”APER3” and ”APER6” are circular apertures of 3 and 6 arcsec diameters, respectively. The magnitudes in the S-PLUS catalogue have not been corrected for Galactic extinction. In this work, we use the information on the RA and DEC positions, the AUTO and APERS3 magnitudes in the twelve filters, the physical position in the CCD, and the parameters on the isophotes of the sources in CG galaxies from the S-PLUS catalogues in DR3.

Our sample of 424 CGs (described in Section 2.1.1) was matched with the S-PLUS DR3 catalogues. We find 340, out of the 424, CGs in the S-PLUS database (80% of the CG sample). These CGs had all their galaxies identified in S-PLUS, with 1092 galaxies at redshifts $0.015 < z < 0.197$. We eliminated 9 galaxies from the total sample because they were visually contaminated by bright stars. In total, we have 1083 galaxies, therefore some CGs have fewer members. This is our final sample for CGs galaxies that will be analysed throughout this thesis.

2.1.1.2 Achival GALEX-SDSS-WISE LEGACY photometric data

In order to complement our analysis, we search for multi-wavelength data in the *GALEX-SDSS-WISE* LEGACY (GSWL) catalogue, published by Salim et al. (2018). We find that 88% of our selected CG galaxies are included in this catalogue, corresponding to 321 CGs with a total of 967 galaxies. Salim et al. (2018) fit the Spectral Energy Distribution (SED) for galaxies in the GSWL catalogue by using the CIGALE code (Noll et al. 2009) and considering the *GALEX*, *SDSS* and *WISE* photometry data calibrated in Herschel-ATLAS. In this work, we will use the SFR derived from their SED fittings to complement our analysis in the following sections.

2.1.2 Control sample: Field galaxies

In order to determine the influence of the environment on the properties of CGs galaxies (e.g. size, colours, and SFRs), we have defined a sample of galaxies located in less dense environments, namely

---

[1] The zero points are available in the auxiliary tables section `https://splus.cloud`

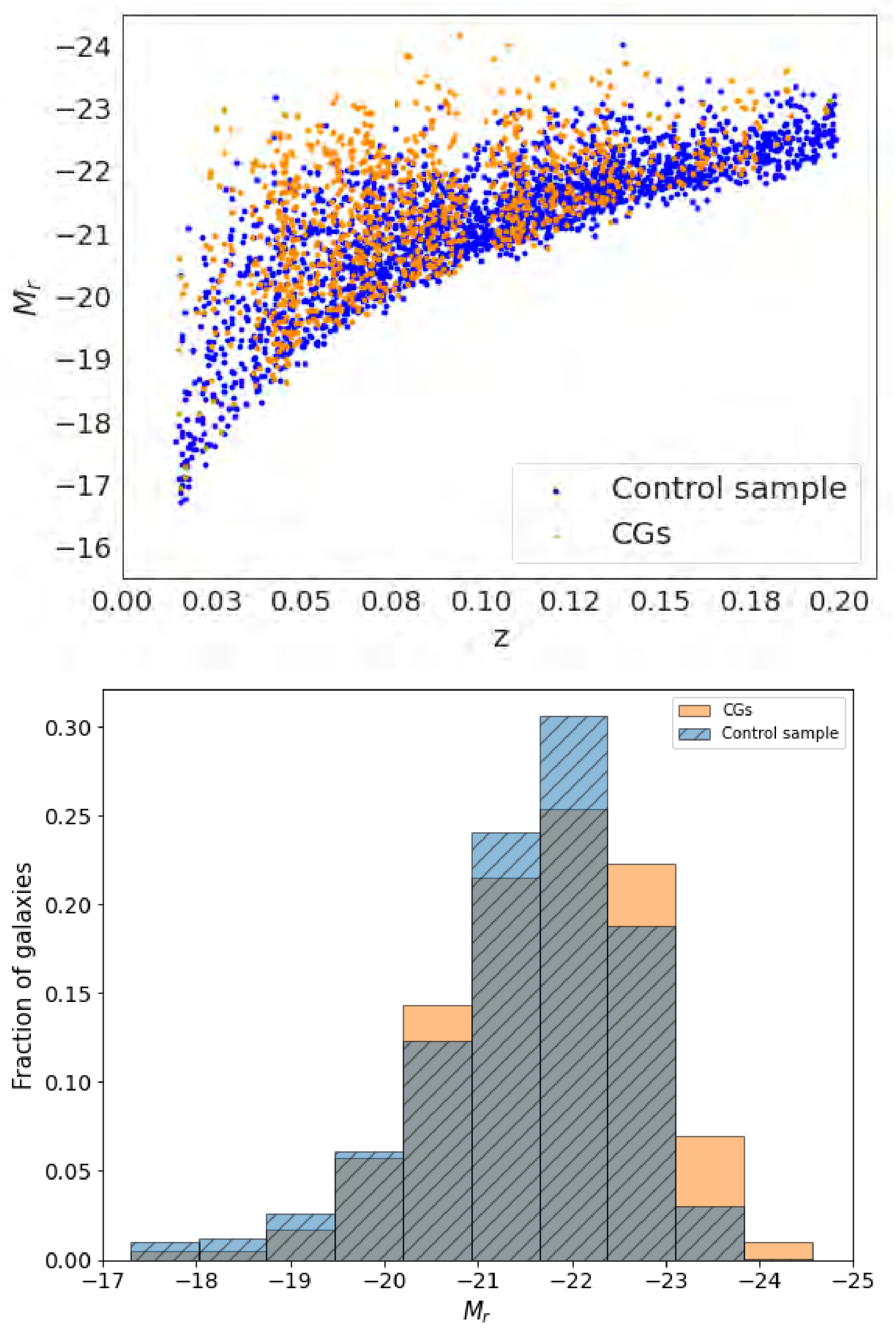

Figure 2.1.1: The upper panel shows the absolute magnitude in *r*-band as a function of redshift, and the lower panel shows the normalised histogram distribution of M_r in both environments. Galaxies in CGs are in orange whereas galaxies in the control sample are shown as blue points. Absolute magnitudes in *r*-band corrected for galactic extinction and with K-correction.

field galaxies, which we use as our control sample. We selected this sample to have the same apparent magnitude in r-band and redshift limits as the sample of galaxies in CGs.

The field galaxies are selected from the catalogue published by Yang et al. (2007) as those labelled as *single-member groups* (i.e. a halo of an individual galaxy) in the Stripe 82 area. Yang et al. (2007) used spectroscopic data from SDSS-DR4 (Adelman-McCarthy et al. 2006) and NYU-VAGC (Blanton et al. 2005) and a similar method to the group finder used by Yang et al. (2005).

We cross-match the field sample with the S-PLUS DR3 catalogue obtaining a sample of 11841 galaxies for the same redshift interval at which we have our CGs sample, $0.015 < z < 0.197$. From this sample, we randomly select a subsample of 2300 galaxies using a Monte Carlo algorithm which preserves the characteristics of the initial sample. We consider from now on only this sample of 2300 control field galaxies for our analysis. We excluded 19 galaxies from this sample due to contamination from saturated stars affecting their flux or because they exhibited low surface brightness (i.e., they are diffuse). The median surface brightness limit of galaxies in the control sample, 24.6 $mag\ arcsec^{-2}$, is slightly higher than that of galaxies in the CGs, 24.2 $mag\ arcsec^{-2}$. For this control sample of 2281 galaxies, we also perform a match with the GSWL catalogue, finding 92% of galaxies in this catalogue.

2.1.3 Final sample of galaxies

The top panel of Figure 2.1.1 shows the r-band absolute magnitude of galaxies as a function of redshift. We estimate the absolute magnitude from $M_r = m_r - 5 \times log(D_L/10pc) - K$. Here, D_L is the luminosity distance calculated from the redshift and K is the K-correction (Chilingarian et al. 2010) [2], used to transform the observed magnitudes into magnitudes in the rest frame. All the galaxies in our sample have observed $(g-r)$ colours within the range of -0.1 to 1.9, which ensures that we can apply the K-correction by Chilingarian et al. (2010). Blue points in the figure are galaxies in our control sample and orange points are galaxies in the CGs, as described in 2.1.1. Magnitudes have been corrected for Galactic extinction by using Cardelli et al. (1989), extinction law with $R_v = 3.1$, and the maps from Schlafly & Finkbeiner (2011). Although in S-PLUS it is possible to reach magnitudes as faint as r-band~ 21, our sample is limited to galaxies spectroscopically selected from the Main Galaxy Sample catalogue in the legacy SDSS. This catalogue is complete for a magnitude of $r \leq 17.77$ (petrosian magnitude corrected for Galactic Extinction). We note that the sample chosen by Yang et al. (2007), Sohn et al. (2016), and Zheng & Shen (2020) used the SDSS r-band magnitude for selecting their samples, whereas in our case, we employed S-PLUS data for the photometric measurements. This difference may account for the minor dispersion observed at the bottom region in the z vs M_r plane (top panel in Figure 2.1.1).

In the bottom panel of Figure 2.1.1 we show that the sample covers absolute magnitudes which range between $M_r = -17$ to $M_r = -24$, with a peak at $M_r = -22$. Since our goal is to study how the environment impacts galaxy evolution, we study all galaxies detected in the CGs, and compare them with a similar magnitude distribution in the field sample, as shown in Figure 2.1.1.

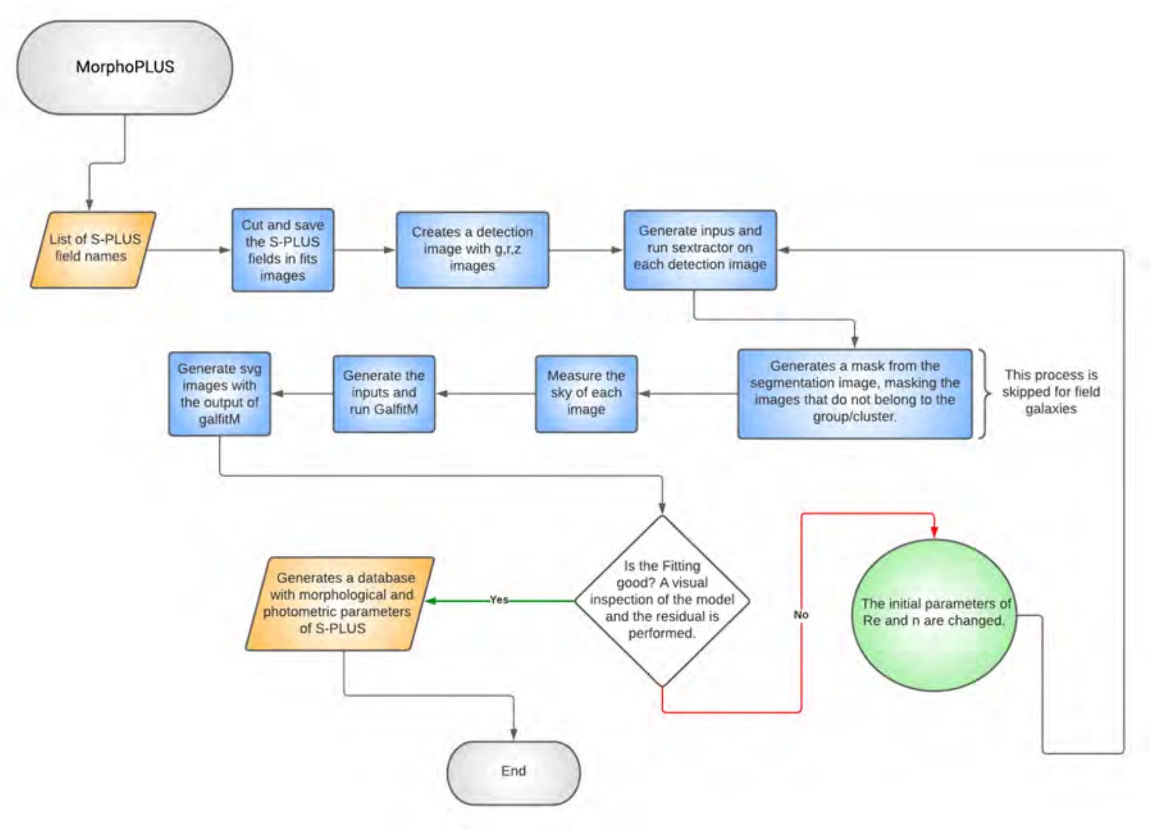

Figure 2.2.1: A flowchart describing morphoPLUS's operation. Required inputs are the catalogue with a list of galaxy coordinates, and magnitude.

2.2 Methodology

2.2.1 MorphoPLUS: morphometric parameters

We developed a code that we named 'MorphoPLUS' [3], which is based on Bash and Python, utilises SExtractor tools, and is built upon the MegaMorph code. MegaMorph facilitates the extraction of morphometric parameters for each galaxy and performs two-dimensional fitting across multiple wavelengths using the GALFITM algorithm, a modified version of GALFIT 3.02 (Peng et al. 2002, Peng et al. 2010a). GALFITM code models the surface brightness of a galaxy by using a two-dimensional analytical function, that can be a Sérsic (Sersic 1968), Nuker (Lauer et al. 1995), de Vaucouleur (de Vaucouleurs 1948) or Exponential (Freeman 1970). Additionally, to extend these functions to multiple wavelengths, free parameters are replaced by wavelength functions, which are a set of Chebyshev polynomials. GALFITM performs multiple fitting components where users can include information regarding the sky background, as well as decompose the galaxy in bulge, disk, and bar. The advantage of using a multi-wavelength morphological fitting over single-band fitting is that it improves the results in terms of accuracy and robustness (Vika et al. 2013). The best fit is determined using the Levenberg-Marquardt (LM) algorithm, minimizing χ^2.

Essentially, MorphoPLUS is automated to take a catalogue as input, containing the list of objects for which we want to perform fitting using S-PLUS data. In Figure 2.2.1, we present the flowchart of the code. The catalogue must be containing the galaxies to be fitted, the code first identifies the corresponding fields in S-PLUS data of the cluster in this case. It then locates the galaxies in those fields and divides each field into sub-images in the 12 filters, making them ready for fitting with GALFITM. It is worth noting that galaxies may sometimes extend to the edges of these subfields due to the automated process. However, the code is designed to recognise galaxies at the edges and exclude them from the fitting process. Subsequently, the code generates images for these edge galaxies, which are four times the size of the original galaxies, for subsequent fitting.

In addition to creating the images and saving them, the code also generates the Point Spread Functions (PSFs) for each filter. These PSFs are modelled using a Moffat function, defined as $PSF(r) = \frac{\beta-1}{\pi\alpha^2}\left[1+\left(\frac{r}{\alpha}\right)^2\right]^{-\beta}$ with $FWHM = 2\alpha\sqrt{2^{1/\beta}-1}$. Both the Full Width Half Maximum (FWHM) and beta parameter (β) are available in the headers of each field for every filter in the S-PLUS images.

With the images of each subfield and individual galaxies prepared, the code proceeds to generate the detection images, which are created by combining the images in the g, r, and z filters. These images are used to produce segmentation images using the SExtractor software (Bertin & Arnouts, 1996). SExtractor masks all the sources it detects, including the galaxies in the catalogue. Subsequently, the codes employ the generated images to construct a new segmentation image, wherein the codes unmask the galaxies in the catalogue that we provide. In this process, the code assigns a numerical value of one to the pixels that are masked and a value of zero to those that are not. This step is crucial because GALFITM requires the mask provided as input to contain zeros for the regions to be fitted.

Afterwards, the code measures the background sky value for each image, calculating the median of pixel values at a 3σ level to exclude different sources. It is important to note that the S-PLUS images already come with the background sky subtracted. With these estimated values, the code proceeds to generate inputs for each subfield. It requires an initial guess for the parameters to be modelled, which are the values estimated in the S-PLUS catalogues, such as the half-light radius, radii that contain

---

[2] The code is available at `http://kcor.sai.msu.ru/`

[3] The code is available at `https://github.com/GMontaguth/MorphoPLUS`

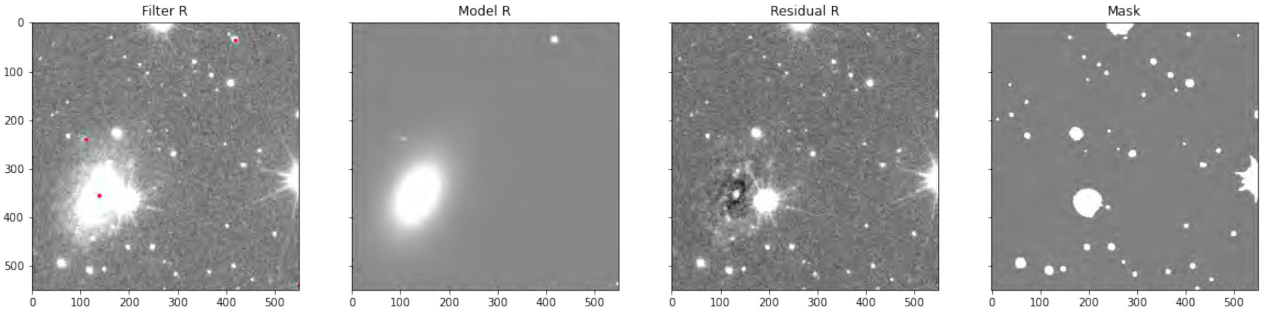

Figure 2.2.2: On the left we present a subfield of S-PLUS in the r-band, next to it on the right the galaxy models, next to this image we present the residual image, and lastly on the right the mask for this subfield.

90% of the light, a/b ratio, apparent magnitudes in the twelve filters, and zero points of the images. These zero points are available as additional tables in the S-PLUS catalogues [4]. For the initial guess parameter for the Sérsic index, the code uses an empirical approximation between concentration, which is the ratio between R_{90} and R_{50}, and n, where $C = 2.770n^{0.466}$ (Andrae et al. 2011).

Then the code runs GALFITM, which, in this case, fits all galaxies with a single component model using a Sérsic profile, as shown in equation 2.2.1:

$$I = I_e \exp\left[-b_n\left(\left(\frac{R}{R_e}\right)^{1/n} - 1\right)\right] \tag{2.2.1}$$

Here, the intensity at the effective radius (R_e), denoted as I_e, is a key parameter. It represents the intensity at the radius containing half of the total light. The parameter b_n is a function of the Sérsic index (n) and has a relationship defined as $\Gamma(2n) = 2\gamma(2n, b_n)$, where Γ represents the Gamma function, and γ denotes the lower incomplete Gamma function (Ciotti (1991)). The Sérsic index (n) plays a crucial role in shaping the light profile.

Then the code generate two tables, one with fits that have a χ^2 less than 2, and another with fits having a χ^2 greater than 2. Additionally, the code creates SVG images containing each subfield in the twelve filters with their models and residuals. For galaxies with $\chi^2 > 2$, we refine the models, accounting for potential errors, such as contamination from a nearby star or interference from the brightness of a neighbouring source affecting the creation of an appropriate mask image. Therefore, we fit the image masks individually for these fields and rerun GALFITM. We also conduct a visual inspection of the fits to perform a sanity check on galaxies with $\chi^2 < 2$, ensuring that the fits are appropriate. Additionally, we reran GALFITM for galaxies where the visual inspection indicated that the fit was not satisfactory. In summary, this 'MorphoPLUS' code is automated to model the surface brightness of galaxies with a single component, in this case, a Sérsic profile for S-PLUS data. Users only need to provide the code with a table containing the catalogue of galaxies of interest.

In Figure 2.2.2 from left to right, we present an example of a galaxy in this sample, the image in the *r*-band, the generated model, the residual, and the mask. Here, we can observe that the mask is suitable for that region of the sky, and the code is capable of fitting the galaxy despite the presence of a nearby star. It is crucial to highlight that Lima-Dias et al. (2021) examined the goodness of the fit by recovering the parameters of simulated galaxies convolved with S-PLUS filters. They found that GALFITM enables the retrieval of the Sérsic index and the effective radius with an uncertainty of approximately 4 percent compared to the values used to model the simulated galaxies. Figure 2.2.3

---

[4] The zero points are available in the auxiliary tables section `https://splus.cloud`

shows an example of a GALFITM output for one of the CGs analysed in this work. In this figure, the top panels display the images in each S-PLUS filter, the middle panels show the light profile model and the bottom panels show the residual image, i.e. the model subtracted from the observed image.

2.2.2 Stellar masses estimation

Bell & de Jong (2001) and Taylor et al. (2011) have demonstrated that a robust and reliable estimate of the stellar mass of a galaxy can be obtained from optical bands, thanks to the mass-luminosity relation, which is derived from stellar population synthesis models. Taylor et al. (2011) used the Single Stellar Population (SSP) models by Bruzual & Charlot (2003) and assumed a Chabrier (2003) Initial Mass Function. In order to correct for the internal extinction of galaxies they use the extinction law proposed by Calzetti (2001). They derived the following relation to estimate M_*/L using the colour $(g-i)_0$, at rest frame, and the absolute magnitude in the i-band, M_i:

$$log_{10}(M_*/M_\odot) = 1.15 + 0.7 \times (g-i)_0 - 0.4 \times M_i \tag{2.2.2}$$

We use Equation 2.2.2 to estimate the stellar mass using the S-PLUS data of the galaxies in our samples, both in the control sample and in the CGs. Figure 2.2.4 shows the histograms of the stellar masses in both environments, in blue and orange for the galaxies in the control sample and in CGs, respectively.

In Figure 2.2.5 we compare the stellar masses that we estimate with those published in the GSWL catalogue (based on SED fitting), where the blue and orange dots represent the galaxies in the control sample and the CGs, respectively. The blue dashed line represents the one-to-one relationship, while the red solid line shows the best linear fit, which has a slope of 1.04 and an RMS of 0.13. The data closely follow the one-to-one relation with some scatter, which indicates that using the colour $(g-i)$ and the Equation 2.2.2 proposed by Taylor et al. (2011), provides a good estimate of stellar mass. We thus use the stellar masses obtained from Equation 2.2.2 throughout this thesis.

2.2.3 Star Formation Rates

The star formation rates (SFR) that we use in this work are those estimated by Salim et al. (2018), based on the SED fitting done using the CIGALE code and the GALEX-SDSS-WISE LEGACY catalogue as mentioned in Section 2.1.2. Those authors assumed a two-component exponential star formation history, one for the younger population and another for the older one. The formation times for the younger component range from 100 Myr to 5 Gyr, where the mass fraction of the younger component must range up to 0.5. The old population times ranged from 850 Myr to 20 Gyr. Using the SFR from the GWLS catalogue and the stellar mass estimated by us in the previous section, we estimate the specific star formation rate as:

$$sSFR = \frac{SFR}{M_*}[yr^{-1}]$$

2.3 Results

We explore in this section the relation between the structural and physical parameters of the galaxies analysed in this work.

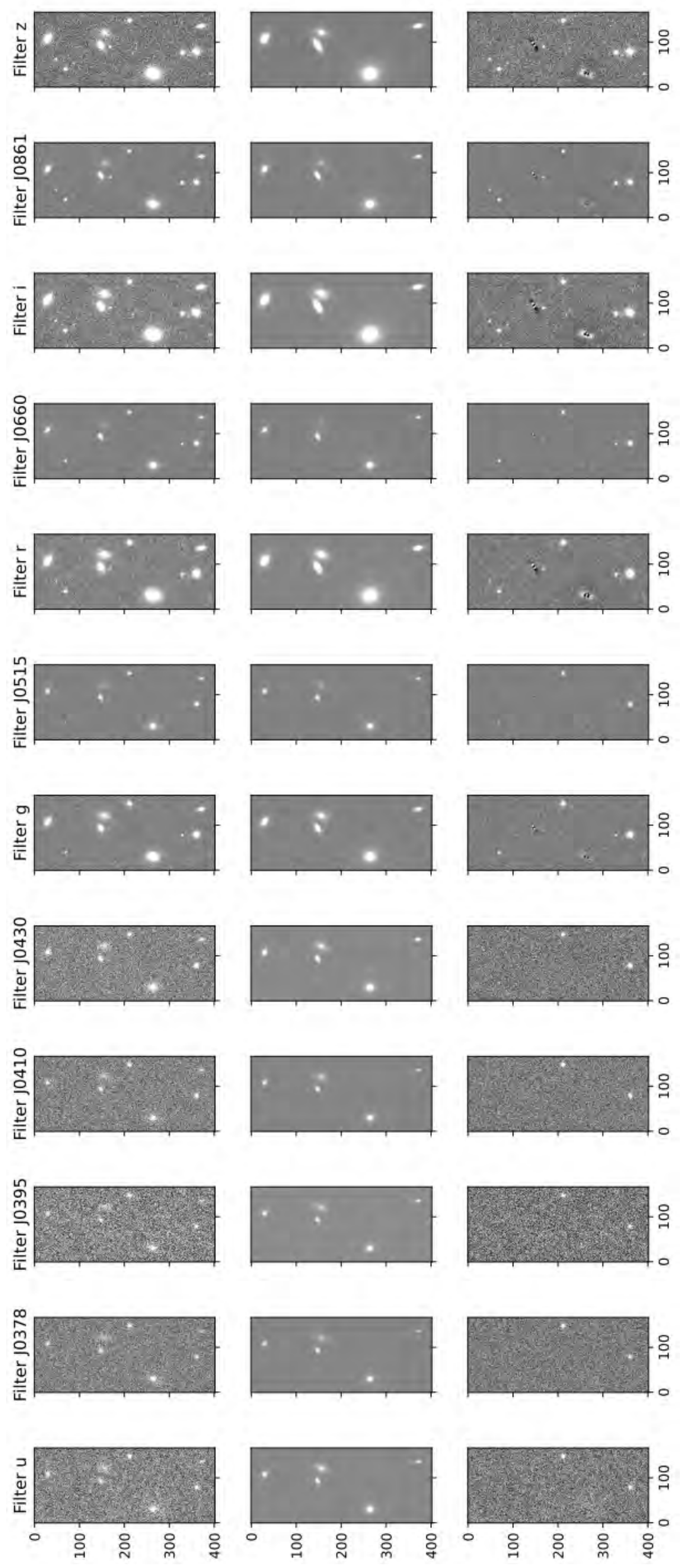

Figure 2.2.3: Left panels: S-PLUS images for one of the CGs analysed in each filter. Middle panels: the model generated using GALFITM. Right panels: the residual, the model subtracted from the observed image. The box size of each plot corresponds to 220” × 92”.

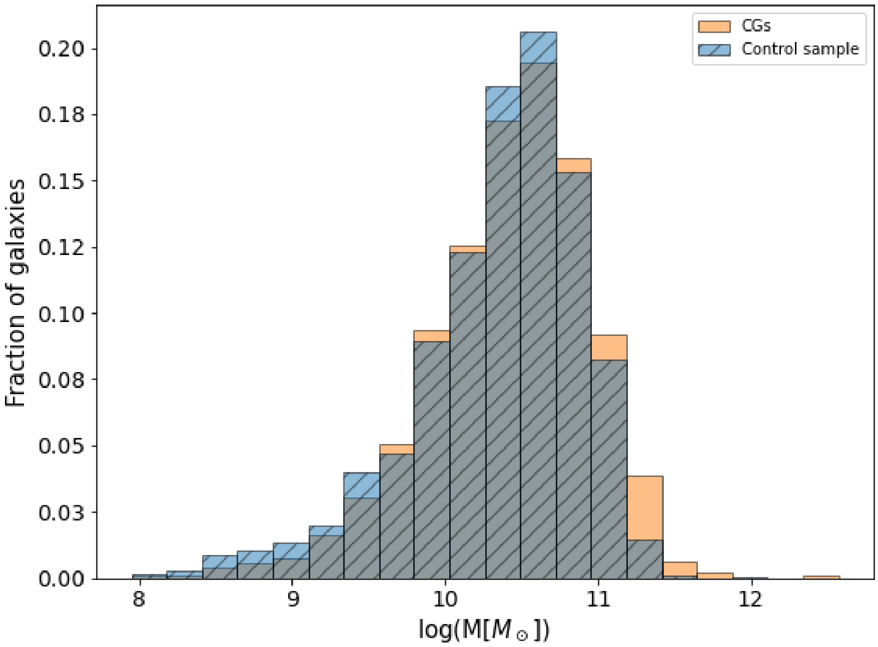

Figure 2.2.4: Normalised histograms of stellar masses for galaxies in CGs (orange) and in the control sample (blue).

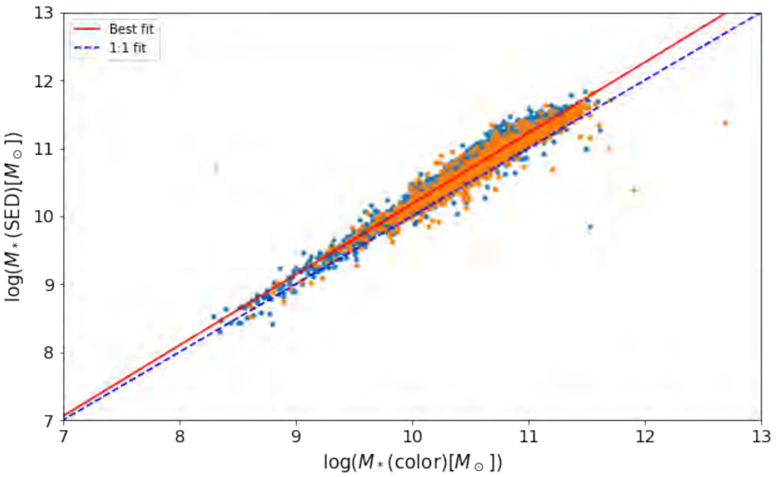

Figure 2.2.5: Comparison between the stellar masses estimated in this work and that estimated in the GSWL catalogue using SED fitting. Orange points represent galaxies in CGs and the blue ones are galaxies in the control sample. The solid line is the one-to-one relationship between the compared parameters.

2.3.1 Structural parameters

2.3.1.1 Classifying galaxies: Late-type, transition, and early-type systems

The colours of galaxies are associated with their predominant stellar populations and are related to their morphology (Morgan & Mayall 1957). In particular, blue galaxies are typically star-forming objects, whereas red galaxies are mostly quiescent, containing red and old stars. Indeed, we may expect a correlation between colours and structural parameters of galaxies (e.g. Vika et al. 2015b). As indicated in section 2.2.1, in this work we characterise the morphology of each galaxy by fitting its light profile with the Sérsic function. Therefore, colours and Sérsic index can be used to separate early-type galaxies (ETGs) from late-type galaxies (LTGs), where red galaxies with high values of n are classified as ETGs and blue galaxies with low values of n are classified as LTGs (Ball et al. 2008, Kelvin et al. 2012, Vika et al. 2015b).

We use the Sérsic index in the r-band and the $(u-r)$ colour to classify galaxies as ETG and LTG following the criteria proposed by Vika et al. (2015b). Galaxies with $n \geq 2.5$ and $(u-r) \geq 2.3$ are ETGs and galaxies with $n < 2.5$ and $(u-r) < 2.3$ are LTGs. The top panel of Figure 2.3.1 shows this classification for galaxies in the CGs. The same classification for our control sample of field galaxies is shown in the bottom panel of Figure 2.3.1. The galaxies located in the top-left region of each $n-$colour diagram, i.e. red colours and $n < 2.5$, are defined as *transition galaxies*, previous authors have named this region as red low-n galaxies (Vulcani et al. 2014) or red disk galaxies, where they used colour and concentration to classify them or just the colour and the morphological classification from Galaxy Zoo (Lopes et al. 2013, Tojeiro et al. 2013). In the Appendix A.1 we present the results we find for the region with $n > 2.5$ and $(u-r) < 2.3$, which we have defined as *Other region*. For Vulcani et al. (2014) the galaxies in this region are a mixture of green and blue high-n.

In Table 2.3.1 we list a summary of the median values for the different physical and morphological parameters obtained for the populations of ETGs, LTGs, and *transition galaxies*, classified as described above (see Fig. 2.3.1). The values outside and inside the parenthesis represent the CGs and the control sample, respectively. We find that the median values of the effective radius and stellar mass are lower in CG galaxies, except for LTGs. The Sérsic index is similar for LTGs in both environments, however, it is slightly higher for *transition galaxies* in CGs, whereas for ETGs this value is slightly higher in the control sample. In addition, The median of $sSFR$ is lower in CGs than in the control sample regardless of the morphological type. Furthermore, in CGs, the percentage of quenched galaxies is higher than in the control sample for all three types of galaxies, where we consider a galaxy to be quenched if $Log(sSFR) \leq -11$, based on the criterion proposed by Wetzel et al. (2013). The implications of these results are discussed in the following sections

Following this classification, and as can be seen in the histogram shown in Figure 2.3.2 and in the first row in Table 2.3.1, there is a larger fraction of ETGs in the CGs than in the control sample, while in the control sample, there is a larger fraction of LTGs and *transition galaxies*. This suggests an environmental difference in the fraction of ETGs and LTGs between the CGs and the control sample. However, it is worth noting that this may be due to a selection effect in the CGs sample since one of the criteria used is that they should have surface brightnesses $\mu_r \leq 26.0$ mag arcsec^2, which favours groups with bright galaxies such ETGs. In addition, the catalogue of CGs used in this work was produced by using optical data, which likely generated a bias toward groups with massive galaxies (Hernández-Fernández & Mendes de Oliveira 2015). This is also reflected in the colour distribution of these galaxies. Figure 2.3.3 shows the histogram of the $(g-r)_0$ colours at rest frame. CG galaxies display a bimodal colour distribution with a red component that dominates, which peaks at a colour $(g-r)_0 \sim 0.75$, with a small tail at bluer colours, while galaxies belonging to the control sample show a clear bimodality.

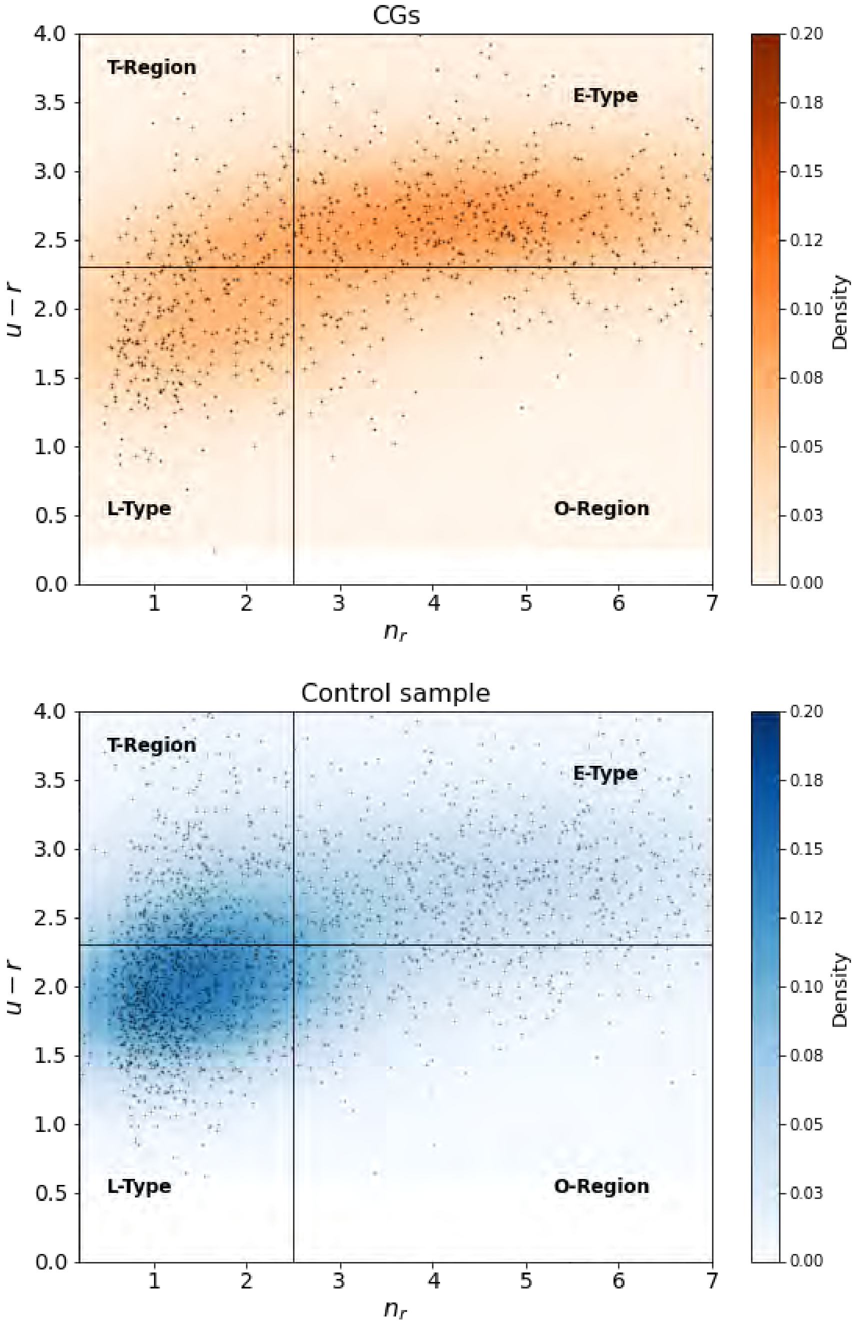

Figure 2.3.1: ETGs, *transition galaxies* (T-Region), LTGs classification, and *other gaxies* (O-Region), using $(u-r)$ colour and Sérsic index in the r-band (n_r), the vertical line is for $n_r = 2.5$ and horizontal for $(u-r) = 2.3$. The upper plot corresponds to the galaxies in CGs and the lower plot to the galaxies in the control sample, in blue and orange are density plots, where the black dots are the original data.

	Early type	**Transition region**	**Late type**
Percentage	52% (33%)	11% (19%)	22% (37%)
Median R_e**[Kpc]**$[r]$	$7.24^{7.70}_{6.44}$ $(8.77^{9.34}_{8.04})$	$5.78^{6.69}_{4.78}$ $(7.01^{7.37}_{6.71})$	$5.31^{5.73}_{4.94}$ $(6.56^{6.84}_{6.31})$
Median $n[r]$	$4.64^{4.78}_{4.52}$ $(4.94^{5.11}_{4.78})$	$1.61^{1.83}_{1.46}$ $(1.41^{1.46}_{1.38})$	$1.19^{1.25}_{1.10}$ $(1.13^{1.18}_{1.10})$
Median $Log(M_*[M_\odot])$	$10.70^{10.75}_{10.67}$ $(10.77^{10.79}_{10.74})$	$10.51^{10.61}_{10.44}$ $(10.63^{10.68}_{10.60})$	$10.07^{10.12}_{10.02}$ $(10.18^{10.21}_{10.14})$
Median $Log(sSFR[\mathbf{yr}^{-1}])$	$-11.99^{-11.91}_{-12.07}$ $(-11.92^{-11.86}_{-12.00})$	$-11.00^{-10.75}_{-11.07}$ $(-10.83^{-10.73}_{-10.97})$	$-10.16^{10.11}_{-10.23}$ $(-10.07^{-10.10}_{-10.03})$
Percentage of quenched galaxies	87% (82%)	50% (45%)	10% (3%)

Table 2.3.1: Median values of the different physical and morphological properties derived for each galaxy population for CGs. The values in parentheses correspond to those of the control sample. The supra and subscript are the values at the 90% confidence interval estimated with the bootstrapping technique for each median. We considered quenched galaxies as those with $Log(sSFR) \leq -11$.

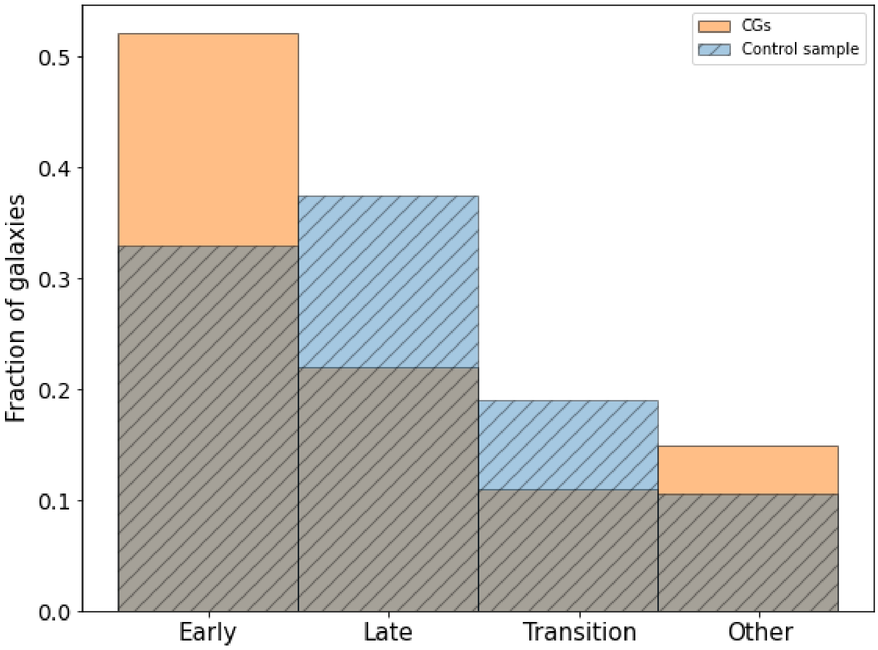

Figure 2.3.2: Histogram of the fraction of galaxies in each population, LTGs, ETGs, *transition galaxies*, and galaxies in the right lower region (other), defined in the text and shown in figure 2.3.1.

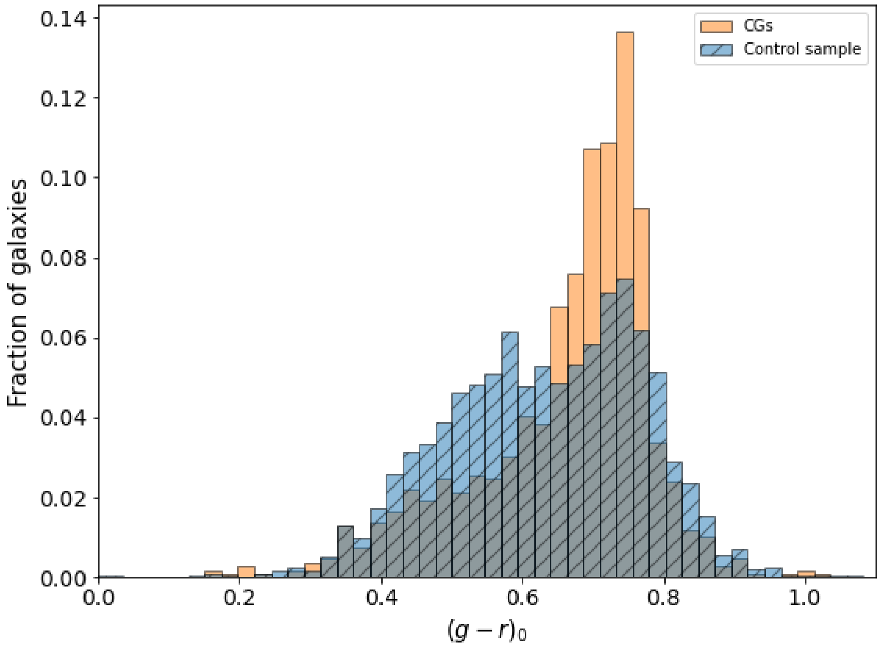

Figure 2.3.3: Histograms of the colour distribution $(g-r)$, for both environments.

2.3.1.2 Sérsic index behaviour as a function of wavelength

Since the Sérsic index is available for each of the 12 S-PLUS filters, we can analyse the median behaviour of this parameter with respect to wavelength, for each population in each environment. In Figure 2.3.4 we show the median Sérsic index that we obtain for each galaxy population, as a function of wavelength. The triangles and circles in Figure 2.3.4 represent the median Sérsic index for the galaxies in the control sample and in CGs, respectively. LTGs, *transition galaxies* and ETGs (as described in section 2.3.1.1) are shown as blue/cyan, green/light green, and red/orange colours, respectively. Uncertainties were estimated from a bootstrapping technique with a confidence interval (CI) of 90%. Top left, top right, and bottom panel show the entire CGs sample, CGs that contain three members, and CGs that contains four or more members, respectively. This separation is made because Hickson (1982), originally proposed that the CGs should have at least 4 members. Given that the Sérsic index is one of the most important parameter in this work, we want to check if there are differences in our results if our sample is subdivided according to the members the CGs have. We note, however, that Duplancic et al. (2013) showed that galaxy triplets satisfying the other CGs selection criteria did not differ in terms of the total star formation activity and global colours from more populated CGs. We find, as it can be seen in Fig. 2.3.4, that there is no difference in the results presented here (Sérsic index as a function of wavelength) when subdividing the sample of CGs. For this reason, we decide that for the following analyses, we would use all galaxies in CGs without discriminating the number of members.

In general, we find that the median of n increases with wavelength. In the case of ETGs in CGs (in the control sample) the value of n increases from the bluest filter to the reddest by $23\%^{29\%}_{16\%}$ ($28\%^{34\%}_{22\%}$). For galaxies in the transition region n increases by $34\%^{49\%}_{17\%}$ ($29\%^{35\%}_{21\%}$). For LTGs we find that n increases by $37\%^{48\%}_{25\%}$ ($38\%^{44\%}_{33\%}$). Also, we note that ETGs in CGs have a 10% lower n in redder filters compared to those of the control sample. In contrast, in the transition region, the increase in the median value of n is 28% higher for the CG galaxies, especially in the red filters. Section 2.3.2 will analyse the *transition galaxies* in more detail, connecting it with other properties such as SFR, R_e, and n.

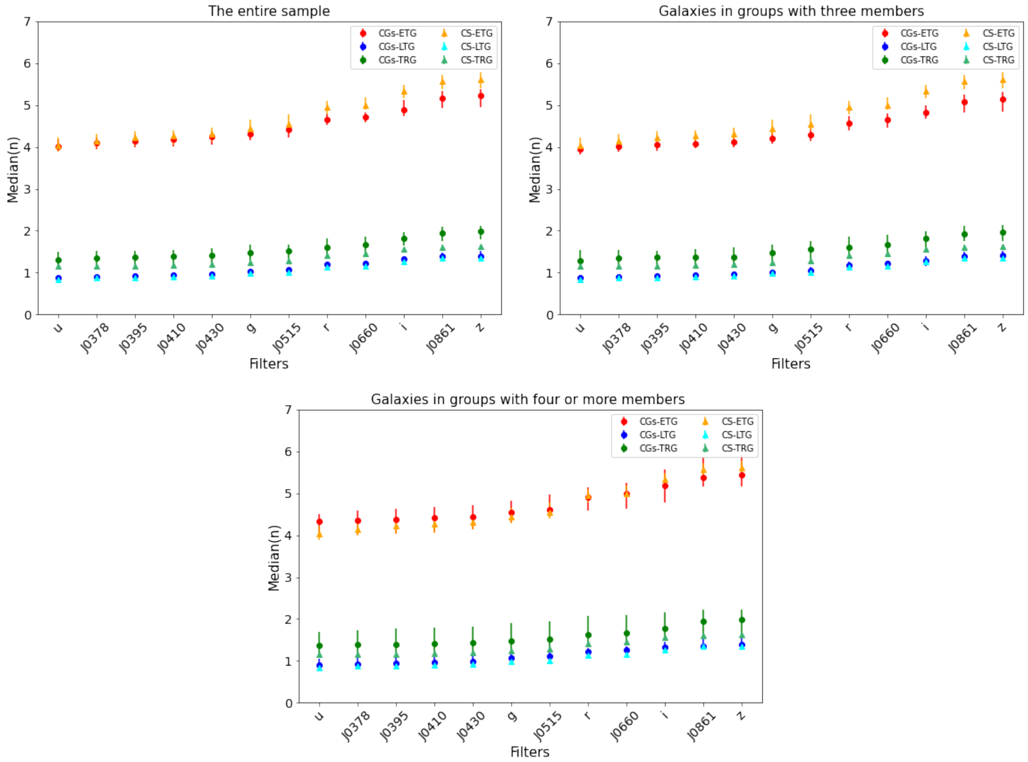
The entire sample

Galaxies in groups with three members

Galaxies in groups with four or more members

Figure 2.3.4: The median Sérsic index (n) as a function of S-PLUS filters for ETGs, LTGs, and *transition galaxies* for the CGs (circles) and the control sample (triangles). The error bars are the 90% confidence interval using bootstrapping. The upper left plots contains the entire sample in both environments, the top right plot for CGs contains the galaxies in groups with three members, and the lower panel only the galaxies in CGs in groups with 4 or more members.

2.3.1.3 Effective radius as a function of mass, Sérsic index, and wavelength

In this subsection, we analyse how R_e behaves as a function of stellar mass, how the structural parameters (n vs. R_e) are related for each galaxy population, and how these relations change with the galactic environment. The correlation between galaxy sizes and masses, for nearby galaxies, suggests that the size of a galaxy is an important key to understand its origin (Conselice 2003). In Figure 2.3.5 we show R_e as a function of stellar mass, for each galaxy population analysed in this work, where blue contours represent galaxies in the control sample and orange contours show galaxies in CGs. The top, middle, and bottom panels show the relation for ETGs, *transition galaxies*, and LTGs, respectively. The relations are displayed in the g, r, and z-band, from the left to right panels. Marginal to the scatter plot there are histograms of each parameter, where the dashed lines represent the median, the shaded regions represent the 90% CI using bootstrapping, and the error bars on the histograms are the Poisson counting uncertainty. In general, we find that there are no significant differences in the size-mass relation between the environments in each population where R_e increases as a factor of the M_*. However, from the marginal distributions we do observe that the median stellar mass for each population is slightly lower in CGs than in the control sample; the difference is bigger for LTGs. We also find that galaxies appear larger, i.e. bigger R_e in the control sample than in CGs. This is in agreement with what was found by Coenda et al. (2012) i.e., galaxies in CGs are smaller than galaxies in the control sample, but it differs from the findings reported by Poliakov et al. (2021), who found that galaxies in CGs are brighter and larger than isolated galaxies. However, they have deeper images, reaching surface brightnesses of ~ 28 mag arcsecond^{-2} in the r-band, therefore they can better trace the fainter component of the galaxies, because we achieve surface brightnesses of ~ 24.5 mag arcsecond^{-2}. In addition, the methodology used by Poliakov et al. (2021) is different than ours, given that they used GALFIT code, on which GALFITM is based. The main difference is that with GALFIT it is possible to perform a fit just in one filter and not simultaneously as with GALFITM, since they only have data in the r-band filter. On the other hand, Deng et al. (2008) find no strong dependence on galaxy size and environment, providing a different result on this topic, which was mainly based on a narrow range of luminosity. One of the possible origins for the discrepancy found with the Deng et al. (2008) study could be that the method used by them to estimate the size is different than ours: they use the half-light radius direct from the image.

In Figure 2.3.6 we show the median effective radius for each galaxy population, as a function of wavelength. The triangles and circles represent the values for the galaxies in the control sample and in CGs, respectively. ETGs, *transition galaxies*, and LTGs are shown as red/orange, green/light green, and blue/cyan colours, respectively. Uncertainties were estimated from bootstrapping with a CI of 90%. We find that the median R_e varies with wavelength for all the populations. In the case of ETGs in CGs (red circles), we find that R_e increases with wavelength until the $J0660$ filter and it begins to decrease from the filters i until z. Overall, this parameter has an increase of 4% between the bluest and the reddest filter. For the control sample (orange triangles) the increase in R_e is close to 8% between the bluest and the reddest filter, where R_e increases until the g filter, and after that, it remains almost constant in the median value of R_e. For the *transition galaxies*, R_e increases only 5% in the CGs galaxies (green circles), where the bluest filters remain almost constant in the median value of R_e. However, the *transition galaxies* belonging to the control sample (light green triangles) show a decrease in R_e at larger wavelengths, by 13%. For the LTGs in the CGs (blue circles), R_e (in median) decreases smoothly, with a difference between the bluest and reddest filter of 4%. In the case of the control sample (cyan triangles) the decrease is slightly more pronounced with a difference of 8%.

In Figure 2.3.7 we show the effective radius as a function of the Sérsic index for the filters, g, r, z, from the left to right, where the blue contours represent galaxies in the control sample and orange contours

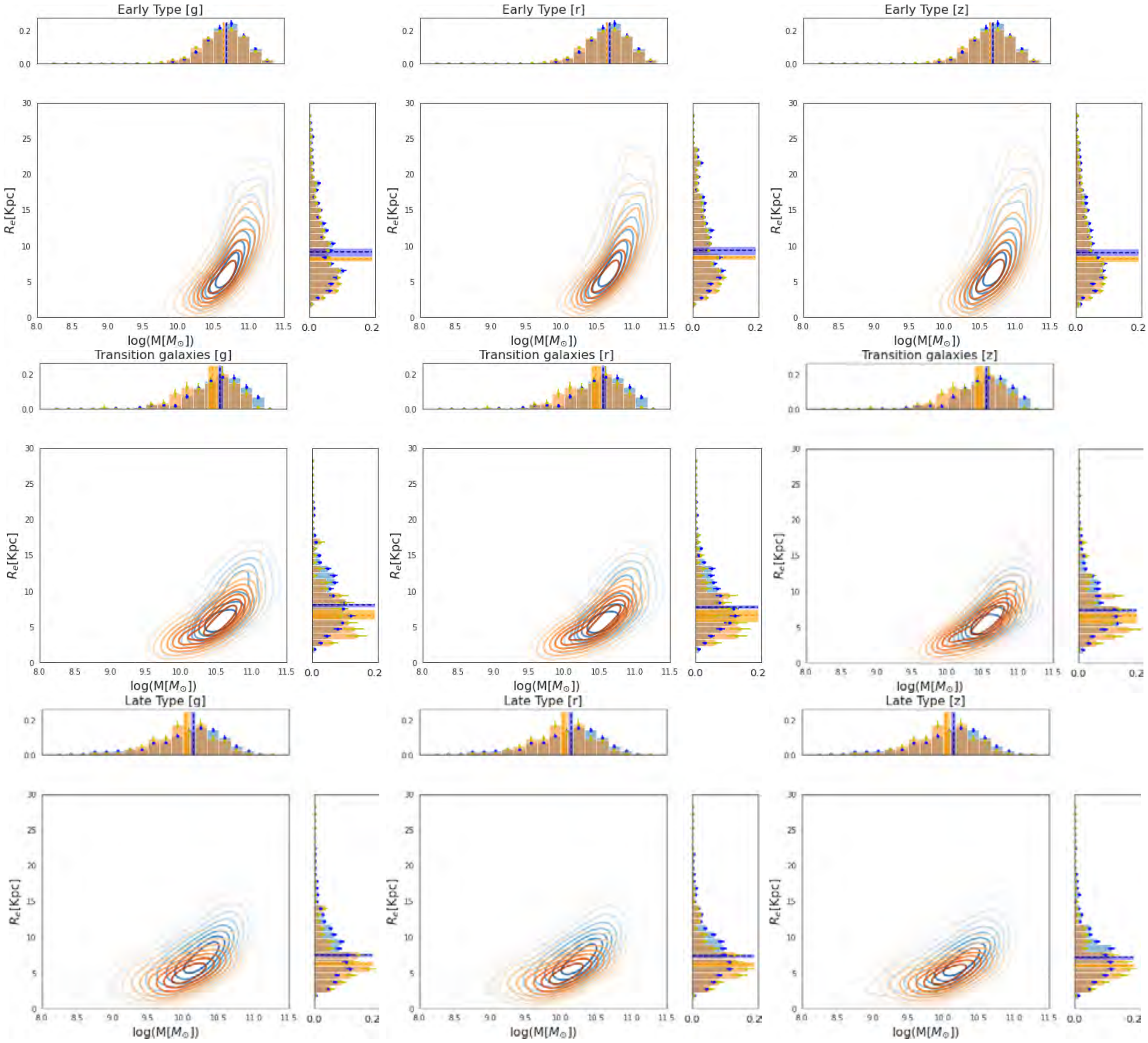

Figure 2.3.5: Effective radius as a function of stellar mass for each of the populations; the top three figures for ETGs, the middle three for those in the transition region, and the bottom three for LTGs in g, r, and z filters from left to right, respectively. Orange contours represent CG galaxies and blue contours are control sample galaxies. At the margin of each plot are histograms of each parameter, in which the dashed lines represent the median and the shaded lines represent the 90% CI using bootstrapping, and the error bars in the histogram bars are the Poisson counting error.

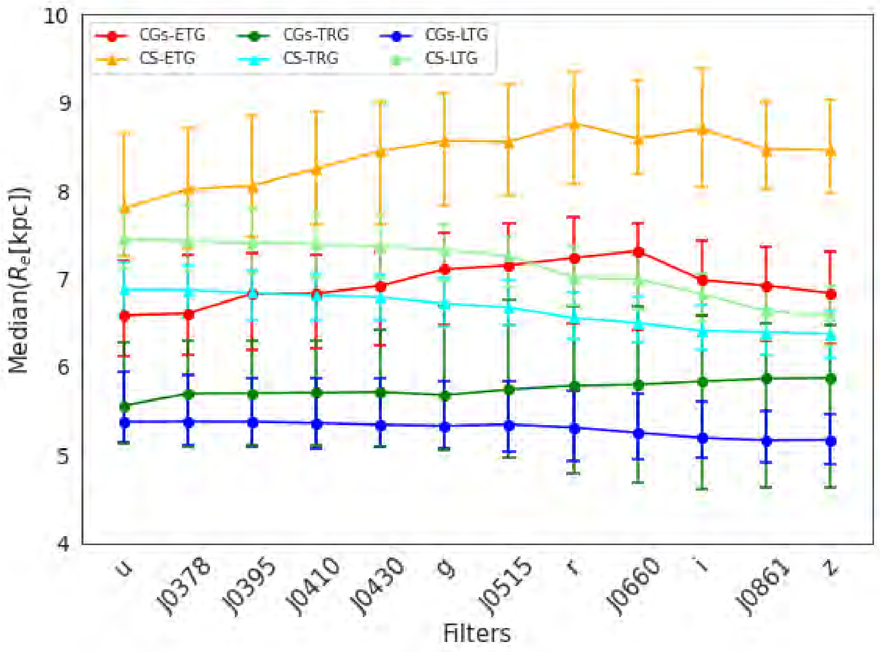

Figure 2.3.6: The median effective radius (R_e) as a function of S-PLUS filters for ETGs, LTGs, and *transition galaxies* for in the control sample (triangles) and in the CGs (circles). The error bars are the 90% confidence interval using bootstrapping.

display the distribution of galaxies in CGs. The top, middle, and bottom panels correspond to ETGs, transition region galaxies, and LTGs, respectively. In general, we find that larger R_e are reached for galaxies in the control sample, as also shown in Figures 2.3.5. In addition, and interestingly, the distribution of *transition galaxies* in CGs exhibits different behaviour, such that there is a bimodal distribution in this diagram, which is not detected in the control sample. This indicates that *transition galaxies* in CG have a secondary population of smaller and more compact objects, i.e. lower values of R_e and larger n, that we define in this work as a *peculiar galaxy population*. We further discuss this peculiar population in Section 2.4.2.

2.3.2 Star formation: statistical differences between the CGs and the control sample

In the top panels of Figure 2.3.8 we show the stellar mass versus SFR for ETGs (left), *transition galaxies* (middle), and LTGs (right), for galaxies in the control sample (blue contours) and in the CGs (orange contours). We find that, in general, galaxies belonging to CGs have lower SFRs than the galaxies in the control sample. We also observe a bimodality in the distribution of SFR for the *transition galaxies* in the control sample, whereas the galaxies in the CGs have a distribution that peaks at the middle of this bimodality (at $Log(SFR[M_{\odot}yr^{-1}]) = -11.2$). The bottom panels of Figure 2.3.8 show the sSFR instated of SFR. We observe that galaxies in CG reach lower values in sSFR than in the control sample. Also, the bimodality previously found in the distribution of SFR as a function of the stellar mass (in the top middle panel of Figure 2.3.8) is observed for *transition galaxies* in the control sample, but we do not find this bimodality in the *transition galaxies* in CGs. Another important detail to note is that the *transition galaxies* have intermediate sSFRs compared to the distributions for the LTG and ETG. To quantify these differences, we measured the median sSFR

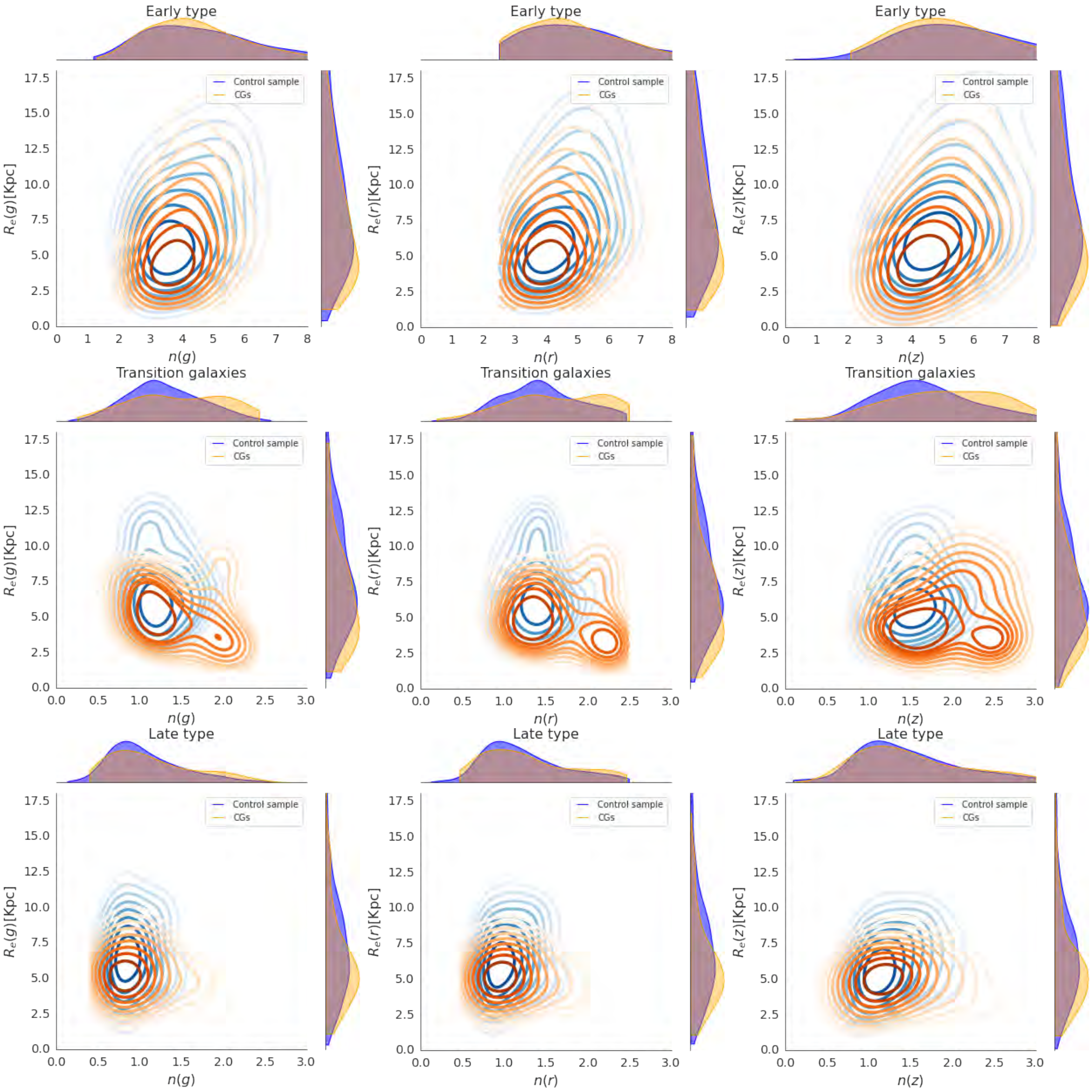

Figure 2.3.7: Contours of effective radius as a function of Sérsic index for each of the populations, the top three figures for ETGs, the middle three for those in the transition region, and the bottom three for LTGs, for each environment in three filters g,r, and z. The distribution of each parameter is shown in the margin of each plot.

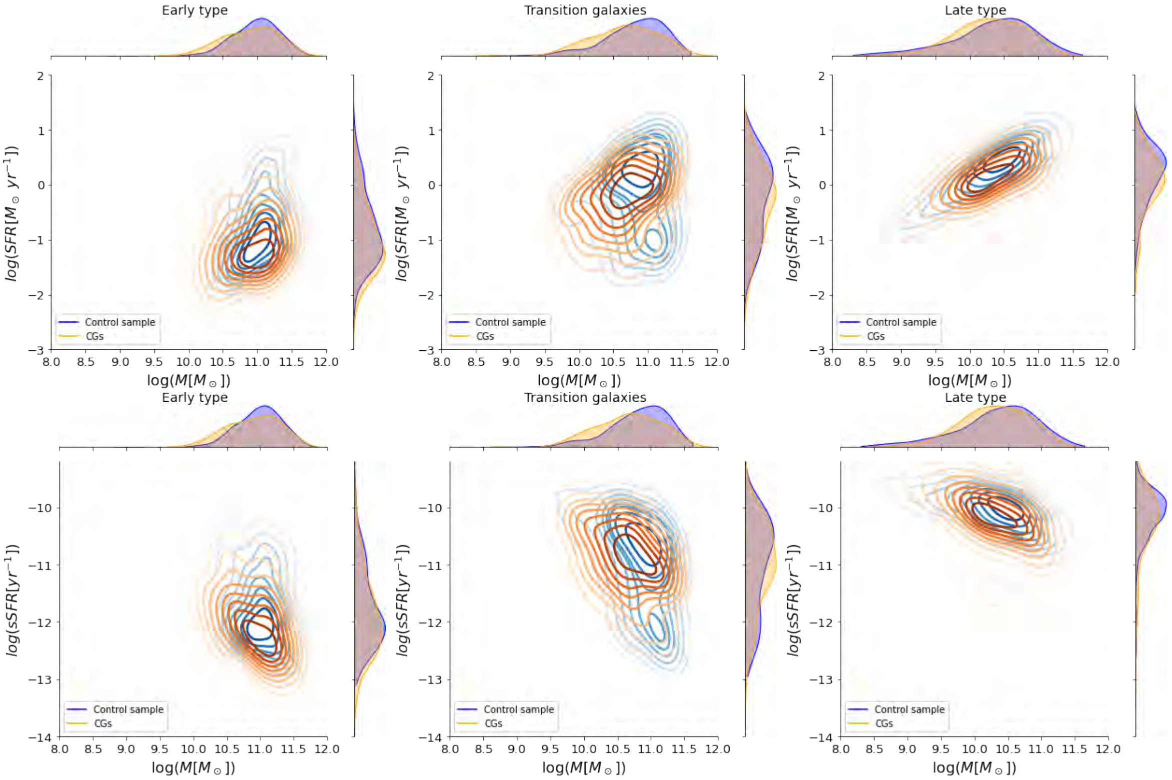

Figure 2.3.8: The three top figures display contours of the logarithm of SFR as a function of the logarithm of stellar mass for each of the populations, while the three bottom figures display sSFR instead of SFR: ETGs on the left, *transition galaxies* on the middle and LTGs on the right. Galaxies in CGs are contours in orange and in the control sample in blue.

for each population, as shown in Table 2.3.1, which is consistent with what we observed in Figures 2.3.8. In CGs, the medians of $sSFR$ are lower compared to the control sample. Additionally, based on the criterion proposed by Wetzel et al. (2013), we observe that CGs contain a larger percentage of quenched galaxies (i.e. $Log(sSFR) \leq -11$), for each galaxy population. This seems to indicate that the CG environment disfavours the star formation activity. To determine whether the differences we find in sSFR between the galaxies in the CGs and the control sample are statistically significant we perform a Kolmogorov-Smirnov (KS) test for the sSFR. We compare the cumulative distribution function (CDF) of this quantity in the CGs and in the control sample and test the null hypothesis that they (i.e. both environments) follow the same distribution. The null hypothesis, in this case, it would mean that, statistically, we cannot be certain of the environmental influence on these populations for star-forming galaxies. We find the null hypothesis to be rejected for ETG and LTG galaxies with $P_{KS} = 0.01$ and 0.005 respectively, while for *transition galaxies* the null hypothesis cannot be rejected with a $P_{KS} = 0.38$. This confirms that the CGs environment may be affecting the star formation process, likely due to tidal interactions, increasing the fraction of quenched galaxies. This scenario will be discussed in more detail in Section 2.4.3.

2.3.3 Correlation between quenching of star formation and morphological transformation

We find morphological and physical differences when comparing galaxies in CGs with respect to galaxies belonging to the control sample. Thus, it is worth exploring if there is any connection be-

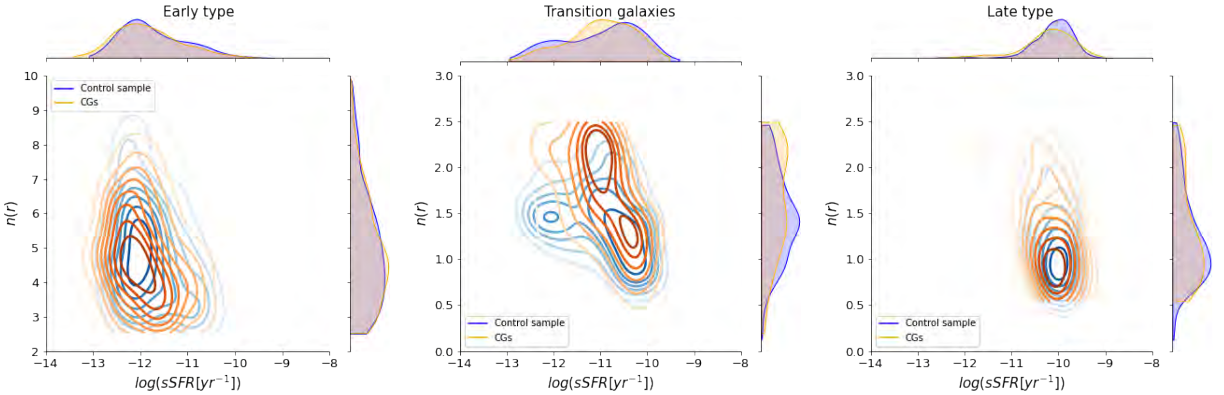

Figure 2.3.9: Contours of the Sérsic index in r-band as a function of the logarithm of the sSFR for each of the populations: ETGs on the left, *transition galaxies* on the middle and LTGs on the right. Galaxies in CGs are contours in orange and in the control sample in blue.

tween the morphological and physical parameters of galaxies in both environments, according to their morphological classification. In Figure 2.3.9, we show the Sérsic index in the r-band as a function of the logarithm of sSFR for the three populations of galaxies: early-type (left plot), transition (middle plot), and late-type galaxies (right plot). The blue contours represent objects in the control sample, while the orange contours represent systems in CGs.

From these plots, we observe that *transition galaxies* have, on average, higher Sérsic indices and lower sSFR values than LTGs, but higher sSFR values compared to ETGs, indicating their intermediate properties as discussed in the previous section. These results, based on sSFR, are in agreement with our criteria to define early, transition, and late-type galaxies, which was based purely on Sérsic index and colors.

Furthermore, we observe that ETGs and LTGs follow a similar distribution in the n-$log(sSFR)$ plane in both environments. However, we find differences when comparing *transition galaxies* in the control sample with those in CGs. While these galaxies in both environments have lower $sSFR$ for higher n_r values; displaying a bimodality in this plane (see Figure 2.3.9), the n_r values are much higher in the CGs for the peak in the bimodality for quenched galaxies (i.e. $log(sSFR) \sim -11$). We find that a significant fraction of the peculiar galaxies defined in Section 2.3.1.3 contributes to the formation of the larger n_r, lower $sSFR$ peak in the bimodality, centred at $n_r \sim 2.1$ and $log(sSFR) \sim -11$. This suggests that the peculiar galaxy population is undergoing both physical and morphological transformations.

2.4 Discussion

In this section, we discuss the physical meaning of the results found, as well as compare them with other works.

2.4.1 Behaviour of the median of Sérsic index and effective radius as a function of wavelength

Figures 2.3.4 and 2.3.6 summarise the dependence of the median value of n and R_e on wavelength. First, we find that galaxies in CGs are smaller, i.e. have lower R_e values, than those in the control sample when comparing each galaxy population. This could be due to the truncation of galaxies due to tidal interactions that strip material from the outer part of galaxies and enrich the intragroup medium.

For ETGs we observe an increase in both parameters with wavelength in both environments. However, the increase is smoother for galaxies in CGs compared to the control sample. The behaviour of these parameters can offer insights into the formation history of ETGs. According to Hopkins et al. (2009), elliptical galaxies are composed of two components that were generated after a violent relaxation from a major merger of two disk galaxies: a larger, older, and red component, and an inner, younger, and bluer stellar component formed during a central starburst produced during the merger. This scenario could explain why we observe an increase in n and R_e with wavelength.

For LTGs, we find that n increases and R_e decrease as a function of wavelength, regardless of the environment. Therefore, at longer wavelengths, we observe a redder and more concentrated population that is likely associated with the presence of bulges in these galaxies. The variation of these quantities is smooth in both environments, but in CGs the change in R_e is even smoother from the bluer to the redder filters. This, together with the lower values of R_e in CGs, suggests that interactions in this environment are smoothing the drop in the R_e values with wavelength. In other words, the outer more bluer parts of LTGs seen in the control sample is not detected in CGs, due to the truncation of galaxies from the interactions in the latter environment.

For *transition galaxies*, we see the same behaviour as in LTGs, with n increasing for redder wavelengths, with a slightly larger increase in CGs than in the control sample. On the other hand, while R_e decreases for the control sample in this type of galaxies, we find an increase of it for CGs. This indicates that R_e in *transition galaxies* behaves similar to that of ETGs in CGs, while *transition galaxies* in the control sample behave in a similar way that LTGs. These results suggest a morphological transformation that occurs in the environment of CGs that does not occur in the control sample of field galaxies. This difference in behaviour is related to the population of peculiar galaxies that exist in CGs (see Section 2.3.1.3), which contain more compact and smaller galaxies. Future studies should pay attention to *transition galaxies* located in CGs given their importance in galaxy evolution (as we discuss below).

La Barbera et al. (2010), Kelvin et al. (2012), and Vulcani et al. (2014) studied the median behaviour of R_e and n, for a sample of galaxies in various environments; i.e. they did not focus on a particular environment and, instead, were interested in having a large sample of galaxies to analyse their general behaviour. La Barbera et al. (2010) focused on ETGs, while the other two studies classified the galaxies according to their n and their colours. These three investigations find that R_e decreases for ETGs and LTGs, from blue to red bands. Furthermore, they find that the average n increases strongly with wavelength for LTGs, while for ETGs they find that the average n increases smoothly until the z/Y filters and is more stable for longer wavelength, for the J, H, and K filters n remains constant. Vulcani et al. (2014) associate these results for LTGs to the fact that the sample is dominated by two-components bulge-disk galaxies, although they also mention that there is likely to be a contribution from stellar population gradients within each component and from dust attenuation. The behaviour for ETGs is interpreted as a superposition of different stellar populations associated with multiple minor merger events, arguing that early-type galaxies are expected to comprise a compact population of red stars formed in situ and a more diffuse, bluer population of stars formed in accreted systems generating their effective radius to decrease with wavelength. It is worth noting that the observations analysed in Vulcani et al. (2014) are shallower than ~ 25 mag arcsec^{-2} (Kelvin et al., 2012), thus it is unlikely to observe the diffuse outer regions in these galaxies. In addition, Lima-Dias et al. (2021) studied the Hydra cluster and found an increase of n with respect to wavelength for the ETGs (13% from u to z) and a decrease of n, by 7% from u to z, for the LTGs, which can indicate that star formation is concentrated in the inner regions.

Differences in the behaviour of the effective radius have been observed between ETG galaxies and findings from earlier studies (La Barbera et al. (2010), Kelvin et al. (2012), and Vulcani et al. (2014)); therefore, it is essential to interpret these results with care. In this study, our goal is to analyse R_e as a function of wavelength in order to investigate whether the environment of CGs affects this morphological feature compared to a less dense environment, such as field galaxies. Previous studies examined a larger sample of galaxies to explore the relationship between colour and structure within galaxies using optical-near-infrared imaging in bright, low-redshift galaxies, without giving relevance to the environment in which these galaxies are found. The differences with the behaviour of the R_e as a function of the wavelength offer a promising opportunity to investigate how the environment impacts R_e changes as a function of wavelength and how this information can be used to further improve our understanding on galaxy formation and evolution, particularly for ETGs. Although this goes beyond the scope of this thesis, it highlights the necessity of addressing this issue through hydrodynamical simulations that would enable us to trace the influence of various interactions on galaxies throughout their history, particularly through a multi-wavelength analysis.

2.4.2 A peculiar galaxy population in CGs: Are we witnessing morphological transformation in CGs?

One of the most interesting results reported in this work is that *transition galaxies* in CGs display a bimodal distribution in the $R_e - n$ diagram, not seen in the control sample. There is a peculiar population of galaxies in CGs identified as having larger Sérsic index and smaller effective radii than galaxies belonging to the control sample. Indeed, in the marginal plots of $R_e - n$, Figure 2.3.7, the distribution of n presents a clear bimodality in CGs that is not observed in the control sample. A KS test based on the cumulative distribution function (CDF) on this parameter allows us to identify statistically if both samples follow the same distribution. We find that the p-value is $P_{KS} = 2.5 \times 10^{-4}$, which confirms what is visually observed in Figure 2.3.7, i.e. that *transition galaxies* from the CG and the control sample do not arise from the same distribution.

This difference found in the population in *transition galaxies* between CGs and the control sample indicates the existence of a galaxy population that is suffering morphological transformation: galaxies become more compact and smaller, thus promoting the transformation of *transition galaxies* into ETG in dense environments. In addition, we have visually inspected all the *transition galaxies* in CGs. We find that 65% of them are disk-like galaxies, 25% have a spheroidal shape, and 10% are undergoing a merger with a close companion. Since these *transition galaxies* have colours redder than the LTGs and moderate sSFRs, they are good candidates to fall into the gap found in the medium infrared (MIR) (Johnson et al. 2007, Gallagher et al. 2008, Tzanavaris et al. 2010, Walker et al. 2010, Walker et al. 2012, Walker et al. 2013, Lenkić et al. 2016). The *transition galaxies* in CGs appear as a unique sample to study, in detail, how the environment affects galaxy evolution.

2.4.3 Physical transformation according to each population type

We find that there are statistical differences in LTG and ETG when comparing the sSFR distribution of galaxies in CGs with the control sample galaxies, while this is not the case for *transition galaxies*. Additionally, the percentage of quenched galaxies is always higher in the CGs compared to the control sample for all galaxy population types. For LTGs a possible scenario that favours the differences found in sSFR between the two environments are tidal interactions, shocks, and turbulence (Alatalo et al. 2015, Bitsakis et al. 2016), causing these gas-rich galaxies to lose material due to interactions in

CGs. This is consistent with the results found by Verdes-Montenegro et al. (2001), where CG galaxies are HI deficient. For the ETGs there is a higher fraction of quenched galaxies with a lower median sSFR in CGs compared to the control sample. Furthermore, ETGs have been found preferentially in more dynamically evolved CGs (see Chapter 3), therefore they have undergone more interactions which explains the differences in the sSFR.

For *transition galaxies*, which are candidate galaxies to be in the green infrared valley (Johnson et al. 2007, Walker et al. 2012, Bitsakis et al. 2016) we do not find statistical differences in the distribution of sSFR for those galaxies in CGs and the control sample. This result does not imply that they come from the same distribution, it simply means that we do not have enough statistical evidence to support that they are from different distributions. It is worth noting, however, that we do find the median of the sSFR to be lower in CGs compared to the control sample for LTGs and *transition galaxies*, and the fraction of quenched galaxies to be higher, indicating that there is an environmental effect in CGs that favours galaxies being quenched. Additionally, the *transition galaxies* in the control sample present a bimodality in the sSFR, not seen in the CGs counterpart: they are either star-forming or quenched, whereas in the CGs we find the galaxies to have intermediate values of sSFR within this bimodality. Note the higher mass of the quenched population in the *transition galaxies* in the control sample.

2.5 Summary and Conclusions

In this work, we used data from 340 compact groups (CGs) in the Stripe 82 region in order to study the evolution of galaxies in dense, low-velocity dispersion environments. In particular, we focus on how this environment affects the morphological and physical properties of galaxies, by comparing to a control sample of isolated galaxies that is analysed in exactly the same way as our CGs sample. Thus, we have an *homogeneous data set of CG and control sample galaxies*. We used multi-wavelength data from the S-PLUS project, which has 12 filters in the optical. By using this data set and the MegaMorph code we estimated the structural parameters for each galaxy. This information was complemented with GSWL catalogue to obtain the SFR. We divided the galaxy population in each sample as early-type (ETGs), late-type (LTGs), and *transition galaxies*, according to their Sérsic index (n) and colour. The most important findings and results from our analysis are:

1. We found that galaxies of all types in CGs have a smaller effective radius than the same type of galaxies located in the control sample. Tidal interactions may favour galaxies losing material in CGs, causing them to have a smaller average effective radius than galaxies in the control sample.

2. We have observed different trends with wavelength in the median values of n and R_e depending on the morphological type and environment. For ETGs, both n and R_e increase with wavelength, with a smoother increase in CGs than in the control sample. This behaviour can be related to the formation history of these galaxies, where major mergers contribute to the formation of a red, older, and larger component, along with a younger, bluer, and inner stellar component formed from gas (Hopkins et al. 2009). For LTGs, n and R_e increase and decrease, respectively, with wavelength, in both environments, indicative of a redder and more concentrated population, likely associated with the presence of bulges in these galaxies. For *transition galaxies*, we observe a different behaviour in CGs compared to the control sample: the R_e behaves like the ETGs in CGs, while it resembles that of the LTGs in the control sample, suggesting a morphological transformation that occurs in the environment of CGs but not in the control sample.

3. In the $R_e - n$ distribution of the *transition galaxies*, we observe a bimodality in CGs, that does not appear in the control sample. Therefore, we find a population of CG galaxies that does not follow the same properties that we observe in galaxies located in less dense environments (control sample); we name them *peculiar galaxy population*. The galaxies that characterise this sub-sample of *transition galaxies* in CGs are smaller and more concentrated, which indicates that these galaxies are undergoing a morphological transformation in CGs.

4. In CGs, there is a higher fraction of quenched galaxies, regardless of galaxy type, compared to the control sample. Furthermore, there are differences in the distribution of sSFR between LTGs and ETGs when comparing the two environments. On the other hand, in *transition galaxies*, there is no statistical differences in the sSFR distribution between the two environments analysed, but there is a higher fraction of quenched galaxies with a lower median sSFR in CGs compared to the control sample. These results suggest that physical processes such as tidal interactions, shocks, and turbulence may play a role in explaining the observed differences in sSFR between CGs and the control sample.

5. We observe an anti-correlation in the n_r-$\log(sSFR)$ plane for *transition galaxies*, which leads to a bimodality in this plane. We find that a significant fraction of the peculiar galaxy population contributes to the formation of the quenched-galaxies peak in this bimodality, suggesting that the peculiar galaxies undergo not only a morphological but also a physical transformation.

The results presented in this chapter highlight the importance of studying the morphological and physical properties of galaxies in CGs in order to understand how dense environments affect their evolution.

Chapter 3

Witnessing the influence of major structures in their evolution

In this chapter, we delve into the dynamical state of the CGs analysed in the previous chapter, alongside exploring their surroundings. As mentioned in Chapter 1, CGs are not necessarily isolated systems and can be embedded within larger structures. Therefore, we investigate how the dynamics and environment surrounding CGs influence the morphological and physical transformations observed in Chapter 2. We found that at least 27% of our sample of CGs are part of major structures, indicating they are non-isolated CGs. *Transition galaxies* in isolated CGs tend to occupy a denser region in the $R_e - n$ plane for $n < 1.75$. Conversely, *transition galaxies* in non-isolated CGs exhibit a smoother increase in n values, suggesting these galaxies have undergone morphological transformations and contribute predominantly to the distribution of more compact galaxies in the $R_e - n$ plane among all *transition galaxies* in CGs, as detailed in Chapter 2. Furthermore, significant differences in the specific star-formation rate (sSFR) distribution are observed between late-type galaxies (LTGs) in non-isolated CGs (with $(u-r) < 2.3$ and $n < 2.5$) and those in the control sample, indicating distinct evolutionary paths for LTGs in non-isolated CGs. Additionally, early-type galaxies (with $(u-r) > 2.3$ and $n > 2.5$) and *transition galaxies* in non-isolated CGs exhibit lower sSFR values and a higher fraction of quenched galaxies compared to those in isolated CGs. Based on our findings, we propose an evolutionary scenario where the major surrounding structures accelerate the morphological transformations of galaxies within CGs and facilitate preprocessing. These results underscore the importance of considering the larger environmental context of CGs when analysing the properties and evolutionary trajectories of their member galaxies.

The outline of this chapter is as follows: we describe our methodology to classify galaxies according to their morphology, the dimensionless crossing time, and the compactness of each CG is described in Section 3.1. We present and discuss our results in Sections 3.2 and 3.3; and finally, our conclusions and summary are laid out in Section 3.4

Based on Montaguth et al. (2024), submitted to A&A.

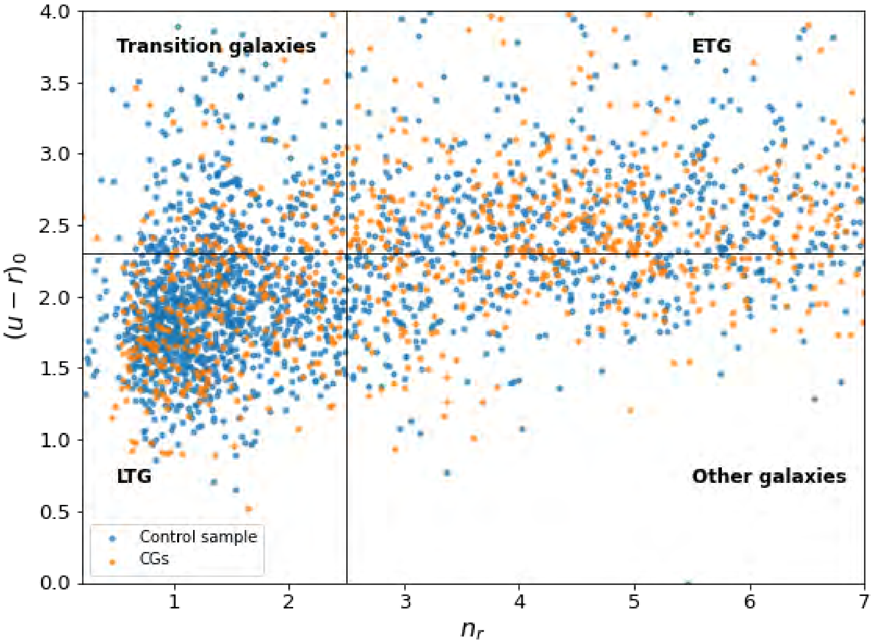

Figure 3.1.1: ETGs, *transition galaxies*, and LTGs classification, using $(u-r)_0$ rest-frame colour and Sérsic index in the r-band (n_r). The vertical line is for $n_r = 2.5$ and the horizontal for $(u-r)_0 = 2.3$. This classification was proposed by Vika et al. (2015b). The blue dots represent the galaxies in CGs, while the orange dots are the galaxies in the control sample.

3.1 Methodology

3.1.1 Morphological classification

In this chapter, we classify galaxies according to their morphology, as defined in Chapter 2. This classification is based on the Sérsic index in the r-band (n) and the $(u-r)$ colours, following the criteria proposed by Vika et al. (2015b). In contrast to Chapter 2, here we have applied the k-correction to the colour $(u-r)$. Therefore the colour $(u-r)_0$ used for the morphological classification is k-corrected. We made this correction because Vika et al. (2015b) show that this technique remains effective up to z$\sim$ 0.1, while our sample extends up to z$\sim$ 0.2. We employ the publicly available software package of Blanton & Roweis (2007) in version $V4\_3$ to obtain de-reddened model magnitudes at $z = 0$. Figure 3.1.1 shows the k-corrected colour $(u-r)_0$ - n diagram. The horizontal line represents the colour $(u-r)_0 = 2.3$ and the vertical line represents a Sérsic index $n = 2.5$. The lower-left quadrant defines our selection of late-type galaxies (LTG), the upper-left quadrant, contains what we name *transition galaxies*, the upper-right quadrant, early-type galaxies (ETGs), and galaxies in the lower-right quadrant are named as *other galaxies*. This correction results in the number of *transition galaxies* decreasing to 85, while in the previous chapter, we had 119. However, this does not significantly affect our results, $R_e - n$ plane is maintained, thus our definition of *peculiar galaxy population* remains.

3.1.2 Dynamical state of the CGs: dimensionless crossing time and compactness

One convenient method for estimating the dynamical state of a group is by using the dimensionless crossing time, $H_o t_c$. It corresponds to the period of time it takes for a galaxy to pass through a group (Moura et al. 2020). H_o is the Hubble-Lemaitre constant, and the crossing time, t_c, was defined by Hickson et al. (1992) as:

$$t_c = \frac{4R}{\pi V}$$

where V is the three-dimensional velocity dispersion defined as $V = [3(\langle v^2 \rangle - \langle v \rangle^2 - \langle \delta v^2 \rangle)]^{1/2}$, $\langle v \rangle$ is the median of the radial velocities of galaxies in the group, and $\langle \delta v^2 \rangle$ is the median of velocity errors squared, which was estimated using the estimated errors in the redshift. We use the value for radial velocities and their errors already obtained in the catalogues of the CGs. R represents the median of the two-dimensional galaxy-galaxy separation vector in kpc. We estimated it by first calculating the separation in angular distances (in arcsec) between each galaxy in the CGs. Then, we determined the median of these separations in arcseconds for each group and converted it to linear distances (in kpc), according to the distance of each group.

We also estimate the compactness parameter, which was defined by Hickson (1982) as the surface brightness of the group. This is the total magnitude of the group galaxies averaged over the smallest circle containing the galaxies:

$$\mu = -2.5log\left(\frac{\sum_{i=1}^{N} 10^{-0.4m_i}}{\pi\theta_G^2}\right)$$

where m_i is the apparent magnitude in r-band of each galaxy in the group, and θ_G is the angular radius of the smallest circle, in arcseconds, which contains all the galaxies within the group. We consider this parameter with the purpose of identifying whether the compactness of CGs has any relation to their dynamical state.

3.2 Results

3.2.1 Dynamical status of the CGs

Figure 3.2.1 shows the compactness as a function of the dimensionless crossing time. The small black dots represent the values for each CG, and the large filled circles with different colours and error bars represent the median values, where the bar on the x-axis is the size of the bin used to estimate the median and the length of the y-axis is the statistical error of a 90% confidence interval (CI) using bootstrapping. In the top panel of Figure 3.2.1, colours of the filled circles represent the median fraction of LTGs, whereas, in the bottom panel, colours indicate the ETG median fraction. We find that CGs with fainter compactness exhibit higher dimensionless crossing times and, an increase in the median fraction of LTGs. Consequently, we observe an increase in the fraction of ETGs for smaller $H_o t_c$ values and brighter compactness values.

Figure 3.2.2 is similar to Figure 3.2.1, but in this case, the dimensionless crossing time is compared with the velocity dispersion (σ_G) of the CG. We find that CGs with lower σ_G have higher values of $H_o t_c$ and thus a larger fraction of LTGs. Whereas the opposite is true for the CGs with a high fraction of ETGs. This is in agreement with the results presented by Moura et al. (2020), who found that when dividing the CGs in low-σ_G (high-σ_G) with $\sigma_G \leq 180\ km/s$ ($\sigma_G > 180\ km/s$), the CGs with low-σ_G have larger crossing times and high fractions of spirals than those having high-σ_G.

In summary, we find that parameters such as crossing time, velocity dispersion, compactness, and LTG/ETG fractions provide clues about the evolutionary stage of a CG. Indeed, CGs having low-velocity dispersion, faint compactness, and a higher LTG fraction display high crossing times values, suggesting that they are at an early stage of interaction, or just formed (Moura et al. 2020). In general terms, these systems are less evolved than those CGs with higher velocity dispersion, brighter compactness, and lower fraction of LTGs.

3.2.2 Connection between velocity dispersion and morphological transformation

In Chapter 2, we discovered a bimodality in the distribution in the $R_e - n$ plane for *transition galaxies* in CGs. There we found a population of peculiar galaxies that are more concentrated (larger n) and smaller (lower R_e) compared to *transition galaxies* in the control sample. As stated above, previous studies have shown that there is a strong relationship in CGs between the galaxy morphology and the velocity dispersion (Hickson et al. 1988, Coziol et al. 2004), such that CGs with a high-velocity dispersion contain fewer LTGs, which we also found in this work (see Figure 3.2.2). This morphology-velocity dispersion relationship is more important in CGs than in cluster or loose groups (Mamon 1986). Additionally, the velocity dispersion is a good proxy of the group's mass. For this reason, Figure 3.2.3 shows the R_e as a function of n for *transition galaxies* in CGs. The top left panel shows *transition galaxies* in CGs with velocity dispersions between $0-200 km/s$. The top right panel shows galaxies in CGs with velocity dispersions ranging between $200 km/s - 800 km/s$. For comparison, the bottom left panel shows *transition galaxies* for all CGs. Finally, the bottom right panel shows *transition galaxies* in the control sample. We note that we choose a cut in $200 km/s$ given that it is the typical velocity dispersion of CGs (Hickson 1982). To create these contour plots, we employed a Kernel Density Estimator to aid in visualising the distribution of our data. Consequently, the colours of the contours represent the joint probability density of $R_e - n$. We observe that *transition galaxies* within CGs, with velocity dispersions (σ_G) lower than $200\ km/s$ do not exhibit a bimodal distribution in n. However, we note that the contours extend to values greater than 1.75 in n, corresponding to the region where the peculiar galaxy population is found in this diagram. The bimodal distribution in the $R_e - n$ plane becomes evident for CGs with $200 < \sigma_G < 800\ km/s$. Furthermore, the marginal plot for n reveals a higher fraction of galaxies with $n > 1.75$, accounting for 49% of the galaxies. This suggests that the process of morphological transformation accelerates in CGs with velocity dispersions exceeding $200\ km/s$, as observed in this range for the peculiar population, which have already undergone morphological transformation. Conversely, at velocities lower than $200 km/s$, galaxies may be undergoing transformation by increasing their Sérsic index slowly and becoming more spheroidal in shape. Another scenario that might contribute to the increase in Sérsic index for galaxies in the low velocity dispersion bin involves galaxies that are merging. However, it is important to highlight that the merger rate is not expected to be high, as it has been reported to be around 7% (Zepf 1993). A similar analysis with LTGs, considering the same two bins of σ_G as above and plotting the R_e contours as a function of n, is shown in Figure 3.2.4. In this case, we observe that as the velocity dispersion of the CGs increases, the distribution of n does not change; in both bins the contours extend up to values of 2.5 in n.

In Table 3.2.1, we illustrate the percentage of each morphological type according to each sigma bin. The percentage of LTGs decreases in CGs with higher dispersion velocities, while the percentage of ETGs increases. For *transition galaxies*, the percentage is similar in both σ_G ranges.

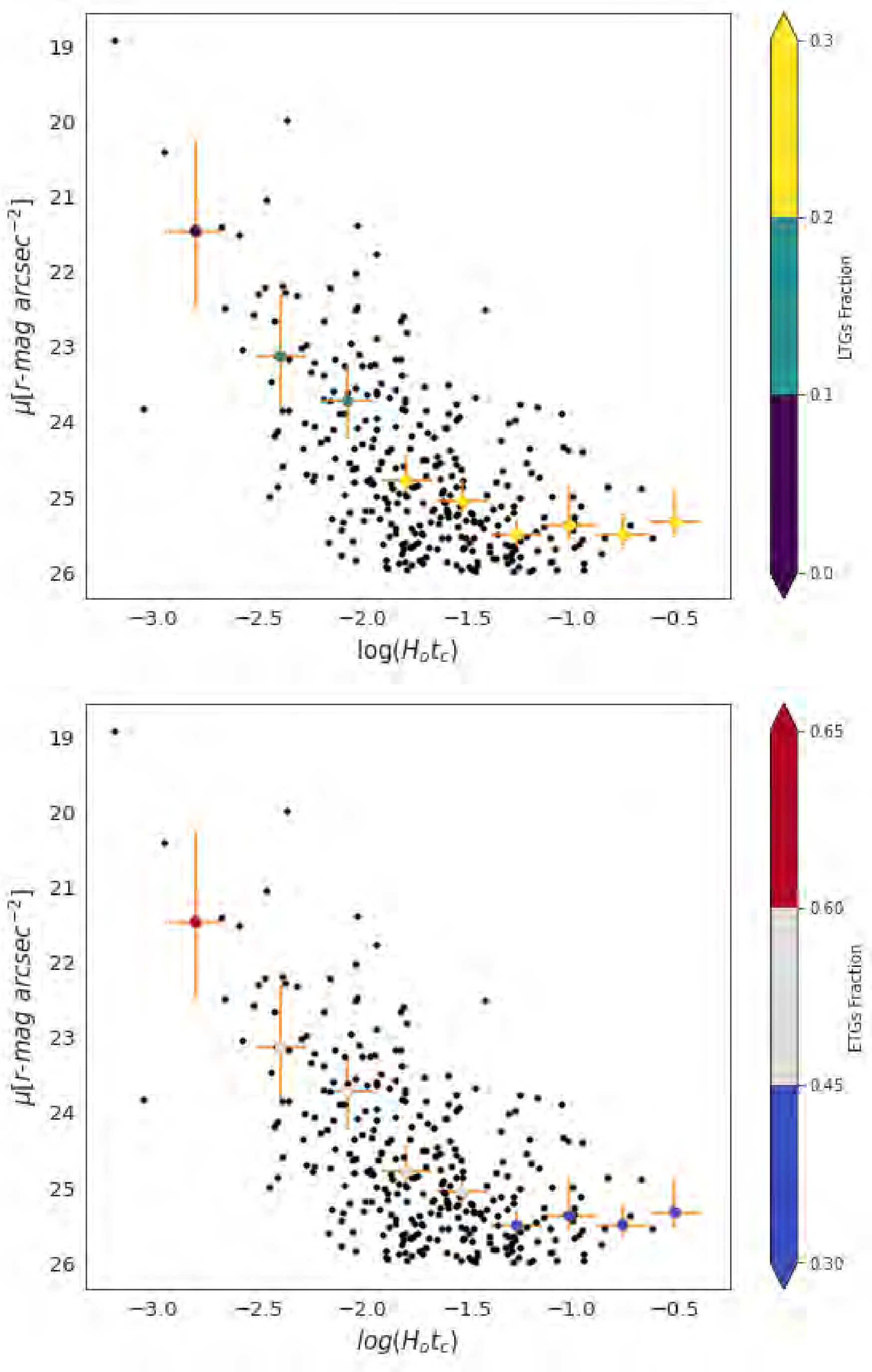

Figure 3.2.1: Dimensionless crossing time vs. compactness for CGs. The points with bars represent the median value, the bar on the x-axis represents the bin size, and the bar on the y-axis is the 90% CI. In the top (bottom) panel, the colour of the points indicates the median fraction of LTGs (ETGs) in each bin. The small black dots represent values for each CG.

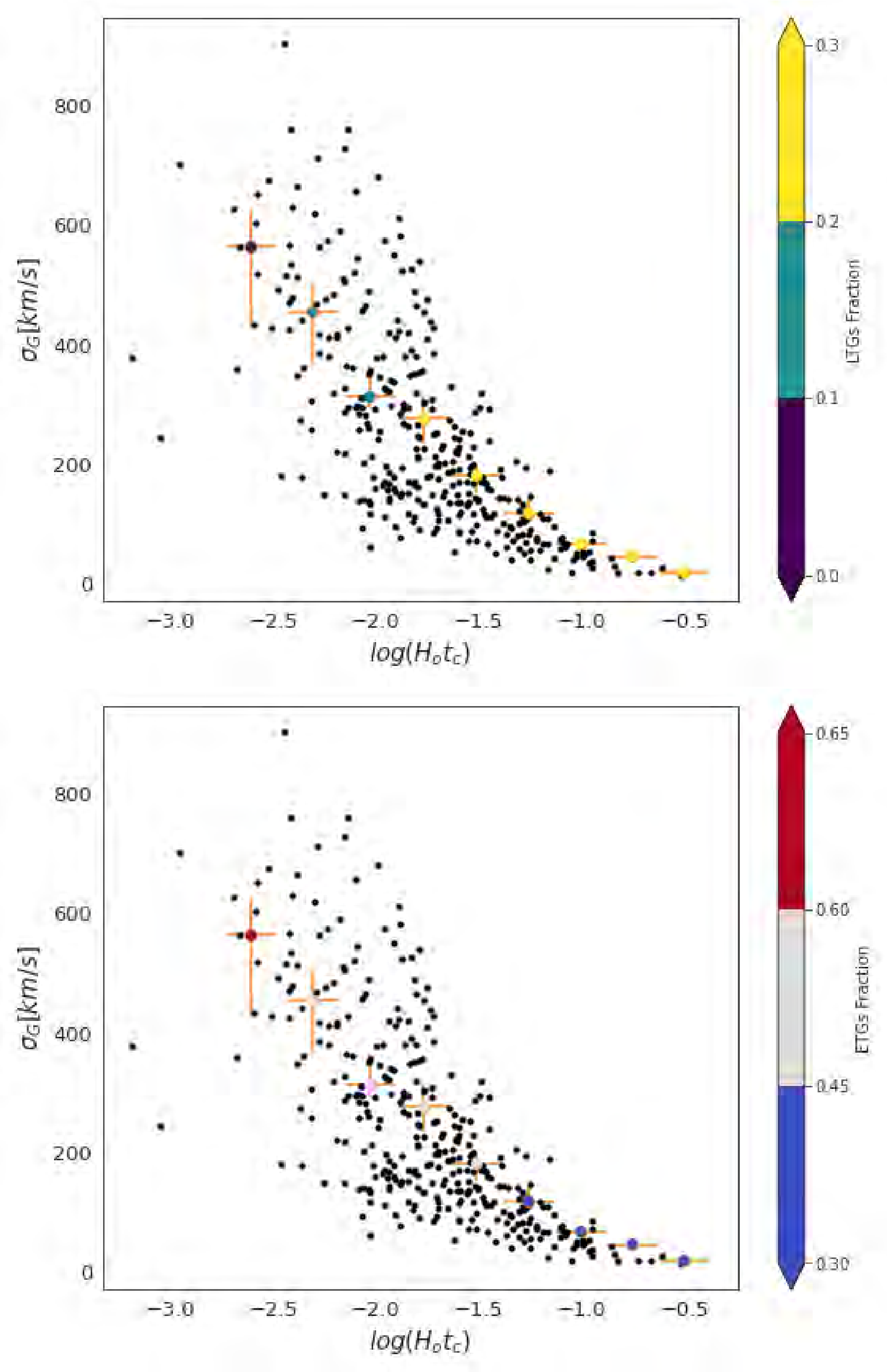

Figure 3.2.2: Velocity dispersion vs. crossing time for CGs. Each black dot represents a CG. The points with bars represent the median value, the bar on the x-axis represents the bin size, and the bar on the y-axis is the 90% CI. In the plot on the top, the colour of the dots indicates the fraction of LTGs in each CG, and in the figure below, the fraction of ETGs.

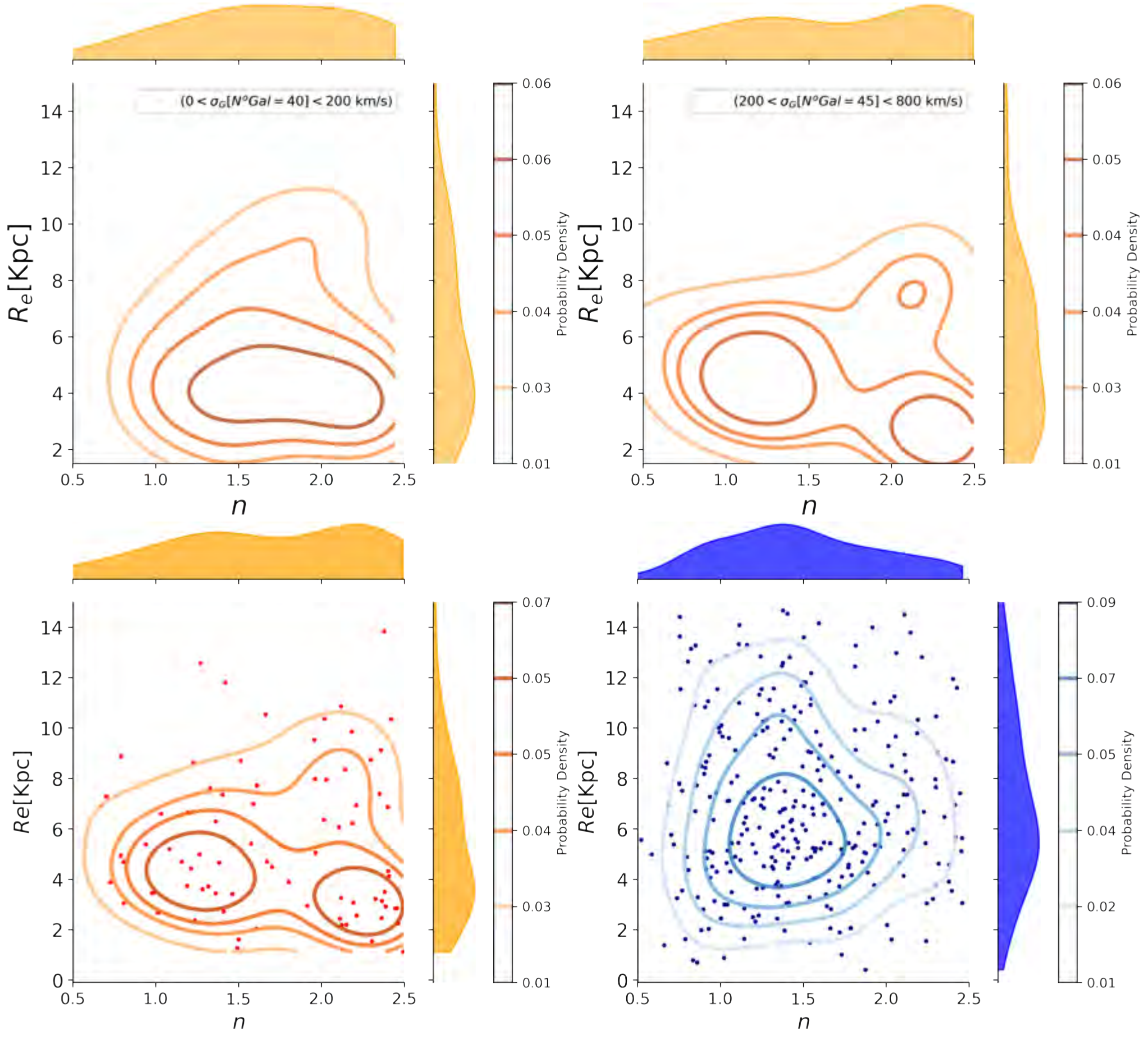

Figure 3.2.3: Contours representing the relationship between effective radius and Sérsic index for *transition galaxies* in the r-band are displayed. Orange contours illustrate the subsample across various velocity dispersion bins for galaxies in CGs, with the number of galaxies in each bin indicated in the upper left corner. Additionally, the *transition galaxies* for all CGs are depicted in orange contours on the left panel, while the control sample is shown in blue contours on the right panel.

σ_G **intervals** $[km/s]$	**Percentage of ETGs**	**Percentage of transition galaxies**	**Percentage of LTGs**
0-200 (175)	32.9%	7.3%	30.1%
200-800 (165)	47.9%	8.2%	17.4%

Table 3.2.1: The percentages of ETGs, *transition galaxies*, and LTGs in the CG velocity dispersion intervals. The number of CGs per σ_G interval is shown in the parenthesis.

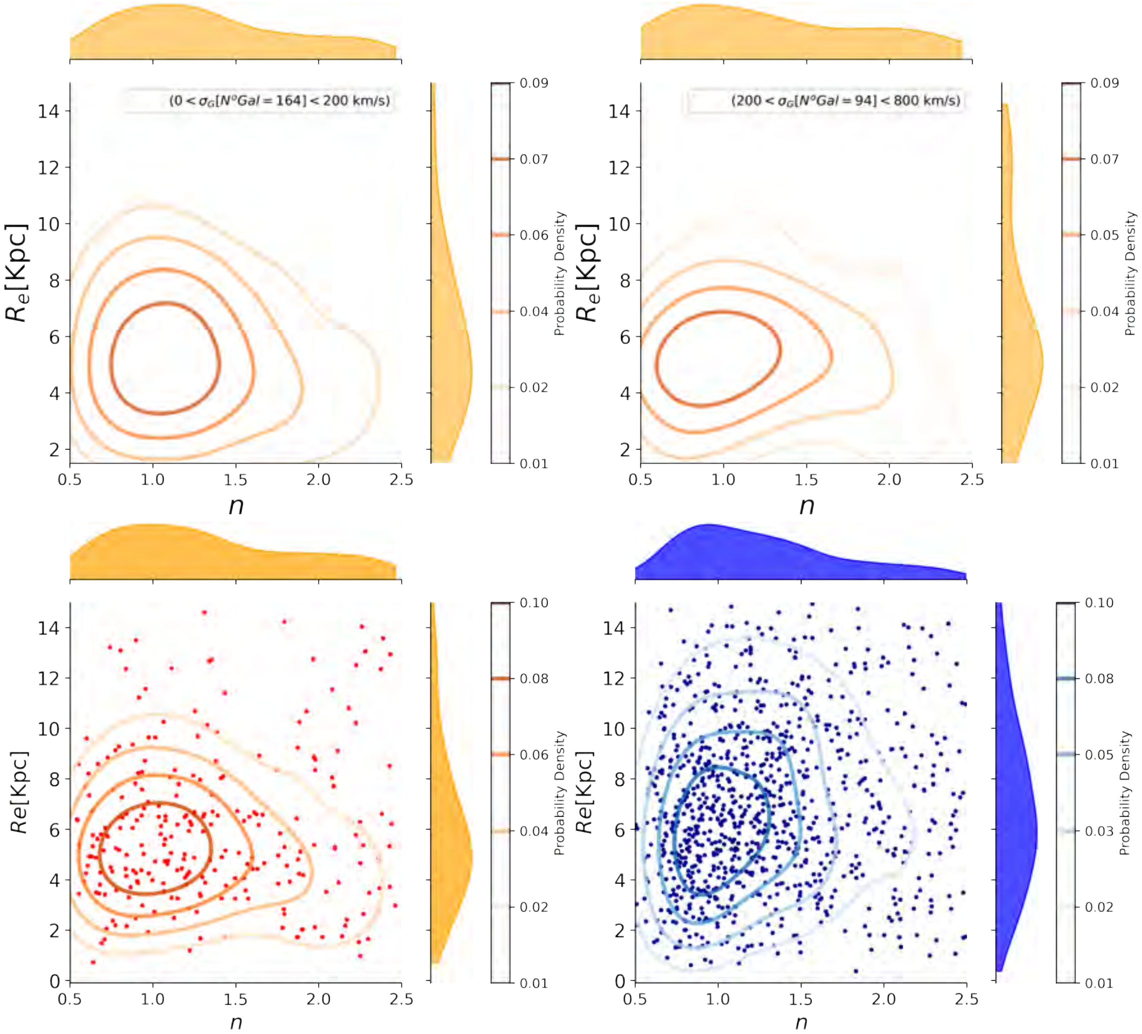

Figure 3.2.4: Contours of effective radius as a function of Sérsic index for LTGs, in r-band. In orange contours for the subsample for different velocity dispersion bins, in the upper left corner are the number of galaxies in each bin. In the bottom panels, we show the LTGs for all CGs in orange contours and for the control sample in blue contours.

3.2.3 The surrounding environment of CGs in our sample

We explore the environment of our CGs sample in the Yang et al. (2007) catalogue, in agreement with the methodology followed by Zheng & Shen (2021). In this catalogue the structures are classified based on the halo-based group method, which employs an iterative approach to estimate the mass of the group. In short, it starts by estimating the luminosity and centre of each group using the Friends-Of-Friends (FOF) algorithm (Davis et al. 1985). Then, it calculates the average mass-to-light ratios of the groups, initially assuming $M/L_{19.5} = 500hM/L$ for the first iteration, where $L_{19.5}$ represents the luminosity of all group members with $M_r - 5log(h) \leq -19.5$ and $h = H_0/(100\ kms^{-1}\ Mpc^{-1})$. Subsequent iterations use ratios from the previous step. This mass estimation is used to derive the size and velocity dispersion of the hosting halo, with the halo size determined by the radius r_{180} where the average mass density is 180 times that of the Universe's average density at a given redshift. These parameters are then used to determine group membership in redshift space, and if a new member is identified, the process iterates to reevaluate the group's centre and other parameters. Therefore Yang et al. (2007) used a different criterion to select the groups in their sample, which is not biased by the isolation and compactness criteria used to select the CGs by Sohn et al. (2016) and Zheng & Shen (2020).

We select all the groups and galaxies in the Stripe 82 that are included in the catalogue by Yang et al. (2007) and perform a cross-match between the right ascension and declination positions of the galaxies in Yang et al.'s groups and the galaxies in our sample of CGs. From this cross-match, we identify the IDs of the groups included in Yang et al. (2007) that had at least one galaxy that, according to our catalogue, is a galaxy in a CG. Using these group IDs, we selected all the galaxies that belong to the groups found by Yang et al. (2007). We find that 226 CGs that we have in our sample are identified as belonging to structures studied by Yang et al. (2007), which corresponds to 67% of our sample. From these 226 CGs, 40% are located in major structures (groups and clusters) or have satellite galaxies beyond three times the radii of the CG and we will call these CGs as non-isolated from now on. This corresponds to 27% of the 340 CGs originally selected in this study. This fraction of non-isolated CGs is what is also found in other studies (ranging from 20% to 95% from a given sample of CGs are non-isolated, e.g., Barton et al. 1998, Andernach & Coziol 2005, Díaz-Giménez & Zandivarez 2015, Zheng & Shen 2021). From the 60% that is left out of the 226, 35% of the CGs share the same members in both Yang et al. (2007) and our catalogue. Adopting Zheng & Shen (2021)'s terminology, we name these systems as isolated CGs. Indeed, there are no additional galaxies detected by Yang within their r_{180} when compared to the galaxies in our catalogue of those CGs. The remaining 25% of CGs identified by Yang et al. (2007) involve fewer galaxies than in our sample. This difference is likely attributed to the velocity selection criteria applied by Zheng & Shen (2020), which potentially overestimates the number of CG members. To summarise, we find that out of 226 CGs that also were identified by Yang et al. (2007), 35% of them are isolated, and 40% are non-isolated. In the following two subsections, we consider only the galaxies in this 75% of the 226 CGs, which corresponds to a total of 170 CGs.

We found that $\sim 45\%$ of non-isolated CGs have σ_G lower than 200 km/s; $\sim 47\%$ have σ_G between $200 - 500$ km/s, and $\sim 8\%$ have σ_G greater than 500 km/s. Therefore, 55% of the non-isolated CGs have a higher velocity dispersion than the average typically attributed to CGs, which is 200 km/s (Hickson et al. 1992). It is important to consider this result because, as we have presented, there is a relationship between the morphology and dynamics of CGs (see Figure 3.2.2). Additionally, Zheng & Shen (2021) and Taverna et al. (2023), found that the velocity dispersion of the CG increases with the density of the environment in which it is located, as it will be discussed in section 3.3.2. This might suggest that these non-isolated CGs have recently fallen into these larger structures or are not dynamically individual subsystems but are more likely the result of chance alignments within larger systems. In the case of the first hypothesis Zheng & Shen (2021) find that the embedded CGs in the outer parts of major structures are dynamically colder than the galaxies in the major structures, i.e. the velocity dispersion is lower in galaxies within non-isolated CGs compared to that of other galaxies in the larger structure. This suggests that these external CGs might, at least, consist of recently accreted groups. This is because it is expected that after the first pericentric passage, the group will disassemble and vitalise, especially in structures like clusters (Benavides et al. 2020, Haggar et al. 2022). In the second scenario, Mamon (1986) and Zheng & Shen (2021) suggest that CGs in the inner parts of major structures could be dominated by chance alignments. In addition, simulations show that between $30\% - 60\%$ of CGs are chance alignments within larger groups (Taverna et al. 2022, Hartsuiker & Ploeckinger 2020). These percentages vary depending on the assumed cosmology and the definition of CGs, as in some studies only those with four or more galaxies are considered, while in others also CGs with three members are considered. Additionally, Tzanavaris et al. (2014) propose that CGs are chance alignments in poor groups.

3.2.4 Morphological transformation: Isolated vs. non-isolated CGs

Figure 3.2.5 shows the effective radius as a function of the Sérsic index for *transition galaxies* in CGs in each environment (top for isolated GCs and bottom for non-isolated CGs). For *transition galaxies* in isolated CGs we do not find the bimodal distribution in the $R_e - n$ plane that we observed for all *transition galaxies* (see bottom left panel in Figure 3.2.3). In fact, we observe that there is a high density in the $n - R_e$ plane for $n < 1.75$. However, the contours for isolated CGs tend to stretch towards higher values of n and lower values of R_e, where we find the population of peculiar galaxies within CGs. In the case of the distribution of non-isolated CGs (see bottom panel of Figure 3.2.5), we also do not observe the bimodality seen in all the *transition galaxies* in the $R_e - n$ plane. Instead, the n values are already higher, reaching the n values of the peculiar galaxies population, i.e., $n > 2$. This finding suggests that the morphological transformation process appears to be more gradual in isolated CGs, whereas non-isolated CGs significantly populate the region of peculiar galaxies. This indicates that for most *transition galaxies* the morphological transformation in non-isolated CGs has already occurred. However, it is important to note that Figure 3.2.5 should not be directly compared with Figure 3.2.3, because the first contains a subset of all the galaxies shown in Figure 3.2.3.

In Figure 3.2.6, we show the fraction of groups where the CGs are located as a function of total stellar mass estimated by Yang et al. (2007) (top panel). In yellow, we show isolated CGs, and in orange, the non-isolated ones. Isolated CGs have lower mass distributions, while non-isolated CGs reach higher values. This implies that group mass is crucial for accelerating the morphological transformations observed in non-isolated CGs. In the next section, we will discuss the impact of these masses on the cessation of the SFR. We also present the fraction of CGs as a function of the velocity dispersion of each CG (bottom panel in Figure 3.2.6), following the same colour pattern. We find that isolated CGs have typically lower values of σ_G, while non-isolated ones reach higher values. Only 27% of isolated CGs reach σ_G greater than 200 km/s, while there are 55% of non-isolated CGs with velocity dispersion exceeding 200 km/s.

3.2.5 sSFR: Isolated and Non-isolated CGs vs. less dense environment

To investigate the influence of the CG environment on the sSFR distribution, in Figure 3.2.7 we show the sSFR as a function of stellar mass. In the top panels, we show the distribution of galaxies in isolated CGs as orange contours, for each population: ETGs, *transition galaxies*, and LTGs from left

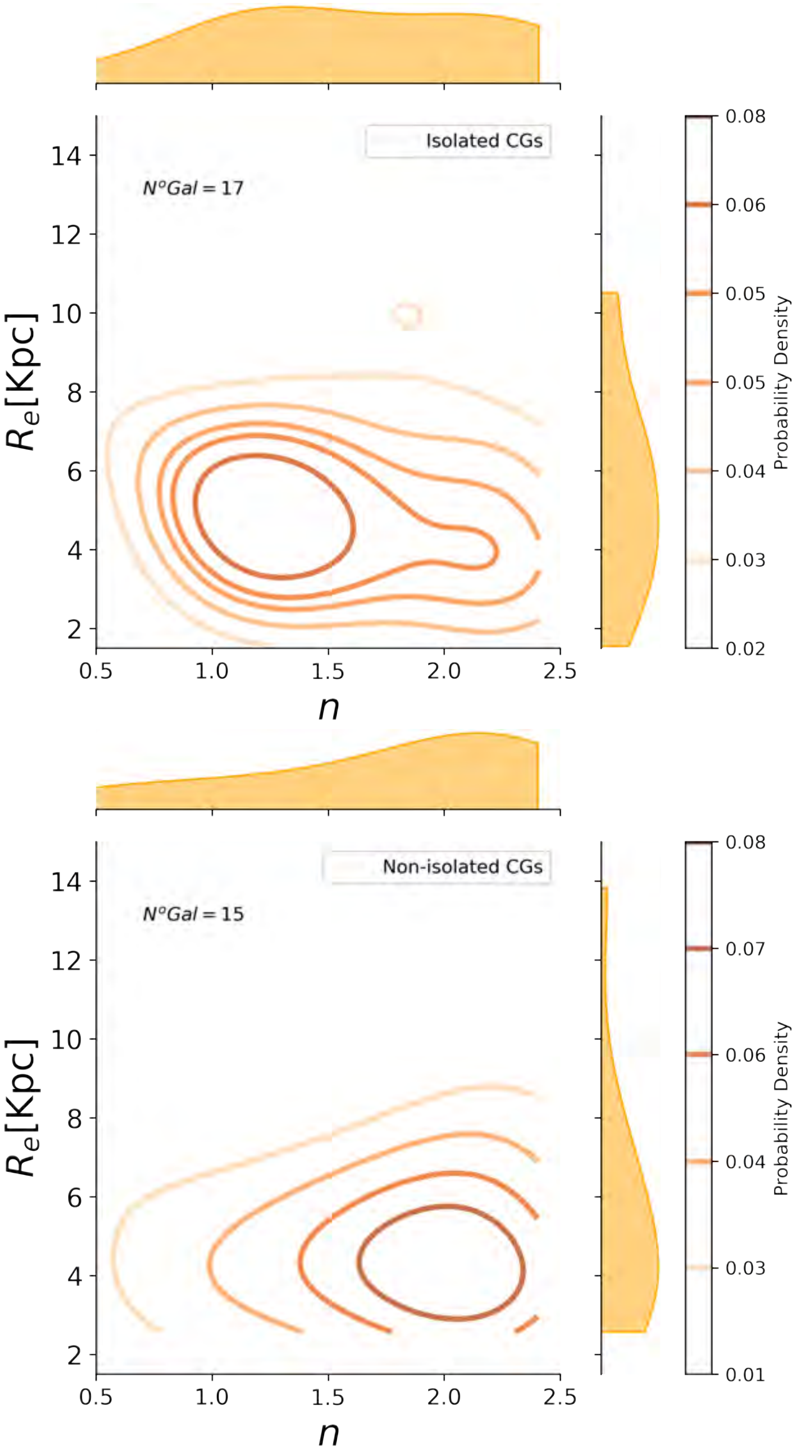

Figure 3.2.5: Contours of effective radius as a function of Sérsic index for *transition galaxies*, in r-band, in isolated CGs (top panel) and non-isolated CGs (bottom panel). In the upper right corner the number of *transition galaxies* that are in each case is indicated.

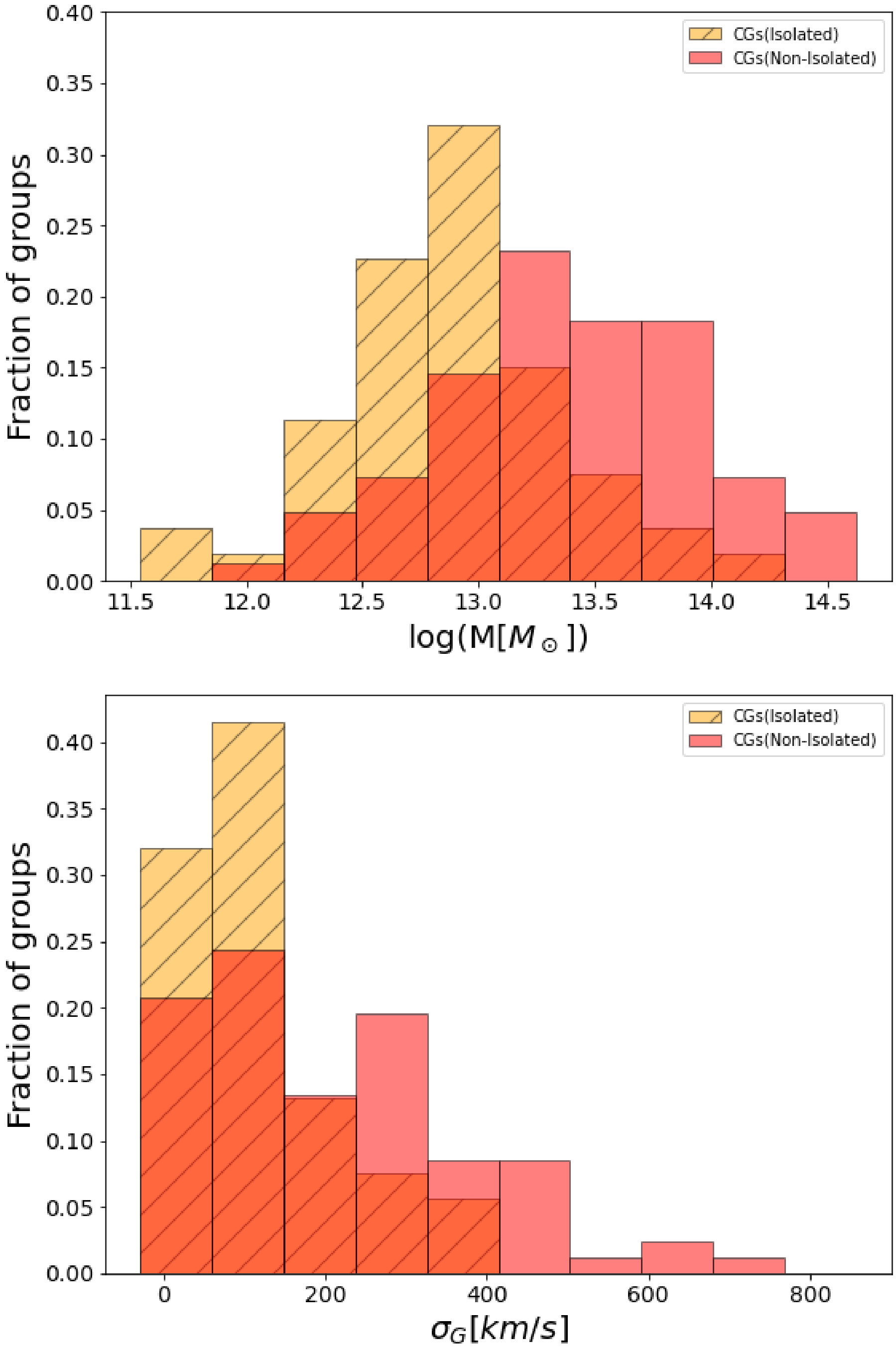

Figure 3.2.6: Histogram of the total stellar mass (top plot) of the groups investigated by Yang et al. (2007), and the velocity dispersion of the CGs (bottom plot). In yellow we show isolated CGs, while in orange, the non-isolated ones.

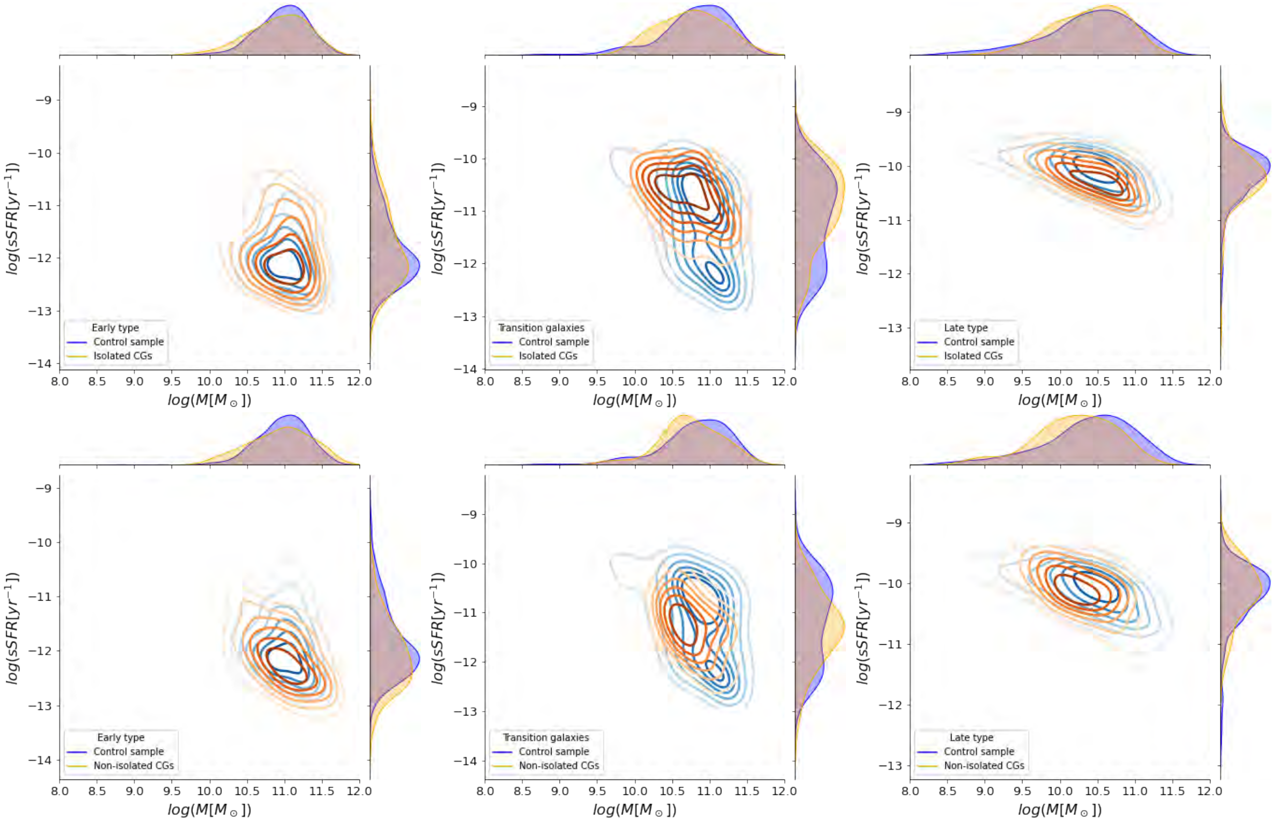

Figure 3.2.7: Contours of log(sSFR) as a function of the stellar mass. In orange contours for CGs, top plots for isolated CGs and bottom plots for non-isolated CGs. The blue contours for galaxies in the control sample. ETGs, *transition galaxies* and LTGs are shown on the left, center and right, respectively.

to right panels, while the control sample galaxies are depicted by blue contours. In the lower panels, the orange contours illustrate the distribution of galaxies in non-isolated CGs.

In the upper-left plot of Figure 3.2.7, we can see that for ETGs in isolated CGs compared to the control sample, there is no difference in sSFR as a function of mass. For *transition galaxies*, a clear bimodality is observed for the control sample, as shown in the upper middle panel of Figure 3.2.7. However, for *transition galaxies* in CGs, the bimodality is not as evident, though there is a subtle bimodality in the sSFR histogram. Meanwhile, LTGs in isolated CGs show a peak with a lower sSFR value compared to the distribution of the control sample, as seen in the upper right plot of Figure 3.2.7. In the case of non-isolated CGs (bottom panels of Figure 3.2.7), the ETGs reach slightly lower values of sSFR compared to the control sample, as seen in the left panel. For *transition galaxie* in non-isolated CGs, the bimodality observed in isolated CGs is no longer present, and the distribution is unimodal with a peak in the middle of the bimodality observed for the control sample, as seen in the middle panel. The distribution of sSFR for LTGs in non-isolated CGs is wider than the corresponding distribution for galaxies in the control sample.

To assess the statistical significance of these visual differences in the sSFR distribution across various morphological types when comparing the two environments mentioned in previous paragraphs, we present in Table 3.2.2 the median of $log(sSFR)$ for each population in both isolated and non-isolated CGs. We find that the median of sSFR is lower in non-isolated CGs compared with isolated CGs except for the LTGs which are similar. The corresponding p-value obtained from a Kolmogorov-Smirnov (KS) test (An 1933, Smirnov 1948) is shown in Table 3.2.2. This test will be used to de-

	$log(sSFR[yr^{-1}])$			**Quenched galaxies**	
	Median for isolated CGs	**Median for non-isolated CGs**	P_{KS}	Isolated CGs	Non-isolated CGs
ETG	$-11.9^{-11.8}_{-12.0}$	$-12.1^{-12.0}_{-12.2}$	$0.27\ (1.7\times10^{-3})$	80%	95%
TG	$-10.7^{-10.5}_{-11.1}$	$-11.3^{-11.0}_{-11.6}$	0.09 (0.18)	44%	71%
LTG	$-10.2^{-10.1}_{-10.3}$	$-10.1^{-10.0}_{-10.2}$	0.14 (0.59)	6%	7%

Table 3.2.2: The median of log(sSFR) for ETGs, transition galaxies, and LTGs in isolated and non-isolated CGs is presented. In the third column, we provide the p-value obtained from a KS test comparing the sSFR of galaxies in each morphological population in isolated CGs with the control sample, indicating in parentheses the p-value when comparing non-isolated CGs with the control sample. In the last two columns, we present the fraction of quenched galaxies, $log(sSFR[yr^{-1}]) \leq -11$ (Wetzel et al. 2013), in isolated CGs and non-isolated CGs.

termine whether the sSFR distribution in isolated CGs (p-value indicated outside the parentheses) or non-isolated CGs (values within parentheses) matches the distribution seen in the control sample. Based on the KS test, we find that the sSFR distribution of LTGs located in isolated CGs shows no significant difference with the control sample. However, the distribution differs for non-isolated CGs compared with the control sample. For ETGs and *transition galaxies*, the sSFR distributions do not differ for isolated and non-isolate CGs with respect to the control sample distribution.

In Table 3.2.2, the percentage of quenched galaxies in isolated and non-isolated CGs is also shown, where we consider a galaxy to be quenched if $log(sSFR) \leq -11$, based on the criterion proposed by Wetzel et al. (2013). However, we would like to emphasise that this value is close to the value that defined the bimodality observed in *transition galaxies* in the control sample (see Figure 3.2.7), which is $log(sSFR) = -11.46$. To estimate this value, we fitted two Gaussians and took the point where they intersect. This value can be used to define when a galaxy is quenched, but we selected the Wetzel et al. (2013) criterion to ensure comparability with other studies. Non-isolated CGs have a higher percentage of quenched galaxies for ETGs and *transition galaxies* compared to the isolated CGs, and this difference is particularly more significant for *transition galaxies*. Simulations indicate that galaxies tend to enter a quenched state preferentially in structures with masses ranging from $10^{13.5}$ to $10^{14.5}M_{\odot}$ (Pallero et al. 2019). This mass range is close to the peak of the mass distribution of non-isolated CGs, as we can observe in Figure 3.2.6. For LTGs, there is no difference in the fraction of quenched galaxies between isolated and non-isolated CGs.

3.3 Discussion

In this study, we examine the morphology characteristics (R_e and n) and sSFR of galaxies within a sample of CGs, selected using the catalogues by Sohn et al. (2016) and Zheng & Shen (2020). This sample is then subdivided into isolated and non-isolated CGs, following the analysis done by Yang et al. (2007). We explore how these properties change based on the environment in which the CGs are situated. Our findings reveal notable differences between isolated and non-isolated CGs, particularly in the population of ETGs and *transition galaxies*, where non-isolated CGs exhibit lower sSFR and a higher fraction of quenched galaxies and more compact and concentrated *transition galaxies*. In the following section, we delve deeper into our results, comparing them with other studies, and propose an evolutionary scenario based on these observational outcomes.

3.3.1 Can the environment of the CGs influence a physical transformation?

In Chapter 2 we compared the same sample of CGs analysed in this work with a control field sample, and suggested that environmental effects lead to a higher proportion of quenched galaxies and a lower median sSFR in CGs. This indicates a cessation of star formation, regardless of galaxy type, where a possible explanation for these differences could be tidal interactions, shocks, and turbulence (Alatalo et al. 2015, Bitsakis et al. 2016), for the specific sample that we studied in that work. In this work, we find that both isolated and non-isolated CGs have higher fractions of quenched galaxies compared to the control sample, and that this fraction is higher for non-isolated CGs with respect to the isolated counterpart. For isolated CGs, the mechanism that likely contributes to their higher fraction of quenched galaxies compared to the field is tidal interactions, which can produce neutral gas loss and heating, enriching the intra-group medium. Additionally, we find that there are statistically significant differences in the distribution of sSFR between the control sample and the CGs, but only for LTGs in non-isolated CGs (see Section 3.2.5). In the case of non-isolated CGs a possible scenario is that galaxies may experience different mechanisms depending on the mass of the group they belong to, resulting in this higher percentage of quenched galaxies. For non-isolated CGs located in low-mass structures, galaxy interactions are expected to be the main driver of transformations. However, for non-isolated CGs in more massive structures mechanisms such as ram-pressure stripping (e.g., Roberts et al. 2021) and galaxy harassment (e.g., Moore et al. 1996b) are more likely to contribute to the differences observed with the KS-test for LTGs.

These non-isolated CGs exhibit higher velocity dispersions (see the bottom panel in Figure 3.2.6), resulting in smaller crossing times, which is indicative of a more dynamically evolved state compared to the isolated CGs. This dynamical difference allows us to observe a lower sSFR and a larger fraction of quenched galaxies in non-isolated CGs. Thus, the physical properties of the CG galaxies are affected by interactions between galaxies within the CG and the interaction of the CG with its surrounding environment.

3.3.2 Evolutionary scheme: The role of the dynamics in CGs and its connection with major structures

As presented in Section 3.2, there is a clear relation between the dynamics of CGs and the morphological transformation. Additionally, we find that approximately 27% of all CGs we studied are not isolated, and their surrounding environment affects in different ways the observed morphological transformation. These non-isolated CGs exhibit lower sSFR compared to their isolated counterparts. Furthermore, according to Zheng & Shen (2021), CGs embedded in larger structures exhibit a correlation between their velocity dispersion and the values displayed by its parent structure (i.e., a larger group or cluster) in which they are embedded. This relationship follows an almost one-to-one pattern for CGs with velocity dispersions less than 500 km/s, such that as the velocity dispersion of the structures that contain the CGs increases, the velocity dispersion of the CGs also increases. However, for velocity dispersion higher than 500 km/s, the CGs are on average 20%-40% below the one-to-one relation. Additionally, we find that 55% of the non-isolated CGs in our sample have a velocity dispersion higher than 200 km/s, which is the average velocity dispersion of the CGs (Hickson et al. 1992). Therefore, by having the velocity dispersion of CGs we can speculate if these systems are part of larger structures. In any case, a detailed spectroscopic analysis of the CGs environment is required to fully understand their connection with larger-scale structures. It is important to note that what we call non-isolated CGs are, in fact, a mixture of embedded and predominant CGs defined by Zheng & Shen (2021). The embedded CGs are found in major structures, and the luminosity of the CG is lower than the luminosity of the *other galaxies* in the major structure. While predominant CGs have higher luminosity than the additional galaxies in the major structure. The correlation between the velocity dispersion of the parent group and the CGs found by Zheng & Shen (2021) is only for embedded CGs, as they did not explore the case of predominant CGs. Recently Taverna et al. (2023) studied the properties of 1368 CGs catalogued by Zandivarez et al. (2022) using SDSS DR16. They found that the velocity dispersion of the CG increases with the density of the environment in which it is located.

Combining the results from Section 3.2.2, we can further categorise CGs into three distinct stages, allowing us to propose an evolutionary scheme, based on the morphological characteristics of their members and the environments they inhabit. These stages allow us additionally to establish correlations with the velocity dispersion of the systems, as mentioned in Section 3.2.3. High σ_G values in this context may indicate a stronger association between the dynamics of CGs and the larger-scale structures they are embedded in. In Figure 3.3.1, we represent how these three stages correlate. In the first stage, there are CGs rich in LTGs, with larger crossing times, which are in an initial or less dynamical evolved state and isolated. In this stage the *transition galaxies* start to become smaller and more compact, appearing as a peculiar galaxy population in CGs, with respect to the control sample, in the $R_e - n$ diagram. Tidal forces pull matter out of the galaxies, which increases the amount of neutral gas in the intra-group medium. This HI gaseous component medium has been observed by several authors (e.g. Verdes-Montenegro et al. 2001, Jones et al. 2022, Cheng et al. 2023a). The second stage includes CGs with a lower fraction of LTGs and smaller crossing times. Here the environment in which the CGs are located plays a relevant role in the evolution of the galaxies accelerating the transformation process that we observe in the *transition galaxies*, increasing the population of galaxies that characterises the CGs, that is the “peculiar” population of *transition galaxies*. In this stage, there is a combination of tidal effects produced by galaxy-galaxy interactions inside the CGs, and the interaction of the CG with its surrounding environment. Finally, in the last stage probably most of the *transition galaxies* have already suffered the morphological transformation that we observe in systems with lower σ_G. It is possible that during this stage, CGs may begin to disrupt within the major structures they inhabit.

Therefore, we suggest that CGs can evolve from scenarios 1 to 3. CGs in stage 1 have three potential ways of evolving: the first one is that these CGs will merge due to dynamical friction (Mamon 1992, Jiang et al. 2008), since the merger rate in groups is inversely proportional to the σ_G^3 of the group/cluster. This scenario is also known as the fast merger model (Mendes de Oliveira & Hickson 1994, Gómez-Flechoso & Domínguez-Tenreiro 2001). The second one is that other groups can accrete them or they can accrete other galaxies and reach stage 2, and the third is to remain virialized depending on the mass of the halo containing it (Gómez-Flechoso & Domínguez-Tenreiro 2001). In stages 2 and 3 the CGs and their environment can be accreted by major structures, which accelerates and promotes the morphological transformation of the *transition galaxies*. Hence, the CGs would move from top to bottom in our scheme presented in Figure 3.3.1, decreasing the fraction of LTGs, and from left to right, increasing their velocity dispersion. The increase in velocity dispersion may be related to a growing mass of the CGs due to the accretion of galaxies or because the CGs are being accreted by other groups. In the first case, this would probably only be seen as a slight increase in velocity dispersion, while in the second case, the dynamics of the CGs would be dominated by the larger structure in which they are embedded. In both cases, in these groups, we would see the morphological transformation of their galaxies accelerated and low values in the crossing time. According to simulations, when a group falls into structures like clusters, the group becomes dynamically hotter, even though the relative velocity of the group remains, on average, lower than the galaxies in the cluster. Additionally, it is expected that after the first pericentric passage, the group will disintegrate (Bahé et al. 2019, Benavides et al. 2020, Haggar et al. 2022). Our proposed evolutionary scenario is

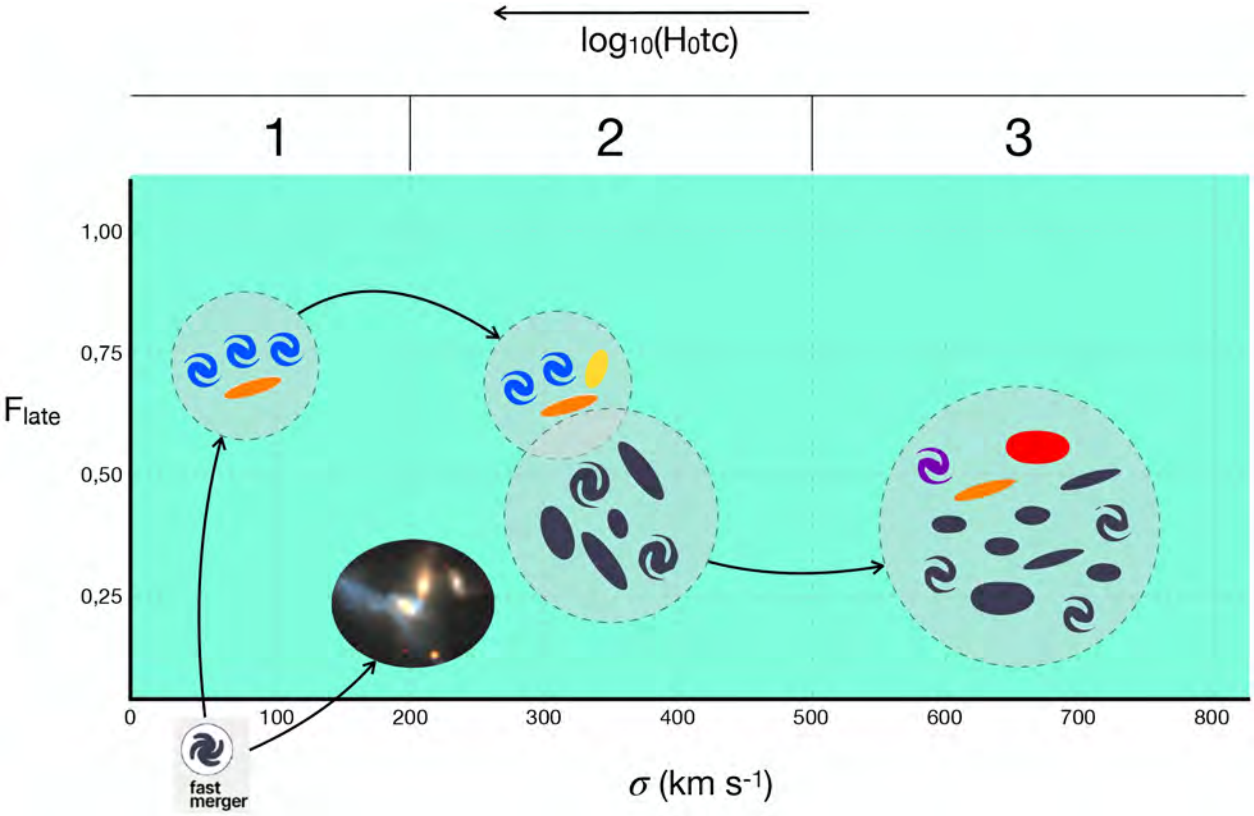

Figure 3.3.1: Evolutionary scheme we propose for CGs. In the x-axis we have the velocity dispersion of CG, in the opposite direction the crossing time which increases as σ_G decreases, having less dynamically evolved CGs. On the y-axis, we have the fraction of LTGs. Our scheme evolves from stages 1 to 3, where the CGs have a lower fraction of LTGs, higher σ, and lower $H_o t_c$. Our results show that this evolution is accelerated in non-isolated CGs.

in agreement with Coziol et al. (2004), who suggest that the formation of CGs embedded in massive structures was earlier than the formation of isolated CGs, which is also supported by Tovmassian et al. (2006). However, we note that the study done by Coziol et al. (2004) was based on a small sample of 27 Hickson CGs, where only $\sim 30\%$ of CGs were isolated, the other 70% were parts of the major structures (groups and clusters).

Our results (sections 3.2.4 and 3.2.5) support the idea that CGs could be responsible for the morphological transformation of galaxies, which is accelerated by the environment in which they are located. They are also responsible for quenching the star formation of galaxies, where the environment again plays a relevant role, by accelerating this process. An extreme example that supports this scenario is the CG falling into the Abell 1367 cluster (Blue infalling group, Cortese et al. 2006). Indeed, Cortese et al. (2006) showed that due to the combination of the effect of the tidal forces in the CG, combined with the ram-pressure of the intra-cluster medium, the galaxies of the CG fragmented, and the ionised gas was ejected, generating the HII regions that are observed close to the galaxies of the CG. Hence, the evolution of galaxies in CGs is affected both by the local environment, i.e., by the fact of being in CGs, and also by the fact that these CGs are part of major structures. This should be taken into account when analysing CGs, given that there is a complex interplay of physical phenomena occurring at both local and major scales.

3.4 Summary and Conclusions

In this chapter we examine 340 compact groups (CGs) located in the Stripe 82 region selected from the catalogues published by Sohn et al. (2016) and Zheng & Shen (2020). We subdivide our sample of CGs into isolated and non-isolated, following a previous study done by Zheng & Shen (2021) and by using the catalogue published by Yang et al. (2007). Our goal is to understand the dynamics of CGs as well as how the environment surrounding them impacts the morphological and physical properties of their galaxy members. We compare our results against a sample of field galaxies, in order to determine the differences within a less dense environment. Galaxies are classified into early-type (ETG), late-type (LTG), and *transition galaxies* based on their Sérsic index and colour. In the following, we summarise our main findings:

1. For our entire sample of CGs we confirm the existence of a correlation between the dimensionless crossing time (dynamical state) and the velocity dispersion (see Figure 3.2.1). Thus, a CG with a higher velocity dispersion, higher compactness, a lower fraction of LTGs, and lower crossing times, are dynamically more evolved than those CGs with shorter velocity dispersion, a higher fraction of LTGs, and larger crossing times.

2. CGs with higher velocity dispersions exhibit a clear bimodal distribution of their *transition galaxies* in the $R_e - n$ plane. However, this bimodality is not clear for *transition galaxies* located in CGs having lower velocity dispersion. This suggests an accelerated morphological transformation process in higher velocity dispersion CGs, where peculiar galaxy populations prevail. Conversely, lower velocity dispersion CGs may indicate a slower morphological transformation, possibly due to gradual changes thanks to the tidal interactions. Although we cannot rule out the scenario that mergers within the CG might also contribute to the morphological transformation. This suggests that the CG environment is ideal for studying the morphological changes that galaxies undergo.

3. We find that at least 27% of our 340 CGs are non-isolated, i.e., they are in major structures.

4. We find that the non-isolated CGs have a wider range of velocity dispersion, reaching $\sigma_G < 800$ km/s. 55% of these non-isolated CGs have velocities dispersion greater than 200 km/s. On the contrary, the isolated CGs have a narrower range, reaching $\sigma_G \leq 400$ km/s, where only 27% of the isolated CGs reach $\sigma_G > 200$ km/s. Therefore, the value of the velocity dispersion may indicate whether the CG is isolated or not.

5. We find that the *transition galaxies* in isolated or non-isolated CGs do not follow the same bimodal $R_e - n$ distribution as all *transition galaxies*, but they contribute to one of the two parts of this bimodality. Indeed, for *transition galaxies* in isolated CGs, we find a high density in the $R_e - n$ plane for $n < 1.75$, suggesting that most of these galaxies have not yet undergone morphological transformation. In contrast, the n distribution in non-isolated CGs increases smoothly towards higher values, approaching the n value of the peculiar galaxy population. This indicates that the galaxies have already undergone a morphological transformation. These findings suggest that the large-scale environment where the CGs reside accelerates morphological transformation.

6. We observe statistical differences in the sSFR distributions for LTGs in non-isolated CGs compared to the control sample, using a KS-test. Therefore, the distributions of LTGs in non-isolated CGs do not follow the same distribution as the control sample.

7. We find that the fraction of quenched galaxies is higher for ETGs and *transition galaxies* in non-isolated CGs than in isolated CGs and the control sample. This indicates that larger structures favour quenching within CG galaxies, hence, the physical properties of CG galaxies are influenced by interactions among galaxies within the CG, as well as interactions between the CG and its surrounding environment.

8. The results summarised above motivated us to propose an evolutionary scenario for CGs, considering their connection to major structures. In this scenario, the major structures where CGs are embedded accelerate the quenching process in CG galaxies and their morphological transformation (see Figure 3.3.1). This, subsequently, influences the CG dynamics because non-isolated CGs have higher velocity dispersions than the isolated ones, suggesting that the dynamics of non-isolated CGs are dominated by the major structure where the CGs are located.

These results add valuable evidence in support of CGs as places of galaxy transformation and evolution raising the opportunity to develop future research of the environments of CGs. We highlight with this work the importance of carrying out detailed studies of the environment in which the CGs are found in order to further understand galaxy evolution in these systems.

Chapter 4

Probing the Window into Environment-Morphology-Nuclear Activity Connection

In this chapter, we will study the sample of galaxies analysed in the previous chapters with the purpose of exploring how the environment impacts nuclear activity in galaxies within CGs. Considering that CGs can be part of major structures (non-isolated CGs), it is unclear how the surrounding environment influences their galaxies. Using ionisation mechanism diagnostic diagrams on Sloan Digital Sky Survey data, in particular the WHAN method, we find a lower AGN fraction in CGs (18.3%) compared to the control sample (26.6%). Different ionisation behaviours were observed in CGs, with reduced SF and AGN in ETGs. However, LTGs in CGs showed a slightly higher AGN fraction than the LTGs in the control sample, possibly due to ongoing gas reservoirs. *Transition galaxies* in CGs also had a slightly higher AGN fraction than their counterparts in the control sample. AGN and SF fractions decreased with higher velocity dispersion, contrasting with Retired Galaxies (RGs) and Passive Galaxies (PGs). Isolated CGs favoured SF and AGN, while non-isolated CGs showed an increase in PG. In scenarios where galaxy interactions enhance gas flow to the galactic centre, potentially driving AGN activity, our findings suggest that the overall lack of gas in CGs may limit nuclear activity despite frequent interactions. However, in LTGs and *transition galaxies*, interactions can still trigger nuclear activity, likely due to these galaxies retaining some of their gas reservoirs. Indeed, in non-isolated CGs, there is a lower fraction of AGN and SF galaxies compared to isolated CGs, where there is a higher fraction of ETGs. This suggests that the environment in which CGs are embedded may accelerate physical transformations, potentially affecting their gas reservoirs. In conclusion, our study indicates a complex relationship between the environment, morphology, and nuclear activity in CG galaxies. Our study also points to the need for an in-depth examination of the gas properties in these galaxies.

This chapter is organised as follows: Section 4.1 describes the cross match between the CG galaxy sample and the control sample with the SDSS spectroscopic data. In Section 4.2, we outline the methodology used to identify the main ionisation mechanism for each galaxy. Sections 4.3 and 4.4 present and discuss our results. Finally, we summarise our findings in Section 4.5.

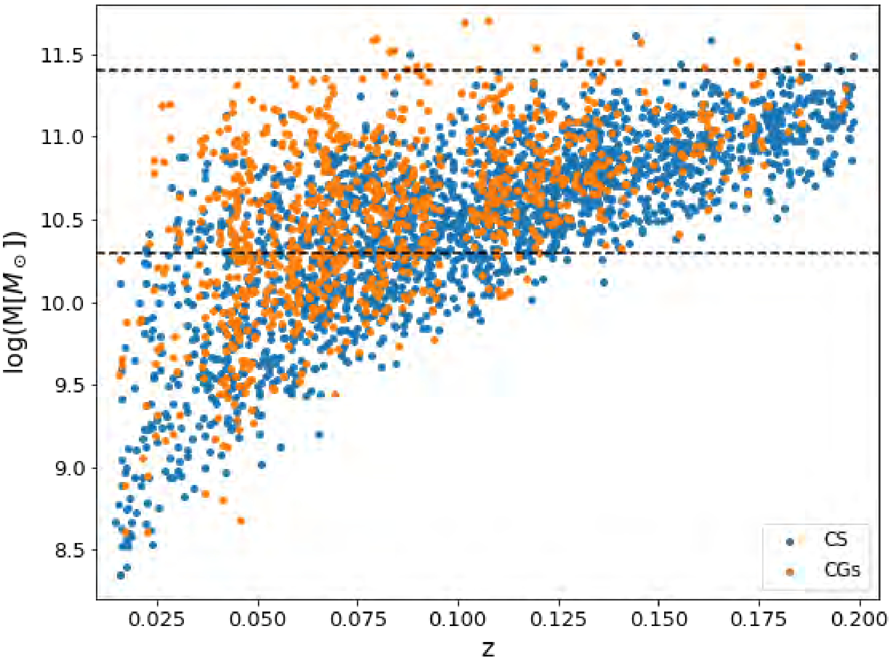

Figure 4.1.1: Stellar mass distribution as a function of redshift, blue dots represent galaxies in the control sample and orange dots represent galaxies in CGs. The dashed lines enclose the galaxies in the subsample that we will use to compare the physical properties of the different galaxy samples ($10.3 \leq log(M[M_{\odot}]) \leq 11.4$).

4.1 Data

4.1.1 Spectroscopic data

The three catalogues we used to select our sample are based on spectroscopic redshift information from SDSS. Therefore, we can use the SDSS spectroscopic information to determine their ionisation mechanisms. The size of the SDSS fibre corresponds to 3 arcseconds in diameter, covering a wavelength range ranging from 3800 to 9200 $\AA$.

We use data from the Portsmouth stellar kinematics and emission-line flux measurements catalogue [1] which is based on the SDSS-DR8 (Aihara et al. 2011). The stellar kinematics and emission line properties in that catalogue were obtained using PPXF (Cappellari & Emsellem 2004) and GANDALF (Sarzi et al. 2006) codes, respectively. GANDALF fits the galaxy spectrum with a combination of single stellar population and Gaussian emission line templates, simultaneously separating stellar continuum and absorption lines from the ionised gas emission, and derives properties like equivalent width, flux, and gas kinematics. Then PPXF is used to obtain the stellar kinematics by fitting the continuum stellar spectrum using the stellar population models by Maraston & Strömbäck (2011) based on the MILES stellar library (Sánchez-Blázquez et al. 2006). The GANDALF code corrects extinction due to the dust in the galaxy using the extinction law proposed by Calzetti (2001), but this code did not make corrections for the extinction of the Milky Way dust (Thomas et al. 2013). We find that 96% of the galaxies in our sample of CGs and the control sample are in galaxy Portsmouth catalogue. The entire sample is not found due to the fibre collision effect in SDSS.

---

[1] Galaxy Properties from the Portsmouth Group: `https://www.sdss4.org/dr17/spectro/galaxy_portsmouth/`

In Figure 4.1.1, we present the stellar mass of galaxies as a function of redshift. The orange data points represent the galaxies in CGs, while the blue data points represent galaxies from the control sample. It is evident that we do not detect faint sources for the higher redshifts present in our sample. Thus, we have a bias towards more massive sources at high redshifts, Malmquist bias (Malmquist 1922).

4.2 Methodology

4.2.1 Ionisation mechanism

Emission lines from a galaxy reveal the nature of the ionising source, such as its power, geometry, chemical composition of the gas, and dust content of the emitting region (Cid Fernandes et al. 2011). Therefore, we can determine the predominant excitation mechanism in the extragalactic objects, which may be due to photoionisation by O and B stars, known as star-forming galaxies; photoionisation by a continuous power-law source, or shock-wave heating, associated with a host of AGN; or photoionisation by hot low-mass evolved stars (HOLMES) (Stasińska et al. 2008, Cid Fernandes et al. 2011). It is possible to classify extragalactic sources with emission lines through diagnostic emission line ratio diagrams, which allow us to discern which is the predominant excitation mechanism. A classical approach to discern the ionisation mechanism is the use of the BPT diagram diagnostic (Baldwin et al. 1981, Kewley et al. 2001, Kauffmann et al. 2003a). Another diagram is proposed by Cid Fernandes et al. (2010) which is known as the WHAN diagram.
In their work, Cid Fernandes et al. (2010) and (2011) introduced a galaxy classification considering "retired galaxies" with HOLMES as their main ionisation source. This classification tackles the LINER debate by distinguishing between low-ionisation AGN and ionisation from post-AGB stars, offering clarity in identifying "genuine AGN". The key is their diagram using $EW(H_\alpha)$ versus $[NII]/H_\alpha$, which usually are the emission lines with better signal-to-noise ratios, enhances classification possibilities for a larger galaxy fraction.
It is important to highlight that Cid Fernandes et al. (2011) introduced a classification that considers five types of ionisation mechanisms:

- Pure star-forming galaxies (SF) are characterized by having: $log([NII]/H_\alpha) < -0.4$ and $EW(H_\alpha) > 3\,Å$.
- Strong AGN (sAGN) are characterised by having: $log([NII]/H_\alpha) > -0.4$ and $EW(H_\alpha) > 6\,Å$.
- Weak AGN (wAGN) are characterised by having: $log([NII]/H_\alpha) > -0.4$ and $3 < EW(H_\alpha) < 6\,Å$.
- Retired galaxies (RG), are characterised by having: $EW(H_\alpha) < 3\,Å$.
- Passive galaxies (PG), which are emission-line-free galaxies, are characterised by having: $EW(NII)$ and $EW(H_\alpha) < 0.5\,Å$.

In the case of the SDSS data, we used an amplitude-over-noise (AoN) ratio greater than two to ensure the detectability of the lines for reliable analysis using emission line ratio diagnostic diagrams (Thomas et al. 2013). However, this criterion excludes galaxies with low signal-to-noise (S/N) emission lines and those lacking emission lines, which are part of the PG according to WHAN. To address this, we examined the discarded galaxies post AoN cut with an average S/N ratio of 10 or more,

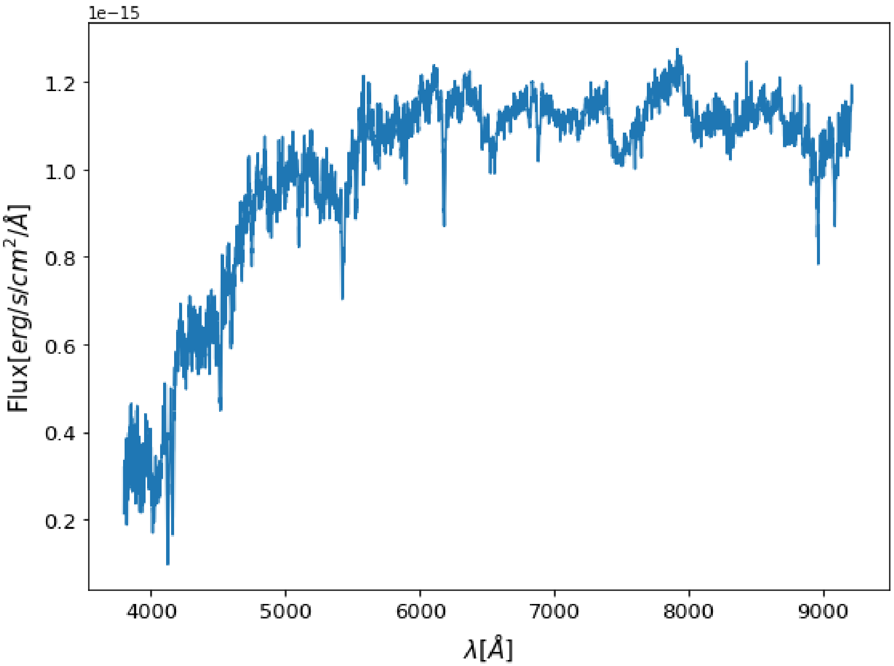

Figure 4.2.1: Example of the spectrum of one of the passive galaxies in the sample.

confirming them as emission line-free PG through visual inspection. Figure 4.2.1 provides an example of such PG galaxies. Galaxies with S/N less than 10 and AoN lower than 2 were categorised as unclassified.

4.2.2 Morphology classification

In Chapter 3, using the colour $(u-r)_0$ and the Sérsic index in the r-band,we classified each galaxy according to its morphology. Following this classification we classify galaxies in Early-Type (ETG) as those with $n > 2.5$ and $(u-r)_0 > 2.3$, and those with values less than these are classified as Late-Type (LTG). In addition, those with $n < 2.5$ and $(u-r)_0 > 2.3$ are called *transition galaxies*, and those with $n > 2.5$ and $(u-r)_0 < 2.3$ are called *other galaxies*.

4.3 Results

4.3.1 Ionisation dominant mechanisms

We selected galaxies from both the CGs and the control sample with the same range in r-band apparent magnitude and redshift to enable a comparison between the two environments. In Figure 4.2.2, the top panel shows the WHAN classification of our CG sample, while the bottom panel is for the control sample, with colours denoting each population in this classification. In Figure 4.3.1, we show the fraction of galaxies according to their main ionisation mechanism based on the WHAN diagram (see Figure 4.2.2). The orange bars represent CGs, while the blue bars represent the control sample. We find a higher fraction of RGs and PGs in CGs. Conversely, the control sample exhibits a higher fraction of SF and AGN than the CGs. We present in Table 4.3.1 the percentage of each ionisation mechanism in both the CG and control samples.

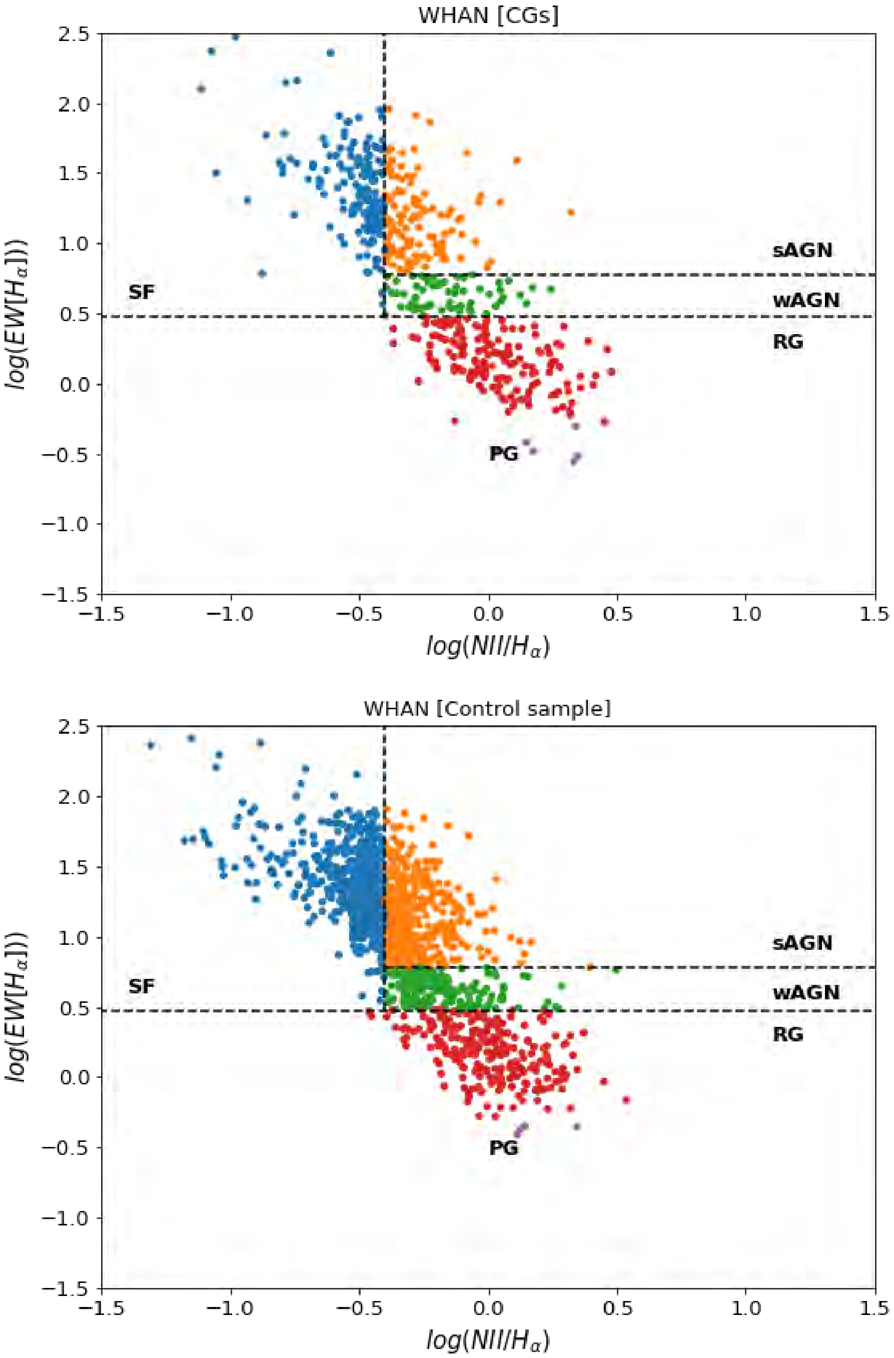

Figure 4.2.2: The top panel presents the WHAN classification of our CG sample, while the bottom panel corresponds to the control sample. Colours represent the different populations in this classification: blue for star-forming galaxies, orange for strong AGN, green for weak AGN, red for retired galaxies, and purple for passive galaxies.

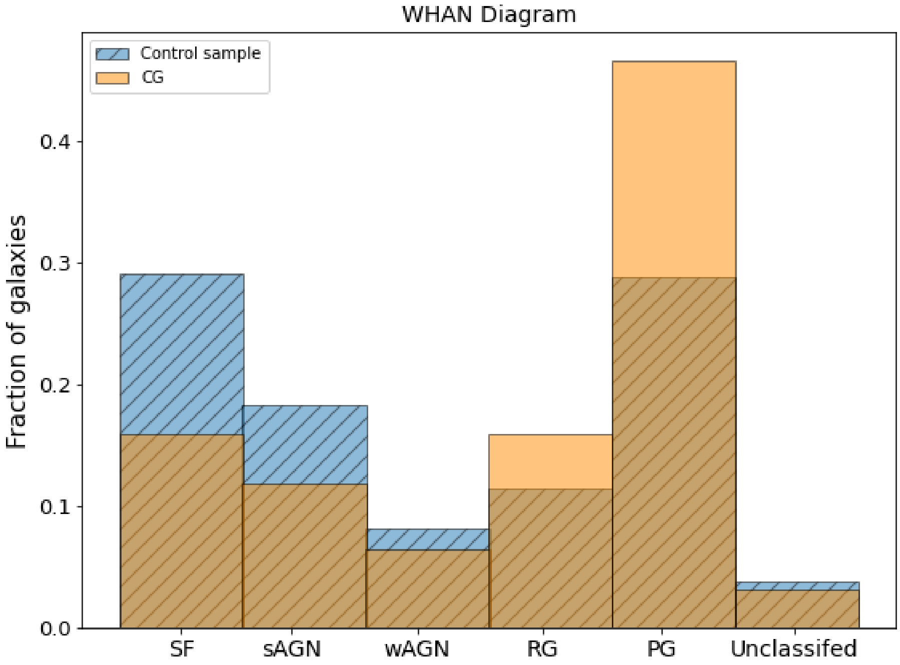

Figure 4.3.1: Histogram of the types of galaxies according to the WHAN classification for the control sample in blue and CGs in orange.

Overall, the total AGN fraction, combining wAGN and sAGN, is lower in CGs than in the control sample. It is essential to note that, with this classification, CGs do not dominate in the AGN fraction compared to field galaxies, in agreement with the findings of Sohn et al. (2013a), who observed a higher fraction of AGN in the control sample. However, this differs from the results of Coziol et al. (1998), Martinez et al. (2007), 2008, who reported a higher fraction of AGN in CGs. This discrepancy may be due to the different methods used to classify galaxies, as we will discuss in Section 4.4.

Galaxy Population	CG Sample (%)	Control Sample (%)
SF	16.3 ± 1.3	29.3 ± 11.1
sAGN	11.9 ± 1.1	18.4 ± 0.9
wAGN	6.4 ± 0.7	8.4 ± 0.6
RG	15.8 ± 1.2	11.4 ± 0.7
PG	46.4 ± 2.1	28.8 ± 1.1
Total AGN (sAGN + wAGN)	18.3 ± 1.8	26.6 ± 1.5

Table 4.3.1: Percentage of galaxy populations in CGs and the control sample.

4.3.2 Ionisation mechanisms according to galaxy morphology

Another way to evaluate the differences that may occur in the ionisation mechanisms in the CGs and the control sample is to consider the morphology of the hosts. To compare different galaxy subsamples, we cannot assume that both samples follow a similar distribution in redshift and mass in both environments. Therefore, we selecte a stellar mass range of $10.3 \leq log(M[M_{\odot}]) \leq 11.4$,

Galaxy type	SF	sAGN	wAGN	RG	PG
All galaxies (%)	4.7 ± 0.8 (12.6 ± 0.9)	11.8 ± 1.3 (19.7 ± 1.1)	6.7 ± 1.0 (10.2 ± 0.8)	20.1 ± 1.7 (15.6 ± 1.0)	53.9 ± 2.8 (37.7 ± 1.6)
Early type (%)	0.3 ± 0.3 (0.9 ± 0.4)	3.2 ± 0.9 (4.6 ± 0.9)	3.2 ± 0.9 (5.4 ± 1.0)	23.4 ± 2.5 (21.3 ± 2.0)	68.5 ± 4.3 (63.9 ± 3.4)
Late type (%)	26.7 ± 5.6 (37.2 ± 6.6)	37.2 ± 6.6 (34.6 ± 2.9)	10.5 ± 3.5 (12.2 ± 1.7)	10.5 ± 3.5 (9.8 ± 1.5)	11.6 ± 3.7 (6.0 ± 1.2)
Transition galaxies (%)	8.9 ± 4.4 (5.0 ± 1.4)	15.6 ± 5.9 (25.2 ± 3.2)	22.2 ± 7.0 (11.2 ± 2.1)	28.9 ± 8.0 (14.9 ± 2.5)	22.2 ± 7.0 (38.8 ± 4.0)
Other type (%)	2.8 ± 1.3 (10.3 ± 1.9)	16.9 ± 3.1 (22.6 ± 2.8)	9.0 ± 2.3 (15.4 ± 2.3)	16.9 ± 3.1 (14.7 ± 2.2)	49.2 ± 5.3 (30.8 ± 3.2)

Table 4.3.2: Percentages of galaxies classified according to their dominant ionisation mechanism based on the WHAN diagram, subdivided by their morphological type. Additionally, the first row shows the total number of galaxies within that narrow stellar mass range ($10.3 \leq log(M[M_{\odot}]) \leq 11.4$). The values in parentheses represent the percentages for galaxies in the control sample, while those outside the parentheses indicate the percentages for galaxies in CGs.

delimited by represented in the horizontal dash lines in Figure 4.1.1. In Table 4.3.2 we show the percentages of galaxies classified according to their main ionisation mechanism, subdivided by their morphological type. Additionally, in the first row, we show the total percent of galaxies within that stellar mass interval for each ionisation mechanism. The values outside the parentheses indicate the percentages for galaxies in CGs, while those inside parentheses represent the percentages for galaxies in the control sample.

Analysing each ionisation mechanism within each morphological type, we find that in ETGs, both environments are dominated by PG and RG. Additionally, we observe that ETGs in the CGs have a lower fraction of AGN and a higher fraction of RG and PG compared to ETGs in the control sample. In LTGs, SF and sAGN dominate in both environments. Comparing LTGs in CGs to the control sample, we find that CGs have a higher fraction of PG and a slightly higher fraction of sAGN, whereas the control sample has a higher fraction of SF and wAGN.

In *transition galaxies*, CGs exhibit a higher fraction of RG, wAGN, and PG, whereas *transition galaxies* in the control sample show a higher fraction of sAGN and PG. Comparing the environments, *transition galaxies* in CGs have a higher fraction of wAGN and RG, while the control sample has a higher fraction of sAGN and PG. In *other galaxies*, PG and sAGN dominate in both environments. CGs show a higher fraction of RG and PG, while the control sample has a higher fraction of SF, sAGN, and wAGN compared to CGs.

4.3.3 Galaxy properties according to their WHAN classification

We use the strength of the 4000 $\mathring{A}$ break (D_{4000}) as a spectral indicator for the mean age of the stellar population, defined as the ratio of the average flux densities in the narrow continuum bands $3850-3950$ $\mathring{A}$ and $4000-4100$ $\mathring{A}$ (Balogh et al. 1999). This data is derived from the MPA–JHU emission line catalogue [2]. In Figure 4.3.2, we present histograms for the D_{4000} index, the Sérsic index

---

[2] The MPA–JHU emission line catalogues are available `https://wwwmpa.mpa-garching.mpg.de/SDSS/DR7/`

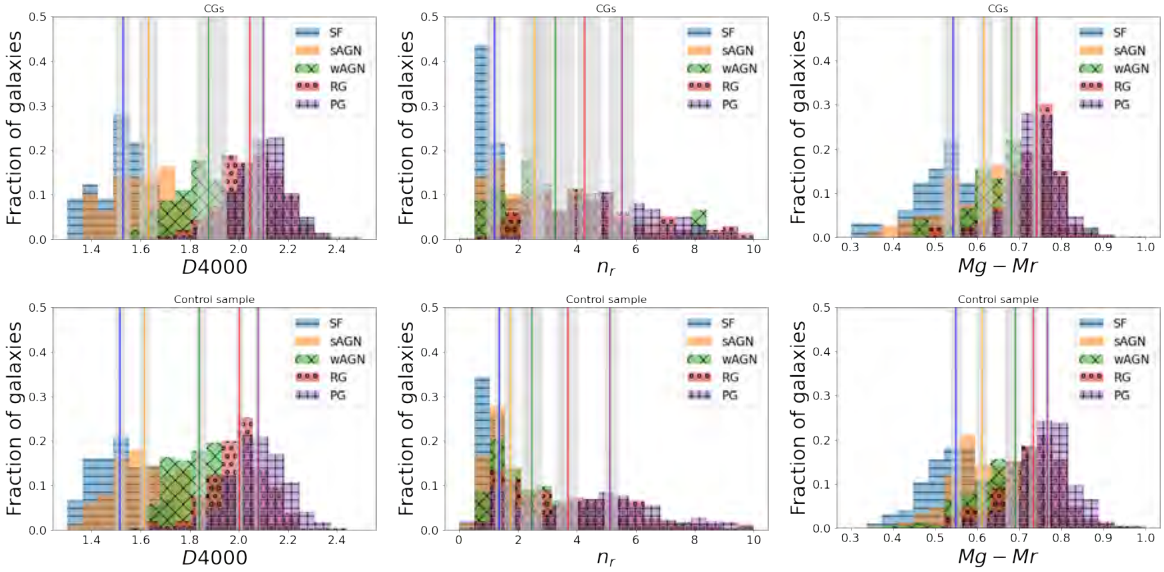

Figure 4.3.2: The histograms display the distribution of three parameters: the 4000 $\AA$ break (left panels), the Sérsic index (middle panels), and the colour $(g-r)_o$ (right panels). The panels in the upper section represent the CGs environment, while the plots in the lower section represent the control sample. Each panel shows the distribution of galaxies for each dominant ionisation mechanism according to the WHAN classification, focusing on galaxies with stellar masses of $10.3 \leq log(M[M_\odot]) \leq 11.4$. The SF galaxies are shown in blue, sAGN in orange, wAGN in green, RG in purple, and PG in red. The vertical lines represent the median value for each galaxy type, and the shaded area represents the 90% confidence interval using bootstrapping.

measured in r-band, and the colour at restframe $(g-r)_o$, for galaxies in the narrow stellar mass range ($10.3 \leq log(M[M_\odot]) \leq 11.4$). The top panels represent galaxies in CGs, while the bottom panels show galaxies in the control sample. Different galaxy types according to the WHAN diagram are represented by different colours: blue for SF, orange for sAGN, green for wAGN, red for RGs, and purple for PGs. Additionally, we present the median (solid line) and its uncertainty for each parameter and each ionisation mechanism, estimated through bootstrapping with a 90% confidence interval (gray region around the solid lines). Based on these plots, we observe that AGN, i.e., sAGN and wAGN, exhibit physical and morphological properties intermediate between SF and PG populations.

It is evident that SF galaxies appear bluer, less compact, and have lower D_{4000} values compared to other populations, indicating the presence of younger stellar populations in both CGs and the control sample. Conversely, PG galaxies are redder, more compact, and have higher D_{4000} values, indicative of older stellar populations. The most notable visual difference between CGs and the control sample lies in the colour distribution of PGs and the distribution of D_{4000} in RG. In CGs, PGs have a bluer colour distribution compared to the control sample. On the other hand, the D_{4000} value in RGs in CGs is higher compared to the control sample, indicating a relatively older population in CGs. Additionally, we see that the medians for n in CGs are higher for AGN, RGs, and PGs compared to the control sample.

In Table 4.3.3, we present the median values for D_{4000}, n, and $(g-r)_o$ for each population in each environment to compare the distributions of different properties between the environments for each ionisation mechanism in galaxies. The values outside the parentheses correspond to CGs, while those inside the parentheses represent the control sample, summarising our findings shown in Figure 4.3.2. Additionally, in the last column, we estimate the p-value after applying the Kolmogorov-Smirnov

Whan Type	**D4000**	n	$M_g - M_r$	P_{ks}
SF	$1.53^{1.56}_{1.50}$ $(1.51^{1.54}_{1.50})$	$1.19^{1.42}_{0.93}$ $(1.38^{1.43}_{1.23})$	$0.55^{0.57}_{0.52}$ $(0.55^{0.56}_{0.54})$	$P_{D400} = 0.68$ $P_n = 0.38$ $P_{(g-r)_0} = 0.86$
sAGN	$1.63^{1.65}_{1.59}$ $(1.62^{1.64}_{1.60})$	$2.61^{2.95}_{2.22}$ $(1.77^{1.91}_{1.56})$	$0.61^{0.64}_{0.60}$ $(0.61^{0.62}_{0.60})$	$P_{D400} = 0.71$ $P_n = 0.001$ $P_{(g-r)_0} = 0.21$
wAGN	$1.87^{1.93}_{1.83}$ $(1.84^{1.86}_{1.83})$	$3.19^{3.91}_{2.42}$ $(2.55^{2.85}_{2.11})$	$0.68^{0.70}_{0.66}$ $(0.69^{0.70}_{0.67})$	$P_{D400} = 0.11$ $P_n = 0.10$ $P_{(g-r)_0} = 0.97$
RG	$2.05^{2.08}_{2.01}$ $(2.01^{1.99}_{2.02})$	$4.30^{4.85}_{4.03}$ $(3.71^{4.05}_{3.29})$	$0.74^{0.73}_{0.75}$ $(0.73^{0.72}_{0.74})$	$P_{D400} = 2.6 \times 10^{-4}$ $P_n = 0.05$ $P_{(g-r)_0} = 0.49$
PG	$2.10^{2.12}_{2.09}$ $(2.08^{2.09}_{2.07})$	$5.52^{5.94}_{5.11}$ $(5.14^{5.39}_{4.95})$	$0.74^{0.74}_{0.75}$ $(0.77^{0.77}_{0.76})$	$P_{D400} = 0.01$ $P_n = 1.38 \times 10^{-5}$ $P_{(g-r)_0} = 5.54 \times 10^{-11}$

Table 4.3.3: Median values of different physical and morphological properties derived for each galaxy with stellar masses of $10.3 \leq log(M[M_\odot]) \leq 11.4$. The values outside the parentheses represent the galaxies in CGs, while those inside the parentheses correspond to the control sample. The superscript and subscript indicate the values at the 90% confidence interval estimated using the bootstrapping technique for each median. In the last column, we display the p-value resulting from comparing the distributions of CG galaxies with those of the control sample for each of the properties: the 4000 $\AA$ break (D_{4000}), the Sérsic index, and the colour.

(KS) test. This test compares the cumulative distribution function of each parameter between CGs and the control sample. Our objective is to evaluate if the distribution of each parameter analysed is consistent in both environments or not, thus testing the null hypothesis. If the p-value is less than 0.05, we reject the null hypothesis, i.e. the environments do not follow the same distribution.

We find that SF galaxies in CGs are slightly less compact and have slightly higher D_{4000} values compared to galaxies in the control sample, but their colour medians are the same. When comparing the distributions of the two environments for each property using the KS test for SF galaxies, we found no significant differences. For sAGN, we found that D_{4000} is slightly higher, they are more compact and have similar colours in CGs compared to the control sample. In this case, we find statistical differences for n, indicating that sAGN have larger Sérsic indices in CGs than in the control sample. For wAGN in CGs, they have slightly higher D_{4000} values and larger n values compared to the control sample. However, we did not find statistical differences. Therefore, in general, we find that AGN hosts in CGs do not exhibit differences in colour and stellar ages of populations compared to the control sample. In contrast, Duplancic et al. (2021) studied AGN in small galaxy systems, and found that galaxy groups when compared to pairs and triplets, have slightly redder colours and older stellar populations. Furthermore, we can observe that, overall, AGN are located in less concentrated galaxies, characterised by lower Sérsic indices, compared to RGs and PGs in both environments. This finding aligns with the results from Duplancic et al. (2021), who found that AGN in groups, triplets, and pairs of galaxies, are less concentrated in comparison with all galaxies in these systems, although they used the concentration index in their study.

For RGs, in CGs, the mean D_{4000} is slightly higher, along with larger n values, and they are slightly redder than galaxies in the control sample. In this case, we observe statistical differences in CGs and the control sample for the distribution of D_{4000}, indicating that RGs in CGs have slightly older populations compared to the control sample. In the case of PGs, we observe that for D_{4000} and n, the medians are larger and the colour is slightly bluer in CGs compared to the control sample, which is confirmed by the KS test, where the null hypothesis is rejected for all three properties. Thus, PGs in CGs do not follow the same distribution as in the control sample.

Based on these findings, we can deduce that AGN hots exhibit younger stellar populations and are less compact than RGs and PGs, but they are more compact and redder than SF galaxies. However, we observe statistically significant differences related to the environment in sAGN, RGs, and PGs. In the case of sAGN, they are more compact in CGs than in the control sample. RGs and PGs tend to have slightly older stellar populations, and PGs are more compact in CGs compared to the control sample.

4.3.4 Galaxy types as a function of stellar mass

Another interesting aspect to analyse is the dependence of the ionisation mechanism as a function of the stellar mass of the host galaxy. In Figure 4.3.3, we present the fraction of galaxies according to each ionisation mechanism as a function of the stellar mass, in orange for CGs, in blue for the control sample. We find that, the fraction of SF galaxies increases for less massive galaxies (upper left panel). Additionally, in the control sample, there is a higher fraction of SF galaxies at all mass ranges compared to the CGs, indicating that star-forming systems live in relatively lower-density environments (Cattorini et al. 2023).

On the other hand, for AGN, the fraction of galaxies shows a peak at around $10^{10.5} M[M_{\odot}]$ (see the upper right panel in Figure 4.3.3), indicating that AGN prefers host galaxies with intermediate stellar mass. This result is consistent with the findings by Duplancic et al. (2021). Furthermore, we observe that the fraction of AGN is higher in the control sample compared to the CGs, but in the bin of less massive galaxies, the fraction is similar.

Additionally, in Figure 4.3.3 in the upper right panel, we also show the individual behaviour of each type of AGN. The dashed orange lines with dot markers represent sAGNs for the control sample, while the dashed orange lines with x markers represent sAGNs for the CGs. The dark olive and green lines represent wAGNs for CGs and the control sample, respectively. In general, we observe that sAGNs follow the overall distribution pattern of AGNs. This is because there is a higher fraction of sAGNs in both environments compared to wAGNs, indicating that it is indeed sAGNs that prefer host galaxies with intermediate stellar masses. This behaviour is similar to the findings by Cattorini et al. (2023), who reported that these galaxies reach their maximum fraction in the stellar mass bins around $10^{10} M_{\odot}$ to $10^{10.5} M_{\odot}$.

On the other hand, we see that the fraction of wAGNs between the CGs and the control sample is similar for less massive bins. However, for the more massive bins, we find that the fraction is higher in the control sample. Interestingly, it is in these bins where the CGs exhibit a higher fraction of RGs compared to the control sample. In the case of RGs (see the bottom left panel in Figure 4.3.3), we see that the fraction of galaxies increases up to $\sim 10^{10.8} M_{\odot}$ and then remains constant for the most massive bin. Additionally, the fraction of galaxies in both environments is very similar, except for the last two bins where the fraction of RGs is higher in CGs. We observe that the fraction of PGs (see the bottom right panel in Figure 4.3.3) increases with the increasing stellar mass of the host for

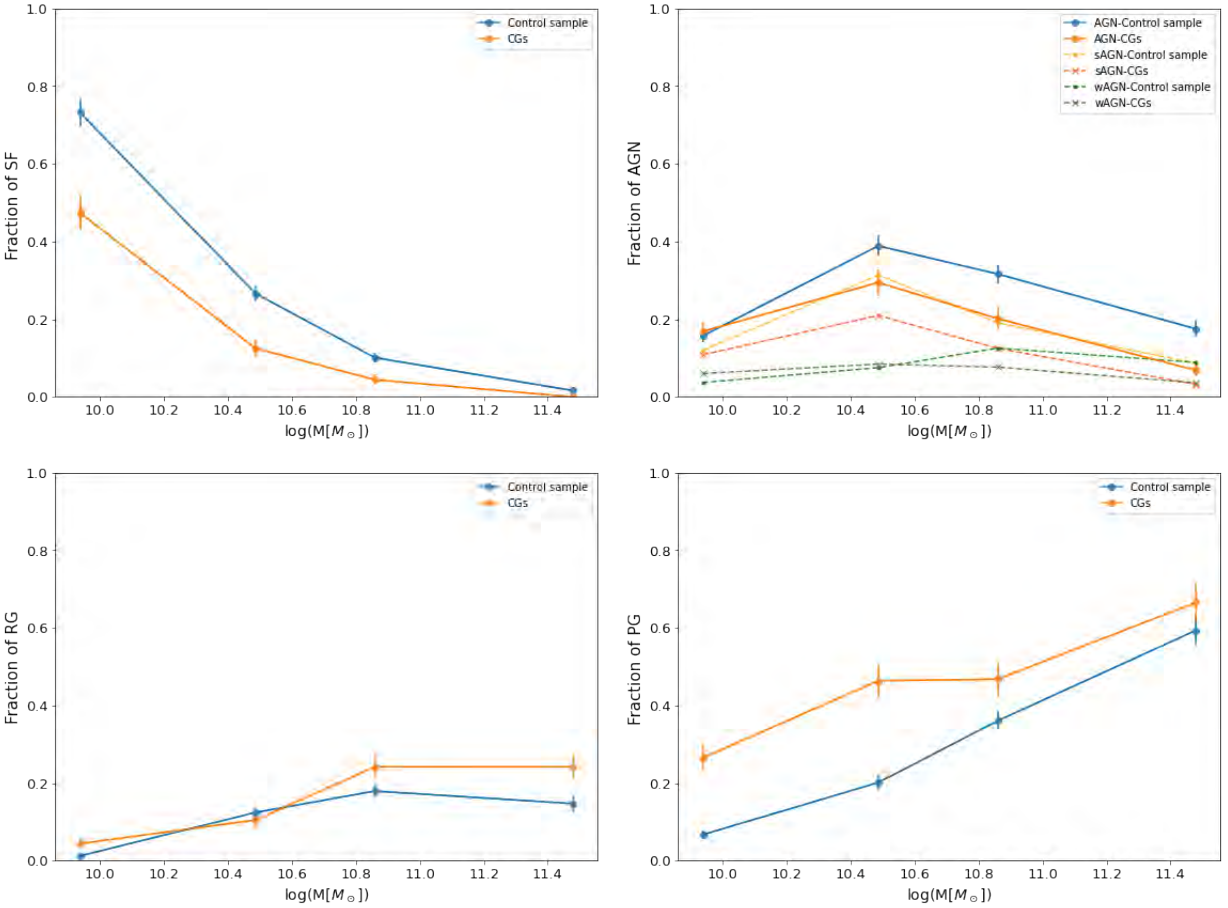

Figure 4.3.3: We analyse the fraction of galaxies according to the dominating ionisation mechanism as a function of the stellar mass, for the entire sample available: SF (top-left panel), AGN (top-right panel), RGs (bottom-left panel), and PGs (bottom-right panel). The blue lines represent the fraction of galaxies in the control sample, while the orange lines represent the fraction in CGs. The error bars reflect the uncertainty in each bin due to Poisson uncertainties.

both environments, where there is a higher fraction at all mass ranges in CGs compared to the control sample.

In summary, while SF galaxies are more frequent in lower-density environments, AGN are also more common in control samples than in CGs, particularly in more massive bins. Additionally, sAGN, which prefers intermediate stellar masses, dominate over wAGN in both environments. RGs and PGs show similar trends in both samples, with a notable increase of PGs in CGs at all stellar masses.

4.3.5 Relation between velocity dispersion and ionisation mechanism

It is worth exploring in our sample if we find any correlation between nuclear activity, and the evolutionary state of CGs that we proposed from the morphological analysis (Chapter 3). In addition, we are able to connect our results with respect to the evolutionary sequence proposed by Coziol et al. (2004). For this reason, in Figure 4.3.4, we present the percentage and its Poisson error for each ionisation mechanism as a function of CGs' velocity dispersion. The velocity dispersion bins we use were selected to have a similar number of CGs in each bin, with 84-85 CGs per bin.

In the top panel in Figure 4.3.4, we include all the galaxies in the CG sample. In the bottom panel in 4.3.4, we consider galaxies within the stellar mass range ($10.3 \leq log(M[M_{\odot}]) \leq 11.4$). According to the top panel in Figure 4.3.4, we find that the fraction of AGN and SF decreases as the velocity dispersion increases. For the highest velocity dispersion bins, greater than 300 km/s, these fractions remain almost constant. On the other hand, the percentage of PGs increases as the velocity dispersion of CGs increases, ranging from 30% to 60%.

In the bottom panel in Figure 4.3.4, we observe that even when considering galaxies within a stellar mass range, the fractions of PGs, RGs, and AGN follow the same trends as when using the entire sample. The only exception to this trend is the SF galaxies. This deviation is because, as we show in Figure 4.3.3, the majority of SF galaxies have lower masses, below $10^{10.4}$.

4.3.6 Is there any connection between the environment where CGs are located and the dominant ionisation mechanisms in their galaxies?

In Figure 4.3.5, we present histograms according to each ionisation mechanism, but in this case, we have separated the galaxies in CGs based on their environment, whether they are isolated or part of major structures, as defined in the Chapter 3. We note that the distribution of stellar mass is similar in both samples. In fact, the hypothesis that the stellar masses of galaxies in isolated and non-isolated CGs follow the same distribution cannot be rejected, as the p-value of the KS test is 0.1. According to Figure 4.3.5, we find that in isolated CGs, histogram in olive color, there is a higher fraction of SF and AGN galaxies, while in non-isolated CGs, histogram in cyan color, there is a higher fraction of PG galaxies.

4.4 Discussion

In this section we discuss the pysical meaning of our findings and contrasts them with previous studies. However, it is important to caution that comparing with other studies may not be entirely fair as they use different methodologies and sample of CGs. Nevertheless, these other studies will be taken as a reference, always considering the findings of Sohn et al. (2013a), who highlighted the significant impact of the AGN selection method on the estimated AGN fraction. This underscores the importance

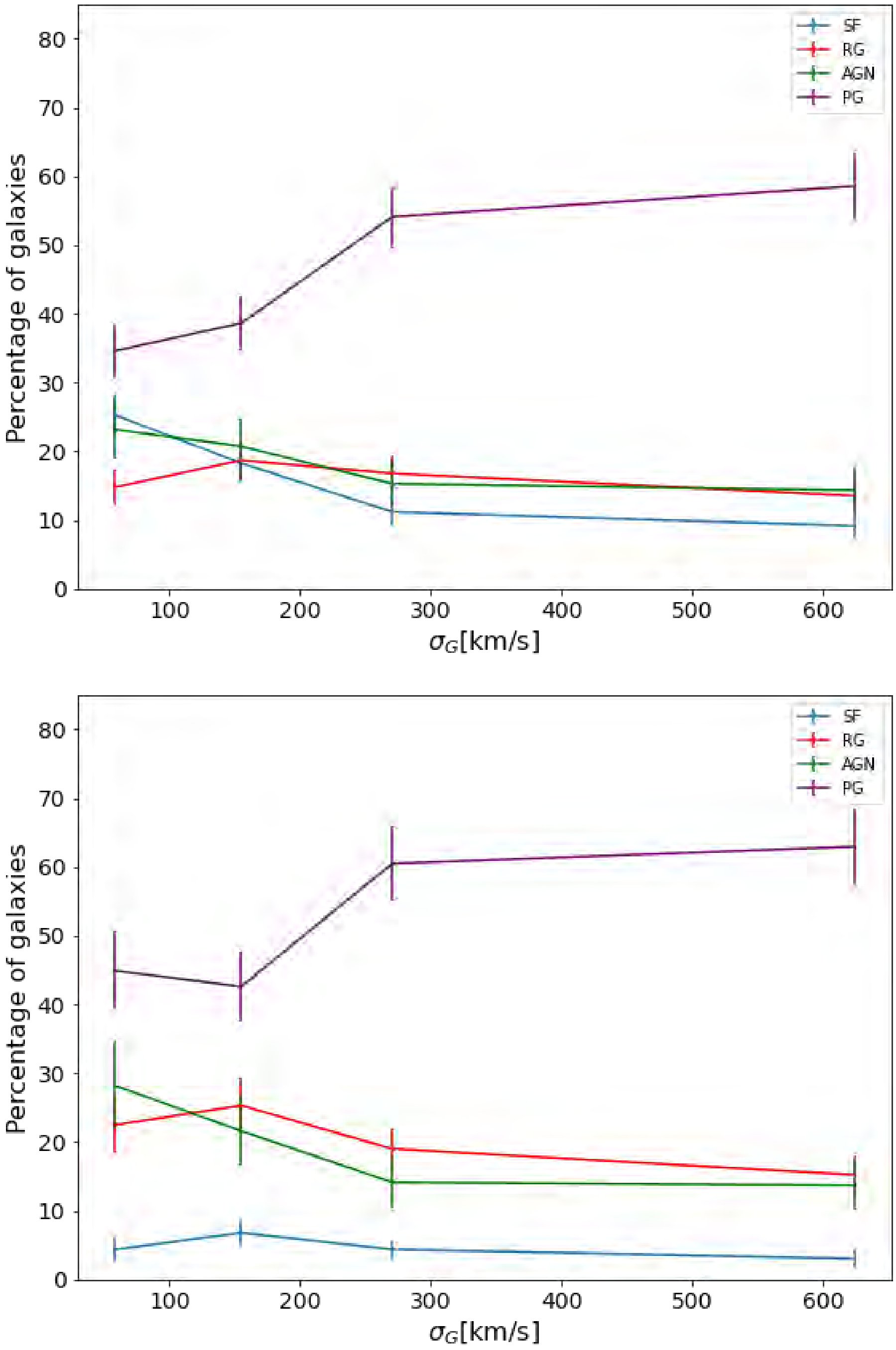

Figure 4.3.4: Percentage of each ionisation type as a function of velocity dispersion. The top plot represents the analysis considering all galaxies inside the CGs, while the bottom plot focuses on CG galaxies within a specific stellar mass range ($10.3 \leq log(M[M_\odot]) \leq 11$).

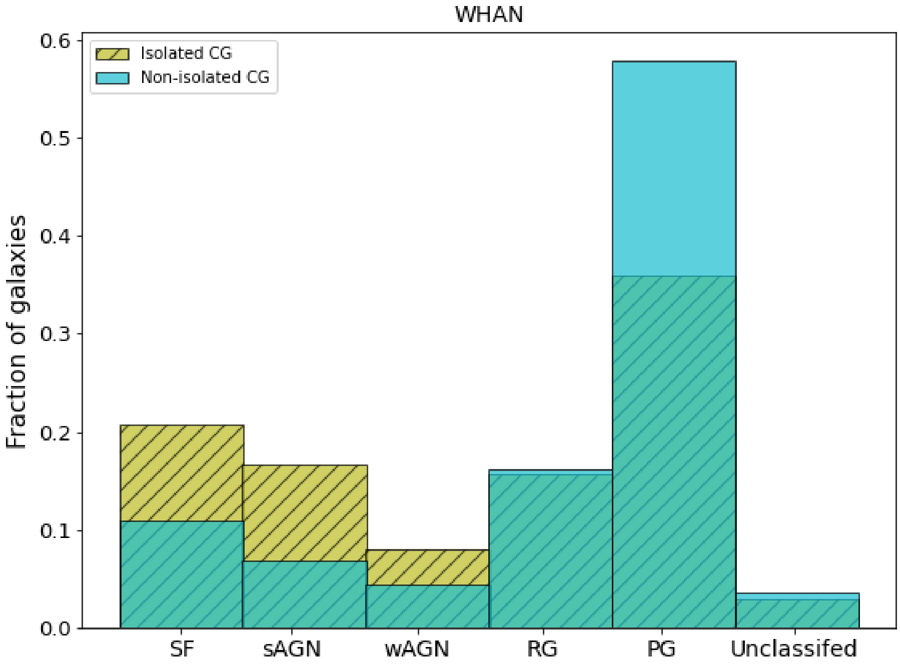

Figure 4.3.5: The fraction of each ionisation type for all galaxies in CGs. In olive, we have the galaxies that are part of isolated CGs, while in cyan, we have the galaxies that are part of non-isolated CGs.

of employing a consistent AGN selection method to ensure a fair comparison across different galaxy samples.

4.4.1 Does the CGs favour AGN?

In general, it is widely discussed that CGs are environments that favour AGN activity. Previous studies (Martinez et al. 2007, 2008, 2010, Bitsakis et al. 2015) have reported a higher fraction of AGN in CGs compared to other environments. However, Shimada et al. (2000) found no differences between the emission-line galaxies between CGs and the field. Also, Sohn et al. (2013a) showed that CGs do not necessarily possess a higher fraction of AGN. In fact, the fraction was lower compared to field galaxies but higher than that of galaxy clusters. They propose that while galaxy-galaxy interactions promote gas flow towards the central region, if the interacting galaxies do not retain sufficient gas, nuclear activity cannot be triggered despite frequent interactions (Park & Hwang 2009, Brown et al. 2023). Previous investigations, considering LLAGN (Coziol et al. 1998), select them based on the $[NII]6584/H_\alpha$ ratio. These galaxies exhibit ambiguous emission lines, potentially misclassified due to ionisation generated from old stars (Stasińska et al. 2008, Cid Fernandes et al. 2011). Despite this ambiguity, they demonstrate the absence of powerful AGN, leading to the conclusion that it is a consequence of gas depletion caused by tidal stripping. It is thus generally agreed that neutral gas depletion in galaxy CGs (Verdes-Montenegro et al. 2001, Jones et al. 2023) affects the accretion rate. It is important to emphasise that Cheng et al. (2023b) found that Stephan's Quintet is not gas-deficient. Instead, this gas is simply located in the outer regions, hidden in the low-density diffuse neutral gas making it impossible to observe in earlier studies. This opens the door to the idea that CGs are not gas-deficient, but rather, their galaxies lose gas through interactions, enriching the intra-group medium.

In our case, we find a lower fraction of AGN in CGs compared to the control sample, which could suggest less available gas to fuel central activity. While we do not have direct gas measurements, this possibility is supported by the lower fraction of star-forming galaxies and the lower sSFR values in our CG sample compared to the control sample (as we show in Chapter 2). Additionally, we observe a higher fraction of RGs and PGs in CGs, which could indicate that galaxies in CGs have less available gas. This higher fraction of RGs may also suggest that CG galaxies have more recently depleted their gas, as RGs tend to exhibit an excess of intermediate-age stellar populations (Herpich et al. 2018). Therefore, it is possible that CGs do not promote a high AGN fraction, potentially due to insufficient gas available to fuel the central region compared to the control sample.

In the study by Sohn et al. (2013a), it was found that the fraction of AGN appears to decrease from field to cluster environment, with CGs falling in between. While the fraction of AGN in LTGs is higher in the field and clusters compared to CGs, the fraction of AGN in ETGs is low in all three environments, with slightly higher fractions in field galaxies. The authors used various classification methods, including the BPT (Baldwin et al. 1981) and WHAN diagrams, to classify the galaxies, with the BPT diagram being the primary method used in the analysis. They associated their results with the lower fraction of AGN in high-density regions, suggesting a lower gas content in CGs compared to field galaxies.

In another study by Bitsakis et al. (2015), the authors examined the fraction of AGN and SF for each morphological type (LTGs and ETGs) as a function of redshift. They had a larger sample of galaxies in CGs compared to ours, allowing for a more significant analysis when dividing galaxies based on morphological type, dynamical state, dominant ionisation mechanism, and redshift bins. Although the objective of their study differs from ours, Bitsakis et al. (2015) examined the evolution of AGN and its relation to the dynamic environment of CGs throughout cosmic time, specifically over the last 3 billion years. Therefore, they characterised the dynamical state of the CGs based on the fraction of ETGs, considering CGs with more than 25% ETGs as dynamically old. They found that the percentage of SFs decreases, while the percentage of AGN increases, with decreasing redshift for both LTGs and ETGs. They also observed that the AGN fraction significantly increases over the past 3 billion years, while the SF fraction decreases. However, they note that their AGN sample may be contaminated by ionisation from post-AGB stars. They also found that the H_α luminosity decreases for AGN at lower redshifts, with median values being lower for ETGs compared to LTGs and for galaxies in dynamically old CGs.

In these two studies that analysed nuclear activity according to morphological type, there is a common factor: gas depletion in galaxies in CGs. This finding aligns with the results obtained in Chapter 2 when analysing the sSFR of this galaxy sample. Regardless of morphological type, we found that the median sSFR was consistently lower in CGs compared to the control sample. In Section 4.3.2, we present the percentages of each ionisation mechanism based on morphological classification. The results are summarised in Table 4.3.2. For ETGs, we observe a lower fraction of SFs and AGN in CGs compared to the control sample. This is consistent with the findings by Sohn et al. (2013a) that these ETGs in CGs likely have a smaller gas reservoir than ETGs in the field. This is further supported by the fact that ETGs in CGs have a higher fraction of RGs and PGs, which are galaxies where star formation has ceased.

In the case of LTGs, we observe that the fraction of AGN, specifically sAGN plus wAGN, is slightly higher in CGs compared to the control sample (see Table 4.3.2). We see a higher fraction of sAGN in CGs compared to the control sample, while the control sample has a higher fraction of wAGN and SFs. For *transition galaxies* in CGs, there is a higher fraction of wAGN and RGs compared to the control sample. On the other hand, in the *other galaxies* category, we have a mixture of galaxies as shown in Chapter 2, which explains the variations between CGs and the control sample.

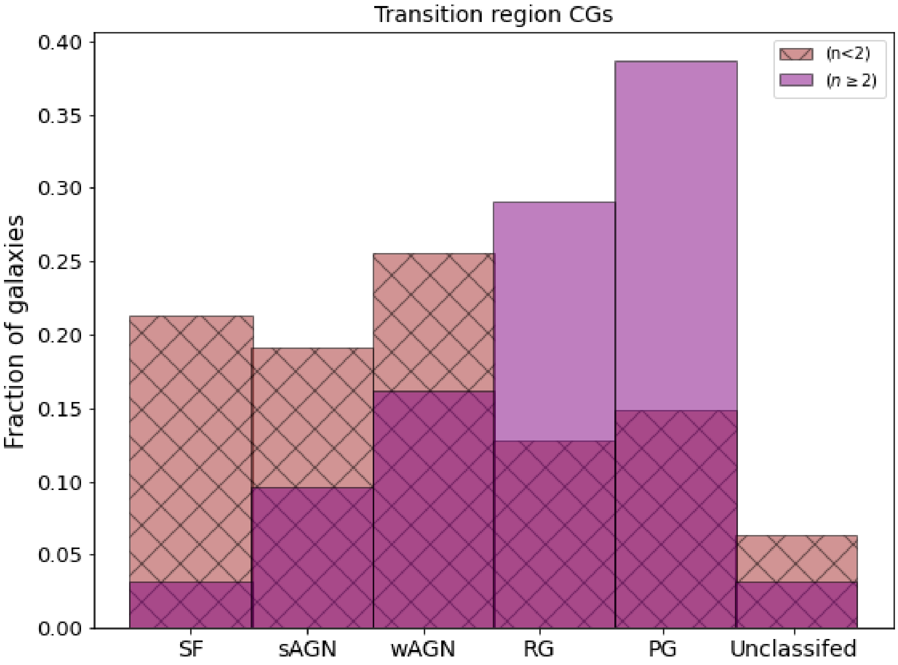

Figure 4.4.1: The fraction of each ionisation type for all transitional galaxies in CGs. In brown, we have the galaxies with a Sérsic index less than two, while in purple, we have the galaxies with a Sérsic index greater than or equal to two.

A scenario where galaxy interactions favour the triggering of AGN due to gas inflow towards the galactic centres may explain the higher fraction of sAGN, as LTG galaxies might not have exhausted all of their gas reservoirs. This scenario could also account for what we observe in *transition galaxies*, where the AGN fraction is slightly higher in CGs compared to the control sample, but in this case, we find a higher fraction of wAGN in CGs. *Transition galaxies* are redder than LTGs, and their specific star formation rate is lower (as shown in Chapter 2), indicating possible smaller gas reservoirs. Therefore, while interactions may favour AGN triggering, the lower gas content could result in a higher fraction of wAGN, consistent with their more compact structure, redder colour, and older stellar populations compared to sAGN.

4.4.2 Transition galaxies

In Chapter 2, we found that *transition galaxies* are more compact, smaller, and have lower sSFR than galaxies in the control sample, suggesting that they are undergoing a physical and morphological transformation. Given this, it is important to analyse the nuclear activity of these types of galaxies. In Figure 4.4.1, we present the different galaxy classifications (based on WHAN) for the *transition galaxies* in CGs. We considered the entire galaxy sample, rather than just the stellar mass sub-sample, as we are dividing the galaxies based on n, since the peculiar galaxies we found in Chapter 2 have n values between 2 and 2.5 for which we divide these galaxies with n values either greater than or equal to 2, or less than 2, and subsequently according to their ionisation mechanism. This ensures that each sub-sample contains at least 20 galaxies, making statistical analysis more robust. After applying a KS test to the stellar mass distribution of both sub-samples, we found a p-value of 0.2, indicating no statistically significant differences in stellar mass distributions, making the two samples comparable. It is important to note that there are relatively few galaxies in this region, with 47 galaxies having

$n \geq 2$ and 31 having $n < 2$. Nevertheless, these results allow us to explore the possible processes these galaxies in CGs may be undergoing, while also contextualising them within the framework proposed in Chapter 3. In Figure 4.4.1, we observe that passive galaxies (PG) and retired galaxies (RG) dominate in galaxies with $n \geq 2$, whereas AGN and star-forming (SF) galaxies are more prominent in galaxies with $n < 2$. Furthermore, in Chapter 2, we identified an anti-correlation in the $n - \log(\mathrm{sSFR})$ plane for all *transition galaxies* in CGs.

These two results lead us to propose a scenario in which nuclear activity could be triggered by gas inflow during galaxy-galaxy interactions (Mihos & Hernquist, 1996; Springel et al., 2005; Di Matteo et al., 2007). In this scenario, galaxies with $n < 2$ might have more cold gas available, as suggested by their higher specific star formation rates compared to galaxies with $n \geq 2$ (see Figure 3.3.1 in Chapter 3). Therefore, galaxies with $n < 2$ could have more cold gas to fuel nuclear activity at their centres. This gas may be gradually consumed or lost, enriching the intra-group medium through various interactions between galaxies. As a result, these galaxies may eventually become unable to sustain nuclear activity, which could speculatively lead to weaker AGN or nuclei lacking any star formation activity, as observed in RG and PG galaxies. At the same time, these galaxies may also become more compact and smaller.

This scenario aligns with the idea that the prevalence of AGN depends on the morphology of the host galaxy at a fixed mass (Sabater et al., 2012). Moreover, Sabater et al. (2013) found that the prevalence of AGN is between 2 to 3 times lower, at fixed mass, in denser environments compared to less dense ones, where Sabater et al. (2013) suggests that stripping or heating of cold gas in these environments may prevent galaxies from sustaining optical AGN activity. In addition, Sabater et al. (2013) found that the prevalence of AGN in galaxies increases by approximately a factor of 2 in galaxies undergoing stronger interactions. The role of galaxy interactions appears to decrease from star-forming nuclei, to Seyferts, to LINERs, and finally to passive galaxies. This is consistent with the evolutionary sequence proposed by other authors, suggesting that interactions can first induce star formation, followed by Seyfert-type AGN, then LINERs, and eventually a passive state (Li et al., 2008; Darg et al., 2010). Therefore, local environment and one-to-one interactions compete in dense environments such as groups and clusters, potentially producing different, or even opposite effects, depending on the nature of the interaction.

4.4.3 Evolutionary scheme

The results obtained so far allow us to propose an evolutionary scheme for CGs outlined in Chapter 3 (see Figure 3.3.1). In this scenario, we suggest three possible stages, determined by the morphological characteristics of their members and their relationship with major structures. In the first stage, CGs likely contain a higher fraction of LTGs and exhibit longer crossing times, indicating an early dynamical evolution and relative isolation. As CGs evolve, gravitational interactions may promote gas loss and morphologically transform their galaxy members, reducing the fraction of LTGs and increasing their compactness. This could also lead to a reduction in the average star formation rates within the CGs, as well as the prevalence of SF nuclei and AGNs, while increasing the fraction of PGs and, to a lesser extent, RGs, which are known to have an excess of intermediate-age (0.1-5 Gyr) stellar populations (Herpich et al. 2018).

In the second stage, CGs might accrete galaxies from their surroundings or be accreted by other groups. This environmental influence would accelerate the transformation process, with the combined effects of galaxy-galaxy interactions and the impact of major structures potentially increasing the peculiar population of *transition galaxies* and reducing the fraction of SF and AGN. There may also be a rise in the fraction of PGs compared to the previous stage.

In the final stage, CGs could undergo disruption within major structures, experiencing a further decline in the fraction of LTGs and star formation, while velocity dispersion increases. This stage suggests that the transformation of galaxies in non-isolated CGs occurs more rapidly, as galaxies interact within the CGs and are also influenced by their surrounding environment.

Part of this scenario is based on the assumption that the gas reservoirs in galaxies within CGs diminish due to various mechanisms affecting them at different stages, such as tidal interactions or ram pressure. However, we do not have direct measurements of gas content for the galaxies in our sample. Instead, this assumption is supported by findings from other studies. For example, the analysis of HI content in Hickson Compact Groups (HCGs) by Verdes-Montenegro et al. (2001) showed significant deficiencies compared to expected values, which were attributed to gas stripping and phase transformation rather than observational limitations. These studies also suggest that HI deficiency increases in HCGs with higher velocity dispersions or with more early-type galaxies, which tend to be more gas-poor. Additionally, Jones et al. (2023), in their study of HI in HCGs, found similar results to Verdes-Montenegro et al. (2001), but also detected cases where gas-poor CGs acquired a new, gas-rich member. They suggest that CGs can accrete gas-rich galaxies from the surroundings, allowing CGs to experience rejuvenation in terms of HI. This opens the door to studying how the environment in which CGs are located plays an important role in the study of HI.

In galaxy groups, Roychowdhury et al. (2022) found a weak correlation between HI mass fraction and group crossing time, suggesting that gas depletion is linked to dynamical evolution. Using data from the ALFALFA and DINGO pilot surveys, they also showed that mean HI fractions tend to decrease as galaxies evolve, especially in groups, where gas reservoirs appear lower compared to isolated galaxies. Furthermore, Morokuma-Matsui et al. (2021) analysed massive Virgo cluster galaxies and indicated that environmental factors, such as ram pressure stripping or strangulation, may play a key role in reducing gas fractions within $3 \times R_{200}$, further supporting the idea that CGs in more advanced stages may experience accelerated gas depletion due to both internal and external processes.

Studies on cold gas in CGs have primarily focused on the HCG sample, emphasising the need for a broader analysis of the CG population. Additionally, it is crucial to investigate how the properties of HI vary based on the environment in which CGs are located. Observations using FAST provide new insights into the distribution of gas in CGs with greater precision. In fact, Cheng et al. (2023b) demonstrate that while the galaxies in Stephan's Quintet are HI deficient, the CG itself is not. Instead, the gas appears to be hidden in low-density diffuse neutral gas, possibly stripped from galaxies due to tidal interactions.

4.5 Summary and conclusions

In this study, we analyse the ionisation mechanisms of 1005 galaxies belonging to Compact Groups (CGs) and 2183 galaxies associated to a control sample, which mainly are field galaxies, and where both samples are located in the Stripe 82 region. Our objective is to investigate whether the environment of CGs promotes nuclear activity compared to the field galaxies and how this nuclear activity is affected by the environment in which the CGs are located. The morphology of this galaxy sample was studied in Chapter 2, where galaxies were categorized into early-type (ETG), late-type (LTG), *transition galaxies*, and *other galaxies* based on Sérsic index and color. Furthermore, we characterised the environments of CGs in Chapter 3, and found that at least 27% of the CGs are not isolated, they are part of major structures. In this Chapter, we explore ionisation mechanisms using the classification method proposed by Cid Fernandes et al. (2010), utilising the WHAN diagram. We classify galaxies as pure star-forming (SF), strong AGN (sAGN), weak AGN (wAGN), retired galaxies (RG), and passive galaxies (PG). The key findings we obtained are:

- The AGN percentage, i.e., the combined wAGN and sAGN, within CGs is 18.3 ± 1.8%. In the control sample, this percentage is 26.6 ± 1.5%. Therefore according to this classification, CGs do not exhibit a high percentage of AGN galaxies compared to the control sample.
- Our analysis reveals distinct ionisation patterns linked to galaxy morphology in CGs compared to the control sample. ETGs in CGs exhibit low SF and AGN fractions compare to the control sample, likely due to limited gas. In contrast, LTGs in CGs exhibit slightly higher AGN fractions, especially sAGN compared to their counterpart in the control sample, possibly due to ongoing interactions that may contribute to fueling AGN activity. *Transition galaxies* in CGs also show a high AGN fraction, primarily wAGN, potentially due to limited gas. Frequent interactions in CGs may favor AGN triggering, particularly when gas reservoirs persist. Overall, CGs tend to have lower AGN fractions compared to control sample galaxies due to a higher proportion of ETGs with depleted gas.
- AGN have lower values of D_{4000}, therefore younger populations and higher compactness than RGs and PGs. They are more compact and redder than SF galaxies. Significant environmental differences exist between sAGN, RGs, and PGs. sAGN in CGs are more compact than in control sample galaxies. RGs and PGS in CGs have slightly older populations compared to its counterpart in the control sample.
- The fraction of AGN and SF decreases as velocity dispersion increases, in contrast to RGs that slightly increase and then decline. Meanwhile, PGs increase with higher velocity dispersions. These results align with the results that we presented in Chapter 3, indicating less dynamically evolved CGs with more LTGs have higher nuclear activity, i.e. SF galaxies plus AGN. CGs evolved to CGs with lower AGN and SF fractions, while the fractions of PGs increase.
- Our analysis of ionisation mechanisms in CGs reveals that the environment significantly impacts the prevalence of different ionisation mechanisms. Isolated CGs harbour higher fractions of SF and AGN galaxies, while non-isolated CGs show an increase in PG. This underscores the role of interactions in depleting available gas and driving central activity.

These results enable us to be consistent with the evolutionary scheme proposed in Chapter 3, where galaxies evolve more rapidly in massive structures. This dynamic scenario promotes physical and morphological transformations within CG galaxies, thereby accelerating processes observed in isolated CGs. Furthermore, this environment leads to reduced nuclear activity probably due to a depletion of the gas reservoirs in the galaxies. Consequently, the more dynamically evolved CGs embedded in major structures exhibit a higher proportion of ETGs, a higher velocity dispersion, and a reduced fraction of SF and AGN, while featuring a high fraction of PG. This significant outcome resonates with the scenario proposed by Coziol et al. (2004), though our study includes a wider range of CGs and a higher percentage of CGs with details about their surroundings. The observed dependence of these properties on the CG environment underscores the fundamental role played by the environment in which CGs are embedded in the evolution of galaxies.

Chapter 5

Tracing Stellar Populations and Gas Content in Compact Group Galaxies: A 3D Comparative Study

In this chapter, we carried out a comprehensive analysis of 459 galaxies within compact groups (CGs) and 1098 field galaxies, which we used as a control sample, to investigate the impact of galaxy interactions in CGs on various physical properties, particularly focusing on ionised gas using IFS data. Galaxies were classified using $(u-r)$ colour and Sérsic index in the r-band, and star-forming spaxels were identified through the BPT diagram.

The 4000 angstrom break (D_{4000}) profile analysis indicates that more massive galaxies generally exhibit higher D_{4000} values, indicative of older stellar populations. Furthermore, galaxies in denser environments, such as CGs, tend to have slightly higher D_{4000} values at fixed stellar mass compared to those in less dense environments. This observation suggests that the stellar populations in CGs might be older. For galaxies with Star Formation Rate Surface Density (Σ_{SFR}) profiles along 0-1.5R_e, we find that lower stellar mass bin galaxies in control samples have steeper Σ_{SFR} gradients, while higher stellar mass bin galaxies in CGs show steeper gradients; however, the profiles are within the error bars. For galaxies that are not star-forming in the central regions but are in the outer regions, those that are part of CGs exhibit higher Σ_{SFR} values with less steep slopes. Regarding oxygen abundance, galaxies generally have higher metallicity in their centres. There are no significant differences in median gradients between CGs and the control sample, although low-mass galaxies in CGs have slightly higher metallicity in their outer regions.

This chapter is structured as follows: Section 5.1 details the data used and the criteria for selecting the CGs and our control field sample. In Section 5.2, we present the methodology for how we select spaxels where the main ionisation mechanism is from young stars to create the radial profile. In Sections 5.3 and 5.4 we present and discuss our results, and we summarise our work in section 5.5.

5.1 Data

In this section, we describe a new selection of CGs of galaxies and a control sample of field galaxies, different than the samples used in previous chapters, that we analyse using Mapping Nearby Galaxies at APO (MaNGA) IFU data (Bundy et al. 2015). This new selection of galaxies is due to the fact that in our original sample of 340 CGs in the Stripe 82 region, in the southern hemisphere, with 1092 galaxies, only 35 galaxies have MaNGA observations. Since the purpose is to statistically study the profiles of the properties of galaxies in this environment, we decided to expand the sample and consider the CGs from the Zheng & Shen (2020) catalogue in the northern hemisphere that coincided with the MaNGA footprint. We will complement our analysis with available catalogues for the galaxies in MaNGA, such as the NASA-Sloan Atlas (NSA) catalogue to obtain morphological parameters and stellar mass. Additionally, we will use the Dynamics and Stellar Population (DynPop) catalogue (Zhu et al. 2023a) to obtain kinematic parameters for the galaxies.

5.1.1 MaNGA data

MaNGA is a significant part of the fourth-generation SDSS-IV (Blanton et al. 2017). This integral-field spectroscopic survey uses 17 Integral Field Units (IFUs), each consisting of 19 to 127 fibres arranged in hexagonal bundles (Drory et al. 2015), and the BOSS spectrographs (Smee et al. 2013) on the 2.5 m Sloan Telescope (Gunn et al. 2006). MaNGA covers a wavelength range of 3600–10000$\AA$ with a spectral resolution of 72 km/s and the spatial resolution is a function of the observational seeing, with a median of 2.54 arcsec FWHM. The MaNGA survey has three main subsamples; the Primary sample (47% of the survey), the Secondary sample (37% of the survey), and the Colour-Enhanced sample (16% of the survey). The Primary sample consists of the galaxies that are covered out to 1.5 R_e while the Secondary sample consists of the galaxies that are covered out to 2.5 R_e. The Colour-Enhanced sample is designed to target rare galaxies such as high-luminosity blue galaxies and low-luminosity red small galaxies. The Colour-Enhanced sample is covered out to 1.5 R_e and can be combined with the Primary sample to make the Primary+ sample.

Our analysis is focused on MaNGA data from data release 17 (DR17; Law et al. 2021), utilising Voronoi binning (Cappellari & Copin 2003) to ensure a minimum signal-to-noise ratio (S/N) of 10 in the g-band for accurate measurements within each spatial bin. The DR17 contains 11273 MaNGA data cubes and we use the data analysis pipeline (DAP) to process the data cubes from the DRP, producing maps of stellar and gas properties for MaNGA galaxies (Westfall et al. 2019a). Stellar kinematics are derived using the penalised pixel-fitting (pPXF) method (Cappellari & Emsellem 2004) with MILES stellar templates (Sánchez-Blázquez et al. 2006, Falcón-Barroso et al. 2011). Gaseous kinematics are fitted simultaneously with pPXF using constructed emission line templates.

5.1.2 CGs sample

To identify CGs galaxies in the MaNGA project, we use the Zheng & Shen (2020) catalogue, which covers a larger region of the sky as it is based on SDSS data. As mentioned in Chapter 2, this catalogue uses data from SDSS-DR14, LAMOST spectra, and the GAMA survey. These authors selected CGs by combining two methods: (i) the Hickson (1982) photometric criterion and (ii) the spectroscopic technique, which involves the difference in radial velocities between the group and each individual galaxy. Each galaxy in a group must satisfy the following criteria: (i) richness and magnitude; $3 \leq N(14.00 \leq r \leq 17.77) \leq 10$, (ii) isolation; $\theta_N \leq 3\theta_G$, (iii) compactness; $\mu_r \leq 26.0$ $mag\ arcsec^{-2}$, and (iv) velocity difference; $|V - V_i| \leq 1000 km/s$ (see Chapter 2).

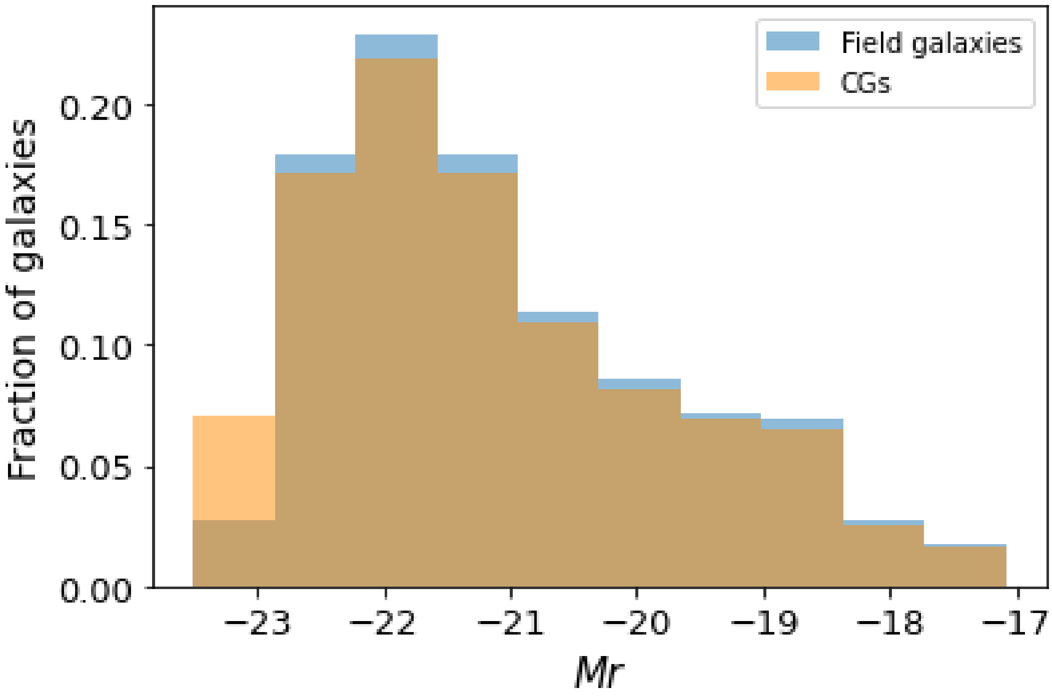

Figure 5.1.1: Distribution of the absolute magnitude in *r*-band of the galaxies we analysed using MaNGA data, with the CG sample in orange and the control sample in blue.

To select the galaxies that are part of CGs, we performed a cross-match between the positions (right ascension and declination) of the galaxies within DR17 and those in the CGs identified by Zheng & Shen (2020). We considered all galaxies in the Zheng & Shen (2020) catalogue to select a large sample of galaxies with IFU data. After the cross-match, we found that 549 galaxies in CGs have data available in MaNGA. These galaxies span a redshift range of $0.01 \leq z \leq 0.14$.

5.1.3 Control Sample

To determine the influence of the environment on the properties of CG galaxies, in the same manner as in Chapter 2, we have defined a sample of galaxies located in less dense environments, namely field galaxies, to use as our control sample. This selection process mirrors the one used in Chapter 2, but the control sample was chosen to follow a similar distribution in absolute magnitude in the r-band and redshift limits as the sample of galaxies in CGs, selected for the spectroscopically resolved analysis.

The field galaxies are selected from the catalogue published by Yang et al. (2007) as those labelled as single-member groups (i.e., a halo of an individual galaxy). We cross-matched the field sample with the MaNGA DR17 catalogue, obtaining a sample of 1933 galaxies. From this sample, we randomly selected a subsample of 1098 galaxies using a Monte Carlo algorithm, which corresponds to twice the number of galaxies in the CGs. Ensuring they follow the same distribution in absolute magnitude in the r-band and lie within the same redshift range.

In Figure 5.1.1, we show the distribution of absolute magnitudes in the r-band, with the distribution for CGs shown in orange and the control sample galaxies in blue. Comparing these distributions with the KS-test allows us to discern if these two distributions do not follow the same distribution. We find that the p-value is 0.1, thus, statistically, these distributions follow the same distribution.

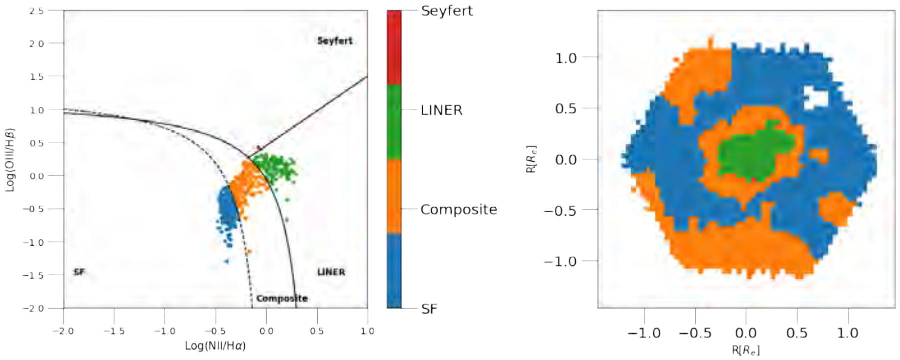

Figure 5.2.1: Left panel: Diagnostic ionisation mechanism diagram, showing the line ratios $[OIII]\lambda5007/H_\beta$ versus $[NII]\lambda6584/H_\alpha$ for the Voronoi-binned regions of a CG galaxy. The dashed line separates the star-forming region (Kauffmann et al. 2003b), and the solid curve indicates the division between star-forming galaxies and AGNs (Kewley et al. 2001). AGNs are further classified into LINERs and Seyferts using the straight solid line (Schawinski et al. 2007). The composite region, located between the dashed and solid lines, includes galaxies with both star formation and AGN activity. Right panel: 2D spatial map showing the classification of the Voronoi-binned regions, where the colours represent the ionisation mechanism: blue for SF spaxels, orange for composite regions, green for LINERs, and red for Seyferts. The x- and y-axes of the 2D map are given in terms of the galaxy's effective radius.

5.2 Metodology

5.2.1 2D Map of Ionisation Mechanisms

Using the MaNGA DAP data products, we classify the spaxels as star-forming, AGN, or spaxels without emission lines. We start by using the Voronoi-binned maps, which ensure a continuum $S/N > 10$. Then, we apply a signal-to-noise cut on the emission lines to ensure that the regions with Voronoi binning have emission lines with $S/N > 5$ in the following lines: $[NII]$, H_α, H_β, and $[OIII]$. From these emission lines, we classify the ionisation mechanism in each spaxel using the diagnostic ionisation mechanism diagram proposed by Baldwin et al. (1981), Kewley et al. (2001), Kauffmann et al. (2003a) to determine which spaxels are star-forming and/or AGN. In Figure 5.2.1 we show an example of this methodology, in the left panel we present the line ratios $[OIII]\lambda5007/H_\beta$ versus $[NII]\lambda6584/H_\alpha$ for the different Voronoi regions of a CG galaxy, using the classification proposed by Kauffmann et al. (2003b) to separate galaxies in the starforming region (dashed line), and the Kewley et al. (2001) classification for galaxies in the transition region between starforming and AGNs (solid curve line). In the AGN region, we classify into LINERs and Seyferts using the classification proposed by Schawinski et al. (2007) (solid straight line). The region between the limits proposed by Kewley et al. (2001) and Schawinski et al. (2007) (delimited by dashed and solid lines) is called the composite region. In the right panel of Figure 5.2.1, we show the 2D map of the classification of the regions with Voronoi binning, where the colours represent each type: blue for star-forming spaxels (SF), orange for spaxles in the composite region, green for spaxels classified as LINER, and red for Seyfert.

Using the analysis shown in Figure 5.2.1 for the whole sample, we select all regions dominated by photoionisation to estimate the star formation rate and metallicity in the galaxies. For this analysis we consider galaxies that display star-forming spaxels at least in a 20% of their surface.

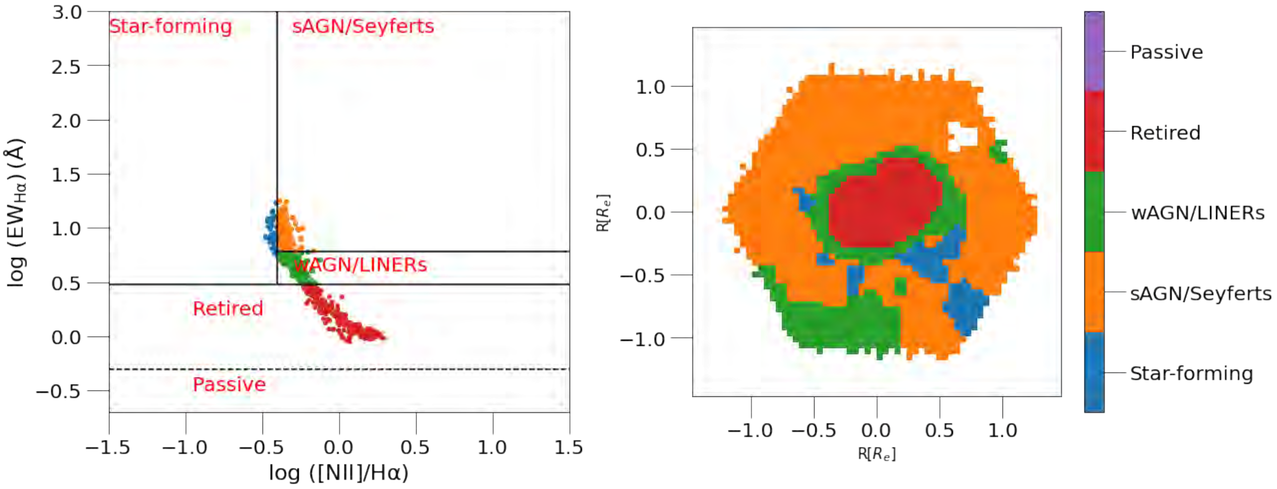

Figure 5.2.2: Example of ionisation mechanisms for the same galaxy in a CG shown in Fig. 5.2.1, using the WHAN diagram. Left panel: we present the WHAN diagram, where each colour represents a different ionisation mechanism: blue for star-forming spaxels, orange for strong AGN, green for weak AGN, red for retired galaxies, and purple for passive galaxies. Right panel: we present the 2D spatial distribution of each spaxel, with the colours corresponding to the ionisation mechanisms from the left panel. The x- and y-axes of the 2D map are given in terms of the galaxy's effective radius.

Additionally, we also classify the spaxels using the diagram proposed by Cid Fernandes et al. (2010), 2011, which, as shown in Chapter 4, is a classification system for ionisation mechanisms that includes five types: SF are characterised by $log([NII]/H_\alpha) < -0.4$ and $EW(H_\alpha) > 6Å$; sAGN are characterised by $log([NII]/H_\alpha) > -0.4$ and $EW(H_\alpha) > 3Å$; wAGN are characterised by $log([NII]/H_\alpha) > -0.4$ and $3 < EW(H_\alpha) < 6Å$; RG are characterised by $EW(H_\alpha) < 3Å$; and PG, which are emission-line-free, are characterised by $EW(H_\alpha) < 0.5Å$. This is with the purpose of comparing the ionisation mechanisms of the central region of galaxies that exhibit star formation in the outermost parts, as is the case for the galaxy shown in the example in Figure 5.2.1. In Figure 5.2.2, for the same galaxy presented in Figure 5.2.1, the left panel displays the WHAN diagram, which shows the logarithm of the equivalent width of H_α as a function of the logarithm of the $[NII]/H_\alpha$ ratio. The horizontal and vertical lines represent the boundaries for each ionisation mechanism. Each colour indicates a type: blue for star-forming spaxels, orange for sAGN, green for wAGN, red for RG, and purple for PG. In the right panel of this figure, we show the 2D map of this classification, where the colours represent each type of ionisation mechanism.

5.2.1.1 Ionisation mechanism according to SDSS data

In Chapter 4, we presented an analysis of the ionisation mechanisms in CGs based on SDSS fibre data wheareas in this Chapter we are using MaNGA data. Therefore, it is essential to ensure consistency between both analyses. To address this, we performed a crossmatch between the SDSS/fibre and SDSS/MaNGA data. We utilised the WHAN diagnostic diagram to compare our analysis, as conducted in Chapter 4. Figure 5.2.3 shows the histogram for each ionisation mechanism type, based on emission lines from the fibre data, for each CG and control sample galaxies analysed in this chapter. As in Chapter 4, we also considered passive galaxies to be those without emission lines, based on a visual inspection in the spectrum from the fibre. Our findings indicate that this CG and control sample galaxies are consistent with the results of Chapter 4, where we observed a higher fraction of PGs and

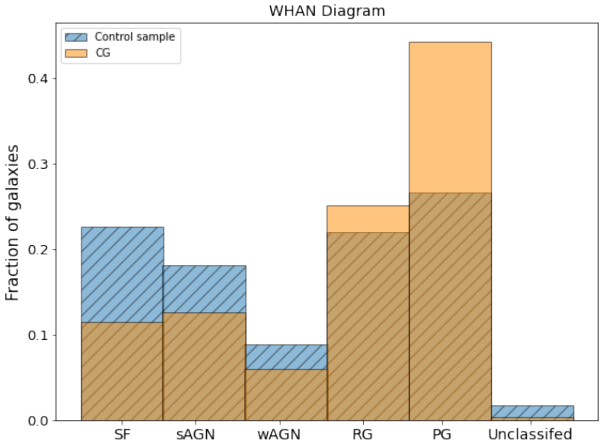

Figure 5.2.3: Histogram comparing the ionisation mechanism types for each galaxy sample analysed in this chapter, using emission line data from SDSS fibres.

RGs in CGs, while the control sample contains a greater fraction of SF galaxies and AGN.

5.2.2 Star Formation from 2D maps

We will analyse the star formation surface density (Σ_{SFR}) instead of the sSFR, because the spaxels of galaxies at different redshifts probe different physical areas. Therefore, it is necessary to normalise the SFR by the physical area. To estimate the star formation, we use the H_α flux, following the relation defined by Kennicutt (1998). We use the angular size of the MaNGA spaxels (0.5 arcsec) and the redshift of the galaxy to estimate the spaxel size in kpc, so the area within the spaxel is the spaxel size in kpc squared. Then, to estimate the area, we use the area maps generated by MaNGA DAP for the Voronoi bins. These maps contain the area bin in spaxels square, which we multiply by the area within each spaxel to determine the physical area of each bin (in kpc^2) for each galaxy. Thus, the Σ_{SFR} is calculated as:

$$\Sigma_{SFR} = 5.5 \times 10^{-42} L_{H_\alpha} \times A_{bin} \tag{5.2.1}$$

where L_{H_α} is the H_α luminosity, which we correct for dust extinction based on the nebular colour excess using the reddening curve of Calzetti (2001). To estimate the nebular colour excess, we assume an intrinsic Balmer decrement $(H_\alpha/H_\beta)_{int} = 2.86$ assuming a $T_e = 10000$ K and an electron density of $n_e = 100$ cm^{-3} (Osterbrock 1989).

5.2.3 Oxygen Abundance

Metallicity is a critical factor in galaxy evolution, shaping processes such as gas cooling, star formation, and dust production. A well-established correlation exists between gas metallicity and stellar mass, with more massive galaxies exhibiting higher gas metallicity (e.g. Lequeux et al. 1979, Tremonti et al. 2004). The spatial distribution of gas metallicity, particularly radial gradients, plays a vital role in understanding galaxy formation. Metallicity gradients not only unveil the origins of scaling relations but also provide insight into how different regions within galaxies evolve. Negative metallicity gradients, lower metallicity at larger radii, have been commonly observed in ionised gas in star-forming galaxies (e.g Zaritsky et al. 1994). Therefore, we explore gas metallicity maps, focusing on photoionised regions where we measure gas-phase metallicities using ratios of strong nebular emission lines. Specifically, we apply the N2 calibrator and the relation proposed by Pérez-Montero & Contini (2009) to obtain the oxygen abundance:

$$12 + \log(O/H) = 8.90 + 0.57 \times \log(N2) \tag{5.2.2}$$

where N2 is the ratio between the $[NII]/H_{\alpha}$ lines. We only consider spaxels with $S/N > 5$ in both emission lines. The scatter in metallicity using this calibrator is 0.34 dex.

5.2.4 Radial Profiles

From the 2D maps, we obtain the metallicity profiles, star formation surface density for star-forming spaxels, and the D_{4000} break for all galaxies in the sample. In order to obtain these profiles, we construct elliptical apertures over the map of the desired quantity, centred at the centre of the galaxy, and set the ellipticity and position angle of these apertures to be the same as those of the galaxy. We take these values from the NSA catalogue. We generate 5 apertures to obtain 4 elliptical rings where we measure the average value of each parameter in each ring. These rings cover up to 1.5 R_e of each galaxy, and the size of each ring is 0.3 R_e. In Figure 5.2.4, we present an example of a galaxy in CGs. In the top panel, on the left, we present the 2D map of the star formation surface density, and on the right, the radial profile, where the y-axis values represent the average within each ring. The error bars indicate the standard deviation within each ring. The middle panel is similar to the top panel but shows the oxygen abundance, and in the bottom panels we present the D_{4000} index for the same galaxy.

5.2.5 Determination of the environment in which the CGs are located

As shown by Zheng & Shen (2021), the CGs from their catalogue are located in different environments according to the catalogue by Yang et al. (2007). In order to define where these systems reside, we follow a similar methodology to Zheng & Shen (2021), as we did in Chapter 3. We select all the galaxies included in the catalogue by Yang et al. (2007) and perform a cross-match between the right ascension and declination positions of the galaxies in our sample of CGs. From this cross-match, we identify the IDs of the groups included in Yang et al. (2007) that had at least one galaxy that, according to our catalogue, is a galaxy in a CG. Using these group IDs, we select all the galaxies that belong to the groups found by Yang et al. (2007) associating these groups and galaxies with the CGs. We find that of the 479 CGs, 427 of them have at least one galaxy in one of the structures identified by Yang et al. (2007).
In these 427 CGs, we identify the three cases observed in Chapter 3: CGs that, according to Yang et al., have the same number of galaxies in both catalogues. According to Zheng & Shen (2021), these are the isolated CGs, of which there are 88 within our sample, representing $\sim 21\%$ of the sample. In Figure 5.2.5 (top left panel) we show an example of an isolated CG, where the galaxies are identified in green as part of the group with $ID = 14044$, according to Yang et al. (2007). Filled circles represent the galaxies that are identified as a CG, in this case, the CG-0781, with the red circles representing the MaNGA data and the yellow circles indicating galaxies without MaNGA data. 276 CGs, representing 65% of our sample, are located in larger structures (groups and clusters); these are referred to as non-isolated CGs. The right panel of Figure 5.2.5 presents an example of a non-isolated CGs that is embedded in a group with $ID = 4$ identified by Yang et al. (2007) that contains 332 galaxies. The remaining 14% of the galaxies belong to CGs that, according to the catalogue by Yang et al. (2007), are associated with different groups. The lower panel of Figure 5.2.5 illustrates this with the example of group CG-0518, which contains four galaxies. According to Yang et al. (2007), two of these

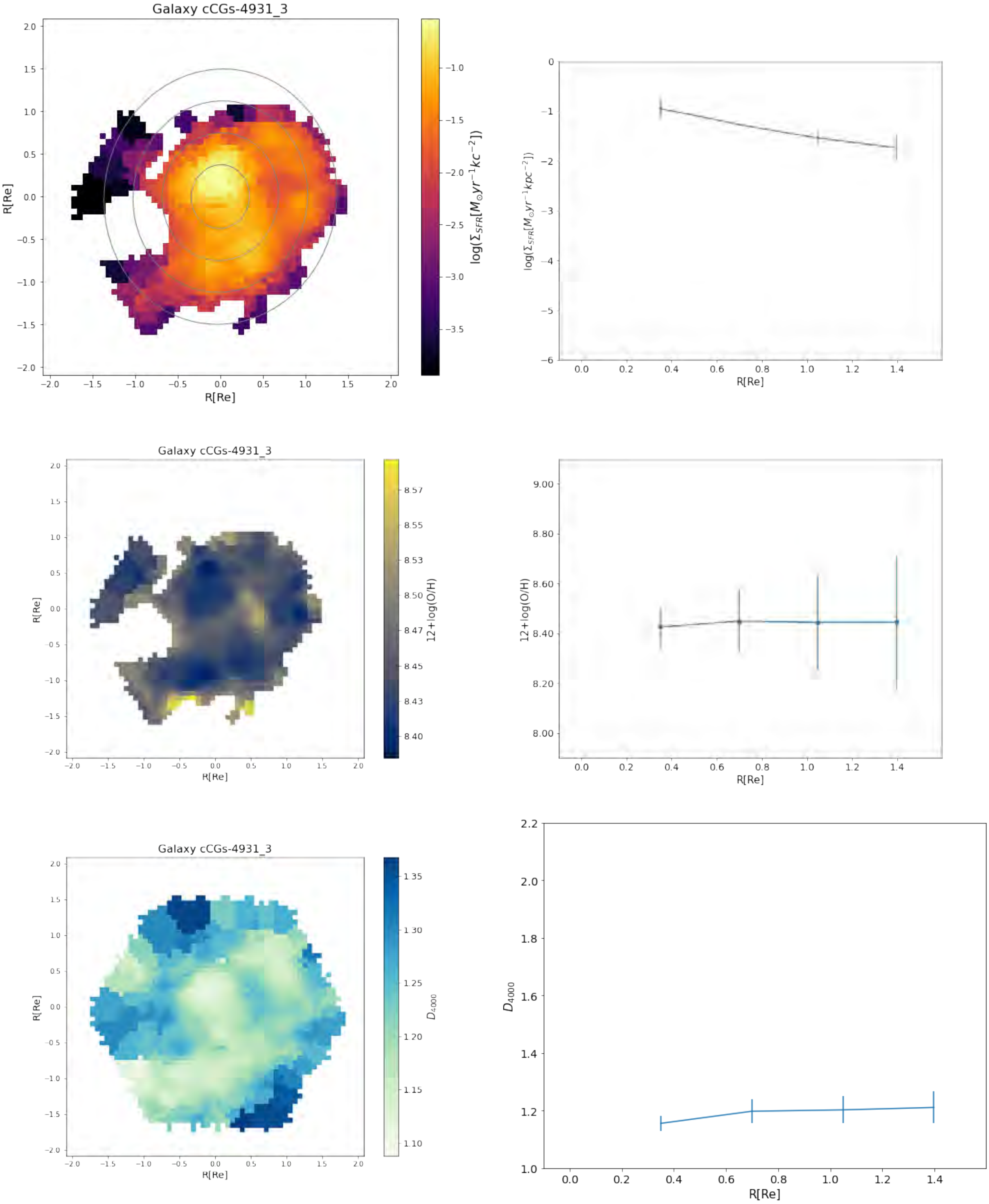

Figure 5.2.4: Example of the radial profile for a galaxy in a CG. The left panels show the 2D map, while the right panels display the radial profiles, where the y-axis values represent the median value within each ring. The error bars indicate the standard deviation within each ring. The top panels present the star formation surface density, the middle panels show the oxygen abundance, and the bottom panels display the D_{4000} index.

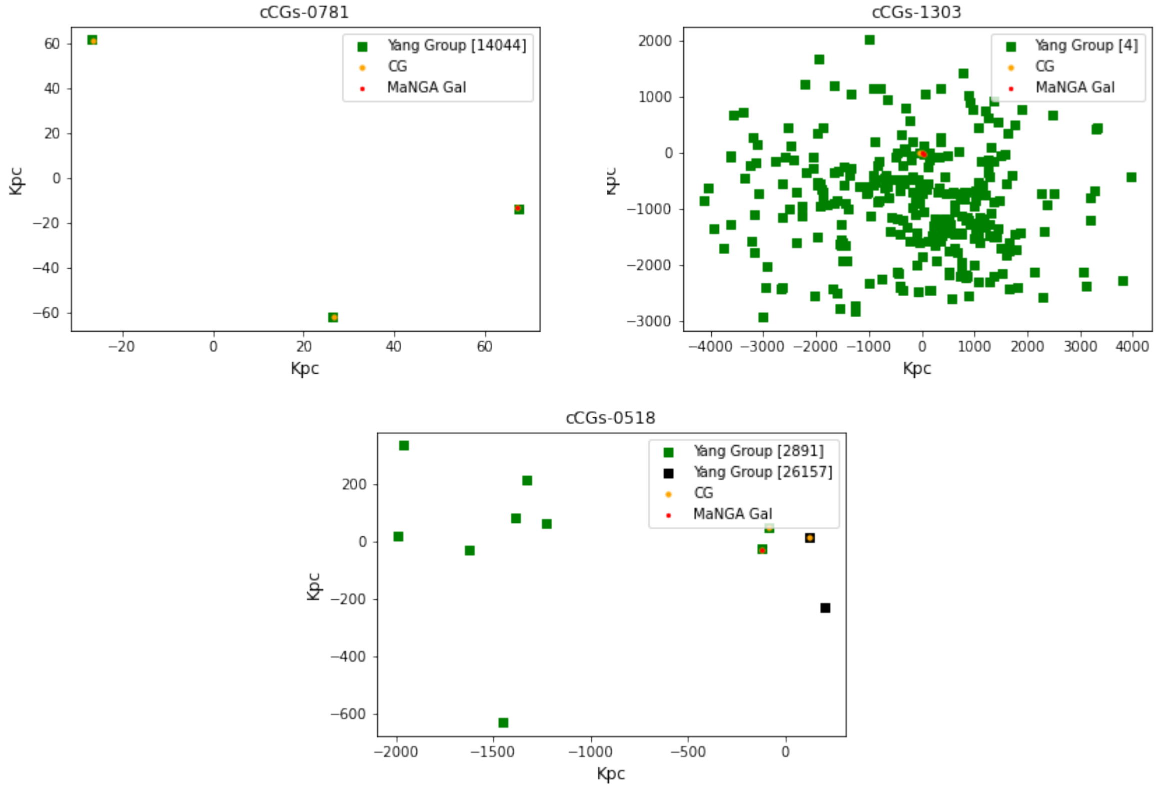

Figure 5.2.5: Examples of galaxies in isolated and non-isolated CGs. The top left panel shows an example of an isolated CG, with galaxies identified by Yang et al. in green. Filled circles represent galaxies in the CGs with the ID cCGs-0781 in the catalogue of Zheng & Shen (2020), with yellow circles indicating galaxies without MaNGA data and the red circle representing the galaxy with MaNGA data. The right panel presents an example of a non-isolated CG embedded in group 4 with 332 galaxies. The bottom panel shows a CG belonging to different groups according to Yang et al. (2007), with CG-0518 having four galaxies, two of which belong to group 2891 and the other two to group 26157.

galaxies belong to a group with ID 2891, which consists of nine galaxies (green squares), while the other two form a pair classified as a group with ID 26157 (black squares). As mentioned in Chapter 3, this difference is likely due to the velocity selection criteria applied by Zheng & Shen (2021), which potentially overestimates the number of CG members.

5.2.6 Morphology classification

In order to compare the physical properties of galaxies in different environments and with different morphologies based on MaNGA data, we applied the same methodology described in Chapter 2. Specifically, we classified our galaxy sample into early-type, late-type, and *transition galaxies* using the classification approach outlined in Chapter 2. This classification scheme is based on the Sérsic index in the r-band and the $(u-r)$ colour, both corrected for k-correction, as proposed by Vika et al. (2015b). Figure 5.2.6 shows the $(u-r)$ versus n_r plot, along with the density profile of the galaxies. The horizontal line at $(u-r) = 2.3$ and the vertical line at a Sérsic index $n_r = 2.5$ define four quadrants: LTGs in the lower-left, *transition galaxies* in the upper-left, ETGs in the upper-right, and *other galaxies* in the lower-right quadrant.

In Figure 5.2.7, we show the fraction of each morphological type in each environment. In the upper

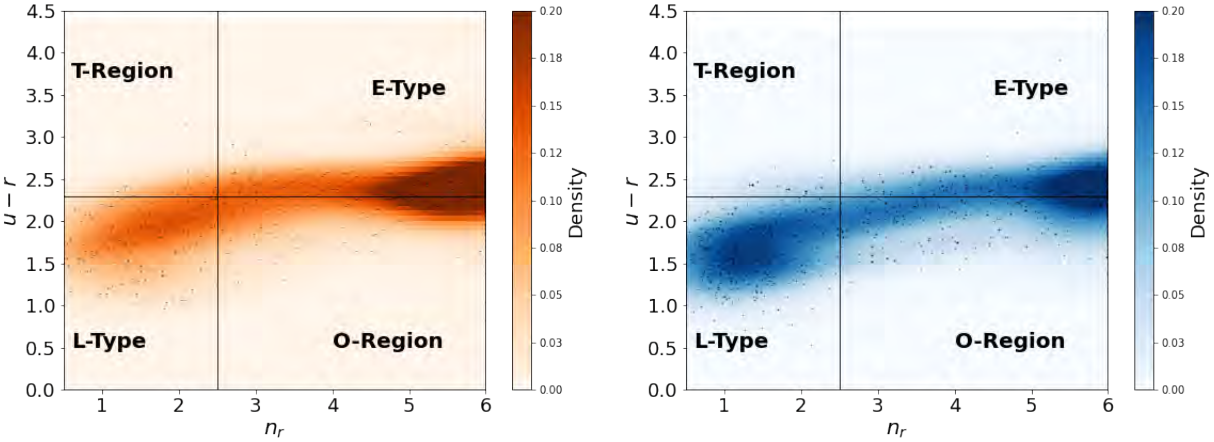

Figure 5.2.6: ETGs, *transition galaxies*, and LTGs classification, using $(u-r)$ colour and Sérsic index in the r-band (n_r) for the sample having MaNGA data. The vertical line is for $n_r = 2.5$ and the horizontal for $(u-r) = 2.3$. The left panel shows the galaxies in the CGs in orange. The right panel shows the galaxies in the control sample in blue.

panel, the orange histogram represents the galaxies in CGs, while the blue represents galaxies from the control sample. We can observe that there is a higher fraction of ETGs in CGs, while in the control sample, there is a higher fraction of LTGs and *other galaxies*. In the lower panel of Figure 5.2.7, we show the fraction of each morphological type for isolated CGs (purple bars) and non-isolated CGs (green bars). According to these histograms, we find that in isolated CGs, there is a higher fraction of LTGs and a lower fraction of ETGs compared to non-isolated CGs. These results agree with what we found in Chapter 3.

5.3 Results

5.3.1 Radial Profiles of D_{4000}

We use the 4000$\mathring{A}$ break (D_{4000}) strength as a spectral indicator of the mean age of the stellar population. This is determined by the ratio of the average flux densities in the narrow continuum bands $3850-3950\mathring{A}$ and $4000-4100\mathring{A}$ (Balogh et al., 1999). D_{4000} maps were obtained using the Marvin package (Cherinka et al., 2019), which were measured in the MaNGA data-analysis pipeline (MaNGA DAP) (Westfall et al. 2019b, Belfiore et al. 2019). From these maps, we obtained profiles as a function of radius.

In the figure 5.3.1, we present the median profile for D_{4000}. To obtain this profile, we calculated the values of all galaxies in each spaxel and measured the median of those values in each ring. The error bars represent the standard deviation. We considered two mass bins: the low-mass bin includes all galaxies with $log(M[M_{\odot}]) < 10.5$ (top left panel), and the high-mass bin includes all galaxies with $log(M[M_{\odot}]) > 10.5$ (top right panel). We show the median profile for galaxies in CGs in orange, with the number of galaxies indicated in the label, and in blue for galaxies from the control sample. Additionally, we performed a linear fit to each profile to determine the slope, in dashed-grey for galaxies in CGs and in dashed-black for the control sample. It can be observed that the profiles have a negative slope, indicating that there is an older population as we approach the centre of the galaxies. It is important to note that regardless of the mass bin considered, the slope is flatter in galaxies in

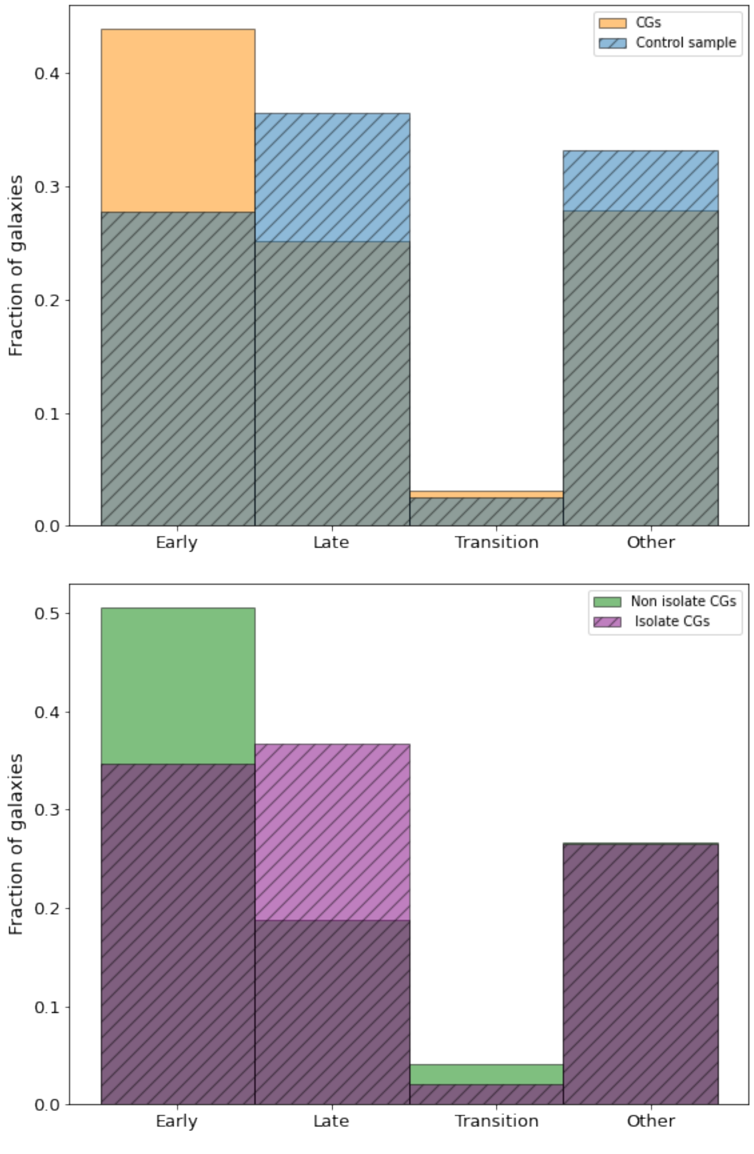

Figure 5.2.7: Fraction of galaxies in each morphology population: ETGs, LTGs, *transition galaxies*, and *other galaxies*. In the upper panel, the orange bars represent the fraction for CG galaxies and the blue bars for the control sample galaxies. In the lower panel, we show isolated CGs in purple and non-isolated CGs in green.

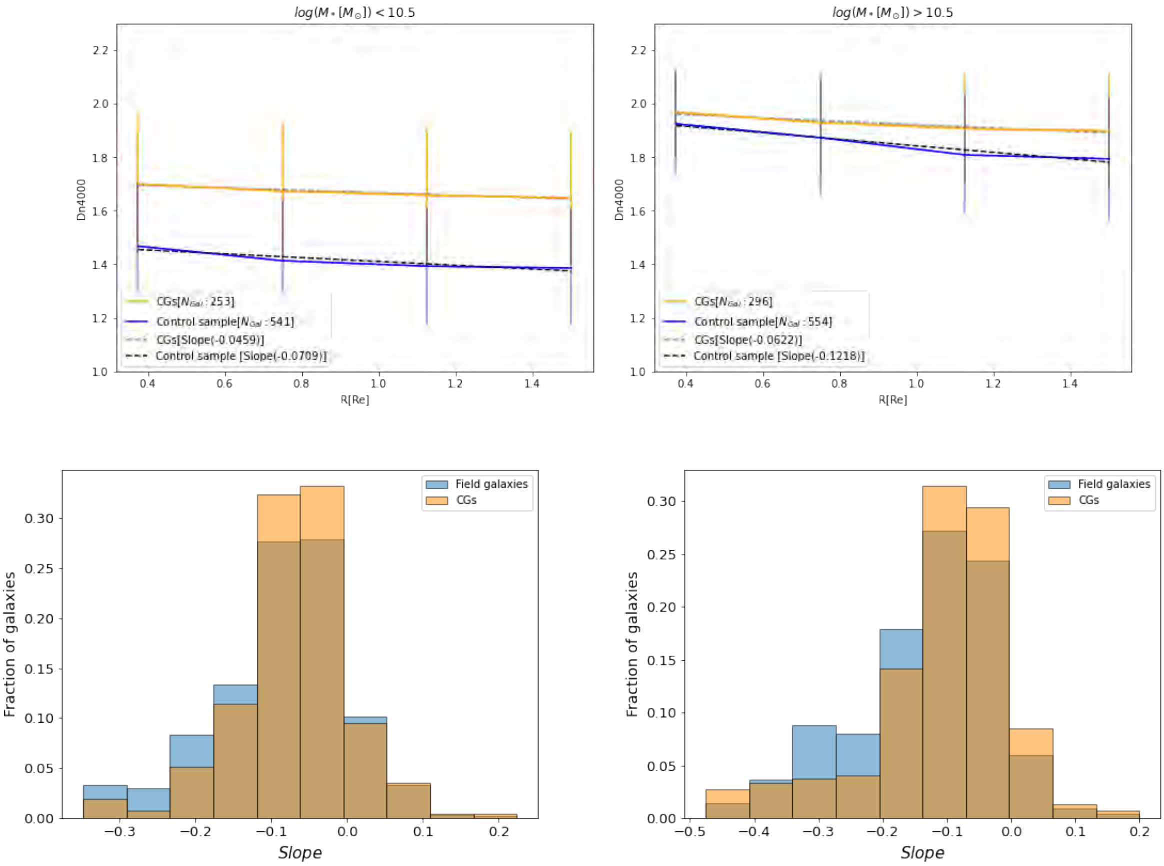

Figure 5.3.1: Median profiles and slope distributions for D_{4000} in CG and control sample galaxies, split into low and high stellar mass bins. Top panels: Median D_{4000} profiles for galaxies with $log(M[M_\odot]) < 10.5$ (left) and $log(M[M_\odot]) > 10.5$ (right). The orange lines represent galaxies in CGs, while the blue lines represent the control sample. Error bars indicate the standard deviation, and linear fits to the profiles are shown in grey (CGs) and black (control sample). Bottom panels: Distributions of the of D_{4000} profiles slopes for each galaxy, for the low-mass bin and the high-mass bin in the left and right panel, respectively.

CGs compared to the control sample. In the low-mass bin, we see that galaxies in CGs have a higher D_{4000} at all radii compared to galaxies in the control sample, suggesting that there is an older stellar population in CGs than in the control sample for less massive galaxies. For the more massive galaxies, the difference between the medians decreased, but the slope of galaxies in the control sample is much steeper than that of the CG galaxies, which may indicate that the distribution of stellar populations is more homogeneous in galaxies in CGs.

On the other hand, we explore the distribution of the slopes of each D_{4000} profile for each galaxy. In the lower panels in Figure 5.3.1, we present the distribution for each stellar mass bin. In the plot on the bottom left, we present the slopes for galaxies with stellar masses of $log(M[M_\odot]) < 10.5$. In this case, both distributions, for galaxies in CGs and the control sample, have a median of -0.4. But when comparing the distributions with a Kolmogorov-Smirnov (KS) test (An 1933, Smirnov 1948), we obtain a p-value of 0.03. Therefore, both distributions are statistically different. In fact, it can be observed that in the bins of negative slopes, there is a larger fraction of galaxies in the control sample, while in the CGs, there is a larger fraction between slopes from -0.1 to 0. So we have galaxies with flatter profiles, which coincides with the result of the median profile. In the case of massive galaxies, the distribution of slopes is shown in the bottom right panel of Figure 5.3.1. For galaxies in CGs, the median value for this distribution is -0.05, and for control sample galaxies, it is -0.08. When we compare the two distributions using the KS-test, the p-value is 2×10^{-4}. Therefore, there are also statistical differences in the distribution, suggesting that massive galaxies ($log(M[M_{\odot}]) > 10.5$) in CGs have more homogeneous stellar populations compared to galaxies in the control sample.

In Figure 5.2.7 we showed that in CGs there is a higher fraction of ETGs in comparison with the control sample. This may be the reason of the difference we see in D_{4000} between the CGs and the control sample.

Due to the correlation between the morphology of galaxies and their underlying stellar populations, ETGs are formed by relatively old stars, while LTGs are composed of relatively young stars (Blanton & Moustakas 2009 see reference in this paper.). To account for this Figure 5.3.2 shows the median profile for each galaxy sample, dividing them by mass range but also by each morphological type. The left column is for galaxies with $log(M[M_{\odot}]) < 10.5$ and the right column is for galaxies with $log(M[M_{\odot}]) > 10.5$. From top to bottom, we present the different morphological types: ETGs, *transition galaxies*, LTGs, and *other galaxies*, respectively.

For the ETGs, we observe that the profiles between environments are consistent within the uncertainties across both stellar mass bins. For *transition galaxies*, we find that, in the low-mass bin, the profiles in both environments are consistent within the uncertainties. However, high-mass *transition galaxies* in CGs exhibit higher D_{4000} values at all radii compared to the control sample, suggesting these galaxies have older stellar populations. Nevertheless, there are only four galaxies in this mass range within CGs. Overall, the limited number of *transition galaxies* in our sample makes the results for this type of galaxy less conclusive.

For the LTGs, we find that in CGs, they generally reach slightly higher D_{4000} values, and in both stellar mass bins, the slope is greater in CGs compared to the control sample, although these differences are more significant in the high-mass bin. Lastly, for the *other galaxies*, we observe a similar behaviour, but in this case, the difference in mean D_{4000} values between CGs and the control sample is larger.

An important aspect to consider is that the stellar mass ranges are broad, which could influence the slight differences observed between environments in the D_{4000} profiles. For this reason, we compared the stellar mass distributions within each range and for each type using the KS-test. The hypothesis that the stellar mass in both environments follows the same distribution is rejected for *transition galaxies* in the most massive bin, with a p-value of 0.03; however, there are too few *transition galaxies* for the result to be reliable. For ETGs, the p-values were 0.01 and 3×10^{-5} for the massive and low-mass bins, respectively, with the median stellar mass being higher in CGs. For *other galaxies* in the most massive bin, the p-value was 0.01 when comparing stellar masses between both environments. Therefore, only the LTGs and *other galaxies* with low stellar mass in both CGs and the control sample exhibit similar distributions, making them comparable. As a result, the observed differences in LTGs across both mass ranges, and in *other galaxies* within the low-mass bin, might be shaped by the CG environment.

5.3.1.1 D_{4000} profiles in isolated and non-isolated CGs

As we showed in Chapter 3, the properties of galaxies in CGs are affected by the environment in which the CG is located. To assess whether the age of the CG galaxies are also affected by the environment, in Figure 5.3.3, we present the D_{4000} profiles for the different environments in which the CGs are found. Galaxies in isolated CGs are shown in purple, while those in non-isolated CGs are shown in green. Additionally, we compare the distribution in each stellar mass range to statistically determine if both environments follow a similar stellar mass distribution using the ks-test. In this case, for the two

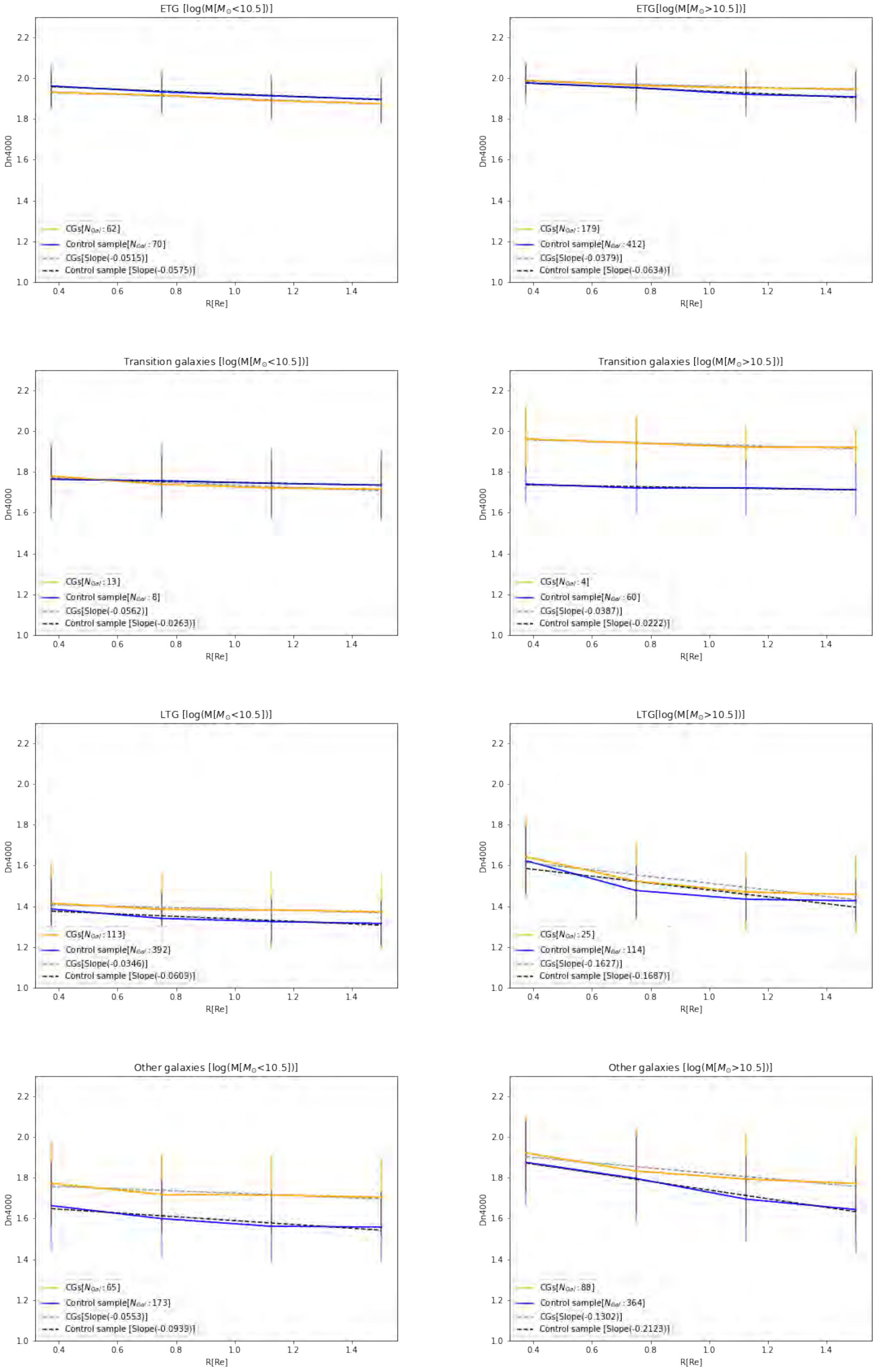

Figure 5.3.2: Median D_{4000} profiles for galaxies in CGs and the control sample, separated by morphological type and stellar mass. The left column shows galaxies with $log(M[M_\odot]) < 10.5$ and the right column shows galaxies with $log(M[M_\odot]) > 10.5$. From top to bottom, the rows represent Early-Type Galaxies (ETGs), *transition galaxies*, Late-Type Galaxies (LTGs), and *other galaxies*. The median profiles are plotted separately for CG galaxies (orange) and control sample galaxies (blue), with error bars indicating the standard deviation.

stellar mass bins across the different morphological types, the p-value was always greater than 0.05. Thus, the stellar mass distributions are similar in both environments for the different morphological types. An exception is the *transition galaxies* in the most massive bin, where there are no galaxies in isolated CGs; therefore, this bin is not considered in this analysis. In general, we observe that D_{4000} reach higher values in non-isolated CGs at all radii, except for LTGs in the most massive stellar mass bin, where in the outer regions of the profile, galaxies in isolated CGs achieve higher values. Another exception is in the *other galaxies* sample in the less massive bin, where both environments have similar values, but the D_{4000} value is slightly higher in the outer regions for isolated CGs. For ETGs and LTGs, the slopes are slightly steeper for galaxies in non-isolated CGs. For transition and *other galaxies*, the slope is slightly steeper for galaxies in isolated CGs.

We observe a difference according to the environment, as galaxies in non-isolated CGs have higher D_{4000} values at all radii compared to galaxies in isolated CGs, indicating they have an older stellar population. Additionally, the D_{4000} profile is flatter for galaxies in non-isolated CGs.

5.3.2 Star Formation and Oxygen Abundance Profiles in Galaxies

To estimate the star formation rate and oxygen abundance, we considered only the spaxels ionised by photoionisation due to young stars, i.e., those classified as star-forming according to the BPT diagram. Additionally, we included only galaxies where at least 20% of the spaxels are star-forming. Therefore, we observe two cases: the first involves galaxies with star-forming spaxels across all radii, as shown in Figure 5.2.4. The second case involves galaxies that only have star-forming spaxels in the outer regions, while the central regions exhibit nuclear activity. Figure 5.2.1 is a clear example of this case, where the central region is classified as LINER or composite according to the BPT diagnostic diagram, whereas the outer region is ionised by young stars. Throughout the text, we refer to the first case as star-forming galaxies, and the second as galaxies with nuclear activity. For a proper analysis, we chose to separate the sample based on the stellar mass of the galaxies and whether they are classified as star-forming galaxies or galaxies with nuclear activity.

In Figure 5.3.4, we present the profile of the Σ_{SFR} as a function of the effective radius. In the top plots, we show the median profile for star forming galaxies. On the left, we have low-mass galaxies, and on the right, we have high-mass galaxies. In the bottom plots, we present in the same manner the galaxies with nuclear activity. The solid lines with error bars represent the median profiles measured for each galaxy sample: orange for galaxies in CGs and blue for the control sample. The error bars indicate the standard deviation for all galaxies. Additionally, we show the best linear fit for each profile, with grey for galaxies in CGs and black for the control sample galaxies. The slopes and intercepts for each fit are presented in Table 5.3.1. For low-mass star forming galaxies, we observe that there is not much difference between the profiles of the galaxies in CGs and those in the control sample (see top left panel of Figure 5.3.4). The only distinction is that in the case of CGs, the slope is less steep in comparison with the control sample, but both environments exhibit higher stellar formation in the central region. For massive star forming galaxies in CGs, we observe a knee-like behaviour, whereas in the control sample, the Σ_{SFR} decreases monotonically with increasing radius. Thus, the slope in CGs is slightly steeper compared to the control sample, although they are consistent within the uncertainties.

For low-mass galaxies with nuclear activity, the profile of galaxies in CGs has a positive slope, indicating higher star formation in the outermost part. However, it is essential to note that there are only four galaxies in this category. Instead for massive galaxies with nuclear activity, we see differences between galaxies in CGs and the control sample, with higher Σ_{SFR} at all radii in the outer part of galaxies in CGs. Additionally, differences in the slope are observed, with a more pronounced slope

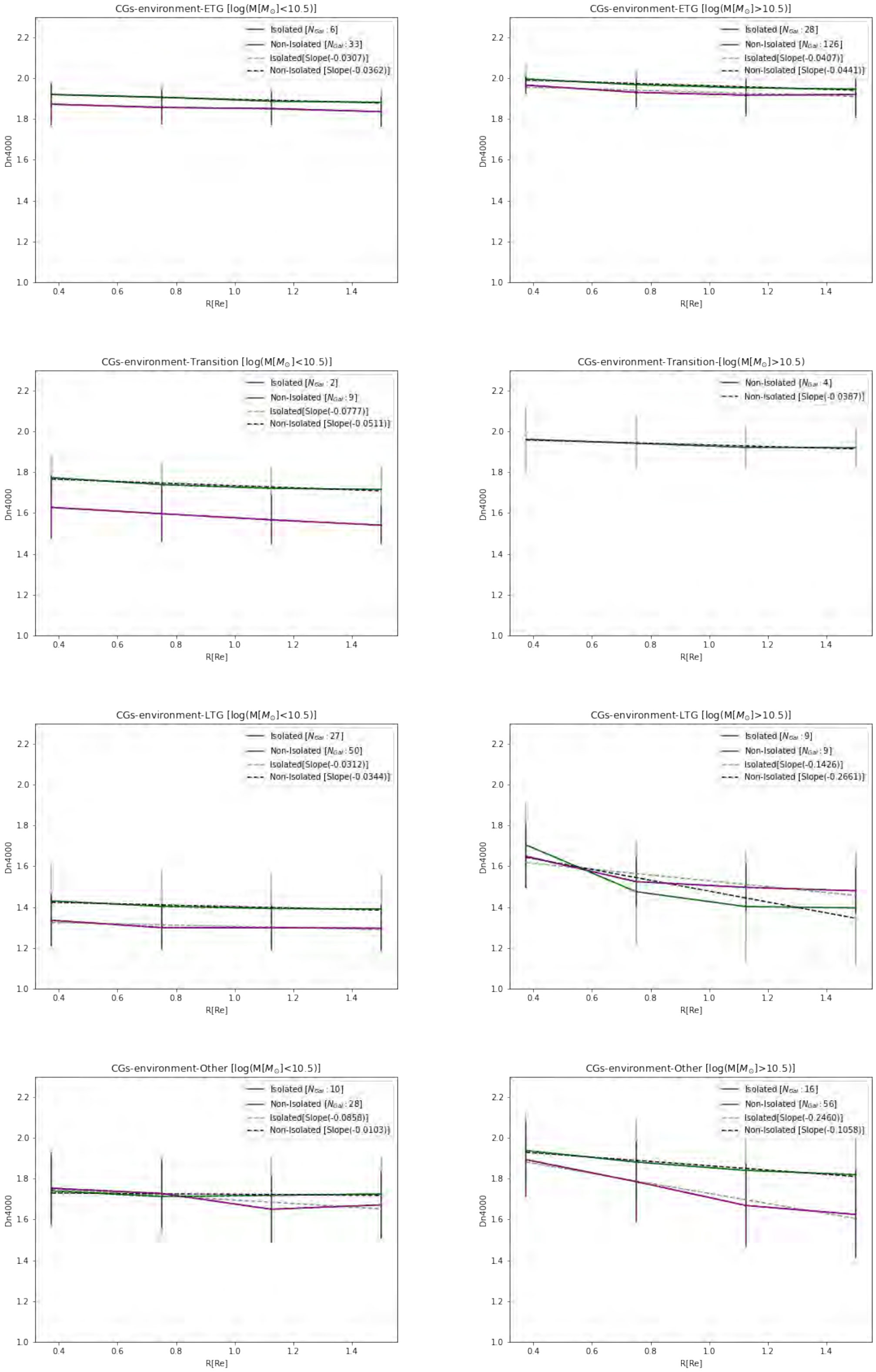

Figure 5.3.3: Median D_{4000} profiles for galaxies in CGs by environment and morphological type. Isolated CGs are shown in purple, and non-isolated CGs in green. The left and right columns represent galaxies with $log(M[M_\odot]) < 10.5$ and $log(M[M_\odot]) > 10.5$, respectively. Rows indicate Early-Type Galaxies (ETGs), *transition galaxies*, Late-Type Galaxies (LTGs), and others.

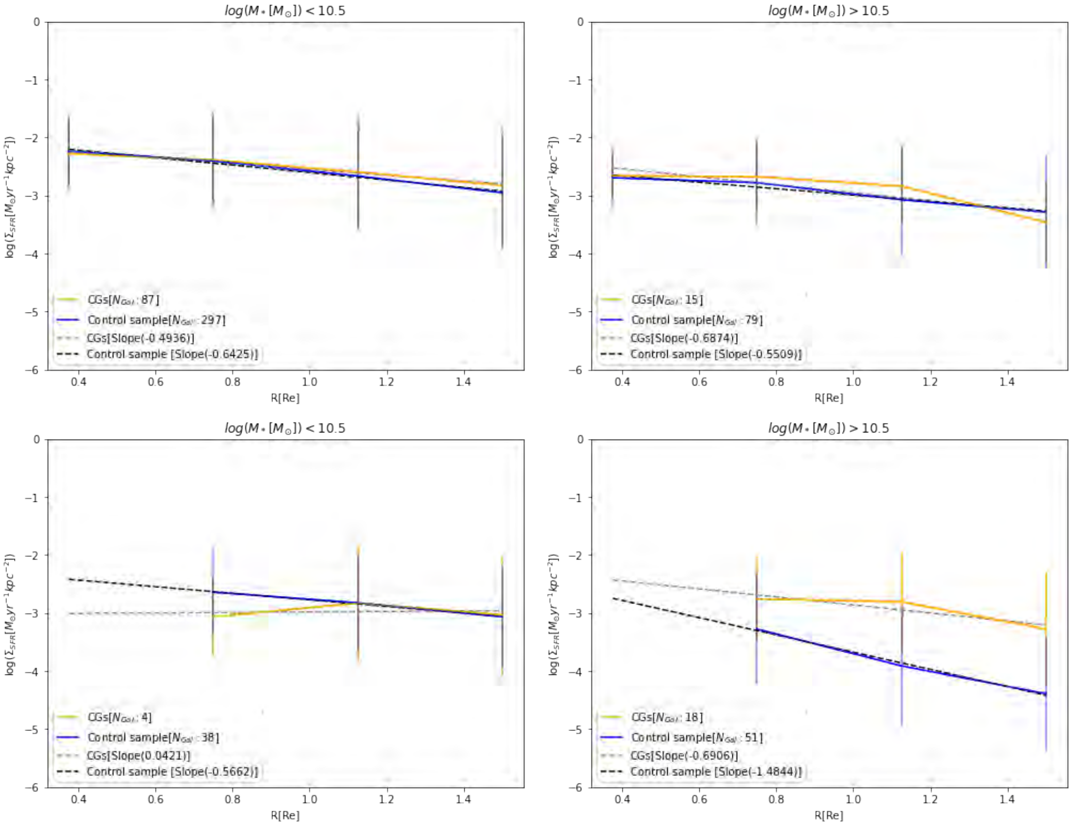

Figure 5.3.4: Profiles of Σ_{SFR} as a function of the effective radius for galaxies with and without complete profiles. The top panels show the median profiles for galaxies with a complete profile: on the left, for low-mass galaxies, and on the right, for high-mass galaxies. The bottom panels show the same for galaxies with an incomplete profile. Solid lines with error bars represent the median profiles for each galaxy sample: orange for galaxies in CGs and blue for the control sample. Error bars indicate the standard deviation. The best linear fits are shown with grey for CGs and black for the control sample.

	Full profile								**Outer profile**							
	$log(\Sigma_{SFR}[M_\odot yr^{-1} kpc^{-2}])$				$12 + log(O/H)$				$log(\Sigma_{SFR}[M_\odot yr^{-1} kpc^{-2}])$				$12 + log(O/H)$			
	$log(M_\odot) < 10.5$		$log(M_\odot) > 10.5$		$log(M_\odot) < 10.5$		$log(M_\odot) > 10.5$		$log(M_\odot) < 10.5$		$log(M_\odot) > 10.5$		$log(M_\odot) < 10.5$		$log(M_\odot) > 10.5$	
Environment	Slope	Intercept	Slope	Intercept	Slope	Intercept	Slope	Intercept	Slope	Intercept	Slope	Intercept	Slope	Intercept	Slope	Intercept
CGs (all)	-0.49	-2.06	-0.69	-2.26	-0.013	8.65	-0.007	8.68	0.042	-3.02	-0.69	-2.17	-0.022	8.71	-0.011	8.70
Control sample	-0.64	-1.96	-0.55	-2.44	-0.025	8.65	-0.012	8.68	-0.57	-2.21	-1.48	-2.19	-0.006	8.69	-0.007	8.69

Table 5.3.1: Linear fits to the profiles of $\log(\Sigma_{SFR})$ and $12 + \log(O/H)$ for each environment and mass range, separating star-forming galaxies based on whether their profiles are complete or incomplete

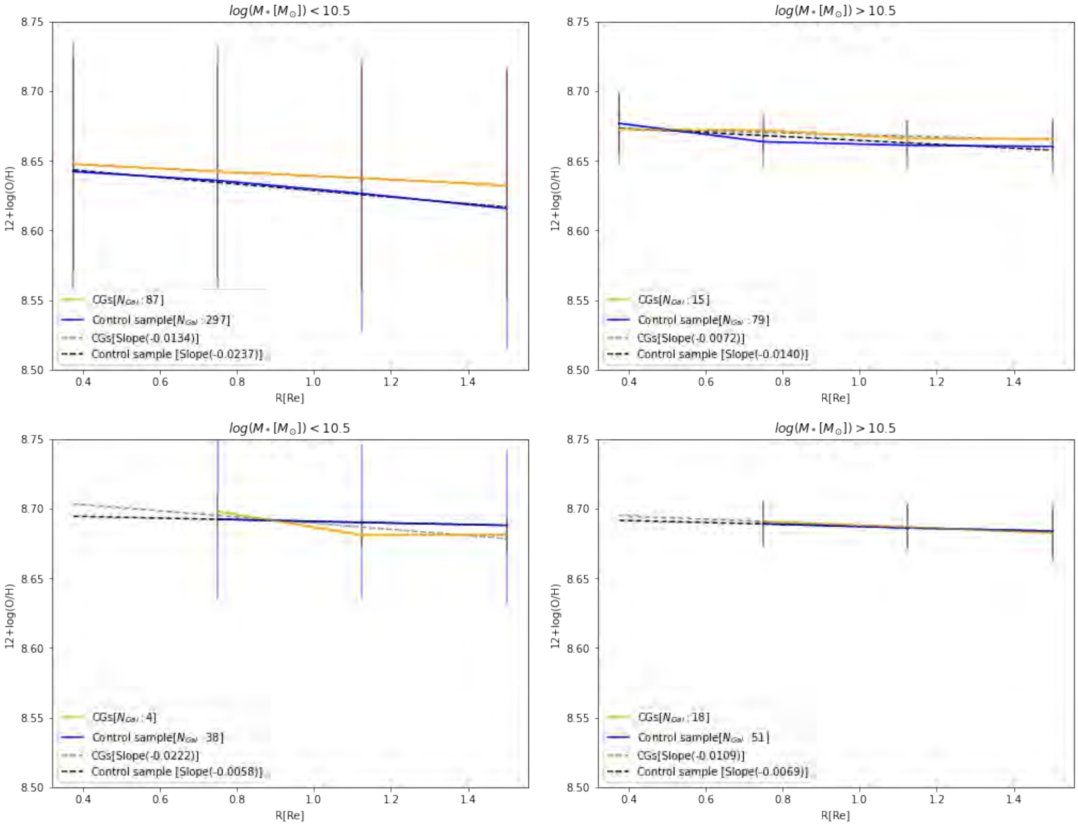

Figure 5.3.5: Profiles of oxygen abundance ($12+\log(O/H)$) as a function of the effective radius for galaxies in different environments and mass bins.

in the control sample.

On the other hand, we also analyse the oxygen abundance profile of these galaxies. In Figure 5.3.5, we present the same figure as Figure 5.3.4, but with $12+\log(O/H)$ on the y-axis. However, unlike the star formation surface density profiles, we do not observe significant differences in the median oxygen abundance profiles between the two environments, regardless of the stellar mass bin or whether they are star-forming galaxies or have nuclear activity. In most cases, the slope of these profiles is slightly negative, indicating that the oxygen abundance decreases from the centre to the outer regions. For lower mass galaxies, we find that those in CGs are slightly more metal-rich than those in the control sample, especially in the outer regions. However, this difference is within the standard deviation of the measured values for both environments. When analysing the two mass bins, we observe that, particularly for star forming galaxies, the more massive galaxies achieve higher oxygen abundance values compared to the lower mass bin in both environments. This is consistent with the known mass–metallicity relation (e.g., Goddard et al. 2017).

5.3.2.1 Comparing properties of galaxies with nuclear activity and star forming galaxies

As shown in the previous section, the biggest differences are found in Σ_{SFR} for galaxies with nuclear activity. It is worth exploring the differences of these galaxies compared to star forming galaxies. It is also possible to explore the different properties such as morphology, colour, stellar mass, and the velocity dispersions of these galaxies. In Figure 5.3.6, these different properties are shown. In the first row, we show the Sérsic index, in the second row, the colour $(u-r)$, the third row, the

	$log(\Sigma_{SFR}[M_{\odot}yr^{-1}kpc^{-2}])$		$12+log(O/H)$	
Environments	Slope	Intercept	Slope	Intercept
Isolate CGs	-0.83	-1.90	-0.005	8.65
Non isolated CGs	-0.60	-2.07	0.006	8.65

Table 5.3.2: Intercept and slope of the best linear fit to the profiles of Σ_{SFR} and oxygen abundance of the galaxies in CGs, dividing them according to whether the galaxies are in isolated CGs or not.

morphological type, the fourth row, the stellar mass, and in the last row, the velocity dispersion measured within one R_e. In the left column, we compare star forming galaxies with galaxies with nuclear activity in CGs. The middle column presents the same comparison but for galaxies in the control sample. The right column presents galaxies that have only the galaxies with nuclear activity, in orange for galaxies in CGs and in blue for the control sample. In this case, we consider galaxies with $9.5 < \log(M_*[M_{\odot}]) < 11$, as this is the mass range where galaxies with nuclear activity are found in CGs. In contrast, the control sample spans a broader mass range. To avoid introducing any bias related to stellar mass, we selected this specific range.
Comparing each environment separately, by examining star forming galaxies versus those with nuclear activity we observe that, in general, galaxies with nuclear activity exhibit a high Sérsic index, are redder, have a higher fraction of *other galaxies* morphological type, are more massive, and have a lower velocity dispersion than their star forming galaxies counterparts. Now, comparing galaxies with nuclear activity in CGs vs. the control sample, we see that the main differences are that CG galaxies have a higher fraction of *other galaxies*, and a lower median $\sigma = 86.2^{95.6}_{80.2}$ km/s compared to galaxies in the control sample with a median $\sigma = 102.4^{110.6}_{96.2}$ km/s.
According to the BPT diagnostic diagram, galaxies with nuclear activity are classified as Seyfert or LINER. However, as mentioned in Chapter 4, there is a debate about whether LINER galaxies are primarily ionised by an AGN or by photoionisation from hot low-mass evolved stars (HOLMES) (Stasińska et al. 2008, Cid Fernandes et al. 2011). To differentiate these cases, we compare the ionisation mechanism maps of the central region based on the BPT and WHAN diagnostic diagrams. According to the 2D maps of the ionisation mechanisms, there are two scenarios for the photoionisation in the central regions of these galaxies. The first scenario involves galaxies classified as Seyfert or LINER according to the BPT diagram, which are also identified as sAGN/wAGN according to the WHAN diagram. The second scenario involves galaxies that are classified as LINER in the BPT diagram, but as retired galaxies according to the WHAN diagram, indicating that the dominant ionisation mechanism is old stars. For CGs, 59% of these galaxies have an AGN in the central region, while the remaining 41% are associated with retired galaxies. In contrast, for galaxies in the control sample, 29% have an AGN, and 71% are retired galaxies, suggesting that galaxies in the control sample are quenching from the inside out.

5.3.2.2 Comparison of Star Formation and Oxygen Abundance in Isolated and Non-Isolated Compact Group

In the left panel of Figure 5.3.7, we present the Σ_{SFR} for the different environments in which the CGs are located, in the same manner as Figure 5.3.3. In Table 5.3.2, we present the slope and intercept that best fit each environment. In this case, there are not significant differences in the profiles, but galaxies in non-isolated CGs exhibit a slightly flatter profile compared to galaxies in isolated CGs. Regarding the oxygen abundance profile (see the right panel in Figure 5.3.7), there are also no significant

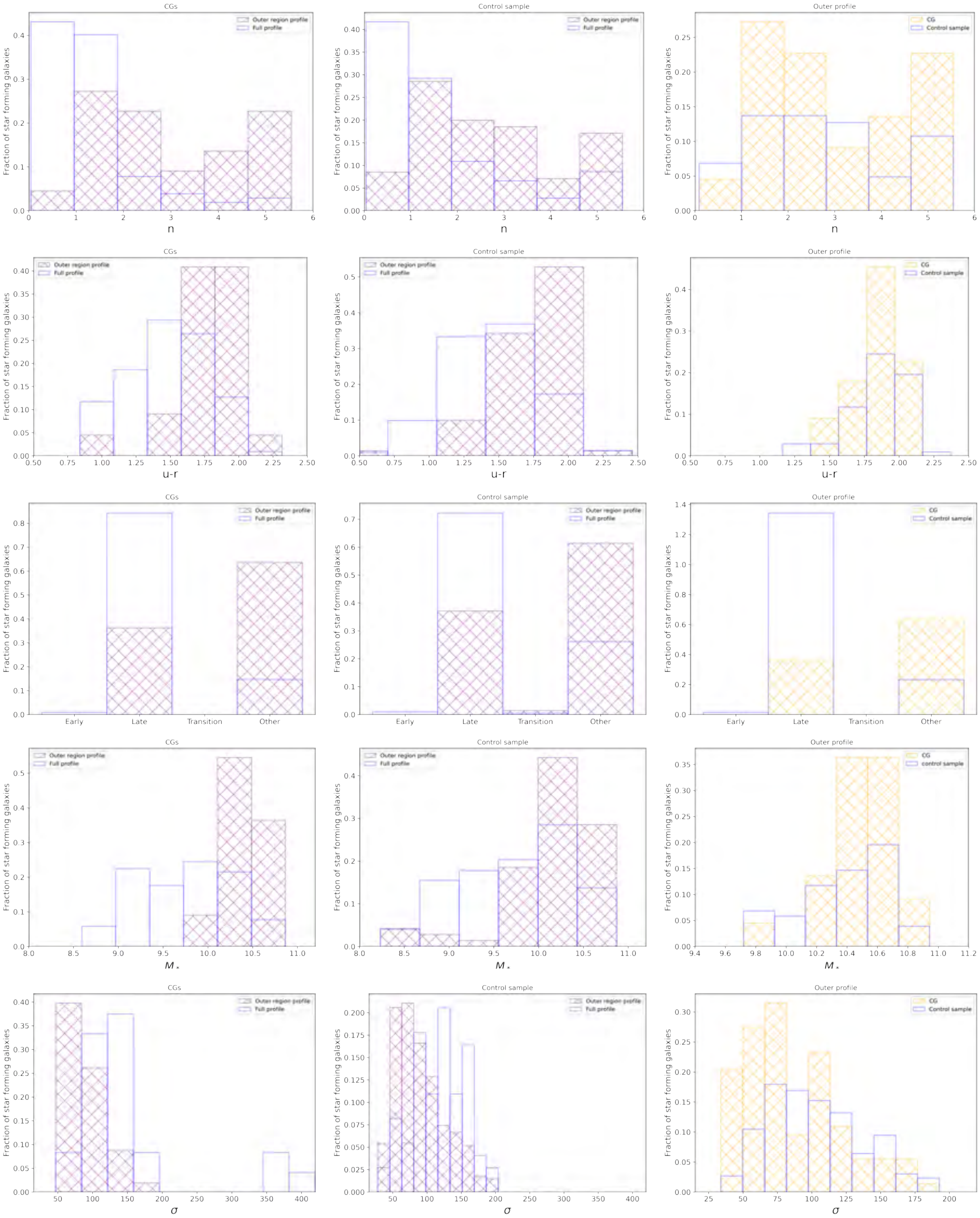

Figure 5.3.6: Comparison of different properties across galaxies. In the first row, the Sérsic index is shown; in the second row, the colour $(u-r)$; in the third row, the morphological type; in the fourth row, the stellar mass; and in the last row, the velocity dispersion measured within one R_e. The left column compares galaxies with complete profiles to those with only the outer part profile for galaxies in CGs. The middle column presents the same comparison but for galaxies in the control sample. The right column shows galaxies having only the outer part profile, with CG galaxies in orange and control sample galaxies in blue.

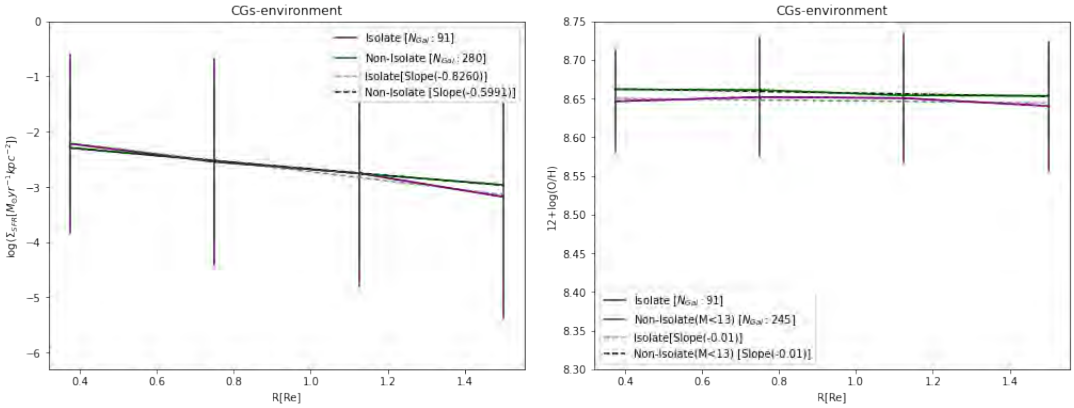

Figure 5.3.7: The left panel shows the star formation surface density (Σ_{SFR}) profiles for galaxies in different environments within CGs, similar to the presentation in Figure 5.3.3. The profiles are compared between isolated and non-isolated CGs. The right panel shows the oxygen abundance profiles.

differences.

5.4 Discussion

5.4.1 Dependence of the D_{4000} Profile on Stellar Mass and Morphological Types in Galaxies

In Figure 5.3.2, we observe a relationship between stellar mass and D_{4000} profile values across different morphological types. Galaxies in the highest mass bin generally exhibit higher D_{4000} values than those in the lowest mass bin, indicating that more massive galaxies tend to have older stellar populations (Kauffmann et al. 2004, Blanton & Moustakas 2009).

We find that galaxies in CGs have higher D_{4000} values compared to the control sample. These results, where D_{4000} is higher in denser environments at fixed stellar mass, are consistent with other studies (e.g., Kauffmann et al. 2004, Paulino-Afonso et al. 2020) but become marginal when considering different galaxy morphology types. When divided by morphological types, we find that D_{4000} values are slightly higher in CGs compared to the control sample at fixed stellar mass, except for ETGs in the lowest mass bin. However, these differences are minor and not statistically significant when considering the uncertainties, as the results for CGs and the control sample are consistent within the error bars.

Another important aspect to consider is that not all galaxies in CGs belong to isolated groups. Therefore, we divide the galaxies based on whether they are part of isolated CGs or not. We find that, in general, galaxies in non-isolated CGs exhibit higher D_{4000} values across the stellar mass bins, except for LTG galaxies in the most massive bin. In this case, the stellar mass distributions for each morphological type and stellar mass bin, for both isolated and non-isolated CGs, follow the same distribution according to the KS test. Thus, these marginal differences in higher D_{4000} values for galaxies in non-isolated CGs likely result from the environment, indicating that their stellar populations may be older and/or more metal-rich compared to galaxies in isolated CGs. However, massive LTGs are an exception, as they are slightly younger or less metal-rich in non-isolated CGs.

5.4.2 Σ_{SFR} gradients and the influence of the environment

We did not find clear signs of dependence between the radial profile of Σ_{SFR} and the environment for those star forming galaxies. However, we did find slight differences in the slopes of the profiles between environments depending on the mass of the galaxies. In the bin of less massive galaxies, we found that the profile is steeper in the control sample galaxies, while in the more massive bin, the slope is steeper in the CGs galaxies. This steeper slope is due to a knee-like behaviour in the profile, which may suggest that the galaxies are quenching from the outside in, as suggested by Lian et al. (2019). However, they found that the slope is steeper for denser environments across all stellar mass ranges. They also mentioned that the trend of Σ_{SFR} with the environment is not very significant in their data. Using data from the Sydney-AAO Multi-Object Integral Field Spectrograph Galaxy Survey and the Galaxy And Mass Assembly, Schaefer et al. (2017) and Medling et al. (2018) found that the star formation density profiles of galaxies are steeper and have lower integrated SFR in denser environments. In fact, they highlight that the reduction in star formation in galaxies in high-density environments occurs primarily in their outskirts. However, in these cases, they reached radii greater than $3R_e$, leading them to propose a scenario of quenching from the outside in, possibly caused by ram-pressure stripping or galaxy interactions. In our case, we cannot rule out this scenario since we are observing the more central region.

For galaxies with nuclear activity, especially the more massive ones, we observed clear differences between the two environments. The galaxies in CGs have higher Σ_{SFR} values at all radii compared to the control sample, and the slope is less steep in the CGs galaxies. Therefore, it is worth exploring the differences between star forming galaxies and galaxies with nuclear activity. Galaxies with nuclear activity are slightly redder, more compact, have a higher fraction of *other galaxies*, and have a lower velocity dispersion than galaxies with a complete profile.

Now, the difference between galaxies with nuclear activity between environments, i.e., when comparing this type of galaxy in CGs with the control sample, is that galaxies in CGs have a higher fraction of *other galaxies* and a lower mean velocity dispersion compared to the control sample galaxies. Additionally, when comparing the ionisation mechanisms for these galaxies in the nuclear region between the BPT diagnostic diagram and the WHAN diagram, we find that in both diagnostic diagrams, 59% of these galaxies in CGs have central ionisation dominated by AGN, while the remaining 41% are RGs in the WHAN diagram. In contrast, in the control sample, 29% coincide with AGN and 71% with RGs. These results suggest that in CGs, there is a higher fraction of AGNs in the nuclear region while maintaining star formation in the outer part. Mulcahey et al. (2022) found that AGN selected based on their current activity are not responsible for suppressing star formation in their host galaxies, indeed revealing that AGN host galaxies typically have higher star formation rates; however, they studied radio AGN and their control sample consisted of non-active galaxies that matched the stellar mass and redshift.

In contrast, galaxies with nuclear activity in the control sample show a higher percentage where the ionisation mechanism in their central region is mainly due to old stars according to the WHAN diagnostic diagram, and they have lower star formation in the outer regions. In fact, Belfiore et al. (2017) found that galaxies with emission lines dominated by post-AGB stars in the centres fall 1 dex below the star formation main sequence when analysing the integrated log(SFR).

Additionally, when comparing isolated and non-isolated CGs, we find no clear difference, only that the slope in isolated CGs is slightly steeper, although this is marginal. Thus, there is no clear trend between the environment and Σ_{SFR} within $1.5R_e$.

5.4.3 Abundance gradients and the influence of the environment

In studies on the distribution of metallicities, it is shown that there is a clear abundance gradient, with the centre of the galaxy being more metallic than the outskirts, for galaxies with stellar masses between $10^9 - 10^{11.5} M_*[M_\odot]$ (e.g., Sánchez-Blázquez et al. 2014, Lian et al. 2018). In Figure 5.3.5, we show that for our sample of galaxies we observe that, in general, they follow this metallicity gradient, being more metallic in the central region. However, we do not find differences in the median metallicity gradient of galaxies in each environment across two bins of stellar mass. The only difference, which is marginal, is that low-mass galaxies in CGs seem to be slightly more metallic in the outer parts compared to their counterparts in the control sample. However, this should be taken with caution as the values of both samples fall within the error bars. Additionally, in the left panel of Figure 5.3.7, we separate the galaxies in CGs according to whether they are in isolated CGs or non-isolated CGs, and we do not find differences in the median profile either. Therefore, our results suggest that there is no dependence on the environment and the median oxygen abundance profile between CGs and the control sample. In Lian et al. (2018), they did not find a clear dependence of oxygen abundance on the environment, except for satellite and low-mass galaxies, which show a very clear trend of higher gas metallicities in denser environments.

One point where our results are consistent with previous works is the dependence of gas metallicity on stellar mass, indicating that the mass of a galaxy plays a much more important role than the environment in regulating the metal enrichment process in galaxies (Goddard et al. 2017, Lian et al. 2018). On the other hand, by dividing the galaxies in CGs according to their environment, that is, whether they are part of isolated CGs or not, we find that there is no significant difference. We only observe that the slope in isolated CG galaxies is slightly steeper than in non-isolated CGs.

Studies on the metallicity profile in CGs have conducted analyses on individual galaxies or groups specifically. For example, Vogt et al. (2015) showed that the oxygen abundance in HCG 91c presents a complex gradient, exhibiting a negative gradient with a marked difference between the inner and outer regions of the galaxy. Additionally, an abrupt drop in oxygen abundance is detected in the outer regions. Torres-Flores et al. (2015) found that there is a smoothly varying distribution in the oxygen abundance between merging galaxies in the compact group HCG 31. This suggests metal mixing between these regions due to the strong gravitational interaction between both galaxies. This system was subsequently studied by Gómez-Espinoza et al. (2023), who found that in the HCG 31 system, the oxygen abundance is mainly high for the mass of the galaxies, and it shows a flat distribution across the different galaxies. They concluded that this is likely due to gas mixing throughout the whole group, probably triggered by the merger. This demonstrates that the interaction between galaxies in CGs affects the distribution of metals, but these studies were conducted on discrete galaxies. Although these studies are based solely on galaxies in CGs that show clear signs of interactions and mergers, ignoring those galaxies that do not present clear signs of strong interaction.

5.5 Summary

In this study, we analysed a sample of 459 galaxies in compact groups (CGs) and 1098 field galaxies, which served as our control sample. The goal of this analysis was to thoroughly investigate the impact of galaxy interactions within CGs on the physical properties of galaxies, with a particular focus on ionised gas, using IFS data. We classified the galaxies based on their morphology using the $(u-r)$ colour and the Sérsic index in the r-band, as done in Chapter 2. Additionally, we categorised the star-forming spaxels using the BPT diagram (Baldwin et al., 1981; Kewley et al., 2001; Kauffmann et al., 2003a). Below, we summarise our main findings. It is important to highlight that these results are within $1.5R_e$:

1. We identify that this sample of galaxies with data from MaNGA shows a higher fraction of ETGs in CGs compared to the control sample, where LTGs dominate. Among CGs, isolated groups tend to have a higher fraction of LTGs and a lower fraction of ETGs compared to non-isolated groups.

2. The crossmatch analysis using the SDSS fibre data for emission lines and the WHAN diagnostic diagram (Cid Fernandes et al. 2010) confirms the findings from Chapter 4. There is a higher prevalence of passive and retired galaxies (RG) in CGs, whereas the control sample has a higher proportion of star-forming (SF) galaxies and active galactic nuclei (AGNs). This consistency across different datasets underscores the influence of the CG environment on the ionisation mechanisms and the activity levels in galaxies.

3. We find that the D_{4000} profile values exhibit a clear dependence on stellar mass, with more massive galaxies showing higher D_{4000} values, suggesting that their stellar populations are generally older. Additionally, galaxies in denser environments, such as CGs, tend to have slightly higher D_{4000} values at a fixed stellar mass compared to those in less dense environments. This observation implies that the stellar populations in CGs might be older.

4. Examining the impact of morphological types, we observed a general trend of higher D_{4000} values in CGs compared to the control sample, but ETGs are an exception. Furthermore, galaxies in non-isolated CGs typically exhibit higher D_{4000} values compared to those in isolated CGs, suggesting environmental effects on stellar population ages or metallicity. However, massive LTGs in non-isolated CGs appear younger compared to those in isolated CGs.

5. For star-forming galaxies, the Σ_{SFR} profiles show that the slopes vary slightly with galaxy mass. Specifically, lower-mass galaxies in control samples exhibit steeper profiles, while higher-mass galaxies in CGs display steeper profiles. However, these differences are not significant as they are consistent within the uncertainties of the Σ_{SFR} profiles for both environments.

6. For galaxies with nuclear activity, i.e. star-forming spaxels in the outer regions and Seyfert or LINER in the centre, those in CGs have higher Σ_{SFR} values and less steep slopes compared to the control sample. Comparing ionisation mechanisms in the nuclear regions using the BPT and WHAN diagnostics diagrams reveals that, in CGs, 59% of galaxies have AGN-dominated central ionisation, while the remaining 41% are dominated by old stars. In contrast, the control sample shows only 29% with AGN-dominated ionisation and 71% with old stars. This indicates a higher prevalence of AGN in the nuclear regions of CGs compared to the control sample, with star formation continuing in their outer parts.

7. Finally, in terms of abundance gradients, we find that galaxies generally exhibit a metallicity gradient with higher metallicity in their central regions. There are no significant differences in median metallicity gradients between CGs and the control sample. Although low-mass galaxies in CGs show slightly higher metallicity in their outer regions compared to their counterparts in the control sample, these differences are not statistically significant. Overall, our findings support the notion that stellar mass is a more influential factor than the environment in regulating metallicity gradients in galaxies.

In general, we do not find significant differences between the control sample and galaxies in CGs, except for galaxies with nuclear activity in terms of Σ_{SFR}. However, it is important to remember that our analysis is conducted within 1.5 R_e, which limits the comparison to the properties of galaxies in regions closest to the centre.

Chapter 6

Galaxy preprocessing in the Abell 1644 cluster: morphological changes in infalling groups

As shown in Chapter 3, non-isolated CGs evolve differently from isolated CGs. Based on this finding, a natural question arises from this thesis: how are the properties of galaxies falling into groups within denser environments affected? This is particularly relevant given that our results suggest that the major structures in which non-isolated CGs are embedded play a significant role in the evolution of member galaxies, accelerating their physical transformations.

For this reason, in this Chapter we decide to investigate how the properties of galaxies change in groups falling into a cluster. We select the Abell 1644 galaxy cluster. Abell 1644 ($z = 0.046$) is a known cluster with substructures within its R_{200} (the radius within which the mean density of a galaxy cluster is 200 times the critical density of the universe at the cluster's redshift), where three substructures, A1644S, A1644N21, and A1644N2, have been identified in previous studies (Johnson et al. 2010, Monteiro-Oliveira et al. 2020). An analysis of the velocity dispersion has shown values of approximately $\sigma \sim 1000$ km/s, indicating a system that is not in equilibrium (Monteiro-Oliveira et al. 2018, Pandge et al. 2019). This conclusion is further supported by X-ray observations, indicating that A1644 is in a post-collision state. Notably, a cold front with a spiral shape has been found at the edge of the southern subcluster (Jones & Forman 1999, Johnson et al. 2010). Simulations using observational data by Monteiro-Oliveira et al. (2020) suggest that these remarkable X-ray features result from a collision between A1644S and A1644N2 that occurred approximately 1.6 billion years ago. These systems now seem to be heading towards another encounter after reaching their maximum separation. Additionally, substructures within about $5 \times R_{200}$ have been identified using data from S-PLUS via the CALSAGOS code (Olave-Rojas et al. 2023).

This comprehensive analysis allows us to explore how the morphological properties of galaxies are influenced by their location within substructures relative to their distance from the cluster, helping us understand the preprocessing they undergo. The Abell 1644 cluster appears to be in the process of colliding with Abell 1631, which has a redshift of 0.047. The R_{200} of Abell 1631 lies within $5 \times R_{200}$ of Abell 1644 (Haines et al. 2023), allowing us to examine how such a complex interacting system affects the properties of galaxies falling into the cluster.

This chapter is organised as follows. We begin by presenting the data used in this study in Section 6.1, followed by a detailed description of the methodology in Section 6.2. This includes an analysis of the substructures in Abell 1644 and the stellar mass distribution of galaxies within these substructures. We then explore the preliminary results and discussions in Section 6.3. The chapter concludes with a

Cluster	RA	DEC	z	$R_{200}[arcseg]$
Abell 1644	194.295	-17.4	0.048	33.88
Abel 1631	193.216	-15.4	0.047	25.88

Table 6.1.1: Data for the Abell 1644 and 1631 clusters estimated by the CHANCES collaboration (Haines et al. 2023).

summary of the findings in Section 6.4.

6.1 Data

We used photometric data from S-PLUS. As discussed in Chapter 2, this dataset allows us to examine large sky regions, covering areas up to five times the R_{200} of the cluster, and provides images in 12 different filters. To identify the galaxies belonging to Abell 1644 within $5 \times R_{200}$, we utilised the photometric redshifts available in S-PLUS from Lima et al. (2022). We selected all galaxies within 3σ of the redshift distribution, centred at the cluster's redshift. In this analysis we obtain a $\sigma_z = 0.016$, which was used to select the members. This selection yielded 3311 galaxies belonging to Abell 1644, which we name the S-PLUS catalog.

Given the uncertainties associated with photometric redshifts, the $3\sigma_z$ sample may be contaminated by objects not truly belonging to the cluster. However, we opted to fit all selected galaxy members, as Abell 1644 is one of the clusters that will be targeted by the Chilean Cluster Galaxy Evolution Survey (CHANCES) (Haines et al., 2023). This survey will offer a comprehensive spectroscopic coverage of cluster galaxies, extending well beyond the virial radius and reaching the infall regions up to $5 \times R_{200}$, using 4MOST (Walcher et al. 2019). With the spectroscopic data from CHANCES and the morphological analysis from S-PLUS, we will be able to conduct a more thorough study of the properties of galaxies in the substructures of this cluster. Furthermore, we used the estimated central positions, redshift, and R_{200} values for the Abell 1644 and Abell 1631 clusters, as provided by Haines et al. (2023). These values are presented in Table 6.1.1.

6.2 Methodology

6.2.0.1 Morphology parameters

The S-PLUS data enables us to investigate how morphological parameters vary across different wavelengths. To obtain these parameters for each galaxy, we use the MorphoPLUS tool, which is based on the MegaMorph code (Bamford et al. 2011, Häußler et al. 2013, Vika et al. 2013). This code was detailed in Chapter 2. We fit a Sérsic profile to all the 3311 galaxies in the sample across 12 filters, allowing us to derive the effective radius (R_e), Sérsic index (n), axis ratio (a/b), and position angle for each galaxy. Although we performed the fitting for all galaxies, we will only analyse a subsample of these galaxies.

6.2.1 Subestructures in Abell 1644

Since the main objective is to study how the properties of galaxies in groups evolve as they fall into denser environments, we use galaxies identified by Olave-Rojas et al. (in preparation) to pinpoint

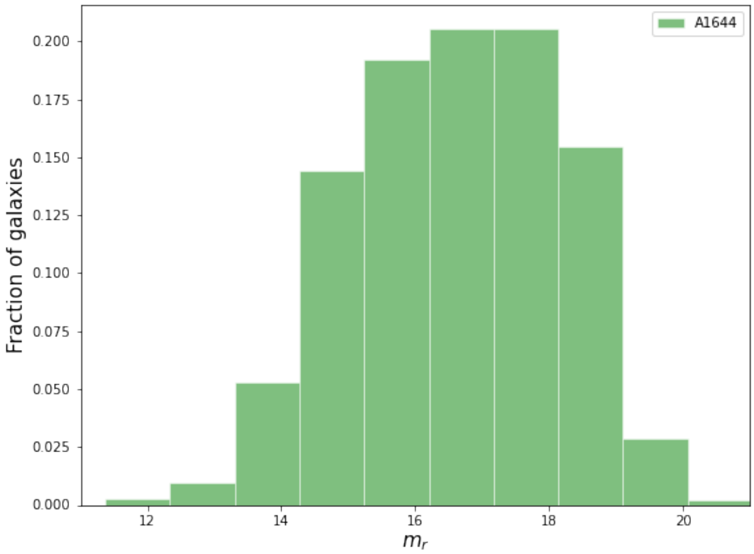

Figure 6.2.1: Distribution of the apparent magnitude in the r-band for galaxies selected as part of the cluster within a $5 \times R_{200}$.

substructures within $5 \times R_{200}$ using Clustering Algorithms Applied to Galaxies in Overdense Systems (CALSAGOS) (Olave-Rojas et al. 2023).

Initially, they selected only the galaxies with spectroscopic redshifts from S-PLUS catalogue within $5 \times R_{200}$. Next, they identified the spectroscopic members of the cluster using a multi-Gaussian fitting approach with Clumberi from CALSAGOS, considering both the position and redshift information of the galaxies and the cluster, and removed interlopers with a 3σ clipping. This process resulted in 208 spectroscopic member galaxies, with a velocity dispersion of 778 ± 53 km/s, $z = 0.045872$, and $\Delta_z = 0.002715$.

Using the values obtained from this initial step, they then cleaned the photometric catalog from S-PLUS to select all galaxies within $5R_{200}$ that had $\sigma_{flag} == 1$ and whose with redshift within the range of $(z_{cl} - 3\Delta_z)$ to $(z_{cl} + 3\Delta_z)$. $\sigma_{flag} == 1$, means that the galaxies are within one sigma in the distribution of the photometric redshift of the cluster centered at 0.047, this σ_{flag} value comes from the catalogue of the photometric redshift estimation by Lima et al. (2022). For these selected galaxies, they performed a photometric member selection using Clumberi, again considering the output values from the spectroscopic sample, and removed interlopers with a 3σ clipping. This thorough process identified 1177 ± 12 galaxies as members based on combined spectroscopic and photometric data, with a velocity dispersion of 1301 ± 19 km/s, a redshift of $z = 0.047425$, and $\Delta_z = 0.002715$. This provides a well-defined sample for studying galaxies within the cluster, significantly reducing contamination from non-cluster galaxies.

To detect substructures, they use the output catalogue from the member selection process, focusing on both the combined photometric and spectroscopic sample, as well as the spectroscopic-only sample. The detection method involves calculating the distance to the third nearest neighbour for each galaxy and setting a minimum sample size of three galaxies for identifying substructures. In the initial catalogue, these distances are computed as Euclidean distances. Additionally, they restrict by treating both samples as photometric, disregarding the redshift information. It is important to highlight that they focus on locating substructures outside R_{200}, which is why any galaxy within R_{200} in projection is considered part of the main halo.

In Figure 6.2.1, we show the distribution of the magnitudes in the r-band for 1177 of the selected

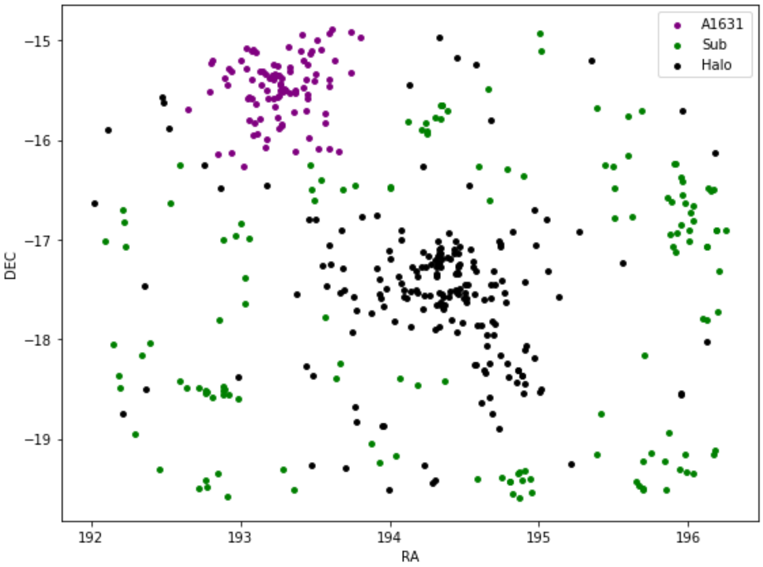

Figure 6.2.2: Spatial distribution of galaxies selected for morphological analysis. Green dots represent galaxies identified as part of a substructure, purple dots represent galaxies in Abell 1631, and black dots represent those not identified as part of a substructure.

galaxies. The completeness of the sample drops beyond a magnitude of 17. Therefore, in the results that we will present, we will focus on galaxies with r-band magnitudes brighter than 17, corresponding to 478 galaxies. In Figure 6.2.2, green dots represent the galaxies belonging to the different substructures identified by Olave et al. (in prep), while the galaxies not identified as part of any structure are shown in black.

6.2.2 Stellar mass

We estimated the stellar mass of the cluster galaxies in the same manner as in Chapter 2, using the colour $(g-i)$ and the empirical equation proposed by Taylor et al. (2011). However, in this case, we approximate that all galaxies are at the same redshift as the central spectroscopic redshift of the cluster. This introduces some error in our measurements, therefore we have considered the photometric uncertain to estimate the error in the stellar mass measurements, resulting in a mass error of 0.2 dex. In Figure 6.2.3, we show the distribution of the stellar masses of the galaxies in our sample from Abell 1644.

6.3 Result and discussion

In this section, we will focus on studying how the morphological properties of galaxies change depending on their distance from the centre of the cluster and whether they are in structures or not. Additionally, we compare these properties across different environments utilising the results from different environments that we presented in previous chapters.

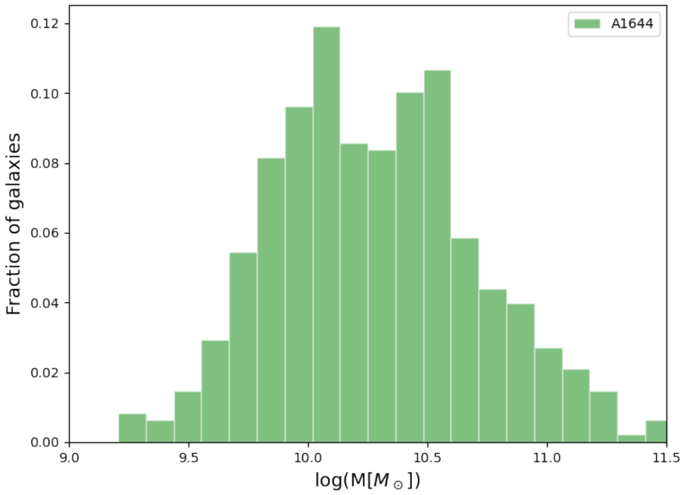

Figure 6.2.3: Normalised histograms of stellar masses for 478 galaxies in Abell 1644 selected as explained in Section 6.2.1.

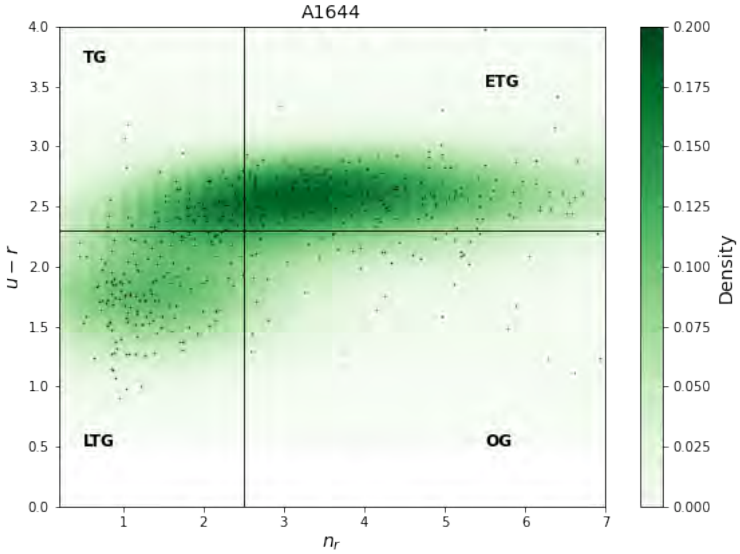

Figure 6.3.1: Colour (u-r) as a function of the Sérsic index in the r-band. The data points represent galaxies within the cluster, and the green background illustrates the density map of these points. The vertical line represents $n_r = 2.5$, and the horizontal line represents $(u-r) = 2.3$, enabling us to classify galaxies based on their morphology into ETG, LTG, *transition galaxies* (TG), and *other galaxies* (OG).

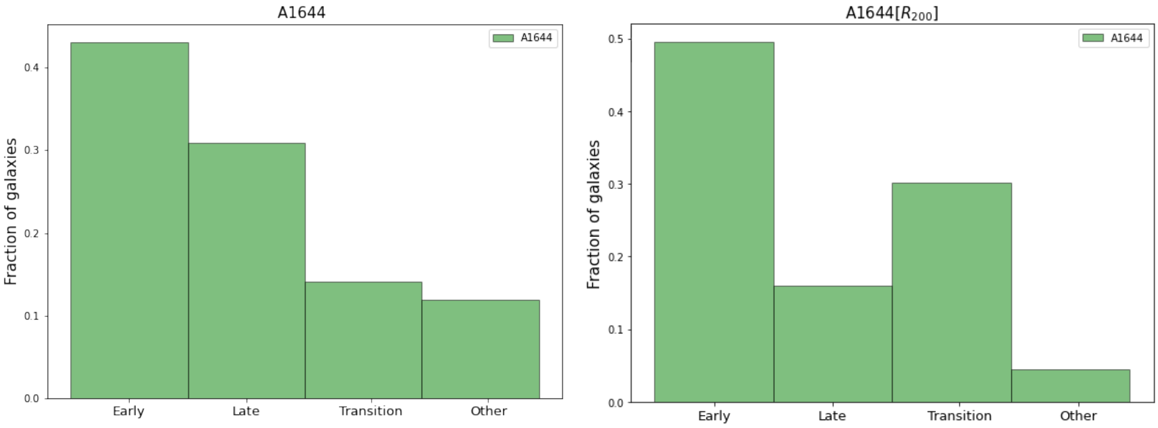

Figure 6.3.2: Histogram of the fraction for each galaxy type according to the morphological classification. On the left panel, we show all galaxies within $5 \times R_{200}$. On the right, we present the galaxies inside R_{200}.

6.3.1 Classifying galaxies according to their morphology

We use the same methodology as outlined in Chapter 2, following the classification proposed by Vika et al. (2015b), using the Sérsic index in the r-band and the $(u-r)$ colour. In this classification, galaxies with $n \geq 2.5$ and $(u-r) \geq 2.3$ are classified as ETGs, while galaxies with $n < 2.5$ and$(u-r) < 2.3$ are classified as Late-Type Galaxies (LTGs). Following the approach proposed in Chapter 2, galaxies with $n < 2.5$ and $(u-r) \geq 2.3$ are referred to as *transition galaxies* and those with $n \geq 2.5$ and $(u-r) < 2.3$ are designated as *other galaxies*. In Figure 6.3.1, we show this classification for the galaxies in Abell 1644, represented by black points, where the lines represent $n = 2.5$ and $(u-r) = 2.3$. Additionally, we present a galaxy density map in this plane. In this density map, an overdensity in the region of ETGs is noticeable. To better observe the distribution of populations, in the left panel in Figure 6.3.2, we show the histogram for each population inside $5 \times R_{200}$, confirming that ETGs are the dominant population in this cluster. In the right panel of Figure **??**, we show the distribution of each morphological type for galaxies within R_{200}, where we find that the fraction of LTGs decreases, while that of ETGs and *transition galaxies* increases.

6.3.2 Morphology classification as a function of distance from the centre of the cluster

The distribution of each population relative to the distance from the cluster centre should also be considered, as one would expect the fraction of ETGs to increase towards the centre due to the higher galaxy density (Dressler 1980, Whitmore & Gilmore 1991). In Figure 6.3.3, we present the fraction of each galaxy type as a function of the distance to the cluster centre in terms of R_{200}. In this case, figures are normalised by the total number of galaxies of each morphological type. Two peaks are observable in the distribution of ETGs, one at the cluster centre and another between $3-4 \times R_{200}$. For *transition galaxies*, we observe an increase in their fraction at the centre, while the fraction of LTGs and *other galaxies* increases at larger distances from the centre.

To explore this further in Figure 6.3.4, we show the distribution of the galaxies in the cluster in the sky, coloured by their morphological types (ETG in red, LTG in blue, *transition galaxies* in green, and *other galaxies* in orange). It is essential to note that between $4-5R_{200}$, our sample is not complete. This is because the fields of S-PLUS are square, with a diameter of 2 degrees, resulting in a square

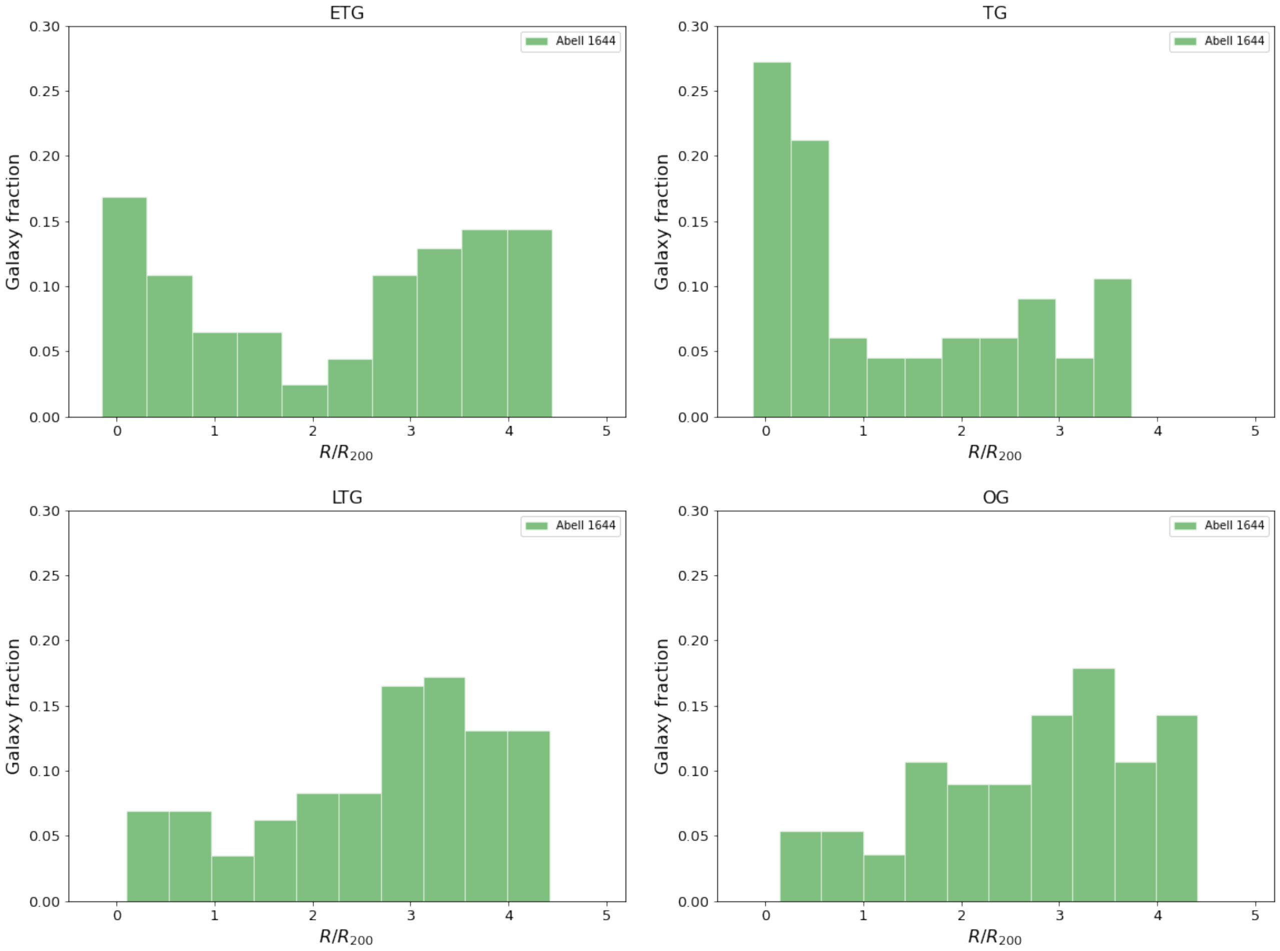

Figure 6.3.3: Distribution of galaxy fractions according to each morphological type as a function of the central distance from the cluster.

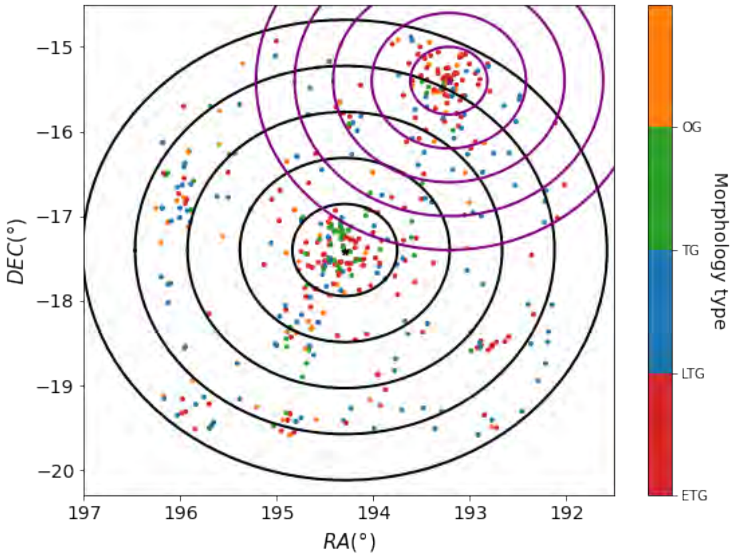

Figure 6.3.4: Galaxy positions in the sky. Colours indicate the morphological type. Additionally, 5 circles have been drawn around the center of Abell 1644 in black, each circle increasing in radius by one R_{200}. Similarly, for Abell 1631, the circles are purple.

observation region without additional observations at the moment. Our data is complete up to 4R200, but we have decided to include galaxies beyond this limit because the Abell 1644 cluster appears to be colliding with Abell 1631, where the centre of this cluster is between the $4-5\times R_{200}$ annulus, as seen in Figure 6.3.4, with the centre of A1644 marked with a black star and the R_{200} annuli marked in rings of the same colour up to $5\times R_{200}$, while the centre of Abell 1631 is marked with its annuli in purple. We can observe that both clusters share members, therefore the second peak in the distributions of ETG and *transition galaxies* is associated with the interaction of both clusters. To verify this, we divide the cluster into the region containing cluster 1631 and the one that does not. For this, we made two divisions: the first by splitting the cluster in half with a horizontal line across the centre in declination, and the second by dividing vertically along the right ascension of the cluster's centre. In this exercise, the fraction of the second peak for ETG and *transition galaxies* disappears when considering the region of the cluster that does not contain Abell 1631.

6.3.3 Sérsic index and effective radius as a function of wavelength

As presented in Chapter 2, there is a dependence between the parameters n and R_e as a function of wavelength for each morphological type. In Figure 6.3.5, we show the median Sérsic index we obtain for each galaxy population as a function of wavelength. Additionally, we show all galaxies within the $5\times R_{200}$ radius, represented as stars; galaxies identified as part of substructures are marked with diamonds, and squares represent galaxies not identified as part of a substructure. In the top panel, we consider all the galaxies identified as part of a substructure, while in the bottom panel, we exclude the galaxies identified within the substructure that coincides with the Abell 1631 cluster. LTGs, *transition galaxies*, and ETGs for the entire cluster are shown in blue, green, and red, respectively. Uncertainties were estimated using a bootstrapping technique with a 90% confidence interval. In general, we find that the median n increases with wavelength. For ETGs, the value of n increases by 33% from the bluest filter to the reddest, for LTGs by 77%, and for *transition galaxies* by 35%.

For galaxies identified as part of a substructure, ETGs (see coral diamonds in the top panel in Figure 6.3.5) show an n increase of 20% from the bluest to the reddest filter. For LTGs (see sky blue diamonds), the increase is 67%, and for *transition galaxies* (see lime green diamonds), it is 53%. For galaxies not identified within a structure, ETGs (see orange squares) show a 26% increase, LTGs show a 74% increase, and *transition galaxies* show a 32% increase. In the bottom panel of Figure 6.3.5, we see that the difference between the mean values for ETGs in substructures, excluding the galaxies of Abell 1631, is closer to the value for all galaxies within $5 \times R_{200}$. Thus, the mean value of n for ETGs in substructures is higher if Abell 1631 is considered as a substructure. In this case, the increase from the bluest to the reddest filter is 37%, 66%, and 42% for ETGs, LTGs, and *transition galaxies*, respectively. We observe that the increase is greater when comparing galaxies in substructures excluding the Abell 1631 galaxies, compared to considering all galaxies in substructures, for both ETGs and LTGs. However, for *transition galaxies*, the increase is larger.

Figure 6.3.6, it is similar to Figure 6.3.5 but we show the median effective radius on the y-axis instead of the median n for each galaxy population as a function of wavelength. The median R_e for all LTGs (see blue stars) is generally larger than the median for all ETGs (see red stars) and *transition galaxies* (see green stars) across all filters. For the behaviour of each type as a function of wavelength, the median R_e for all ETGs increases in the redder filters, with an 11% increase from the bluest to the reddest filter. For all LTGs and *transition galaxies*, the behaviour is quite flat across the filters. Quantifying the difference between the bluest and reddest filters, there is a very slight increase of 2% for LTGs and less than 1% for *transition galaxies*.

For the median R_e behaviour in galaxies belonging to a substructure or not, Figure 6.3.6 shows that ETGs in substructures (see orange diamonds) are larger across all filters than ETGs not identified as part of a substructure (see coral squares). The median R_e for ETGs in substructures increases by 11% in the redder filters (see top panel in Figure 6.3.6). In the case of ETGs in substructures, excluding the galaxies of Abell 1631, the increase is 23%. In contrast, ETGs not identified as part of any substructure have a relatively flat behavior, with a 4% increase from the bluest to the reddest filter.

LTGs in substructures (see sky blue diamonds in the top panel in Figure6.3.6) are smaller than other LTGs (see cyan squares), with both sub-samples showing minimal R_e variation across filters, at 1% from the bluest to the reddest filter. Excluding the Abell 1631 galaxies from those considered as part of a substructure, the behaviour of LTGs changes (see sky blue diamonds in the bottom panel in Figure6.3.6). In this case, we see that the median values of R_e fall between those of all LTGs within $5 \times R_e$ and those not identified as part of a substructure. The variation across filters is also small, with an increase of 3% from the bluest to the reddest filter.

transition galaxies in substructures (see lime green diamonds) are larger than the other *transition galaxies* (see medium green squares) across all wavelengths. Interestingly, the median R_e for *transition galaxies* in substructures is larger in blue filters compared to red ones, with a 7% decrease from the bluest to the reddest filter. However, when excluding the *transition galaxies* in substructures that belong to Abell 1631, we observe that the median values in the bluer filters are similar to those of all *transition galaxies*. In the redder filters, starting from r, the median R_e is higher for those that are part of a substructure compared to the total galaxy sample and those not identified as part of a substructure. The increase is 10% from the blue filters compared to the red ones for the *transition galaxies* in substructures, excluding the galaxies of Abell 1631. For *transition galaxies* that were not identified as part of a substructure, the size fluctuates slightly with wavelength, with a 2% decrease from the red to the blue filter.

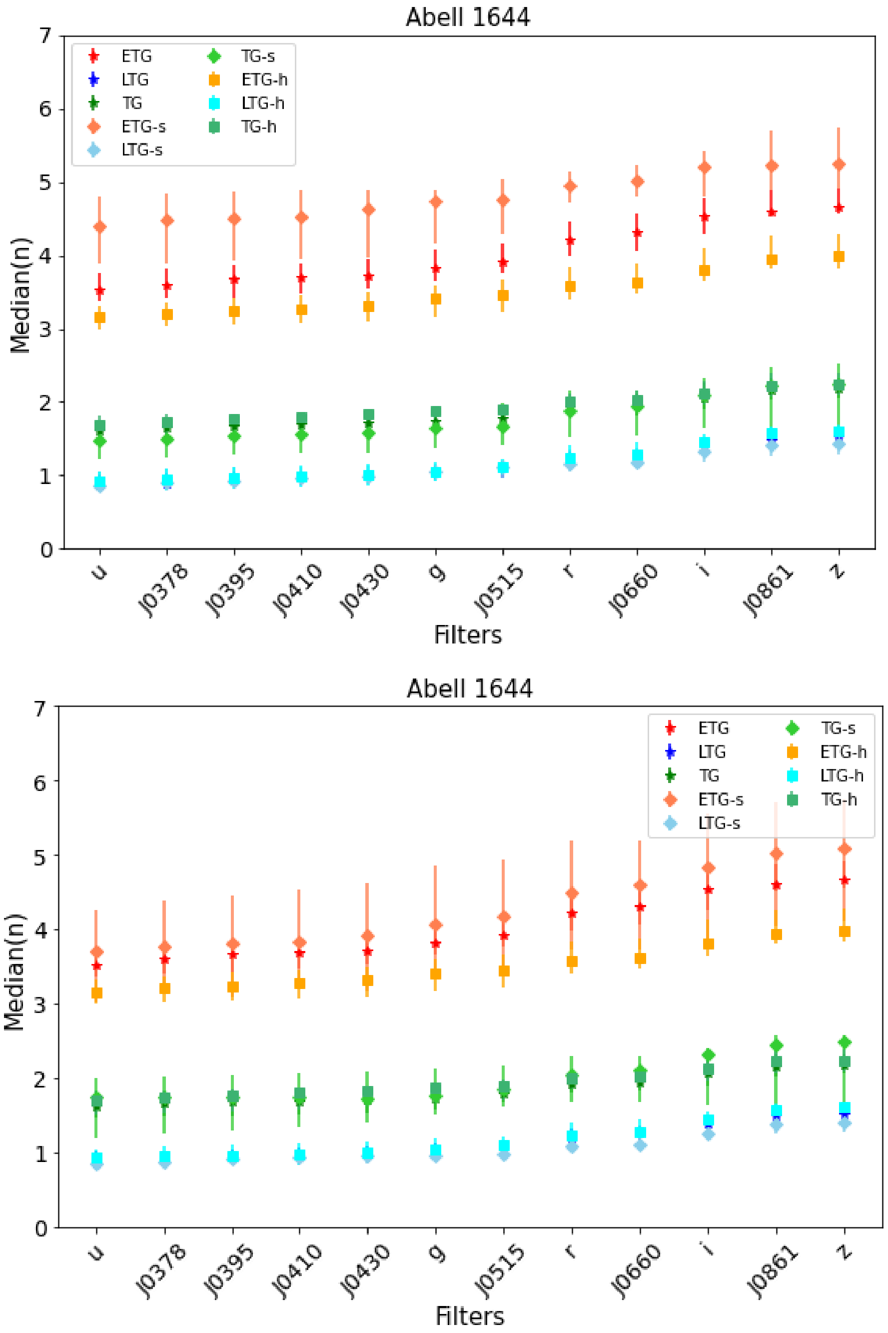

Figure 6.3.5: The median Sérsic index (n) as a function of S-PLUS filters for ETGs (red/orange/coral), LTGs (blue/cyan/sky blue), and *transition galaxies* (green/light green/lime green) for all the galaxies in Abell 1644 (stars), galaxies identified as a part of a substructure (diamonds), and not identified as part of a substructure (squares). The error bars are the 90% confidence CI using bootstrapping. In the top panel, we consider all the galaxies identified as part of a substructure. In the bottom panel, we exclude the galaxies identified within the substructure that coincides with the Abell 1631 cluster.

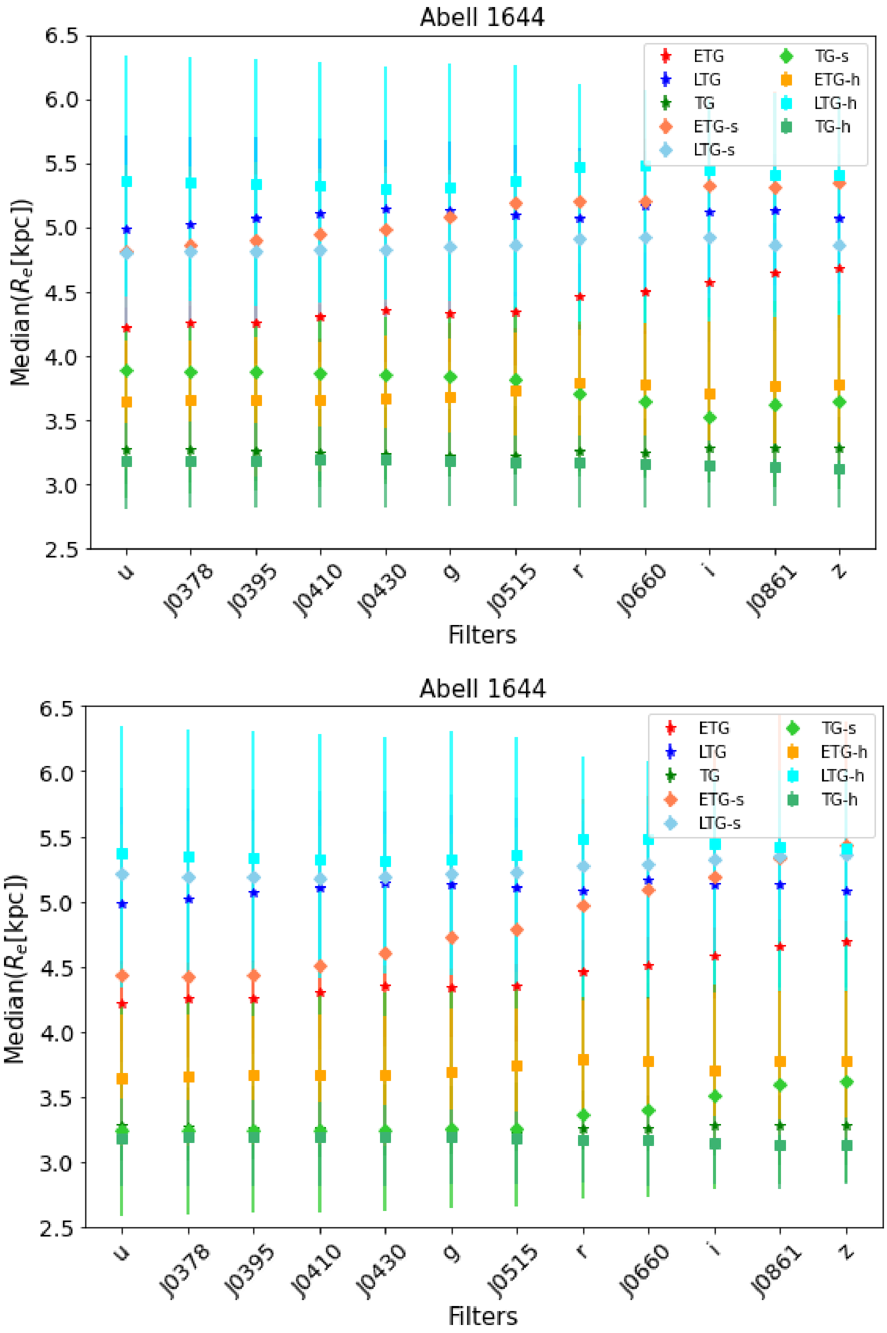

Figure 6.3.6: The effective radius (R_e) as a function of S-PLUS filters for ETGs (red/orange/coral), LTGs (blue/cyan/sky blue), and *transition galaxies* (green/light green/lime green) for all the galaxies in Abell 1644 (stars), galaxies identified as a part of a substructure (diamonds), and not identified as part of a substructure (squares). The error bars are the 90% confidence CI using bootstrapping. In the top panel, we consider all the galaxies identified as part of a substructure. In the bottom panel, we exclude the galaxies identified within the substructure that coincides with the Abell 1631 cluster.

6.3.4 Sérsic index and effective radius as a function of the centre of the cluster

Is the dependence on galaxy size, whether they are part of a structure or not, mainly due to this factor or their distance from the cluster centre?. For instance, ETGs in substructures are located outside the R_{200}, while those not identified in substructures dominate the cluster centre. On the other hand, LTGs that were not identified in substructures are larger, suggesting that LTGs in substructures might be newly accreting and have not undergone clear pre-processing, since within the cluster, there is not a high fraction of LTGs. This second hypothesis is difficult to answer as it would require a more detailed analysis with spectroscopic information, but we can analyse how galaxy size varies as a function of the distance to the cluster centre.

In Figure 6.3.7, we present the median of R_e (left panel) as a function of the distance to the cluster centre for each morphological type, where the error bars are uncertainties estimated from a bootstrapping technique with a 90% confidence interval. In the top panel left, we consider all the galaxies identified as part of a substructure, while in the bottom left panel, we exclude the galaxies identified within the substructure that coincides with the Abell 1631 cluster. The median size of all ETGs (red stars in the left panel in Figure 6.3.7) in the sample decreases for galaxies closer to the centre, with a reduction of 54% when comparing the outermost bin containing galaxies between $3-5 \times R_{200}$ with the central bin containing all galaxies within R_{200}. In the case of LTGs (blue stars), there is no such marked trend, but it is observed that for galaxies between the centre of the cluster and $3 \times R_{200}$ the size of LTGs decreases towards the cluster centre, with a reduction of 41%. Those results are in agreement with Cypriano et al. (2006), who found that cluster elliptical galaxies in the inner, denser regions of clusters are approximately 5% smaller than those in the outer regions. Pranger et al. (2017) also found that cluster disc galaxies show a higher overall Sérsic index and are more compact than field discs, both by $\sim 15\%$. For *transition galaxies* (green stars), the median size fluctuates between bins without a clear trend; comparing the outermost bin $(3-5 \times R_{200})$ with the centre of the cluster, i.e., galaxies within R_{200}, the R_e is smaller by 21%.

For the subsample of galaxies in substructures compared to those not identified as part of these substructures, in left panel in Figure 6.3.7 we show that ETGs in substructures (see orange diamonds in the top left panel) are bigger by 66% between $3-5 \times R_{200}$ and 22% between $1-3 \times R_{200}$ compared to ETGs not identified as part of a substructure (see coral squares). In the case of considering ETGs in substructures, excluding the galaxies of Abell 1631 (see orange diamonds in the bottom left panel), they are larger by 65% between $3-5 \times R_{200}$ and 14% between $1-3 \times R_{200}$ compared to ETGs not identified as part of a substructure.

LTGs in substructures (see sky blue diamonds in the top left panel in Figure 6.3.7) within $3-5 \times R_{200}$ are 20% smaller than galaxies not identified as part of the structure (see cyan squares). Excluding the galaxies of Abell 1631 from the substructures, this value is 14% (see sky blue diamonds in the bottom left panel in Figure 6.3.7). While between $1-3 \times R_{200}$, the sizes of the two subsamples are comparable, with a difference of 3% and excluding the galaxies of Abell 1631 from the sample of galaxies in substructures, this value is 2%.

For *transition galaxies*, in the $3-5 \times R_{200}$ bin, there are only galaxies in substructures (see lime green diamonds)); in the bin containing galaxies between $1-3 \times R_{200}$, *transition galaxies* in substructures are 13% larger than those not in substructures (see medium green squares in top left panel), it is the same value when excluding the galaxies of Abell 1631.

In the right panel of Figure 6.3.7, we present the median of n as a function of the distance to the centre. In the top panel, we consider all the galaxies identified as part of a substructure, while in the bottom panel, we exclude the galaxies identified within the substructure that coincides with the Abell 1631 cluster. For all ETGs (red stars), the median of n decreases with decreasing distance to the centre,

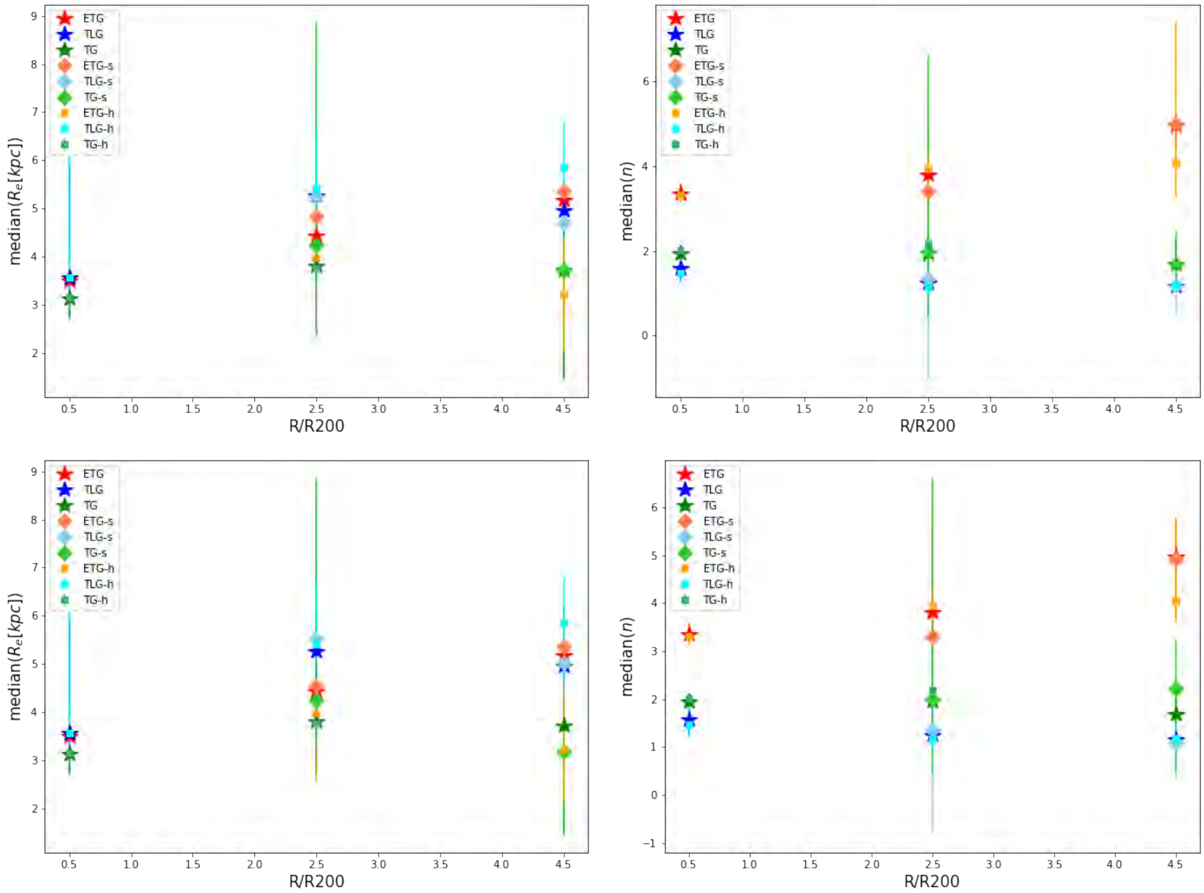

Figure 6.3.7: Left panel: The median effective radius as a function of distance to the cluster centre, where we consider bins of $0 - R_{200}$, $1 - 3R_{200}$, and $3 - 5R_{200}$. For ETGs (red/orange/coral), LTGs (blue/cyan/sky blue), and *transition galaxies* (green/light green/lime green) among all galaxies in Abell 1644 (stars), galaxies identified as part of a substructure (diamonds), and those not identified as part of a substructure (squares). Error bars represent the 90% confidence interval using bootstrapping. Right panel: Similar to the left panel, but in this case, the y-axis is the median Sérsic index. In the top panels, we consider all the galaxies identified as part of a substructure. In the bottom panels, we exclude the galaxies identified within the substructure that coincides with the Abell 1631 cluster.

with n decreasing by 50% when comparing the median of the outermost bin to galaxies within R_{200}. For all LTGs and all *transition galaxies*, the median of n slightly increases with the distance from the centre by 27% and 22%, respectively. These results indicate that as galaxies fall into the cluster, they undergo morphological transformations. For ETGs, galaxies become smaller and less compact. In the case of LTGs, they become smaller and more compact. Meanwhile, *transition galaxies* become more compact as they fall into the cluster.

Comparing the median n as a function of distance to the centre, based on whether galaxies were identified as part of a substructure, reveals differences only for ETGs. ETGs identified as part of the substructure (see orange diamonds) in the $3-5R_{200}$ bin show higher values than those not associated with substructures (see coral squares). However, these differences remain within the error bars. For the $1-3R_{200}$ bin, ETGs in substructures exhibit smaller n values compared to those not identified as part of a substructure. Additionally, excluding the galaxies of Abell 1631 from the sample of ETGs in substructures does not alter the trend. (see bottom right panel in Figure 6.3.7)

In the case of LTGs, we see that the trend between all galaxies and then dividing them based on whether they were identified as part of a substructure or not does not actually change if we include the LTGs from substructures that belong to Abell 1631 (see the right panels).For the *transition galaxies*, we observe a similar behaviour: n increases as we approach the centre in almost all cases, considering all *transition galaxies* and those identified as part of a substructure or not (see the top right panel in Figure 6.3.6). However, excluding the galaxies of Abell 1631, we see in the bottom right panel of Figure 6.3.6 that in the two outermost bins for *transition galaxies* in substructures beyond R_{200}, the median n decreases towards the centre, similar to what we observe for the ETGs.

6.3.5 Effective radius as a function of mass

Another interesting relationship to explore is the mass-size relation. In Figure 6.3.8, we present the effective radius as a function of stellar mass for each morphological type. From top to bottom, we have ETGs in the first row, *transition galaxies* in the next row, followed by LTGs, and *other galaxies* in the last row. In the left column, we present all selected galaxies; in the middle column, galaxies are identified as part of a substructure; and in the right column, galaxies are not identified as part of substructures.

For ETGs and *other galaxies*, a higher stellar mass corresponds to a larger R_e. ETGs in substructures exhibit higher stellar masses and larger R_e values compared to those not identified as part of a substructure. Conversely, for *other galaxies*, those not identified as part of a substructure can reach larger radii and masses than *other galaxies* identified as part of substructures. In the case of *transition galaxies* (see the second row of panels in Figure 6.3.8), there is no clear relationship between stellar mass and effective radius, but *transition galaxies* in substructures tend to have higher M_* and R_e compared to those not identified as part of a structure. For LTGs, the mass-size relationship is not as clear as it is for ETGs and *other galaxies*, but it is still present, with LTGs being more massive than the other two morphological types. LTGs not identified as part of substructures show a higher fraction of galaxies with masses greater than $log(M_*[M_\odot]) > 10$.

6.3.6 Effective radius has a function of the Sérsic index

As we presented in Chapter 2, we use the $R_e - n$ plane to identify morphological differences between the CGs and the control sample. In this case, it allows us to compare galaxies in substructures with those not identified as part of them for each morphological type. In Figure 6.3.9, we show the $R_e - n$ contours for the r-band. From top to bottom, we present ETGs, *transition galaxies*, LTGs, and

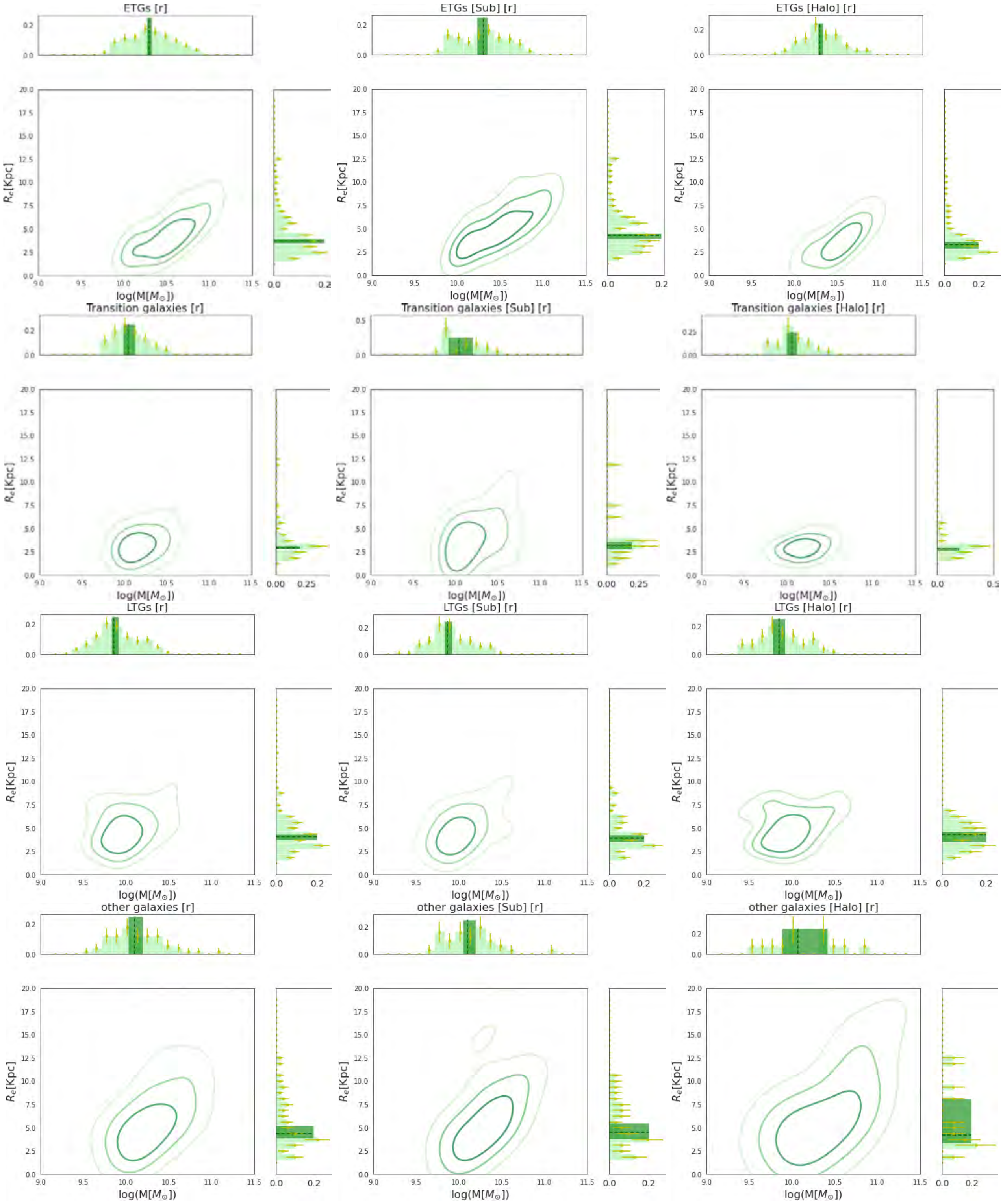

Figure 6.3.8: Effective radius as a function of stellar mass for each population: the top row for ETGs, the next row for *transition galaxies*, the penultimate row for LTGs, and the bottom row for 'Other' galaxies within $5 \times R_{200}$, categorised as within substructures and not identified as substructures from left to right, respectively. Each plot includes histograms at the margins showing the distribution of each parameter, where dashed lines indicate the median and shaded regions represent the 90% confidence interval using bootstrapping. Error bars on the histogram bars denote Poisson counting errors.

other galaxies. From left to right, we present all galaxies for each morphological type, those in substructures, and those not identified as part of a substructure.

For the ETGs in substructures, we see that they have larger R_e and n values compared to those not identified as part of a substructure. This indicates that ETGs in substructures are larger and light is more concentrated than their counterparts that were not classified as part of a substructure. However, caution is needed when interpreting this result because, as shown in the left panel of Figure 6.3.10, there are ETGs within the R_{200} of the Abell 1631 cluster. In the case of *transition galaxies*, those in substructures reach higher R_e and lower n values compared to galaxies not identified as part of a substructure, with contours extending to $n \sim 1.0$. Figure 6.3.10 shows that most *transition galaxies*, which were not identified as part of a substructure, are found within the R_{200}. Additionally, from the previous section, we see that n increases with decreasing distance to the cluster centre, suggesting that *transition galaxies* in substructures are undergoing morphological transformation as they fall towards the cluster centre, becoming smaller and more compact. For LTGs, the contours extend to $n \sim 2.0$ for both cases, suggesting that both samples are undergoing morphological transformation. In the case of *other galaxies*, there are no significant differences between those belonging to substructures and those that do not, except that galaxies in substructures achieve larger n value.

6.3.7 Morphological Distribution of Galaxies in Compact Groups, Field, and Abell 1644

Throughout this thesis, we have analysed three types of environments, CGs, field galaxies, and galaxies in Abell 1644. Therefore, it is worth exploring the morphological differences between these three environments. To compare these environments, it is necessary to examine their absolute magnitude distributions. In the top panels of Figure 6.3.11, we show the distribution of absolute magnitude in the r-band for galaxies in Abell 1644 (in green). In the left panel, we compare these with galaxies in CGs (in orange), and in the right panel, with galaxies in the control sample (in blue). These galaxies correspond to those analysed in Chapter 2. In both cases, we observe that galaxies in Abell 1644 have a different distribution compared to the other environments. Furthermore, both CG and control sample galaxies have a broader distribution in redshift.

Thus, we selected CG and control sample galaxies with an absolute magnitude between -19.6 to -22.2 in the r-band, and that was within a redshift range around the cluster's redshift, between 0.048 ± 0.01. This results in a subsample of 177 galaxies in CGs and 166 in the control sample. The bottom panels of Figure 6.3.11 show the distributions of these subsamples for CGs (left panel) and the control sample (right panel). We will use these subsamples to compare with the galaxies in Abell 1644.

In the top panels of Figure 6.3.12, we present the effective radius as a function of the Sérsic index for the three environments: the green contours show the distributions of galaxies in Abell 1644, the orange contours represent CG galaxies, and the blue contours correspond to galaxies in the control sample. The left panel displays ETGs, the middle panel shows *transition galaxies*, and the right panel shows LTGs. In the case of ETGs, no significant differences are observed between the environments. The only small distinction is that ETGs in CGs show slightly more concentrated light profiles compared to the control sample and cluster galaxies. For *transition galaxies*, we observe differences across the three environments: control sample galaxies display a unimodal distribution centred around $n \sim 1.7$, while CG galaxies show the bimodal distribution discussed in previous chapters. However, in this r-band magnitude range, the region of *peculiar galaxies* ($n \geq 2$) shows a lower density of galaxies. In the case of *transition galaxies* in Abell 1644, the highest-density contours are centred around $n \sim 2$, the region of peculiar galaxies, suggesting that most galaxies have likely undergone a

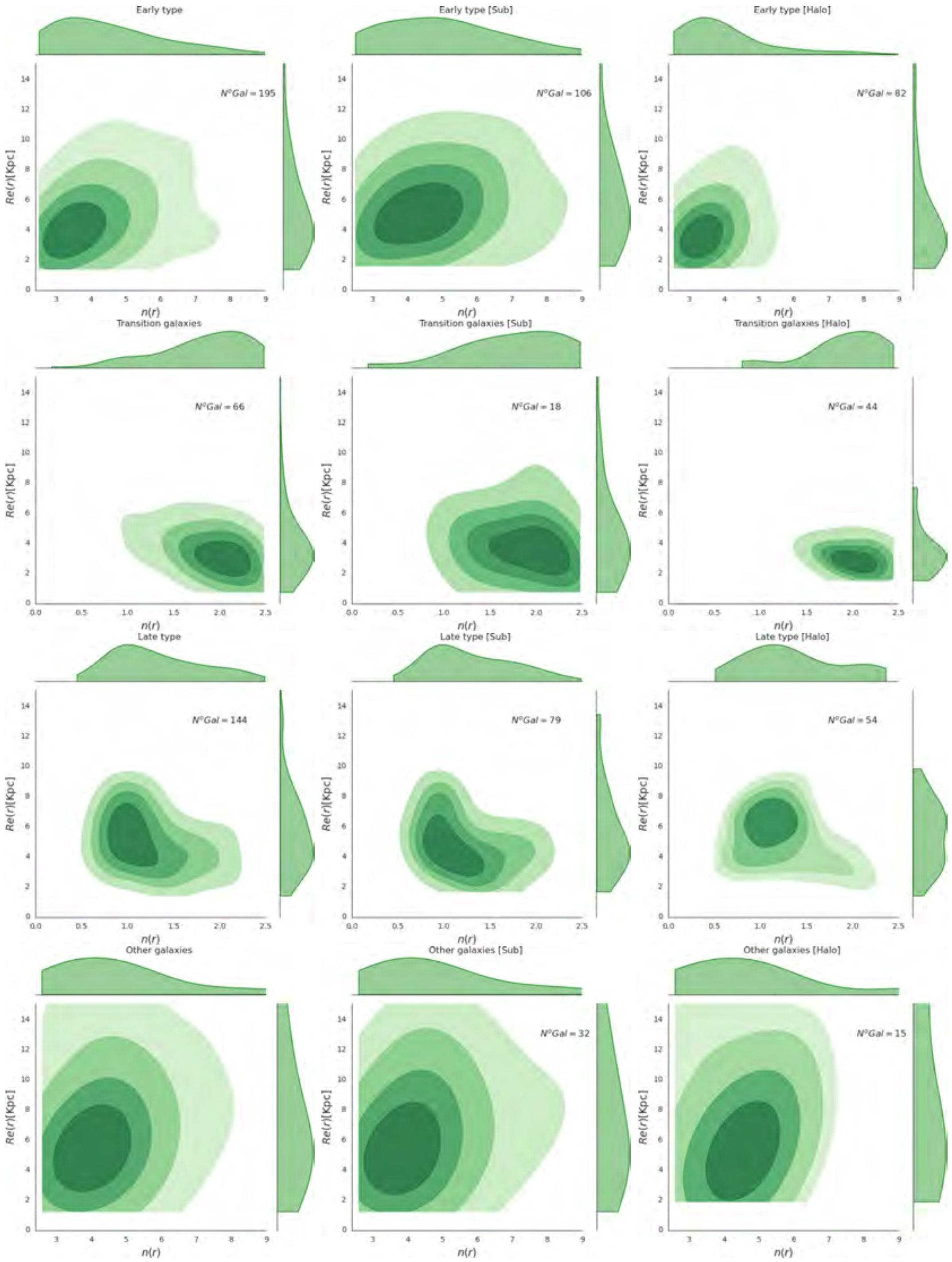

Figure 6.3.9: Effective radius as a function of Sérsic index for each population: the top row for ETGs, the next row for *transition galaxies*, the penultimate row for LTGs, and the bottom row for 'Other' galaxies within $5 \times R_{200}$, categorized as within substructures and not identified as substructures from left to right, respectively. The distribution of each parameter is shown in the margin of each plot.

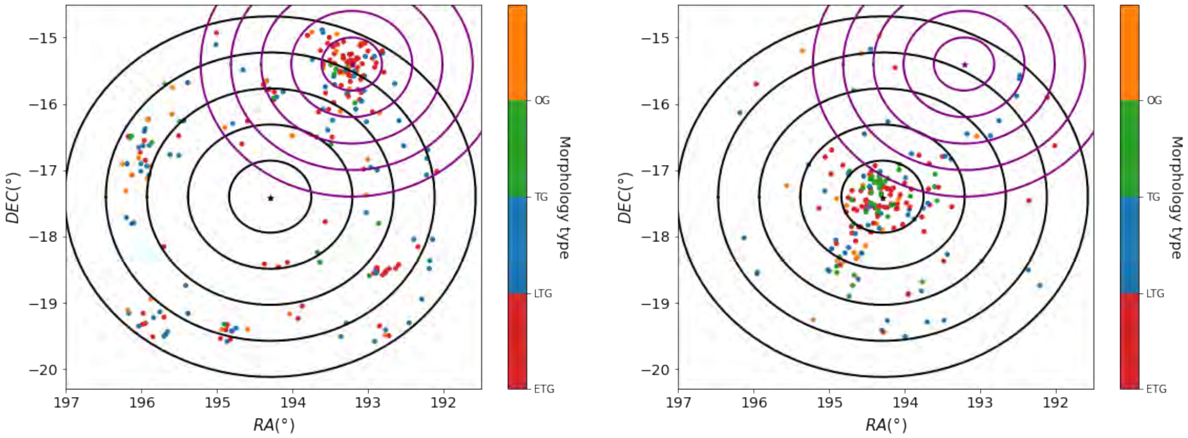

Figure 6.3.10: Galaxy positions in the sky. Similar to Figure 6.3.4, but in this case, the left panel only contains galaxies identified as part of a substructure, while the right panel contains galaxies not identified as part of a substructure.

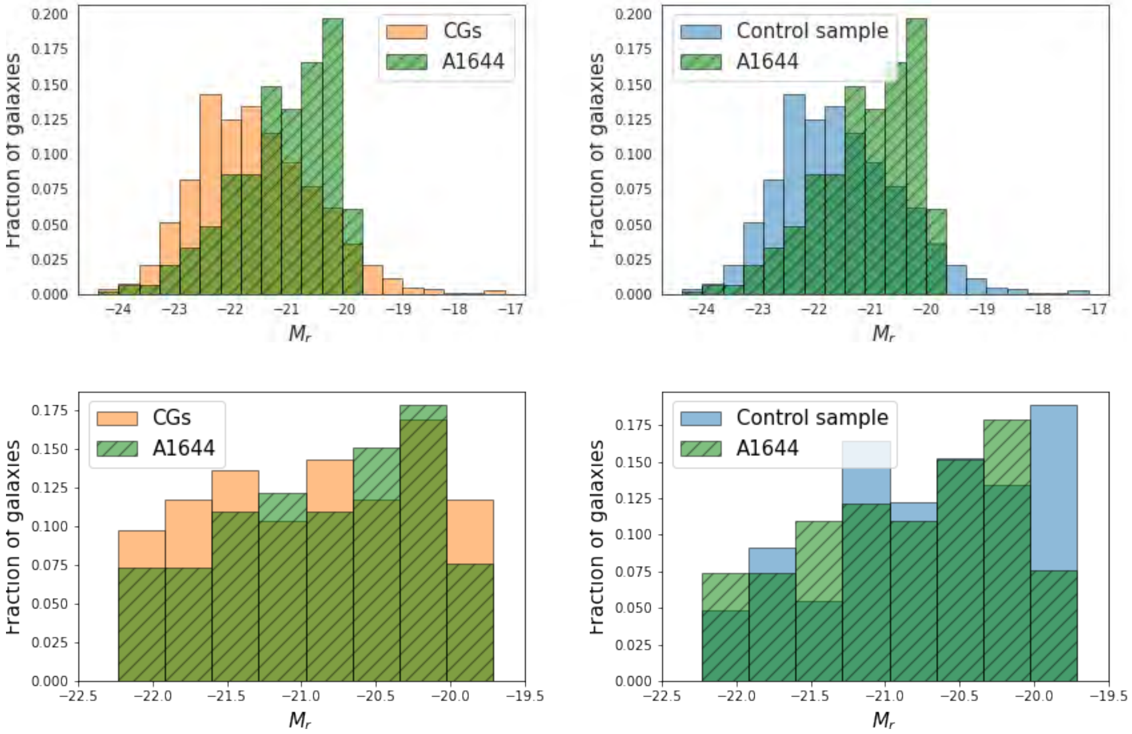

Figure 6.3.11: Absolute magnitude distribution in the r-band for galaxies in three environments: Abell 1644 (green), CGs (orange), and the control sample (blue). Top panels: The left panel compares the magnitude distribution of galaxies in Abell 1644 with those in CGs, while the right panel compares Abell 1644 galaxies with the control sample. In the bottom panels, we present the same comparisons but for a subsample of CGs and control galaxies with magnitudes between -19.6 to -22.2 in the r-band, and within a redshift range around the cluster's redshift, between 0.048 ± 0.01.

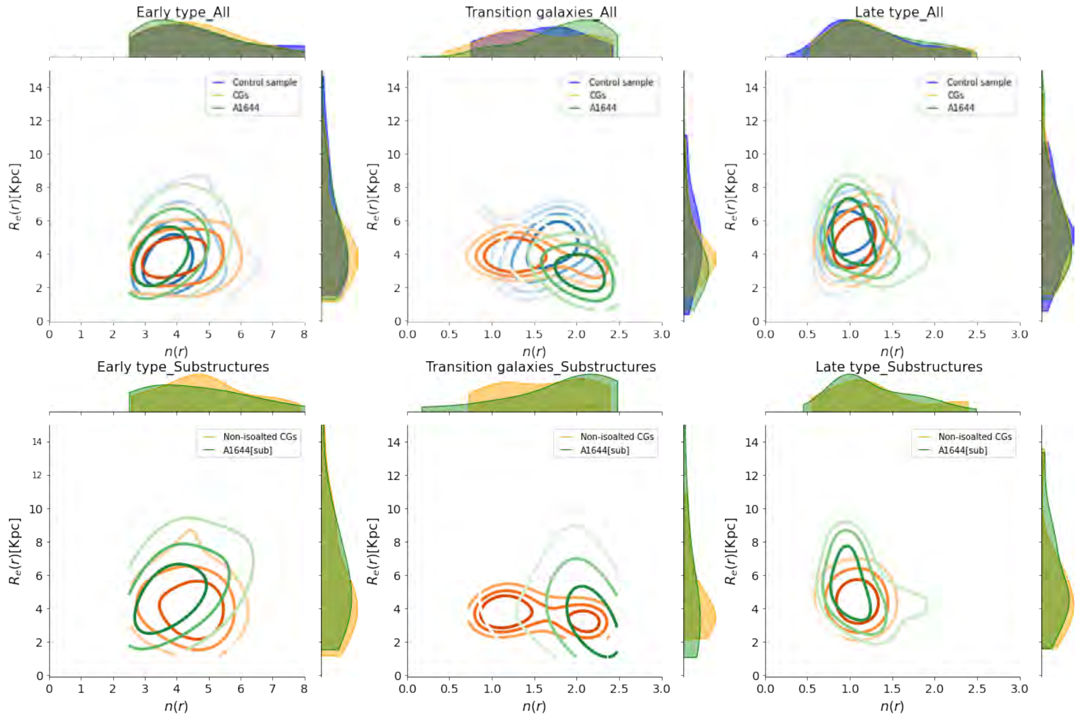

Figure 6.3.12: Effective radius as a function of the Sérsic index for galaxies in Abell 1644, CGs, and the control sample. Top panels: The green contours represent galaxies in Abell 1644, orange contours represent CG galaxies, and blue contours correspond to the control sample galaxies. Bottom panels: Galaxies in Abell 1644 substructures and non-isolated CGs. The left panel displays ETGs, the middle panel shows *transition galaxies*, and the right panel shows LTGs.

morphological transformation as observed for the galaxies in CGs that are not isolated (Chapter 3). For LTGs, the most notable difference is observed in cluster galaxies, where the contours extend up to $n \sim 2$, suggesting that some galaxies are undergoing morphological transformation, leading to more compact light profiles.

In the bottom panels of Figure 6.3.12, we present Abell 1644 galaxies in substructures without considering the galaxies detected as part of Abell 1631 and non-isolated CG galaxies. For ETGs (see the bottom-left panel), no major differences are found between the two environments. For *transition galaxies* in CGs, we observe bimodality, suggesting that in this magnitude range (from -22.2 to -19.5), non-isolated CG galaxies are undergoing morphological transformation. In contrast, for galaxies in Abell 1644 substructures, most have already undergone a transformation and display a larger average Sérsic index n. In the case of LTGs, we observe that those in the substructures of Abell 1644 reach higher Sérsic indices compared to the other two environments. This could suggest that morphological transformations are occurring in LTGs, rather than in *transition galaxies*, as is the case in CGs.

6.4 Sumary

In this Chapter, we explored the morphological properties of galaxies that are infalling into the Abell 1644 cluster as a galaxy group, focusing on how these properties change based on the distance from the cluster centre. Our analysis revealed several key findings:

- Distance from cluster centre: we observed significant variations in galaxy properties depending on their distance from the cluster centre. ETGs and *Transition Galaxies* showed peaks in their fraction distributions near the cluster centre and between $3-4\times R_{200}$. This fraction is due to the presence of another cluster, Abell 1631. LTGs and *other galaxies* exhibited a increasing trend in their fractions as the distance from the cluster centre increased.

- Effect of substructures: galaxies identified as part of substructures displayed different morphological characteristics compared to those not in substructures. ETGs in substructures had larger and more concentrated Sérsic indices compared to those outside ETGs in substructures. LTGs in substructures were generally smaller. *Transition galaxies* in substructures appeared to undergo morphological transformation, becoming more compact as they fell into the cluster.

- Sérsic index and effective radius: The median Sérsic index and effective radius varied across different wavelengths and environments. ETGs showed an increase in the Sérsic index with redder wavelengths, and those in substructures had a higher median index compared to those ETGs substructures in the outside part of the cluster. LTGs in substructures had slightly lower median Sérsic indices in redder filters in comparison with their counterparts that were not classified as part of a substructure, suggesting different evolutionary paths.

- Mass-size relation: The effective radius of both ETGs and *other galaxies* shows a positive correlation with stellar mass. ETGs within substructures extend to higher stellar masses and larger effective radii compared to those outside substructures. LTGs also follow a mass-size relation, though it is less pronounced than in ETGs. Additionally, LTGs in substructures located in the outermost regions of the cluster tend to be more massive on average than those in substructures closer to the cluster centre.

- Comparing effective radius as a function of Sérsic index across different environments: For LTGs the results suggest that morphological transformations may be more pronounced in galaxies within the substructures of Abell 1644, as indicated by higher Sérsic indices. In contrast, in CGs, these transformations could be occurring primarily in *transition galaxies*.

Chapter 7

Summary

Since the discovery of galaxies beyond our own, a wide variety of types with different colours, shapes, and sizes have been observed. This naturally raises questions about how galaxies transform and evolve. Observations reveal that galaxies in the local universe exhibit bimodality: most are either red galaxies with little or no recent star formation and morphologically early-type galaxies, or blue galaxies, late-type galaxies with star formation (e.g., Strateva et al. 2001, Bell et al. 2004, Baldry et al. 2006). Between these extremes, there are galaxies with intermediate properties. Thus, a persistent question is how galaxies evolve from star-forming spirals to quiescent ellipticals. It has been found that internal mechanisms related to star formation and AGN feedback can play a role (e.g., Efstathiou 2000, Peng et al. 2010a, Fabian 2012). Additionally, there are environmental mechanisms related to how galaxies interact with their surroundings that also drive these galaxy transformations (e.g., Toomre & Toomre 1972, Moore et al. 1996a, Peng et al. 2010a). Among these environmental mechanisms are galaxy interactions and mergers, which are more common in galaxy groups (e.g., Coziol & Plauchu-Frayn 2007), however, we can not exclude other phenomena such as ram pressure stripping. This leads to the notion that galaxies may have already undergone environmental effects—such as gas depletion and morphological changes—before groups are accreted into clusters, a process known as pre-processing (e.g., Eckert et al. 2014, Haines et al. 2015, Lopes et al. 2013). Understanding the physical processes causing pre-processing in groups is crucial for comprehending galaxy evolution in different structures within the Universe.

In particular, compact groups (CGs) are a type of galaxy group that are ideal for studying how galaxy interactions shape physical properties, due to their high galaxy densities comparable to cluster cores and their low-velocity dispersions (Hickson 1982). Studies have revealed that these systems act upon galaxies faster and more effectively in the process of transforming galaxies from star-forming to quiescent (Coenda et al. 2012, Walker et al. 2010, Bitsakis et al. 2015).

In this context, this thesis has focused on analysing the physical properties of galaxies in CGs to understand how dense environments affect galaxy evolution. Therefore, I selected data from 340 CGs in the Stripe 82 region and compared the properties of these galaxies with field galaxies, which it is our control sample. We used multi-wavelength data from the S-PLUS project (Mendes de Oliveira et al. 2019) and estimated the structural parameters of each galaxy using the MegaMorph code (Bamford et al. 2011,Häußler et al. 2013,Vika et al. 2013), complemented with the GSWL catalogue (Salim et al. 2018) to obtain the star formation rate (SFR). Additionally, we selected a second sample of 549 galaxies in CGs with MaNGA data to study the properties of these galaxies using IFU data. We also selected a new control sample of 1,098 field galaxies that also have MaNGA data.

We classify the galaxies using the Sérsic index in the r-band (n_r) and their $(u-r)$ colour, following the method proposed by Vika et al. (2015b). Galaxies with $(u-r)> 2.3$ and $n_r > 2.5$ are early-type galaxies (ETGs), while galaxies with lower or equal values are late-type galaxies (LTGs). In this thesis, we call galaxies with red colours and low Sérsic indices as *transition galaxies* and galaxies with blue colours and high Sérsic indices as *other galaxies*. We found that 52% of the CG galaxies analysed in this thesis are ETGs, 11% are *transition galaxies*, 22% are LTGs, and the remaining 15% are *other galaxies*. In the control sample, 33 %, 19%, 37%, and 11% are ETGs, *transition galaxies*, LTGs, and *other galaxies*, respectively. Thus, the CG sample has a higher fraction of ETGs compared to the control sample, while the control sample has a higher fraction of LTGs.

In Chapter 2, we find that galaxies of all types in CGs have a smaller effective radius compared to galaxies of the same type in the control sample, consistent with the findings of Coenda et al. (2012). This suggests that tidal interactions in CGs favor the loss of material from galaxies, resulting in a smaller average effective radius. Additionally, different trends with wavelength were observed in the median values of Sérsic index (n) and effective radius (R_e) depending on the morphological type and environment. For ETGs, both n and R_e increase with wavelength, with a smoother increase in CGs than in the control sample. For LTGs, n increases and R_e decreases with wavelength in both environments, indicating a redder and more concentrated population, likely associated with the presence of bulges. The results for n as a function of wavelength for ETGs and LTGs are consistent with those found by La Barbera et al. (2010), Kelvin et al. (2012), Vulcani et al. (2014), and Lima-Dias et al. (2021). However, for the variation of R_e, the mentioned studies (except Lima-Dias et al. 2021, who did not explore how this parameter changes with wavelength) agree on the decrease of R_e for redder filters for LTGs but not for ETGs, as they found that R_e also decreases. These studies (La Barbera et al. 2010, Kelvin et al. 2012, Vulcani et al. 2014) were interested in larger samples of galaxies to explore the relationship between color and structure within galaxies using optical-near-infrared imaging in bright, low-redshift galaxies, without giving relevance to the environment in which these galaxies are found. The differences in the behavior of R_e as a function of wavelength offer a promising opportunity to investigate how the environment impacts R_e, modifying it as a function of wavelength and how this information can be used to further improve our understanding of how the environment helps transform the shape of galaxies. In the case of *transition galaxies*, a different behaviour in CGs compared to the control sample was observed: R_e behaves like that of ETGs in CGs, while it resembles that of LTGs in the control sample, suggesting a morphological transformation occurring in galaxies associated to the CG environment.

In the $R_e - n$ distribution of *transition galaxies*, we observe a bimodality for CGs. One part of this bimodal distribution follows the same trend seen in the control sample, while another population, characterised by smaller R_e and larger n, is absent in the control sample. We refer to this distinct group as the *peculiar galaxy population*, suggesting they may be undergoing morphological transformation. Furthermore, CGs contain a higher fraction of quenched galaxies (defined as $log(sSFR) \leq -11$ based on the criterion proposed by Wetzel et al. 2013) regardless of galaxy type, compared to the control sample. This suggests that mechanisms such as tidal interactions, shocks, and turbulence likely contribute to the observed differences. These morphological results and the sSFR highlight the potential of CGs as ideal systems for galaxy pre-processing. An anti-correlation in the n-$log(sSFR)$ plane for *transition galaxies* leads to bimodality in this plane, with a significant fraction of the *peculiar galaxy population* contributing to the formation of the quenched galaxies, indicating both morphological and physical transformation. Therefore, these *transition galaxies* are candidate galaxies to be in the green infrared valley of CGs (e.g., Johnson et al. 2007, Gallagher et al. 2008, Walker et al. 2012).

In Chapter 3 We find the same correlation between dimensionless crossing time and velocity dispersion in CGs that has been observed in previous studies (e.g. Moura et al. 2020), indicating that CGs with higher velocity dispersion are more dynamically evolved. In addition, *transition galaxies* in CGs with higher velocity dispersions exhibit a clear bimodality in the $R_e - n$ plane, which is not evident for those in CGs with lower velocity dispersions. This suggests an accelerated morphological transformation process in CGs with higher velocity dispersions. Moreover, by cross-matching our CG sample with the catalog of Yang et al. (2007), who identifies groups with different numbers of members based on the halo-based group finder algorithm (Yang et al. 2005), we find that at least 27% of the CGs analyzed in this thesis are not isolated, i.e., they are part of a larger group. Additionally, we identified that 23% of all CGs have the same number of galaxies in the CGs and in the group identified by Yang et al. (2007), which, following the methodology of Zheng & Shen (2021), we classify as isolated CGs. Non-isolated CGs have higher velocity dispersions compared to isolated CGs, where 55% of non-isolated CGs have σ_G greater than 200 km/s, while in isolated CGs only 27% have higher values. As indicated by Zheng & Shen (2021) and Taverna et al. (2023), the velocity dispersion value may indicate whether the CG is isolated or not.

We also explore the $R_e - n$ plane for *transition galaxies* discerning whether they were part of isolated or non-isolated CGs. We found that *transition galaxies* in isolated CGs do not follow the same $R_e - n$ bimodal distribution as all *transition galaxies*, but they contribute to one of the two parts of this bimodality. Indeed, for *transition galaxies* in isolated CGs, we find a high density in the $R_e - n$ plane for $n < 1.75$, suggesting that most of these galaxies have not yet undergone morphological transformation. In contrast, the n distribution for *transition galaxies* in non-isolated CGs increases smoothly towards higher values, approaching the n value of the peculiar galaxy population. This indicates that the galaxies have already undergone a morphological transformation. These findings suggest that the major environment where the CGs reside accelerates morphological transformation.

We find that the fraction of quenched galaxies is higher for ETGs and *transition galaxies* in non-isolated CGs than in isolated CGs and the control sample. This indicates that major structures favor quenching within CG galaxies; hence, the physical properties of CG galaxies are influenced by interactions among galaxies within the CG, as well as interactions between the CG and its surrounding environment. Additionally, we found that the stellar mass of isolated CGs is lower compared to non-isolated CGs. In fact, the median of the distribution of non-isolated CGs is $10^{13.5}M_{\odot}$, which is in the range of structures with masses between $10^{13.5}$ to $10^{14.5}M_{\odot}$, where Pallero et al. (2019), using the EAGLE simulation, found that galaxies tend to enter a quenched state preferentially. This indicates that group mass is crucial for accelerating the transformations observed in non-isolated CGs.

With these results, we propose an evolutionary scheme for CGs, considering their connection to major structures. In this scenario, the major structures where CGs are embedded accelerate the quenching process in CG galaxies and their morphological transformation (see Figure 3.3.1). This subsequently influences the CG dynamics because non-isolated CGs have higher velocity dispersions than the isolated ones, suggesting that the dynamics of non-isolated CGs are dominated by the major structure where the CGs are located. We distinguish three stages:

- First stage: CGs are dominated by late-type galaxies with longer crossing times, often isolated and in an early stage of dynamical evolution. Morphological transformation begins here with the appearance of more compact *transition galaxies*.

- Second stage: CGs show a lower fraction of late-type galaxies and shorter crossing times compared to the first stage. These CGs were accreted by other groups or accreted galaxies from their surroundings. The environment accelerates the morphological transformation process, increasing the population of peculiar *transition galaxies*.

- Third stage: Most *transition galaxies* in CGs have undergone significant morphological transformations. In this phase, CGs may begin to be part of the major structures they inhabit (Bahé et al. 2019, Benavides et al. 2020, Haggar et al. 2022). An example of this state is the big infalling group (BIG), which is a CG falling into the cluster Abell 1367 discovered by Cortese et al. (2006), where the kinematics of the stars and gas show that the BIG is shaped by pre-processing produced by gravitational interactions in the local group environment combined with ram-pressure stripping by the global cluster halo (Fossati et al. 2019).

This evolutionary scenario is in agreement with Coziol et al. (2004), who suggest that the formation of CGs embedded in massive structures was earlier than the formation of isolated CGs, although the study by Coziol et al. (2004) was based on a small sample of 27 Hickson CGs. In this thesis, we have expanded the analysis by including 340 additional CGs, comprising a total of 1092 galaxies. Additionally, the results of Pompei et al. (2007) further support this scenario. Their study of Southern CGs (SCGs) revealed that SCGs, on average, contain more spiral members than HCGs. SCGs display a higher level of central star formation but have similar levels of nuclear activity, such as LINERs and AGNs, compared to HCGs. This indicates that SCGs are, on average, younger than HCGs.

In Chapter 4, using available spectroscopic data for both the CGs and the control sample of galaxies in SDSS, we analysed the ionisation mechanisms using the WHAN diagram (Cid Fernandes et al. 2010). Our analysis reveals that the percentage of AGN (including both weak AGN and strong AGN) in CGs is lower than in the control sample, with values of 18.3% ± 1.8 and 26.6% ± 1.5, respectively. This result was also found by Sohn et al. (2013b), although it is important to note that this result differs from those found by other authors (e.g. Martinez et al. 2007, 2008, 2010, Coziol et al. 1998). However, the comparison may not be entirely fair, as Sohn et al. (2013a) demonstrated that diagnostic diagrams impact the estimated AGN fraction. Therefore, comparing results obtained using different diagnostic methods may not be ideal. We also observe distinct ionisation patterns linked to galaxy morphology, with ETGs in CGs showing lower fractions of SF and AGN activity, likely due to their limited or absent gas reserves. In contrast, LTGs in CGs display slightly higher AGN fractions, particularly in strong AGN, likely driven by ongoing interactions that contribute to fuelling AGN activity. *Transition galaxies* in CGs also exhibit a higher fraction of weak AGN, suggesting limited gas availability. The overall lower AGN fraction in CGs compared to the control sample is attributed to a higher fraction of ETGs, which is consistent with the findings of Sohn et al. (2013a), who suggested that the nuclear activity of compact group galaxies is not strong due to a lack of gas supply, even though they may experience frequent galaxy–galaxy interactions and mergers that could trigger nuclear activity.

The fraction of AGN and SF decreases with increasing velocity dispersion in CGs, while RGs and PGs become more prevalent, especially in more dynamically evolved CGs with higher velocity dispersions. This behaviour, where the fraction of active galaxies (SF plus AGN) decreases with increasing velocity dispersion, is consistent with previous findings based on smaller samples (Coziol et al. 2004). We also investigated how the fraction of each galaxy type, classified by their ionisation mechanisms, varies depending on the environment in which the CGs are located. We find that galaxies in isolated CGs show higher fractions of SF and AGN galaxies, whereas galaxies in non-isolated CGs exhibit a higher fraction of PGs, underscoring the role of environmental interactions in depleting gas and influencing central activity. This is consistent with our finding that more evolved CGs, as proposed in Chapter 3, which are embedded in major structures, have a higher proportion of ETGs, higher velocity dispersion, and lower fractions of SF and AGN, along with a significant increase in PGs, in comparison to isolated CGs. These results support the evolutionary scenario we propose, in which galaxies in massive structures undergo rapid physical and morphological transformations, likely leading to reduced nuclear activity due to gas depletion. This aligns with the findings of Coziol et al. (2004), who suggests that CGs in massive structures evolve more rapidly or formed earlier than isolated CGs, whose evolution primarily depends on their own mass.

In the context of analysing galaxy properties in CGs using IFU data, it has been common to study specific galaxies and/or CGs that exhibit clear signs of interactions or mergers. These studies (e.g.

Torres-Flores et al. 2013a,Vogt et al. 2015, Gómez-Espinoza et al. 2023) collectively highlight that interactions between galaxies in CGs significantly influence the distribution of metals. In those studies, complex gradients and abrupt changes in oxygen abundance were identified, or smooth metal distribution between interacting galaxies was observed, indicating metal mixing. However, that was done for a few CGs and, hence, a homogeneous analysis of a larger sample of CGs galaxies was lacking. In this thesis, we analyse such a homogeneous and large sample in Chapter 5: we selected 549 galaxies in CGs and 1098 field galaxies, all with IFU data from MaNGA. We find that the D_{4000} profile values exhibit a clear dependence on stellar mass, with more massive galaxies showing higher D_{4000} values, indicating that their stellar populations are generally older.

Additionally, galaxies in denser environments, such as CGs, tend to have slightly higher D_{4000} values at a fixed stellar mass compared to those in less dense environments. This suggests that stellar populations in CGs might be older or more metal-rich (Kauffmann et al. 2004, Paulino-Afonso et al. 2020). When studying morphological types, the general trend of higher D_{4000} values with increasing stellar mass remains, though an exception to this trend is ETGs and *transition galaxies*, particularly in the lowest mass bin. Moreover, galaxies in non-isolated CGs typically show higher D_{4000} values than those in isolated CGs, implying environmental effects on stellar population ages or metallicity, with the exception that massive LTGs in non-isolated CGs appear younger or less metal-rich.

For galaxies dominated by star formation, i.e., those where the main ionisation mechanism at all radii is photoionisation by young stars, he Σ_{SFR} gradients reveal that the slopes of profiles vary slightly with galaxy stellar mass. Specifically, lower mass galaxies in control samples exhibit steeper profiles, while higher mass galaxies in CGs display steeper profiles. However, these differences are not significant as they fall within the error bars, which are the standard deviations.

For galaxies exhibiting nuclear activity—defined as those with star-forming spaxels only in the outer regions and classified as Seyfert or LINER in the central region according to the BPT diagnostic diagram—we found that those in CGs have higher Σ_{SFR} values and less steep slopes compared to the control sample. To further analyze the central ionisation mechanisms, we compared the BPT diagnostic diagram with the WHAN diagram and divided the sample of galaxies with nuclear activity into two groups. The first group includes galaxies where both diagnostic diagrams indicate that AGN is the dominant ionisation mechanism in the centre. The second group comprises galaxies that, while classified as LINER according to the BPT diagram, are identified by the WHAN diagram as having central ionisation primarily due to old stars. We observed a higher fraction of AGNs in galaxies with nuclear activity in CGs, whereas in the control sample, a larger fraction of galaxies shows central ionisation driven by old stars. This result aligns with Mulcahey et al. (2022), who observed that AGNs do not necessarily suppress star formation in their host galaxies. Additionally, galaxies in the control sample, where old stars predominantly drive central ionisation, exhibit lower star formation rates in the outer regions, consistent with the findings of Belfiore et al. (2017).

Regarding oxygen abundance gradients, galaxies generally exhibit a metallicity gradient with higher metallicity in their central regions (e.g Sánchez-Blázquez et al. 2014). There are no significant differences in median metallicity gradients between CGs and the control sample. Although low-mass galaxies in CGs show slightly higher metallicity in their outer regions compared to their counterparts in the control sample, these differences are not statistically significant. Overall, our findings support the notion that stellar mass is a more influential factor than the environment in regulating metallicity gradients in galaxies.

Expanding on the insights from Chapter 3, where we presented different trends in the physical and morphological properties of non-isolated compared to isolated CGs; we then focus in Chapter 6 on investigating how these properties change in galaxies within groups that are infalling into denser environments. Accordingly, we studied the properties of galaxies in the galaxy cluster Abell 1644, covering a range of $5 \times R_{200}$, with the objective of examining the morphological properties of galaxies falling into groups within this cluster. We found significant variations in galaxy properties depending on their distance from the cluster centre, with ETGs and *transition galaxies* peaking near the centre and at $3-4 \times R_{200}$, likely influenced by the presence of Abell 1631. In contrast, LTGs and *other galaxies* showed a decreasing trend in their fractions as they moved further from the cluster centre. The impact of substructures was notable, with galaxies within substructures exhibiting distinct morphological characteristics. ETGs in substructures had higher and more concentrated Sérsic indices, while LTGs in these substructures were generally smaller, indicating recent accretion. *Transition galaxies* in substructures appeared to become more compact as they approached the cluster. Additionally, variations in the Sérsic index and effective radius across different wavelengths highlighted differing evolutionary paths: ETGs in substructures had higher median Sérsic indices compared to those outside, while LTGs in substructures had slightly lower median Sérsic indices in redder filters. Finally, for LTGs, morphological transformations seemed more pronounced within the substructures of Abell 1644, as indicated by higher Sérsic indices, whereas in compact groups, such transformations appeared to be primarily occurring in *transition galaxies*.

As a general conclusion of this thesis, I want to highlight that our findings suggest that when analysing the properties of galaxies in CGs, it is essential to consider the major structures where CGs are located because this can significantly affect the evolution of their galaxy members. The physical properties of CG galaxies are influenced by both the galaxy-galaxy interactions within the CGs and the interactions of the CGs with their environment.

Chapter 8

Future Perspectives

In this chapter, I will introduce a series of follow-up studies that build upon the research presented in this thesis. These subsequent investigations are designed to further explore and deepen our understanding of how the environment influences galaxy properties, specifically by studying groups.

8.1 Future Research Directions for Abell 1644: Linking Previous Studies and Detailed Spectroscopic Analysis

In Chapter 6, we present the results of the morphological analysis for Abell 1644. However, a deeper analysis is necessary, linking previous studies. For this reason, the next steps to consider are:

- Compare with previous research: conduct a detailed comparison with earlier studies to deepen the analysis of these results. This will help contextualise findings within the broader scientific literature and highlight any unique aspects or discrepancies that deserve further investigation.
- Spectroscopic analysis of subsample: Use the subsample of galaxies with spectroscopic information to verify which galaxies, identified outside R_{200} and not part of a substructure, are falling into the cluster individually. This analysis should include studying the phase-space diagram to determine how the morphological properties of galaxies differ between those falling as part of a substructure versus those falling individually.

These steps will enhance the understanding of how morphological properties vary with cluster environment and substructure membership, providing deeper insights into galaxy evolution within clusters.

8.2 Kinematics in CG galaxies: Tully-Fisher relation

In this thesis, we explore the physical properties of galaxies in CGs using MaNGA observations. This sample offers a valuable opportunity to study the kinematics of galaxies in CGs, as previous studies have analysed a maximum of 36 galaxies, making the MaNGA sample statistically significant for advancing our understanding of galaxy kinematics in CGs. Additionally, as highlighted in this thesis, it is crucial to distinguish between isolated CGs and non-isolated ones, since the major structures embedding the CGs influence the evolutionary paths of their galaxies.

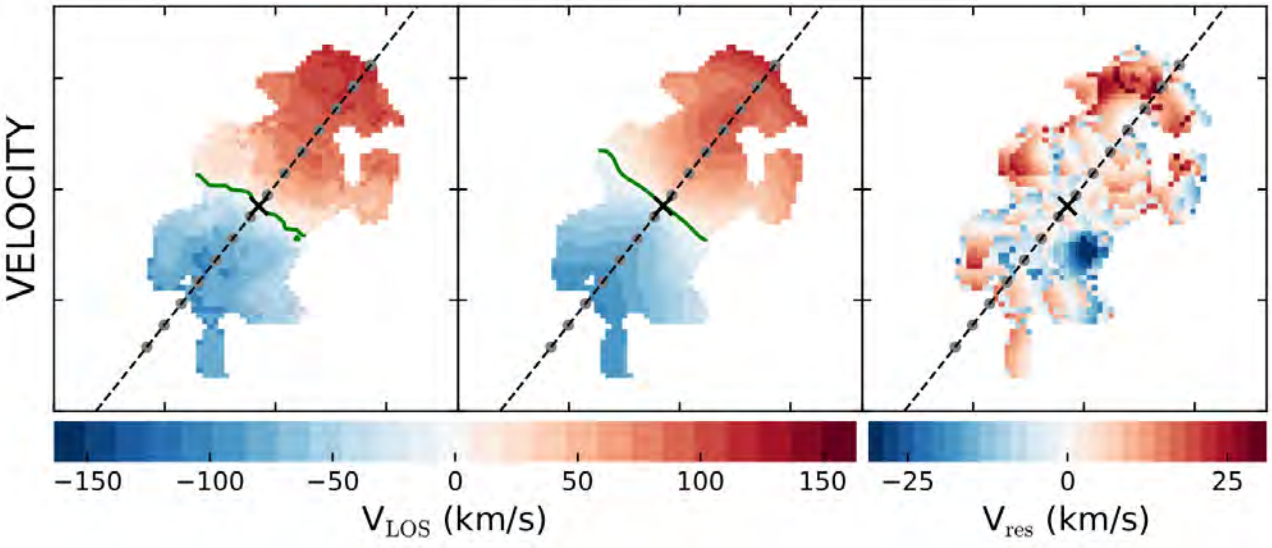

Figure 8.2.1: An example of one of the galaxies from our CG sample. The left panel shows the observed velocity map estimated from the H_{α} cube, the middle panel displays the model velocity map generated by BAROLO, and the right panel shows the residuals (observed velocity map minus the model).

Objective: To investigate the kinematic properties of galaxies in CGs compared to a control sample of field galaxies, in order to explore how these properties affect their position in the Tully-Fisher relation. This includes analysing rotational velocity, velocity dispersion, and asymmetries in gas kinematics. Additionally, the study will examine the impact that the environment embedding the CGs may have on the kinematics of their members compared to galaxies in isolated CGs.
Methodology: We will analyse the gas kinematics of galaxies using MaNGA data. The kinematic modelling is performed using the 3D BAROLO software (Di Teodoro & Fraternali 2015), which creates a disc model for the rotating gas based on H_{α} emission lines, in Figure 8.2.1 shows an example of one of the galaxies in our CG sample, modelled using BAROLO. Using parameters such as disc inclination and position angle, derived from the Jeans Anisotropic Modelling method estimated by Zhu et al. (2023b). We will compare the results between galaxies in CGs and the control sample to assess the impact of their environments on their kinematic behaviour.

8.3 Properties of galaxies around CGs

We know that CGs are not always isolated groups; they are sometimes part of larger structures ranging from loose groups to clusters. Depending on the group sample studied, the percentage of non-isolated CGs may vary between 20-90%. In a recent study analysing galaxy colours in CGs embedded in different environments in the large-scale universe structure, such as filaments, nodes, voids, and loose groups, and comparing them with galaxies around CGs, Taverna et al. (2024) found that the fractions of red galaxies are generally higher for CGs than for other structures or the field, especially in less dense environments. This suggests that the main differences observed in the fractions of red galaxies in CGs compared to those in the corresponding environment are due to processes occurring inside CGs. The influence of the global environment, i.e., where the CGs are located, can be seen mainly in how the overall physical properties of CGs change with the environment, which likely causes differences observed in the fraction of red galaxies in CGs when comparing high and low-density

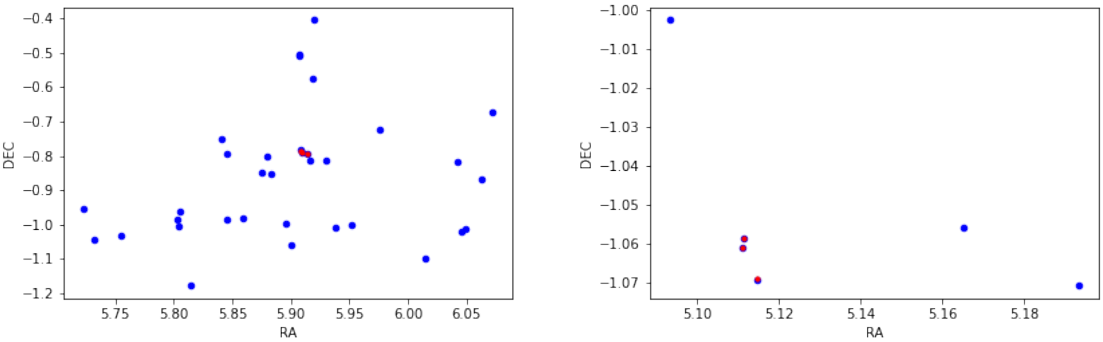

Figure 8.3.1: Two examples of CGs embedded within other structures are depicted in the figure below. The galaxies belonging to the CGs are represented in red, while the galaxies from the Yang et al. (2007) catalogue are shown in blue.

environments.

On the other hand, the physical nature of CGs is still not well understood, posing a challenge at the observational level due to the lack of access to 3D information on each CG. Therefore, there is contamination from groups that appear compact but are only chance alignments. Analysing the properties of galaxies around CGs can provide clues, along with analysing the positions of CGs in larger structures, to better understand how these structures evolve.

Objective: To gain a broader understanding of how environments impact the evolution of CGs, I aim to explore the properties of galaxies within major-scale structures. By comparing these properties with those of galaxies in CGs, I seek to identify any similarities or correlations. This comprehensive analysis will provide insights into how environmental factors influence the evolution of CGs and contribute to our overall understanding of galaxy evolution.

Methodology: During This thesis, I found that 40% of 226 CGs are not isolated but belong to major-scale structures. My focus was solely on analysing the galaxies within the CGs, neglecting those belonging to the major structures. Therefore, the idea is to analyse the morphological properties through morphological fitting in multiple bands using a Sersic profile with my MorphoPLUS code, utilising the photometric images from S-PLUS. Additionally, we can study the physical properties of these galaxies using spectra from SDSS, as these groups are located in Stripe 82 and have catalogues available with emission lines, allowing us to analyse star formation, ionisation mechanisms, and use spectral indices such as the D_{4000} spectral break index, which serves as a proxy for stellar population ages. This analysis aims to compare the properties of galaxies in the larger structures versus galaxies within the CGs.

8.4 Morphology analysis in galaxy groups

It has been observed that galaxies in CGs tend to have older stellar populations compared to loose groups (Coenda et al. (2012)), especially among early-type galaxies, and late-type galaxies in dynamically old CGs display two distinct populations: one with normal star formation rates and another with significantly reduced star formation. This implies that the transition from star-forming to quiescent states happens rapidly in CGs, making them an extreme environment for such transformations. These findings align with this thesis when compared with field galaxies. However, still other questions remain open: what occurs when comparing with a more diverse sample of groups? Are the physical transformations observed in CGs unique to this environment, or can similar transformations be observed in other group types?

Objective: The objective of this project is to study galaxy groups to understand how low-mass structures influence galaxy evolution and facilitate pre-processing. Additionally, this future study aims to compare these groups with CGs to assess whether similar transformations occur in both environments. By examining the properties of galaxies within different group structures, including star formation rates, and morphological properties, this research seeks to elucidate the role of low-mass structures in shaping galaxy evolution and to provide insights into the processes driving galaxy transformation within various group environments.

Methodology: I will identify groups in S-PLUS data using the catalogue by Tago et al. (2006) and analyse their morphological parameters using MorphoPLUS code. Star formation rates will be estimated through SED-fitting using codes such as CIGALE or Bagpipes, using the magnitudes from the S-PLUS catalogues. This research will provide insights into the processes driving galaxy transformation within groups of galaxies with a large range of members.

Appendix A

A.1 Other region

In the fourth quadrant of the classification proposed by Vika et al. (2015b), and shown in Figure 2.3.1, we find a population of blue galaxies having high Sérsic indices. We find that 14.9% and 10.4% of CGs and control sample galaxies lie in this region, respectively. In Figure A.1.1 we observe no significant difference between the median effective radius for the environment of each population. Furthermore, the $R_e - n$ distribution for each population (shown in Figure A.1.2) does not show significant variations and reaches similar values to the ETGs in the R_e. In this region the mean $Log(sSFR)$ is $-11.2^{-11.7}_{-10.9}$ for the CGs and $-10.6^{-10.8}_{-10.5}$ for the control sample (in a 90% confidence interval, in both cases using SDSS data). In Figure A.1.3 we show the contours for the SFR and $sSFR$ as a function of stellar mass for galaxies in the other region. We observe that the galaxies in CGs span a wider range in the plots compared to the control sample. In particular, we observe a bimodality in galaxies in CGs (lower panels), which could indicate that in this region there is a mixture of different types of galaxies.

For this reason, we made a visual inspection of the galaxies in this region. We found that 49% of CGs galaxies have an expected shape; 40% have a disk-like shape and 11% have clear signs of merger. In the case of the control sample, we found a 38% of spheroids and 62% of disk-like objects. This explains why we observe similar $R_e - n$ counterpoints to the ETGs, since spheroidal galaxies would dominate in this plot. In the case of the SFR-mass plots disk-like galaxies dominate, explaining the high values found in the median. This is because 36% of the star-forming galaxies located in CGs, in the fourth quadrant of Figure 2.3.1, have spheroidal shape or show signs of merging, while in the control sample 22% have spheroidal shape.

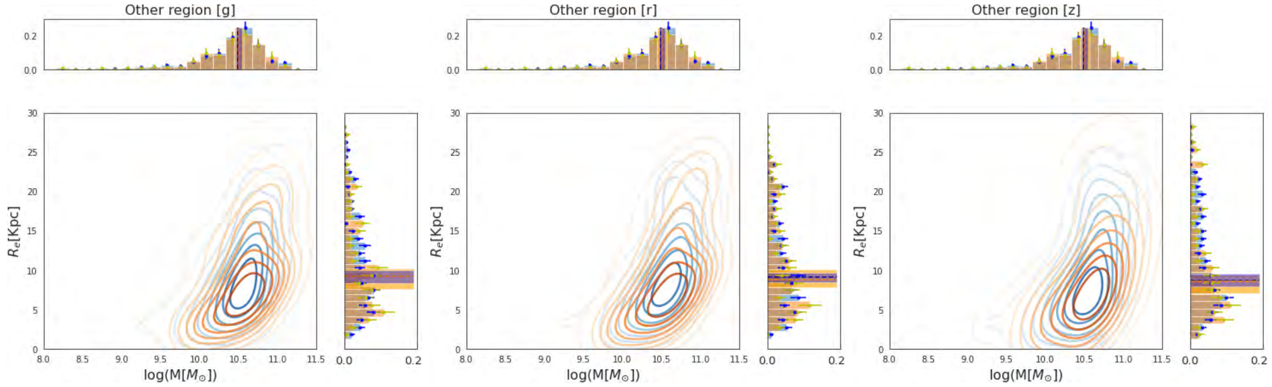

Figure A.1.1: Effective radius as a function of stellar mass for galaxies in the other region, in g,r and z filters from left to right of the plot, respectively. Blue contours are control sample galaxies and orange contours represent CG galaxies. At the margin of each plot are histograms of each parameter, in which the dashed lines represent the median and the shaded lines represent the 90% CI using boostrapping, and the error bars in the histogram bars are the Poisson counting error.

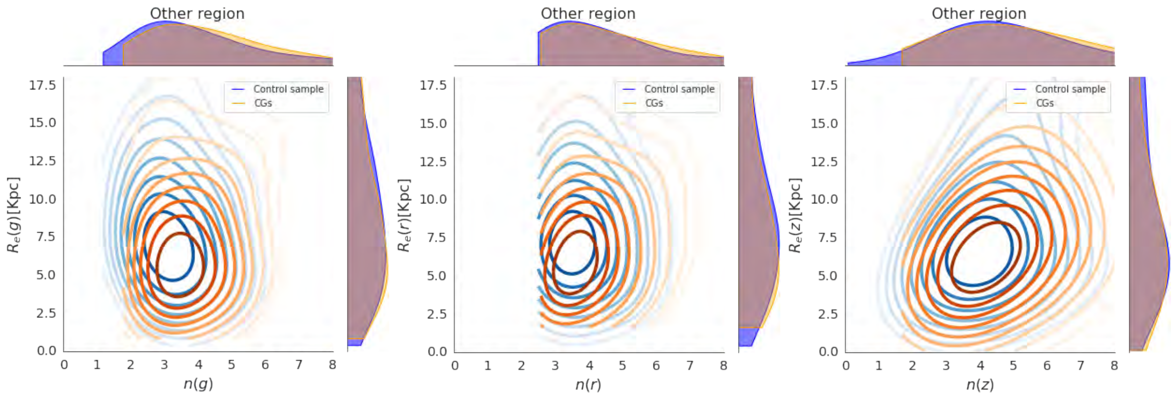

Figure A.1.2: Same as figure 2.3.7 but for galaxies in the region that we call other.

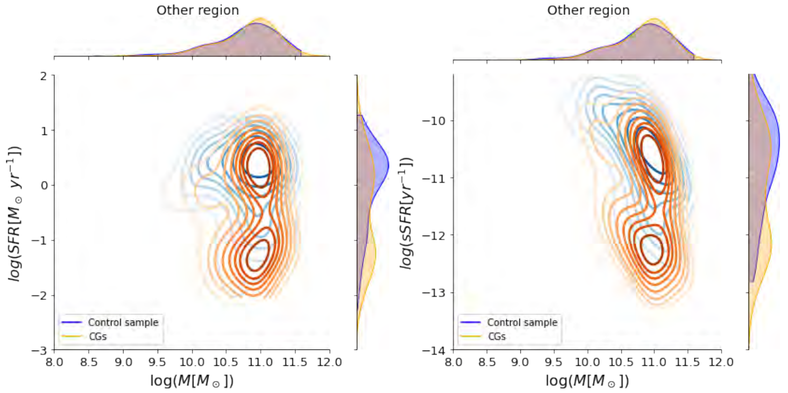

Figure A.1.3: The contours for the SFR (left plot) and $sSFR$ (right plot) as a function of stellar mass for galaxies in the other region. In blue contours for galaxies in the control sample, and in orange contours for CGs. ETGs.

Acknowledgments

Siempre escuché que hacer un doctorado es como correr una maratón, pero, desde mi perspectiva, no lo veo así. Más bien, el doctorado se asemeja a esos cuatro o cinco meses de entrenamiento que te preparan para completar la maratón el día de la carrera. Es en ese período donde la disciplina y la constancia, acumulando kilómetros, juegan un papel clave, incluso en esos días en que faltan las ganas o la motivación para entrenar.

El apoyo de las personas que me acompañaron en este largo proceso ha sido fundamental. Como en una maratón, no se corre solo: están quienes te animan desde el costado, quienes entrenan contigo y quienes te recuerdan por qué comenzaste. Quiero agradecer, en primer lugar, a mis asesores, Sergio Torres y Antonela Monachesi, por guiarme durante estos años con su dedicación y constante retroalimentación, ayudándome a formarme como académica. Agradezco también su apoyo incondicional a lo largo de esta investigación, especialmente durante los dos años que realicé el doctorado desde Colombia. Tanto ellos como yo tuvimos que aprender a superar los retos de la pandemia y la virtualidad.

Extiendo mi agradecimiento a las personas del Departamento de Astronomía por compartir conmigo su pasión por la disciplina, por hacerme sentir bienvenida. A Facundo Gómez, por sus valiosas sugerencias y discusiones científicas, y junto con Carolina Andrade, por su paciencia y apoyo con los trámites migratorios. Agradezco también a Claudia Mendes y Ricardo Amorín, por dedicar su tiempo cada semestre para escuchar mis avances y enriquecer las discusiones con sus sugerencias. En esta misma línea, agradezco al tribunal de mi defensa: Yara Jaffe, Analía Smith, Rodrigo Carrasco y Ricardo Amorín, por leer este manuscrito y por los comentarios que mejoraron el texto.

Quiero dar las gracias también a mis compañeros Dania, Camila, Eli, Eunice, Nico, Alex, Fer, Ciria, Noe y Franklin, por acompañarme día a día, por ser una constante fuente de apoyo y por enseñarme tantas palabras en 'chileno'. Gracias por las tardes de fútbol, los domingos de pintura y los innumerables cafés después del almuerzo. Al grupo de colombianos, Leidy, Uchima y Frank, por estar siempre cuando los necesitaba. A Lorena Vergara y Esaú Muñoz, por abrirme las puertas de su hogar y hacerme sentir parte de su familia en tantas festividades, compartiéndome su cultura y tradiciones.

Desde niña, decía que quería estudiar las estrellas, y desde entonces mi mamá y mi hermana han sido mi apoyo incondicional, siempre impulsándome a alcanzar mis sueños. Su amor y confianza en mí han sido esenciales para que hoy esté aquí, cumpliendo esa meta que nació cuando era pequeña. A mis sobrinas, Sharon y Sara, les agradezco por iluminar mis días con su alegría y hacer este camino más llevadero con su cariño.

Esta tesis fue realizada gracias al financiamiento de ANID a través de la 'Beca de Doctorado Nacional' N. 21202024. Agradezco también el apoyo financiero de la Sociedad Max Planck mediante un Partner Group grant y del Programa de Investigación e Innovación Horizon 2020 de la Unión Europea bajo el acuerdo de beca Marie Sklodowska-Curie N.º 734374, proyecto acrónimo: LACEGAL, lo que me permitió viajar al Instituto Max Planck para desarrollar una parte de esta tesis. Adicionalmente, agradezco el apoyo del proyecto Basal FB210003 del Centro de Astrofísica y Tecnologías Afines (CATA). Finalmente, expreso mi agradecimiento a la colaboración de S-PLUS y al apoyo de la Vicerrectoría de Investigación y Posgrado por el respaldo institucional que ha permitido la participación del Departamento de Astronomía en el proyecto S-PLUS.

Bibliography

Abadi M. G., Moore B., Bower R. G., 1999, MNRAS, 308, 947

Abazajian K. N., et al., 2009, ApJS, 182, 543

Adelman-McCarthy J. K., et al., 2006, ApJS, 162, 38

Aguerri J. A. L., Zarattini S., 2021, Universe, 7, 132

Aihara H., et al., 2011, ApJS, 193, 29

Alatalo K., et al., 2015, ApJ, 812, 117

Alberts S., Noble A., 2022, Universe, 8

Almeida-Fernandes F., et al., 2022, MNRAS, 511, 4590

Alonso M. S., Lambas D. G., Tissera P., Coldwell G., 2007, MNRAS, 375, 1017

An K., 1933, Giorn Dell'inst Ital Degli Att, 4, 89

Andernach H., Coziol R., 2005, in Fairall A. P., Woudt P. A., eds, Astronomical Society of the Pacific Conference Series Vol. 329, Nearby Large-Scale Structures and the Zone of Avoidance. pp 67–76 (`arXiv:astro-ph/0406327`)

Andrae R., Jahnke K., Melchior P., 2011, MNRAS, 411, 385

Argudo-Fernández M., Shen S., Sabater J., Duarte Puertas S., Verley S., Yang X., 2016, A&A, 592, A30

Bahé Y. M., et al., 2019, MNRAS, 485, 2287

Baldry I. K., Balogh M. L., Bower R. G., Glazebrook K., Nichol R. C., Bamford S. P., Budavari T., 2006, MNRAS, 373, 469

Baldwin J. A., Phillips M. M., Terlevich R., 1981, PASP, 93, 5

Ball N. M., Loveday J., Brunner R. J., 2008, MNRAS, 383, 907

Ballesteros J., Gonzalez J. J., 1994, in American Astronomical Society Meeting Abstracts. p. 52.15

Balogh M. L., Morris S. L., Yee H. K. C., Carlberg R. G., Ellingson E., 1999, The Astrophysical Journal, 527, 54

Bamford S. P., Häußler B., Rojas A., Borch A., 2011, in Evans I. N., Accomazzi A., Mink D. J., Rots A. H., eds, Astronomical Society of the Pacific Conference Series Vol. 442, Astronomical Data Analysis Software and Systems XX. p. 479

Barton E., Geller M., Ramella M., Marzke R. O., da Costa L. N., 1996, AJ, 112, 871

Barton E. J., de Carvalho R. R., Geller M. J., 1998, AJ, 116, 1573

Belfiore F., et al., 2017, MNRAS, 466, 2570

Belfiore F., et al., 2019, AJ, 158, 160

Bell E. F., de Jong R. S., 2001, The Astrophysical Journal, 550, 212–229

Bell E. F., et al., 2004, ApJL, 600, L11

Benavides J. A., Sales L. V., Abadi M. G., 2020, Monthly Notices of the Royal Astronomical Society, 498, 3852

Bertin E., Arnouts S., 1996, Astronomy and astrophysics supplement series, 117, 393

Bitsakis T., Dultzin D., Ciesla L., Krongold Y., Charmandaris V., Zezas A., 2015, MNRAS, 450, 3114

Bitsakis T., et al., 2016, MNRAS, 459, 957

Blanton M. R., Moustakas J., 2009, ARA&A, 47, 159

Blanton M. R., Roweis S., 2007, AJ, 133, 734

Blanton M. R., et al., 2005, AJ, 129, 2562

Blanton M. R., et al., 2017, AJ, 154, 28

Brasseur C. M., McConnachie A. W., Ellison S. L., Patton D. R., 2009, MNRAS, 392, 1141

Brown W., Patton D. R., Ellison S. L., Faria L., 2023, MNRAS, 522, 5107

Bruzual G., Charlot S., 2003, MNRAS, 344, 1000

Bundy K., et al., 2015, ApJ, 798, 7

Burbidge E. M., Burbidge G. R., 1959, ApJ, 130, 23

Byrne-Mamahit S., Hani M. H., Ellison S. L., Quai S., Patton D. R., 2023, MNRAS, 519, 4966

Caldwell N., Rose J. A., Sharples R. M., Ellis R. S., Bower R. G., 1993, AJ, 106, 473

Calzetti D., 2001, PASP, 113, 1449

Cantalupo S., 2010, MNRAS, 403, L16

Cappellari M., Copin Y., 2003, MNRAS, 342, 345

Cappellari M., Emsellem E., 2004, PASP, 116, 138

Cardelli J. A., Clayton G. C., Mathis J. S., 1989, ApJ, 345, 245

Carroll B. W., Ostlie D. A., 2017, An introduction to modern astrophysics, Second Edition

Cattorini F., Gavazzi G., Boselli A., Fossati M., 2023, A&A, 671, A118

Cenarro A. J., et al., 2019, A&A, 622, A176

Chabrier G., 2003, PASP, 115, 763

Cheng C., et al., 2023a, ApJ, 954, 74

Cheng C., et al., 2023b, The Astrophysical Journal, 954, 74

Cherinka B., et al., 2019, AJ, 158, 74

Chilingarian I. V., Melchior A.-L., Zolotukhin I. Y., 2010, Monthly Notices of the Royal Astronomical Society, 405, 1409

Choi Y.-Y., Park C., Vogeley M. S., 2007, ApJ, 658, 884

Cid Fernandes R., Stasińska G., Schlickmann M. S., Mateus A., Vale Asari N., Schoenell W., Sodré L., 2010, MNRAS, 403, 1036

Cid Fernandes R., Stasińska G., Mateus A., Vale Asari N., 2011, MNRAS, 413, 1687

Ciotti L., 1991, A&A, 249, 99

Coenda V., Muriel H., Martínez H. J., 2012, A&A, 543, A119

Conselice C. J., 2003, ApJS, 147, 1

Cortese L., Gavazzi G., Boselli A., Franzetti P., Kennicutt R. C., O'Neil K., Sakai S., 2006, A&A, 453, 847

Coziol R., Plauchu-Frayn I., 2007, AJ, 133, 2630

Coziol R., de Carvalho R. R., Capelato H. V., Ribeiro A. L. B., 1998, The Astrophysical Journal, 506, 545–556

Coziol R., Brinks E., Bravo-Alfaro H., 2004, AJ, 128, 68

Cristóbal-Hornillos D., et al., 2015, in Highlights of Spanish Astrophysics VIII. pp 798–803

Cypriano E. S., Sodré Laerte J., Campusano L. E., Dale D. A., Hardy E., 2006, AJ, 131, 2417

Da Rocha C., Mendes de Oliveira C., 2005, MNRAS, 364, 1069

Darg D. W., et al., 2010, MNRAS, 401, 1552

Davis M., Efstathiou G., Frenk C. S., White S. D. M., 1985, ApJ, 292, 371

De Rosa A., et al., 2015, Monthly Notices of the Royal Astronomical Society, 453, 214–221

De Vaucouleurs G., 1959, Classification and Morphology of External Galaxies. Springer Berlin Heidelberg, Berlin, Heidelberg, pp 275–310, doi:10.1007/978-3-642-45932-0˙7, `https://doi.org/10.1007/978-3-642-45932-0_7`

Deng X. F., He J. Z., Wu P., 2008, A&A, 484, 355

Di Matteo P., Combes F., Melchior A. L., Semelin B., 2007, A&A, 468, 61

Di Teodoro E. M., Fraternali F., 2015, MNRAS, 451, 3021

Díaz-Giménez E., Zandivarez A., 2015, A&A, 578, A61

Díaz-Giménez E., Taverna A., Zandivarez A., Mamon G. A., 2020, MNRAS, 492, 2588

Diaz-Gimenez E., Zandivarez A., Mamon G., 2021, Monthly Notices of the Royal Astronomical Society, 503, 394

Domínguez Sánchez H., Huertas-Company M., Bernardi M., Tuccillo D., Fischer J. L., 2018, Monthly Notices of the Royal Astronomical Society, 476, 3661

Dressler A., 1980, ApJ, 236, 351

Drory N., et al., 2015, AJ, 149, 77

Duplancic F., O'Mill A. L., Lambas D. G., Sodré L., Alonso S., 2013, MNRAS, 433, 3547

Duplancic F., Lambas D. G., Alonso S., Coldwell G. V., 2021, MNRAS, 504, 4389

Díaz-Giménez E., Mamon G. A., Pacheco M., Mendes de Oliveira C., Alonso M. V., 2012, Monthly Notices of the Royal Astronomical Society, 426, 296

Eckert D., et al., 2014, A&A, 570, A119

Efstathiou G., 2000, MNRAS, 317, 697

Eke V. R., Baugh C. M., Cole S., Frenk C. S., Navarro J. F., 2006, MNRAS, 370, 1147

Ellison S. L., Patton D. R., Simard L., McConnachie A. W., 2008, The Astronomical Journal, 135, 1877

Ellison S. L., Patton D. R., Mendel J. T., Scudder J. M., 2011, Monthly Notices of the Royal Astronomical Society, 418, 2043

Ellison S. L., Viswanathan A., Patton D. R., Bottrell C., McConnachie A. W., Gwyn S., Cuillandre J.-C., 2019, Monthly Notices of the Royal Astronomical Society, 487, 2491

Faber S. M., Jackson R. E., 1976, ApJ, 204, 668

Fabian A. C., 2012, ARA&A, 50, 455

Falcón-Barroso J., Sánchez-Blázquez P., Vazdekis A., Ricciardelli E., Cardiel N., Cenarro A. J., Gorgas J., Peletier R. F., 2011, A&A, 532, A95

Fossati M., Fumagalli M., Gavazzi G., Consolandi G., Boselli A., Yagi M., Sun M., Wilman D. J., 2019, MNRAS, 484, 2212

Freeman K. C., 1970, ApJ, 160, 811

Gallagher S. C., Johnson K. E., Hornschemeier A. E., Charlton J. C., Hibbard J. E., 2008, ApJ, 673, 730

Gavazzi G., Fumagalli M., Cucciati O., Boselli A., 2010, A&A, 517, A73

George K., Subramanian S., Paul K. T., 2019, A&A, 628, A24

Goddard D., et al., 2017, MNRAS, 465, 688

Gómez-Espinoza D. A., Torres-Flores S., Firpo V., Amram P., Epinat B., Contini T., Mendes de Oliveira C., 2023, MNRAS, 522, 2655

Gómez-Flechoso M. A., Domínguez-Tenreiro R., 2001, ApJL, 549, L187

Goto T., Yamauchi C., Fujita Y., Okamura S., Sekiguchi M., Smail I., Bernardi M., Gomez P. L., 2003, Monthly Notices of the Royal Astronomical Society, 346, 601

Graham A. W., Janz J., Penny S. J., Chilingarian I. V., Ciambur B. C., Forbes D. A., Davies R. L., 2017, ApJ, 840, 68

Gunn J. E., Gott J. Richard I., 1972, ApJ, 176, 1

Gunn J. E., et al., 2006, AJ, 131, 2332

Haggar R., Kuchner U., Gray M. E., Pearce F. R., Knebe A., Yepes G., Cui W., 2022, Monthly Notices of the Royal Astronomical Society, 518, 1316

Haines C. P., et al., 2015, ApJ, 806, 101

Haines C., et al., 2023, The Messenger, 190, 31

Hartsuiker L., Ploeckinger S., 2020, MNRAS, 491, L66

Häußler B., et al., 2013, MNRAS, 430, 330

Hayward C. C., Hopkins P. F., 2017, MNRAS, 465, 1682

Hernández-Fernández J. D., Mendes de Oliveira C., 2015, MNRAS, 453, 1965

Herpich F., Stasińska G., Mateus A., Vale Asari N., Cid Fernandes R., 2018, Monthly Notices of the Royal Astronomical Society, 481, 1774

Hickson P., 1982, The Astrophysical Journal, 255, 382

Hickson P., Kindl E., Huchra J. P., 1988, ApJ, 331, 64

Hickson P., Mendes de Oliveira C., Huchra J. P., Palumbo G. G., 1992, ApJ, 399, 353

Hopkins P. F., Lauer T. R., Cox T. J., Hernquist L., Kormendy J., 2009, ApJS, 181, 486

Hubble E. P., 1925, Popular Astronomy, 33

Hubble E., 1926, Contributions from the Mount Wilson Observatory / Carnegie Institution of Washington, 324, 1

Hubble E. P., 1936, Realm of the Nebulae

Hunter D. A., Elmegreen B. G., 2004, AJ, 128, 2170

Hunter D. A., Gallagher J. S., Rautenkranz D., 1982, ApJS, 49, 53

Jiang C. Y., Jing Y. P., Faltenbacher A., Lin W. P., Li C., 2008, ApJ, 675, 1095

Johnson K. E., Hibbard J. E., Gallagher S. C., Charlton J. C., Hornschemeier A. E., Jarrett T. H., Reines A. E., 2007, AJ, 134, 1522

Johnson R. E., Markevitch M., Wegner G. A., Jones C., Forman W. R., 2010, ApJ, 710, 1776

Jones C., Forman W., 1999, ApJ, 511, 65

Jones L. R., Ponman T. J., Horton A., Babul A., Ebeling H., Burke D. J., 2003, MNRAS, 343, 627

Jones M. G., et al., 2018, A&A, 609, A17

Jones M. G., et al., 2022, arXiv e-prints, p. arXiv:2211.15687

Jones M. G., et al., 2023, A&A, 670, A21

Kauffmann G., Haehnelt M., 2000, MNRAS, 311, 576

Kauffmann G., et al., 2003a, MNRAS, 341, 33

Kauffmann G., et al., 2003b, MNRAS, 346, 1055

Kauffmann G., White S. D. M., Heckman T. M., Ménard B., Brinchmann J., Charlot S., Tremonti C., Brinkmann J., 2004, MNRAS, 353, 713

Kelkar K., et al., 2023, A&A, 680, A54

Kelvin L. S., et al., 2012, MNRAS, 421, 1007

Kennicutt Robert C. J., 1998, ARA&A, 36, 189

Kewley L. J., Dopita M. A., Sutherland R. S., Heisler C. A., Trevena J., 2001, ApJ, 556, 121

Khoperskov S., Haywood M., Di Matteo P., Lehnert M. D., Combes F., 2018, A&A, 609, A60

Kormendy J., Bender R., 1996, ApJL, 464, L119

Kormendy J., Illingworth G., 1982, ApJ, 256, 460

La Barbera F., de Carvalho R. R., de La Rosa I. G., Lopes P. A. A., Kohl-Moreira J. L., Capelato H. V., 2010, MNRAS, 408, 1313

Lacy M., et al., 2004, ApJS, 154, 166

Lambas D. G., Alonso S., Mesa V., O'Mill A. L., 2012, A&A, 539, A45

Lauer T. R., et al., 1995, AJ, 110, 2622

Law D. R., et al., 2021, ApJ, 915, 35

Lee B. C., et al., 2004, AJ, 127, 1811

Lenkić L., et al., 2016, MNRAS, 459, 2948

Lequeux J., Peimbert M., Rayo J. F., Serrano A., Torres-Peimbert S., 1979, A&A, 80, 155

Li C., Kauffmann G., Heckman T. M., Jing Y. P., White S. D. M., 2008, MNRAS, 385, 1903

Lian J., et al., 2018, MNRAS, 476, 3883

Lian J., Thomas D., Li C., Zheng Z., Maraston C., Bizyaev D., Lane R. R., Yan R., 2019, MNRAS, 489, 1436

Lima-Dias C., et al., 2021, MNRAS, 500, 1323

Lima E. V. R., et al., 2022, Astronomy and Computing, 38, 100510

Lintott C. J., et al., 2008, Monthly Notices of the Royal Astronomical Society, 389, 1179

Lisenfeld U., Appleton P. N., Cluver M. E., Guillard P., Alatalo K., Ogle P., 2014, A&A, 570, A24

Lopes P. A. A., Ribeiro A. L. B., Rembold S. B., 2013, Monthly Notices of the Royal Astronomical Society, 437, 2430

Lopes P. A. A., Ribeiro A. L. B., Brambila D., 2024, MNRAS, 527, L19

Lovisari L., Ettori S., Gaspari M., Giles P. A., 2021, Universe, 7, 139

Malmquist K., 1922, Arkiv Mat. Astr. Fys., 16, 23

Mamon G. A., 1986, ApJ, 307, 426

Mamon G. A., 1992, ApJL, 401, L3

Maraston C., Strömbäck G., 2011, MNRAS, 418, 2785

Martig M., Bournaud F., Teyssier R., Dekel A., 2009, ApJ, 707, 250

Martin D. C., et al., 2007, ApJS, 173, 342

Martinez M., del Olmo A., Perea J., Coziol R., 2007, ESO ASTROPHYSICS SYMPOSIA, p. 163–167

Martínez M. A., del Olmo A., Coziol R., Focardi P., 2008, The Astrophysical Journal, 678, L9–L12

Martínez M. A., Del Olmo A., Coziol R., Perea J., 2010, The Astronomical Journal, 139, 1199–1211

McConnachie A. W., Ellison S. L., Patton D. R., 2008, MNRAS, 387, 1281

McConnachie A. W., Patton D. R., Ellison S. L., Simard L., 2009, MNRAS, 395, 255

Medling A. M., et al., 2018, Monthly Notices of the Royal Astronomical Society, 475, 5194

Mendel J. T., Ellison S. L., Simard L., Patton D. R., McConnachie A. W., 2011, MNRAS, 418, 1409

Mendes de Oliveira C., Hickson P., 1994, ApJ, 427, 684

Mendes de Oliveira C., Amram P., Plana H., Balkowski C., 2003, AJ, 126, 2635

Mendes de Oliveira C., et al., 2019, Monthly Notices of the Royal Astronomical Society, 489, 241

Mihos J. C., Hernquist L., 1996, ApJ, 464, 641

Montaguth G. P., et al., 2023, Monthly Notices of the Royal Astronomical Society, 524, 5340

Montaguth G. P., et al., 2024, arXiv e-prints, p. arXiv:2406.14671

Monteiro-Oliveira R., Cypriano E. S., Vitorelli A. Z., Ribeiro A. L. B., Sodré L., Dupke R., Mendes de Oliveira C., 2018, MNRAS, 481, 1097

Monteiro-Oliveira R., Doubrawa L., Machado R. E. G., Lima Neto G. B., Castejon M., Cypriano E. S., 2020, MNRAS, 495, 2007

Moore B., Katz N., Lake G., Dressler A., Oemler A., 1996a, Nature, 379, 613

Moore B., Katz N., Lake G., Dressler A., Oemler A., 1996b, Nature, 379, 613

Morgan W. W., Mayall N., 1957, Publications of the Astronomical Society of the Pacific, 69, 291

Morokuma-Matsui K., Kodama T., Morokuma T., Nakanishi K., Koyama Y., Yamashita T., Koyama S., Okamoto T., 2021, ApJ, 914, 145

Moura T. C., et al., 2020, MNRAS

Mulcahey C. R., et al., 2022, A&A, 665, A144

Noll S., Burgarella D., Giovannoli E., Buat V., Marcillac D., Muñoz-Mateos J. C., 2009, A&A, 507, 1793

Oda S., Ueda Y., Tanimoto A., Ricci C., 2018, The Astrophysical Journal, 855, 79

Olave-Rojas D. E., Cerulo P., Araya-Araya P., Olave-Rojas D. A., 2023, MNRAS, 519, 4171

Osterbrock D. E., 1989, Astrophysics of gaseous nebulae and active galactic nuclei

Oxland M., Parker L. C., de Carvalho R. R., Sampaio V. M., 2024, MNRAS, 529, 3651

Pallero D., Gómez F. A., Padilla N. D., Torres-Flores S., Demarco R., Cerulo P., Olave-Rojas D., 2019, MNRAS, 488, 847

Pan Z., Kong X., Fan L., 2013, ApJ, 776, 14

Pandge M. B., Monteiro-Oliveira R., Bagchi J., Simionescu A., Limousin M., Raychaudhury S., 2019, MNRAS, 482, 5093

Park C., Hwang H. S., 2009, ApJ, 699, 1595

Paulino-Afonso A., Sobral D., Darvish B., Ribeiro B., Smail I., Best P., Stroe A., Cairns J., 2020, A&A, 633, A70

Peng C. Y., Ho L. C., Impey C. D., Rix H.-W., 2002, AJ, 124, 266

Peng C. Y., Ho L. C., Impey C. D., Rix H.-W., 2010a, AJ, 139, 2097

Peng Y.-j., et al., 2010b, ApJ, 721, 193

Peng Y., Maiolino R., Cochrane R., 2015, Nature, 521, 192

Pérez-Montero E., Contini T., 2009, MNRAS, 398, 949

Poliakov D., Mosenkov A. V., Brosch N., Koriski S., Rich R. M., 2021, Monthly Notices of the Royal Astronomical Society, 503, 6059

Pompei E., Dahlem M., Iovino A., 2007, A&A, 473, 399

Pranger F., Trujillo I., Kelvin L. S., Cebrián M., 2017, MNRAS, 467, 2127

Ribeiro A. L. B., de Carvalho R. R., Capelato H. V., Zepf S. E., 1998, ApJ, 497, 72

Roberts I. D., van Weeren R. J., McGee S. L., Botteon A., Ignesti A., Rottgering H. J. A., 2021, A&A, 652, A153

Rose J., 1977, The Astrophysical Journal, 211, 311

Roychowdhury S., et al., 2022, ApJ, 927, 20

Rubin V. C., Ford W. Kent J., 1970, ApJ, 159, 379

Rubin V. C., Hunter D. A., Ford W. Kent J., 1991, ApJS, 76, 153

Sabater J., Verdes-Montenegro L., Leon S., Best P., Sulentic J., 2012, A&A, 545, A15

Sabater J., Best P. N., Argudo-Fernández M., 2013, MNRAS, 430, 638

Sabater J., Best P. N., Heckman T. M., 2015, MNRAS, 447, 110

Salim S., Boquien M., Lee J. C., 2018, ApJ, 859, 11

Sánchez-Blázquez P., et al., 2006, MNRAS, 371, 703

Sánchez-Blázquez P., Rosales-Ortega F., Diaz A., Sánchez S. F., 2014, MNRAS, 437, 1534

Sanders D. B., Soifer B. T., Elias J. H., Madore B. F., Matthews K., Neugebauer G., Scoville N. Z., 1988, ApJ, 325, 74

Sarzi M., et al., 2006, MNRAS, 366, 1151

Schaefer A. L., et al., 2017, MNRAS, 464, 121

Schawinski K., Thomas D., Sarzi M., Maraston C., Kaviraj S., Joo S.-J., Yi S. K., Silk J., 2007, MNRAS, 382, 1415

Schlafly E. F., Finkbeiner D. P., 2011, ApJ, 737, 103

Schmitt H. R., 2001, The Astronomical Journal, 122, 2243

Sersic J. L., 1968, Atlas de Galaxias Australes

Shapley H., Curtis H. D., 1921, Bulletin of the National Research Council, 2, 171

Shimada M., Ohyama Y., Nishiura S., Murayama T., Taniguchi Y., 2000, The Astronomical Journal, 119, 2664–2685

Smee S. A., et al., 2013, AJ, 146, 32

Smirnov N., 1948, The annals of mathematical statistics, 19, 279

Sohn J., Hwang H. S., Lee M. G., Lee G.-H., Lee J. C., 2013a, The Astrophysical Journal, 771, 106

Sohn J., Hwang H. S., Lee M. G., Lee G.-H., Lee J. C., 2013b, ApJ, 771, 106

Sohn J., Geller M. J., Hwang H. S., Zahid H. J., Lee M. G., 2016, The Astrophysical Journal Supplement Series, 225, 23

Spergel D. N., et al., 2003, ApJS, 148, 175

Springel V., et al., 2005, Nature, 435, 629

Stasińska G., et al., 2008, MNRAS, 391, L29

Stephan M., 1877, Monthly Notices of the Royal Astronomical Society, 37, 334

Strateva I., et al., 2001, AJ, 122, 1861

Tago E., et al., 2006, Astronomische Nachrichten, 327, 365

Taverna A., Díaz-Giménez E., Zandivarez A., Mamon G. A., 2022, MNRAS, 511, 4741

Taverna A., Salerno J. M., Daza-Perilla I. V., Díaz-Giménez E., Zandivarez A., Martínez H. J., Ruiz A. N., 2023, MNRAS, 520, 6367

Taverna A., Díaz-Giménez E., Zandivarez A., Martínez H. J., Ruiz A. N., 2024, MNRAS, 527, 4821

Taylor E. N., et al., 2011, MNRAS, 418, 1587

Thomas D., et al., 2013, Monthly Notices of the Royal Astronomical Society, 431, 1383–1397

Tojeiro R., et al., 2013, Monthly Notices of the Royal Astronomical Society, 432, 359

Toomre A., Toomre J., 1972, ApJ, 178, 623

Torres-Flores S., de Oliveira C. M., Amram P., Plana H., Epinat B., Carignan C., Balkowski C., 2010, Astronomy & Astrophysics, 521, A59

Torres-Flores S., Mendes de Oliveira C., Plana H., Amram P., Epinat B., 2013a, Monthly Notices of the Royal Astronomical Society, 432, 3085

Torres-Flores S., Mendes de Oliveira C., Plana H., Amram P., Epinat B., 2013b, Monthly Notices of the Royal Astronomical Society, 432, 3085

Torres-Flores S., Amram P., Mendes de Oliveira C., Plana H., Balkowski C., Marcelin M., Olave-Rojas D., 2014, MNRAS, 442, 2188

Torres-Flores S., Mendes de Oliveira C., Amram P., Alfaro-Cuello M., Carrasco E. R., de Mello D. F., 2015, ApJL, 798, L24

Tovmassian H., Plionis M., Torres-Papaqui J. P., 2006, A&A, 456, 839

Tremonti C. A., et al., 2004, ApJ, 613, 898

Tully R. B., Fisher J. R., 1977, A&A, 54, 661

Tzanavaris P., et al., 2010, ApJ, 716, 556

Tzanavaris P., et al., 2014, The Astrophysical Journal Supplement Series, 212, 9

Variawa M. Z., Van Zyl T. L., Woolway M., 2022, IEEE Access, 10, 19539

Veilleux S., Osterbrock D. E., 1987, ApJS, 63, 295

Verdes-Montenegro L., Yun M. S., Williams B. A., Huchtmeier W. K., Del Olmo A., Perea J., 2001, A&A, 377, 812

Verdes-Montenegro L., Del Olmo A., Iglesias-Páramo J. I., Perea J., Vílchez J. M., Yun M. S., Huchtmeier W. K., 2002, A&A, 396, 815

Vika M., Bamford S. P., Häußler B., Rojas A. L., Borch A., Nichol R. C., 2013, MNRAS, 435, 623

Vika M., Vulcani B., Bamford S. P., Häußler B., Rojas A. L., 2015a, A&A, 577, A97

Vika M., Vulcani B., Bamford S. P., Häußler B., Rojas A. L., 2015b, Astronomy & Astrophysics, 577, A97

Vogt F. P. A., Dopita M. A., Borthakur S., Verdes-Montenegro L., Heckman T. M., Yun M. S., Chambers K. C., 2015, MNRAS, 450, 2593

Vulcani B., et al., 2014, MNRAS, 441, 1340

Wake D. A., et al., 2017, AJ, 154, 86

Walcher C. J., et al., 2019, The Messenger, 175, 12

Walker L. M., Johnson K. E., Gallagher S. C., Hibbard J. E., Hornschemeier A. E., Tzanavaris P., Charlton J. C., Jarrett T. H., 2010, AJ, 140, 1254

Walker L. M., Johnson K. E., Gallagher S. C., Charlton J. C., Hornschemeier A. E., Hibbard J. E., 2012, AJ, 143, 69

Walker L. M., et al., 2013, ApJ, 775, 129

Westfall K. B., et al., 2019a, AJ, 158, 231

Westfall K. B., et al., 2019b, AJ, 158, 231

Wetzel A. R., Tinker J. L., Conroy C., van den Bosch F. C., 2013, MNRAS, 432, 336

Whitmore B. C., Gilmore D. M., 1991, ApJ, 367, 64

UNIVERSIDAD
DE LA SERENA
CHILE

DEPARTAMENTO
ASTRONOMÍA